Eruptions and Equilibria in the Solar Corona

OLIVER EDWARD KINGDON RICE

Eruptions and Equilibria in the Solar Corona

Oliver E. K. Rice

A Thesis presented for the degree of
Doctor of Philosophy

Department of Mathematical Sciences
Durham University
United Kingdom
2020-2024

Abstract

The dynamic behaviour of the Solar Corona is dominated by its magnetic field. Complex magnetic structures can form in the corona which have the potential to catastrophically erupt, releasing vast amounts of energy in the form of coronal mass ejections – eruptions which can ultimately result in increased space weather activity. This thesis discusses a variety of numerical methods used to model the coronal magnetic field, including new approaches and techniques that could theoretically be used to improve space weather predictions.

The thesis consists of three relatively unconnected chapters. We first describe a new magnetic field model which calculates a magnetofrictional equilibrium with an imposed solar wind profile. These 'outflow fields' appear to approximate the real coronal magnetic field more closely than the established potential field model, take a similar time to compute, and avoid the need to impose an artificial source surface. Including the solar wind tends to increase the open magnetic flux compared to a potential field, reducing the well known discrepancy with in situ observations.

These equilibrium fields can be used as initial conditions for the bulk of our research, which is the application of both magnetofrictional and MHD models to investigate which quantity or quantities can best predict the loss of equilibrium of magnetic flux ropes – one of the primary mechanisms behind coronal mass ejections. Using a very large parameter study in 2.5D, we find that in our models eruptions can be predicted reliably using certain ratios between measurable diagnostic quantities.

We finish the thesis by describing in detail the development of a brand-new magnetofrictional model, based on an icosahedral grid. Although we have not yet used this code to its full potential, preliminary tests indicate that this new model could be useful in future simulations involving the prediction of magnetic flux rope eruptions.

Declaration

The work in this thesis is based on research carried out at the Department of Mathematical Sciences, Durham University, United Kingdom. No part of this thesis has been submitted elsewhere for any other degree or qualification and it is all my own work unless referenced to the contrary in the text.

Acknowledgements

First and foremost, I would like to thank my supervisor Anthony Yeates for generally being excellent. From the conception of the original project and securing my funding to our ever-helpful weekly meetings and bafflingly prompt replies to emails, I cannot imagine receiving better academic support from anybody. Above all I have appreciated the way in which we work together to solve problems, and the freedom I have had to explore my own ideas.

I'd also like to thank my Mum and Rai for their support and interest in my work (and not making me get a proper job), and Alice for always being there to help, especially when things aren't going so well and I feel a bit lost. And of course my Dad, who always requested I print copies of my papers so he could continually re-read them and show them proudly to his friends.

Outside of academia, I would not have chosen to stay in Durham were it not for the wonderful people that this city seems to attract. Continual pub trips, fires, concerts and weekends away with bellringers, musical people and others have made the last few years quite so enjoyable. I would not have changed anything.

Finally, I'd like to thank the staff and students in the Applied Maths Group for making the academic environment here so welcoming, and to the STFC for providing my funding.

Contents

Dedication

Dedicated to and in memory of my father, who would have loved to read this thesis.

CHAPTER 1

Introduction

1.1 The Sun

Being the most obvious thing in the sky, the source of all the energy in the solar system and indisputably essential for life on Earth, the Sun has been an object of interest to humanity for quite some time. Although for most of recorded history the ability of the Sun to produce seemingly limitless energy was attributed to the supernatural, we now know it to be sustained by nuclear fusion – the process by which hydrogen ions bond together to form helium, producing a large amount of energy as they do so. The Sun is primarily composed of hydrogen (around 73 %), with the remainder mainly helium [1]. Fusion can only take place where the pressure and temperature are very high, and as such it only occurs near the centre, in the core. The structure of the Sun is shown in Figure 1.1.

From about 0.25 to 0.7 solar radii (the solar radius being around 6.96×10^5km) we find the radiative zone, where fusion reactions are rare. Here radiative transfer and thermal conduction are the primary source of the heat transfer away from the core [2]. In this zone the plasma temperature falls from around 15×10^6 K down to 1.5×10^6 K. This region is relatively dynamically stable as the density gradient is

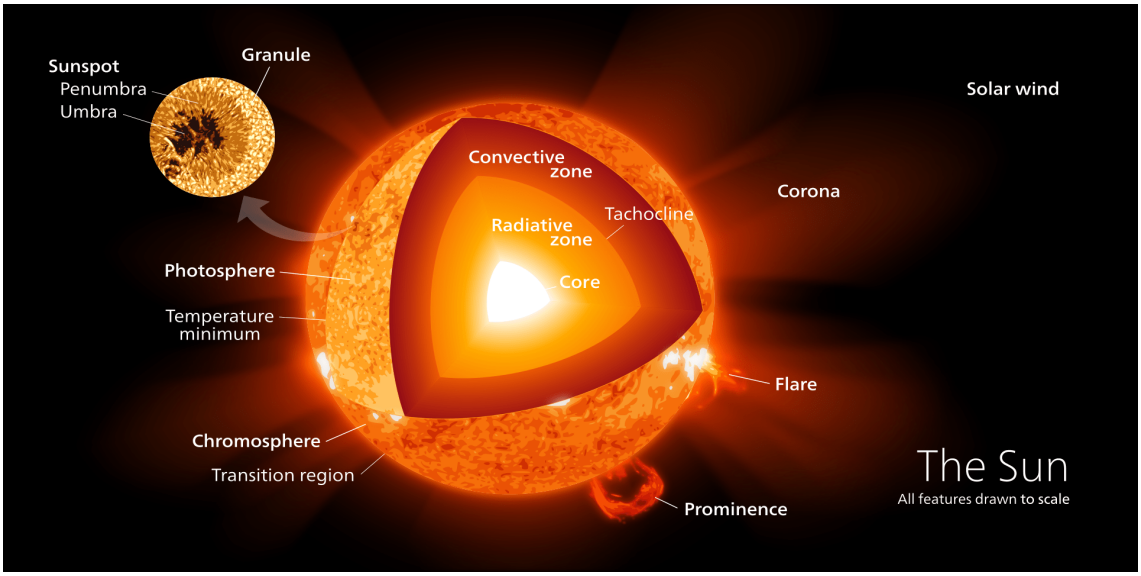

Figure 1.1: Cutaway diagram of the structure of the Sun, roughly to scale. From `https://www.universetoday.com/40631/parts-of-the-sun/`.

not particularly high. In contrast, further from the core (from around 0.7 radii to near the solar surface) we have the convective zone, where the plasma itself moves in large convection cells, transporting energy to the surface more quickly than radiation alone. It is this dynamic process that leads to many of the phenomena observed in the solar atmosphere. Of particular note is the process known as 'supergranulation', where the motion of convection cells beneath the solar surface cause large-scale flows on the photosphere. These flows drag the coronal magnetic field around, potentially causing it to become twisted. By the time the plasma has reached the top of the convective zone it has cooled considerably, to an average of 5.6×10^3 K.

The 'surface' of the Sun is not as well-defined as for a rocky planet. However, most of the light we observe on Earth has originated directly from the photosphere – the point at which the plasma ceases to be opaque. Hence most observations throughout history have been of the photosphere, and there is indeed much to be observed. Historically, the most notable features observed on the photosphere were sunspots: regions where the surface appears considerably darker than its surroundings. This is due to their being cooler, at around half the average surface temperature. The first records of sunspot observations are from ancient China [3], and they have been studied extensively ever since.

A particularly significant discovery was of the Solar Cycle, the 11-year period

over which solar activity waxes and wanes. At the peak of the solar cycle (known as solar maximum) we observe the largest number of sunspots, as well as increases in magnetic activity and frequency of solar flares. The concept of such a cycle was first hypothesised in the 18^{th} Century [4], although it took until George Hale [5] in 1908 for the link between sunspots and magnetic fields to be established. It was found reasonably soon afterwards that the overall magnetic field of the sun changes polarity after each cycle. The precise mechanism behind the cycles is still an active area of research, as is the prediction of the strength and timing of solar maxima.

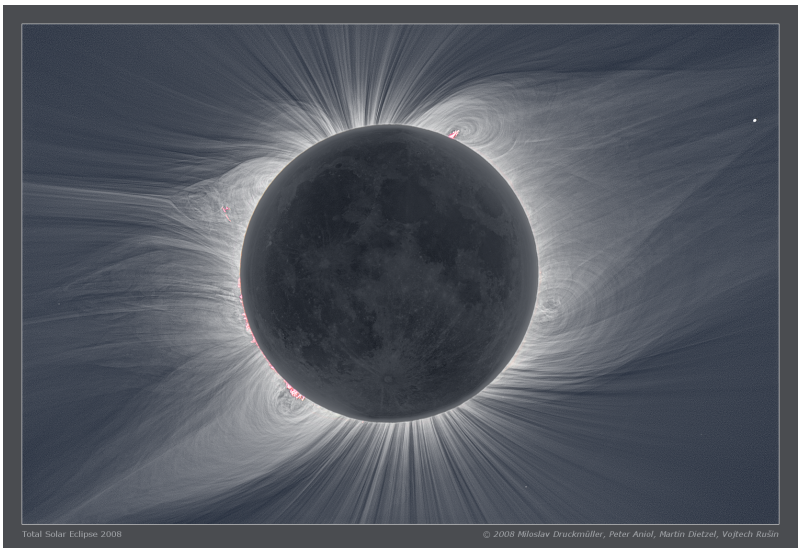

Figure 1.2: White light image of the corona taken during the 1st August 2008 total solar eclipse and processed by M. Druckmüller. We observe coronal holes at the poles, alongside coronal arcades, streamers and prominences. From `http://www.zam.fme.vutbr.cz/~druck/Eclipse/Index.htm`.

Above the photosphere lies the chromosphere, a relatively thin layer (a few thousand kilometres) which is transparent to most visible light. The chromosphere is less dense and slightly cooler than the photopshere, except near its upper boundary where the temperature rises rapidly through the 'transition region' into the solar atmosphere, or 'corona'. The corona is considerably less dense than the photosphere, and is also far hotter – up to several million Kelvin. This counter-intuitive temperature increase is of great interest to many researchers, who as yet have failed to reach a general consensus as to its cause. Historically, the corona was only visible during solar eclipses (as in Figure 1.2), when the far brighter photosphere is conveniently obscured by the Moon. Although eclipses are still arguably the best time to make

observations of the corona, with the aid of a coronagraph it can be observed at other times, and several classes of features have long been identified. The structure of the magnetic field in the corona varies throughout the solar cycle. At solar minimum (the 'quiet sun') the magnetic field in the corona has a relatively simple dipolar structure, like the field produced by a bar magnet aligned with the poles. Near the poles the magnetic field is open (the magnetic field lines do not connect back to the surface) – such locations are known as 'coronal holes'. Around solar maximum the corona is far more interesting, as the magnetic field structure is more complex and we are more likely to observe features such as coronal loops, magnetic flux ropes and solar flares.

In this thesis we focus almost entirely on the corona, and in particular the configuration of the magnetic field within it. Due to the low density of the plasma in this region, the magnetic field structure dominates the dynamics (as opposed to the fluid itself), with the development and application of the methods we use reflecting this. This dominance of the magnetic field can be quantified by calculating the 'plasma beta' (β) – the ratio of the fluid pressure to magnetic pressure. In the corona the plasma beta is generally very low. Of particular relevance to our research is the formation of magnetic flux ropes, which are twisted bundles of magnetic flux. These flux ropes can become unstable and result in coronal mass ejections (CMEs), violent events during which large amounts of plasma and energy are ejected from the Sun.

These events are significant enough that their effects can be felt on Earth, as the disturbances in the magnetic field propagate through interplanetary space (encouraged by the solar wind) and interact with the Earth's magnetic field. These interactions are responsible for increases in the intensity of the aurorae, and the effects from large CMEs have been known to damage satellites and adversely affect power distribution networks. Thus the prediction of such events would be advantageous, and is the primary justification behind our research.

1.2 Structure of this Thesis

We continue in this chapter by introducing existing work relevant to my PhD research. This includes the study of solar phenomena related (if only tangentially) to the main focus, including the differential rotation of the solar surface, the solar wind and coronal mass ejections (CMEs). We will then outline some of the most common magnetic field models, including potential field, source-surface (PFSS), magnetofriction and full magnetohydrodynamics (MHD). We then discuss the concept of magnetic helicity, and finish with a brief review of recent research particularly relevant to my own – in particular the proposed 'eruptivity index'.

Chapter 2 details the content of my first paper ([6]), which introduces a new method for the calculation of steady-state coronal magnetic fields, taking into account a prescribed solar wind outflow velocity. These fields take a similar time to compute as the established PFSS fields, but have some significant advantages.

In Chapter 3 we then discuss the main focus of my PhD research – predicting magnetic flux rope eruptions. We have undertaken extensive parameter studies using two modelling methods (magnetofriction and MHD) in both Cartesian and polar coordinates and have sought to determine theoretically measurable scalar quantities that can be used to make reliable predictions of future eruptions. The results from this study have been published in two papers ([7, 8]), with the first of these based on only the Cartesian magnetofrictional model, and the second introducing two new models, including full MHD. We have sucessfully identified several scalar quantities that appear to be good predictors of eruptivity, at least in our simple 2.5D cases, and note that the flux rope behaviour is generally consistent between magnetofriction and MHD.

Chapter 4 discusses my unpublished progress on a new magnetofrictional code, using an icosahedral grid to model the entire corona. This includes discussion of the advantages of using such a grid, the procedure for optimising the grid and the implementation of differential operators on a non-regular lattice. We compare the outflow fields calculated using the method from Chapter 2 to equilibria with solar wind outflow on the new icosahedral grid and find that the two models are in agreement.

We then conclude with a discussion on the possible uses of the existing research and how it can be extended further, with the ultimate aim being to make real-time predictions of flux rope eruptions and their subsequent effects on Earth.

1.3 Phenomena Relevant to Our Work

1.3.1 Solar Rotation

Unlike the Earth, the Sun is not a rigid body and as such it is free to rotate at different rates, depending on latitude. It rotates fastest at the equator, where a single rotation takes around 25 days, and is slowest at the poles where a single rotation takes around 38 days [9]. This considerable difference causes the photosphere to shear relative to itself, in turn dragging around the coronal magnetic field which is essentially attached to the photosphere at its base.

The rotation of the Sun was first observed by tracking the movements of sunspots on the surface, but as sunspots are rarely found at latitudes higher than 30° this is not sufficient to provide accurate measurements of rotation speeds at all latitudes. The use of magnetogram data (measuring the strength of the radial magnetic field) from the photosphere improved the precision of magnetic feature tracking on the surface such that differential rotation profiles could be estimated across the entire surface (eg. [10, 11]) although the long intervals between successive observations meant that there was considerable disagreement amongst the literature.

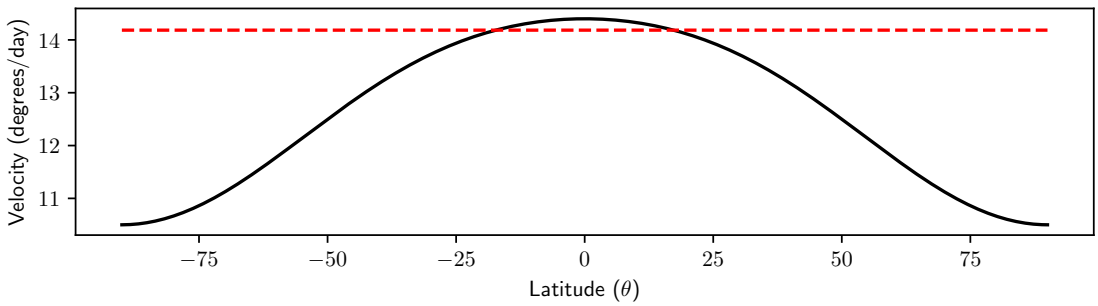

Figure 1.3: The photospheric rotation rate according to [9], in degrees/day as given by Equation 1.2, plotted in solid black. The Carrington rotation rate is plotted for reference in red.

In this thesis we adopt the frequently used differential rotation profile of [9], namely that the rotation rate at the surface is

$$2.902 - 0.464 \sin^2\theta - 0.328 \sin^4\theta \text{ microrad s}^{-1}, \tag{1.1}$$

or in more intuitive units

$$14.4 - 2.30 \sin^2\theta - 1.6 \sin^4\theta \text{ deg day}^{-1}, \tag{1.2}$$

where θ is the solar latitude, measured from the equator. This is plotted in Figure 1.3, along with the Carrington rotation rate for reference. This rotation profile was deduced from 15 years' worth of daily magnetograms obtained from the Mount Wilson telescope, essentially by comparing successive observations against each other. We use this profile for all of the simulations in this thesis which use spherical coordinates. Conversion to code units and the choice of a reference frame are discussed further for the specific models in Chapter 3.

In the context of our research, the differential rotation of the surface is significant as it causes coronal loops and arcades (regions where the magnetic field lines connect back to the surface) to become sheared as the footpoints (where the loops attach to the photosphere) move along the surface at different rates. This introduces the shear that is necessary to form magnetic flux ropes, among many other features.

Is it not particularly relevant to the research in this thesis, but it should be noted that this rotation profile does not extend uniformly all the way to the core of the Sun. The rotation rate in the upper regions of the convective zone is slightly higher than at the surface, and from around 0.7 solar radii ($0.7R_\odot$) down to the core the rotation speed is almost independent of latitude – the Sun rotates roughly uniformly at approximately the Carrington rate (one rotation per 25.38 days). Thus there is a region at around $0.7R_\odot$ known as the Tachocline [12] at which the rotation rate changes rapidly at most latitudes. These results studying regions deep within the Sun have been deduced relatively recently from helioseismology.

1.3.2 The Solar Wind

The Solar Wind, proposed and observed since the early 20th century but first justified by Eugene Parker in his seminal 1958 paper ([13]) is a supersonic stream of charged particles emanating from the Sun. Its presence not only affects the behaviour of the magnetic field in the solar corona, and as such is directly relevant to our research, but the flow outward from the Sun is responsible (at least partially) for accelerating plasma emitted from the Sun potentially as far Earth and beyond. This mechanism allows the behaviour of the solar magnetic field to influence the Earth's magnetosphere.

The models we use in our research do not require a sophisticated solar wind model, and as such although Solar Wind research is a vast field unto itself we do not delve into a great detail here. However, we do require justification for the imposed solar wind velocities (or boundary conditions) used in our models, and so we will derive the imposed velocity profile used in Chapters 2 and 3, repurposed from Parker's paper [13].

We begin by neglecting the effect of the magnetic field in the solar corona – the precise opposite of many assumptions used later in this thesis. We then seek to find a hydrodynamic equilibrium with a radial velocity profile that can later be explicitly combined with our magnetic field models. In order to find an equilibrium solution whereby the plasma pressure is zero at infinity, we assume a steady radial velocity field satisfying the equations of continuity, momentum and the ideal gas law:

$$\nabla \cdot (\rho \mathbf{v}) = 0 \tag{1.3}$$

$$\rho(\mathbf{v} \cdot \nabla)\mathbf{v} = -\nabla p + \rho \mathbf{g} \tag{1.4}$$

$$p = \rho R T, \tag{1.5}$$

where $\mathbf{v}$ is the velocity field, $\mathbf{g}$ the gravitational force (which can alternatively be expressed as the gradient of a potential $\mathbf{g} = \nabla\Psi$), ρ the density, T temperature, p gas pressure and R the ideal gas constant. We assume spherical coordinates, and radial dependence of the variable fields. The gravitational force is also radial and

equal to

$$\mathbf{g} = -\frac{GM_\odot}{r^2}\mathbf{e}_r, \tag{1.6}$$

with G the gravitational constant and $M_\odot$ the mass of the Sun. We assume a time-independent solution, and as such the continuity equation (1.3) for $\mathbf{v} = v(r)\mathbf{e}_r$ becomes

$$v(r)r^2\rho = D, \tag{1.7}$$

for some constant D. The momentum equation (1.4) reduces to

$$\rho v\frac{dv}{dr} = -\frac{dp}{dr} - \frac{GM_\odot\rho}{r^2}. \tag{1.8}$$

We now assume that the solar wind expansion is isothermal (there exist more complex models which relax this assumption but this is sufficient for our purposes). In this case, we can simplify the equations by re-expressing them in terms of the constant sound speed

$$c_s = \sqrt{\gamma\frac{p}{\rho}}, \tag{1.9}$$

where the constant γ is the specific heat capacity ratio. It appears that Parker sets γ to unity, so we shall here as well.

Using the sound speed equation to eliminate the pressure p we can obtain

$$\rho v\frac{dv}{dr} = -c_s^2\frac{d\rho}{dr} - \frac{GM_\odot\rho}{r^2} \tag{1.10}$$

$$v\frac{dv}{dr} = -c_s^2\frac{1}{\rho}\frac{d\rho}{dr} - \frac{GM_\odot}{r^2}. \tag{1.11}$$

To eliminate the density entirely we use the continuity equation:

$$\frac{1}{\rho}\frac{d\rho}{dr} = r^2 v\frac{d}{dr}\left(\frac{1}{r^2 v}\right) \tag{1.12}$$

leading to

$$v\frac{dv}{dr} = -c_s^2 r^2 v\frac{d}{dr}\left(\frac{1}{r^2 v}\right) - \frac{GM_\odot}{r^2}. \tag{1.13}$$

Expanding the derivative and rearranging:

$$v\frac{dv}{dr} = -c_s^2 r^2 v\left(-\frac{2}{r^3 v} - \frac{1}{r^2 v^2}\frac{dv}{dr}\right) - \frac{GM_\odot}{r^2} \tag{1.14}$$

$$v\frac{dv}{dr} = -c_s^2\left(-\frac{2}{r} - \frac{1}{v}\frac{dv}{dr}\right) - \frac{GM_\odot}{r^2} \tag{1.15}$$

$$\left(v - \frac{c_s^2}{v}\right)\frac{dv}{dr} = \frac{2c_s^2}{r} - \frac{GM_\odot}{r^2}. \tag{1.16}$$

Defining a 'critical radius' $r_c = \frac{GM_\odot}{2c_s^2}$ (at which the velocity equals the sound speed) allows this to be integrated more easily:

$$\left(v - \frac{c_s^2}{v}\right)\frac{dv}{dr} = \frac{2c_s^2}{r^2}(r - r_c) \tag{1.17}$$

$$\frac{v^2}{2} - c_s^2 \ln\left|\frac{v}{c_s}\right| = 2c_s^2\left(\ln\left|\frac{r}{r_c}\right| + \frac{r_c}{r} + \frac{C}{4}\right), \tag{1.18}$$

with some constant of integration C. The integration of the logarithms has been performed such that the velocity only appears relative to the sound speed, and the radius only relative to the critical radius. This is now an implicit equation for the radial velocity v, depending only on constants.

The choice of the constant C affects the nature of the solutions considerably. To see this, consider the contours of the function

$$f(r, v) = \frac{v^2}{c_s^2} - 2\ln\left|\frac{v}{c_s}\right| - 4\left(\ln\left|\frac{r}{r_c}\right| + \frac{r_c}{r}\right), \tag{1.19}$$

which are shown in Figure 1.4.

We can narrow down the possibilities for the constant C by considering these contour lines. A reasonable physical solution must have zero (or very small) velocity at the solar surface, and we also require that the velocity is positive throughout – this leaves two possibilities. The first are the contour lines in Figure 1.4 which start at the origin, increase in velocity as far as the critical radius r_c and then fall back to zero. These slow solutions are sometimes referred to as the 'solar breeze'. The second is the contour line starting at the origin and becoming supersonic ($v = c_s$) at the critical radius, with the velocity continuing to increase beyond this point.

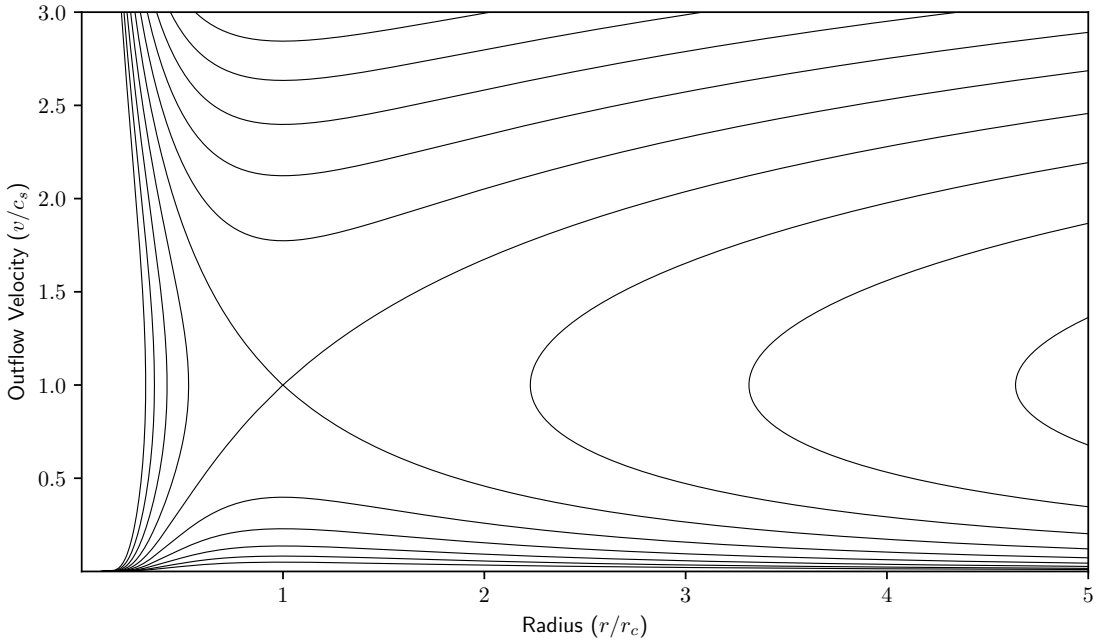

Figure 1.4: Contour plot of the function $f(r, v) = \frac{v^2}{c_s^2} - 2\ln|\frac{v}{c_s}| - 4(\ln|\frac{r}{r_c}| + \frac{r_c}{r})$, with each contour line representing a potential solution to the Parker Solar Wind Model. The solution for fast solar wind is the line passing through the origin and $(1, 1)$, corresponding to $f(r, v) = -3$.

This corresponds to the 'fast solar wind', and is the velocity profile we choose to approximate in our simulations.

Choosing the constant C such that $v(r_c) = c_s$ gives $C = -3$, so the implicit solution for the velocity is

$$\frac{v^2}{c_s^2} - 2\ln\left|\frac{v}{c_s}\right| = 4\left(\ln\left|\frac{r}{r_c}\right| + \frac{r_c}{r}\right) - 3. \tag{1.20}$$

We wish to find an implicit approximation of this for the implementation of the solar wind into our models.

At this point we need to find approximate values for the constant terms in this equation, to motivate neglecting some of the terms. Assuming the corona is isothermal, the sound speed c_s is given by the equation

$$c_s = \sqrt{\frac{k_b T_0}{m_p}}. \tag{1.21}$$

Taking the temperature of the corona to be 1×10^6 K [2], along with the Boltzmann

constant k_b and proton mass m_p gives $c_s \approx 91\,\mathrm{km/s}$. The critical radius r_c is then

$$r_c = \frac{GM_\odot}{2c_s^2}. \tag{1.22}$$

Using the gravitational constant G and the mass of the sun $M_\odot \approx 2 \times 10^{30}\,\mathrm{kg}$ gives a critical radius of $r_c \approx 11.5R_\odot$ (later in this thesis we use $r_c = 10R_\odot$, also commonly used in the literature – this makes no functional difference to our simulations). Thus, given our simulation domain only extends (in general) to $2.5R_\odot$ we can assume the ratio r/r_c is reasonably small, as is the ratio v/c_s. Thus we can neglect the first term in the implicit equation and can rearrange to give

$$-2\ln\left|\frac{v}{c_s}\right| = 4\left(\ln\left|\frac{r}{r_c}\right| + \frac{r_c}{r}\right) - 3 \tag{1.23}$$

$$\ln\left|\frac{v}{c_s}\right| = -2\ln\left|\frac{r}{r_c}\right| - 2\frac{r_c}{r} + \frac{3}{2} \tag{1.24}$$

$$\frac{v}{c_s} = A\left(\frac{r_c}{r}\right)^2 e^{-2\frac{r_c}{r}}, \tag{1.25}$$

with $A = e^{3/2}$. We can then rewrite this such that the velocity profile satisfies the upper boundary condition $v(r_1) = v_1$, for the upper boundary $r = r_1$ (usually $2.5R_\odot$):

$$v_{\mathrm{out}}(r) = v_1 \frac{r_1^2 \mathrm{e}^{-2r_c/r}}{r^2 \mathrm{e}^{-2r_c/r_1}}. \tag{1.26}$$

This is the velocity profile that we use in the coronal equilibria code (Chapter 2), and for the axisymmetric spherical models in the eruptivity criteria study (Chapter 3). Figure 1.5 compares this approximation to the 'true' Parker solution, and we see that the profiles are acceptably similar up to around $5R_\odot$ (which is larger than the domains used in our models). The precise nature of the velocity profile does not tend to affect the behaviour of the magnetofrictional models too greatly, in any case.

In fact, the solar wind term used in previous magnetofrictional studies (eg. [14])

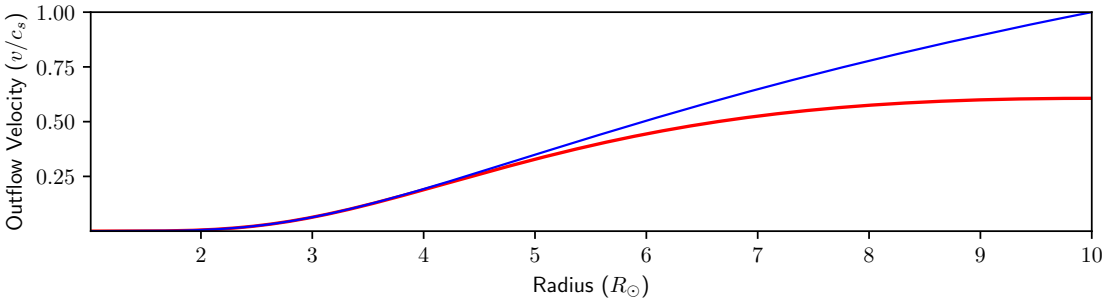

Figure 1.5: Comparison of the 'true' Parker solution (in blue) with our explicit approximation (in red), up to 10 Solar Radii (the critical radius).

instead use a simple power law, such as

$$v(r) = \left(\frac{r}{r_1}\right)^{11.5}, \tag{1.27}$$

which is not at all realistic but serves its intended purpose of encouraging eruptive behaviour.

As some of our simulations are in Cartesian coordinates, it seems prudent to check whether such a steady-state solution with positive vertical velocity can also be found in Cartesian geometry. In Chapter 3 we will discuss the boundary conditions necessary to encourage such a solution to form (in the absence of a magnetic field) but here we examine the analytical case.

We assume the continuity, momentum and ideal gas equations as for the spherical coordinate case, but now impose a gravitational field

$$\mathbf{g} = -\frac{G\rho}{1+y^2}\mathbf{e}_y, \tag{1.28}$$

where y is the vertical direction, assuming the domain is $0 < y < 1$, and G is a constant. Fixing this constant is difficult as the unrealistic geometry of the Cartesian domain means the radial coordinate in spherical space cannot map exactly to the vertical coordinate in Cartesian space. In any case, a realistic value of the gravitational force is higher than that which we use in the simulations, wherein we reach a compromise between computational time and physical accuracy. In these

coordinates the continuity and momentum equations become

$$v\rho = A, \tag{1.29}$$

for a constant A, and

$$\rho v\frac{dv}{dy} = -\frac{dp}{dy} - \frac{G\rho}{1+y^2}. \tag{1.30}$$

Proceeding in the same manner as the spherical coordinate case (eliminating the pressure and density) we obtain

$$v\frac{dv}{dy} = c_s^2\frac{1}{v}\frac{dv}{dy} - \frac{G}{1+y^2}, \tag{1.31}$$

or

$$(v - \frac{c_s^2}{v})\frac{dv}{dy} = -\frac{G}{1+y^2}. \tag{1.32}$$

This can be integrated to give an implicit equation for $v(y)$:

$$\frac{v^2}{2} - c_s^2\ln|\frac{v}{c_s}| = -c_s^2\int\frac{G}{1+y^2}\,dy = c_s^2(-G\arctan(y) + C). \tag{1.33}$$

Note that any solution $v(y)$ here also corresponds to a solution $-v(y)$, so care must be taken in the code to ensure the positive solution is naturally favoured, either using the boundary conditions or a sufficiently positive initial condition. Unlike in the spherical case, the only physical constraint on the constant C is that the solution is single-valued (the wind does not turn back on itself). This corresponds to

$$C \leq \frac{1+G\pi}{2}. \tag{1.34}$$

The contours of the function

$$f(y,v) = \frac{v^2}{2} - \ln|v| + \arctan(y) \tag{1.35}$$

are shown in Figure 1.6, with the case satisfying this inequality (the fastest-possible speed) highlighted in red. We observe that the positive physical solutions are nonzero at $y = 0$ and increase modestly toward the top of the domain, which is qualitatively

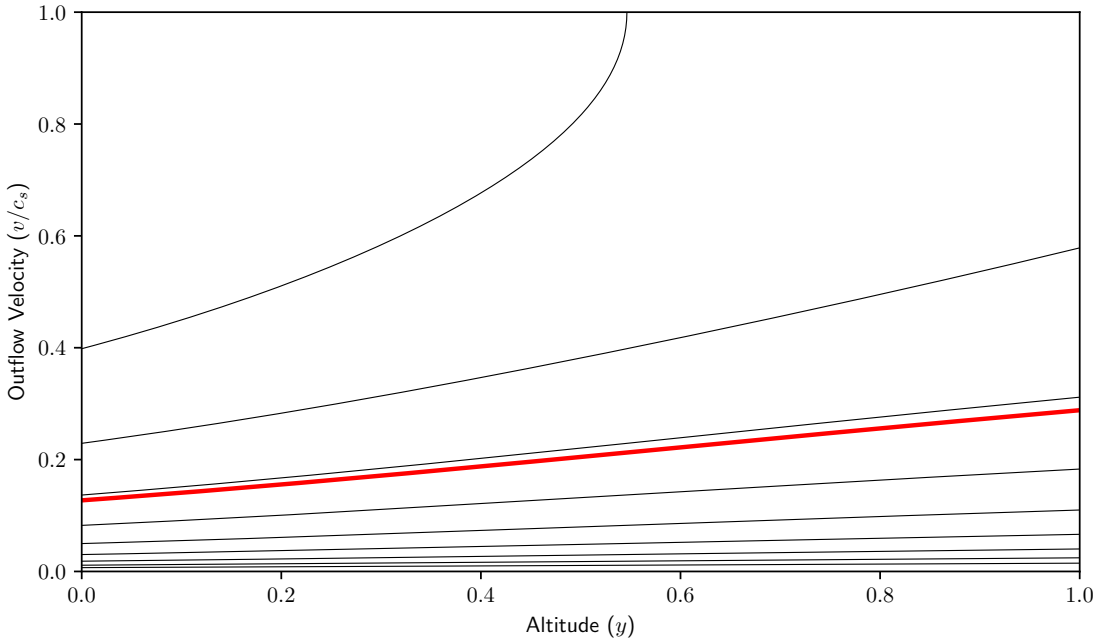

Figure 1.6: Contour plot of the function $f(y, v) = \frac{v^2}{2} - \ln|v| + \arctan(y)$, equivalent to the case with the constants $G = 1$ and $c_s = 1$. The fastest-possible physical solution is shown in red – all the contour lines below this are valid solutions.

quite different to the spherical coordinate case. This is to be expected to a degree, as the Cartesian domain can only correspond to a region relatively near to the solar surface. The equilibria reached by the LARE code in the absence of a magnetic field (see Chapter 3 for details) are consistent with these solutions.

1.3.3 Flux Ropes and CMEs

Much of the research in this thesis is on the study of eruptive events in the solar corona – specifically coronal mass ejections (CMEs). These are large ejections of heated plasma from the low corona out into interplanetary space ([15]), accompanied by significant changes to the magnetic field. The material ejected by an eruption can then propagate through interplanetary space and interact with the Earth's magnetic field, which can be potentially problematic. CMEs are associated with flaring (another phenomenon observed in the lower corona), but are distinguished by the ejection of plasma rather than merely light.

There are many mechanisms proposed for the large buildup and release of energy associated with CMEs. It is generally accepted that flows on the solar surface cause

the magnetic field in the lower corona to become twisted in various ways, with an accompanying increase in magnetic energy. Such magnetic configurations can be very complex, and can exist in quasi-equilibrium for some time. If this equilibrium is lost, an eruption occurs and the built-up energy is released relatively quickly, often in only a few hours ([16]). Figure 1.7 shows an image of a CME in progress, illustrating the sheer size of a large eruption.

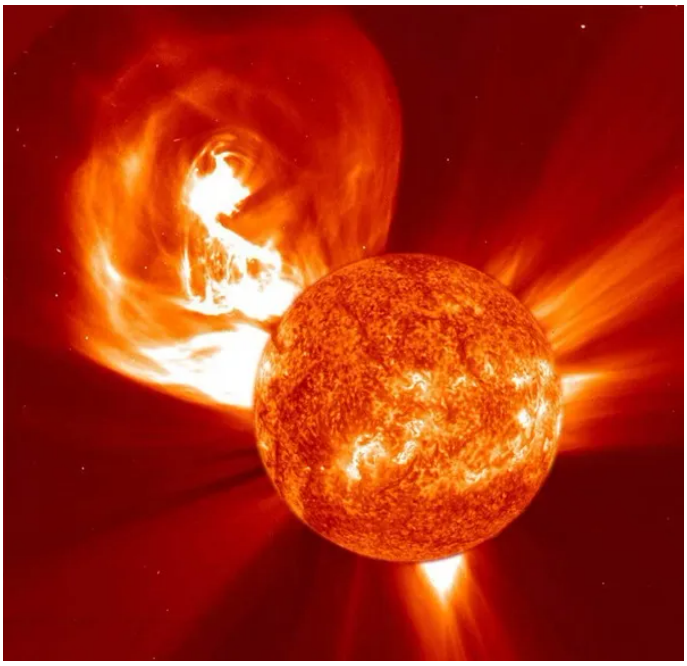

Figure 1.7: Image of a coronal mass ejection on 16th April 2012, taken by the Solar Dynamics Observatory (credit to NASA).

The proposed mechanisms for CMEs can be roughly categorised into two groups: the 'breakout model' and the 'flux injection model'. While the magnetic field is in equilibrium, the forces of magnetic pressure from a twisted magnetic field act upwards and are balanced by magnetic tension from an overlying magnetic field. In the breakout model (eg. [17]), magnetic reconnection removes overlying flux until these forces are no longer in balance, then resulting in a loss of equilibrium.

The flux injection model (eg. [18]) instead proposes that the topology of the magnetic field prior to a CME is in the form of a magnetic flux rope. Such a flux rope exists in quasi-equilibrium until the current, poloidal flux, twist, or some other parameter becomes too great and there is a catastrophic loss of equilibrium. Such instabilities are discussed further in Section 1.5. This theory more closely resembles

the models we employ in this thesis.

The poloidal flux in the rope itself originates either from shearing motions on the solar surface or emergence of the sheared structure from the convective zone. Shearing motions can occur due to various factors: either the differential rotation of the Sun or the effects of supergranulation on the surface due to motion below the photosphere. The mechanism behind flux rope formation is described in [19], with the rough process illustrated in Figure 1.8 (reproduced from that paper). A magnetic arcade sits above a line of zero polarity on the surface (the polarity inversion line, or PIL). Shearing then causes the magnetic footpoints to move in opposite directions on each side of the PIL, and additional flows towards the PIL then bring these footpoints together, forming the helical structure of a flux rope.

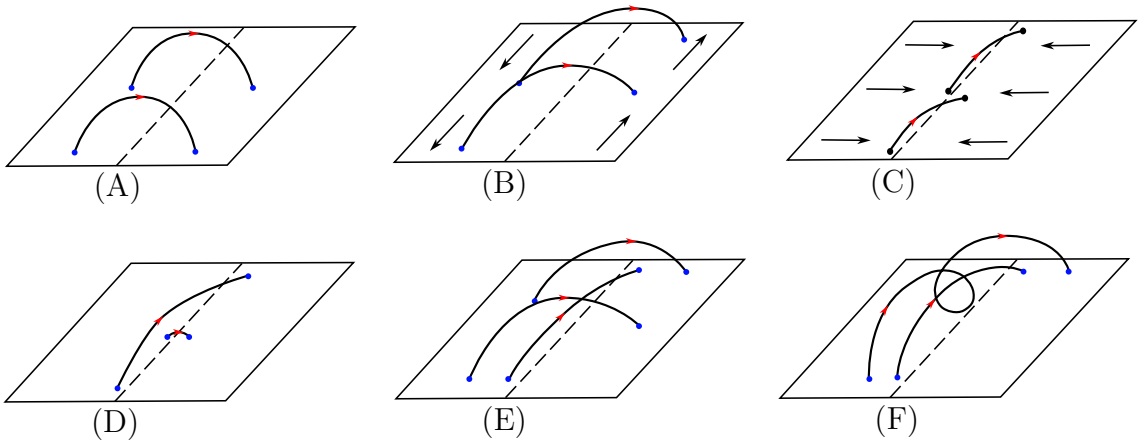

Figure 1.8: The formation of a flux rope due to shearing and flux cancellation of a magnetic arcade. In panel (B) the arcade is sheared along the PIL. The magnetic footpoints are then brought closer together in panel (C) due to the effect of photospheric diffusion. These footpoints can then reconnect at the PIL to form a twisted structure – a flux rope (in panel (F)). Recreated from Figure 1 of [19].

Once a flux rope has formed, these surface motions can continue to increase the size of the rope and the twist of the magnetic field, processes generally accompanied by corresponding increases in the magnetic energy and magnetic helicity. Eventually, if the magnetic pressure in the rope becomes high enough to resist both the magnetic tension from the overlying field and the gravitational force on the plasma within it, then the rope can erupt. However, it is equally possible for the flux cancellation at the PIL to result in the flux rope diffusing away into irrelevance without any rapid release of energy. The conditions for an eruption to occur are complex, and are

discussed in more detail in Section 1.5 and Chapter 3.

Determining the precise conditions for such a flux rope eruption is still very much an open question. Our work in Chapter 3 focuses on determining which, if any, measurable properties of the magnetic field can be used to predict an eruption.

1.4 A Brief Summary of Magnetic Field Models

This section will describe three models that can be used to represent the magnetic field in the solar corona. These models are used for different purposes throughout the work in this thesis, but are by no means a comprehensive list. Although not directly relevant to this thesis, we also discuss linear and non-linear force free fields as these models may be useful predictive tools in future, in combination with the results from Chapter 3.

1.4.1 MHD and Magnetofriction

MHD

The most physically accurate magnetic field models we employ in this thesis use the full set of magnetohydrodynamic equations. These combine the fluid equations with Maxwell's magnetic field equations. If one were to have infinite computing power and a perfectly comprehensive set of boundary conditions then full MHD would always be used, but this is naturally often not the case.

We start with the magnetic field: Maxwell's equations. The first of these is Faraday's Law of induction:

$$\frac{\partial \mathbf{B}}{\partial t} = -\nabla \times \mathbf{E} \tag{1.36}$$

which describes how the magnetic field $\mathbf{B}$ is influenced by an electric field $\mathbf{E}$.

We then have the low-freqency Ampère's Law:

$$\mu_0 \mathbf{j} = \nabla \times \mathbf{B}, \tag{1.37}$$

describing the magnetic field generated by an electric current density $\mathbf{j}$ (or vice

versa). The displacement current term from the more general Ampère's Law can be neglected for our purposes as the relevant velocities are far from relativistic. The constant μ_0 is the permittivity of free space, equal to $4\pi \times 10^{-7}\,\mathrm{N/A^2}$. In the interest of being mathematicians and the general simplification of things, we can set this constant to unity without loss of generality, although care must be taken with units throughout.

The third of the equations we use is the solenoidal condition, the constraint that we must not have magnetic monopoles. Mathematically, this means that the divergence of the magnetic field is zero:

$$\nabla \cdot \mathbf{B} = 0. \tag{1.38}$$

This is consistent with Faraday's Law without constraint on the electric field as the divergence of the curl of the electric field is zero. Extreme care must be taken in numerical models to ensure that the magnetic field remains divergence-free. Some models do this by an adjustment at each timestep (known as divergence cleaning, discussed in [20]), but all of the models in this thesis instead employ a vector potential $\mathbf{A}$, such that

$$\mathbf{B} = \nabla \times \mathbf{A}. \tag{1.39}$$

Faraday's Law can then be rewritten as

$$\frac{\partial \mathbf{A}}{\partial t} = -\mathbf{E} + \nabla\Phi, \tag{1.40}$$

which is if anything simpler to calculate than in the original form. The addition of the arbitrary vector potential $\nabla\Phi$ does not affect the dynamics and so is generally neglected from the equations – but it does play a significant part in the discussion on helicity in Section 1.6. The method used in the LARE2D code ([21], used in Chapter 3) to ensure this condition is more complex, but is fundamentally the same approach.

In addition to Maxwell's equations we also require Ohm's Law for electrically

conductive fluids:

$$\mathbf{E} = \eta\mathbf{j} - \mathbf{v} \times \mathbf{B}. \tag{1.41}$$

The first term here is proportional to the electric current density $\mathbf{j}$, with a constant resistivity η. The second term accounts for the relative motion of the fluid, which has a velocity field $\mathbf{v}$. In the solar corona, the effect of the resistivity is relatively small, and most of the electric field is generated from the motion of the fluid itself. These magnetic field equations (including the solenoidal condition) can be combined to form the MHD induction equation:

$$\frac{\partial \mathbf{B}}{\partial t} = \nabla \times (\mathbf{v} \times \mathbf{B}) + \eta \Delta \mathbf{B}. \tag{1.42}$$

If it were not for the velocity field $\mathbf{v}$, we would now have a closed system of equations. To compute the velocity (or more accurately the change in the velocity) we must also use the fluid equations. We start with the continuity and momentum equations:

$$\frac{D\rho}{Dt} = -\rho \nabla \cdot \mathbf{v} \tag{1.43}$$

$$\frac{\mathrm{D}\mathbf{v}}{\mathrm{D}t} = \frac{1}{\rho}\mathbf{j} \times \mathbf{B} - \frac{1}{\rho}\nabla P + \mathbf{g}, \tag{1.44}$$

introducing the density and pressure fields ρ and P. The gravitational force is imposed as $\mathbf{g}$. Note that this differs from the non-magnetic momentum equation by the addition of the Lorentz force term $\frac{1}{\rho}\mathbf{j} \times \mathbf{B}$, which describes the influence of the magnetic field on the fluid. The derivatives here are material derivatives (moving with the fluid), lending themselves to the velocity remap method used in the LARE code.

We can then close the system completely with the equation for the internal fluid energy ϵ (which is proportional to the fluid temperature) and the ideal gas law:

$$\frac{\mathrm{D}\epsilon}{\mathrm{D}t} = -\frac{P}{\rho}\nabla \cdot \mathbf{v} + \frac{\eta}{\rho}j^2 \tag{1.45}$$

$$\epsilon = \frac{P}{\rho(\gamma - 1)}, \tag{1.46}$$

where we observe internal energy contributions from both friction in the fluid motion and the magnetic energy lost from the resistivity η. The ideal gas law relates the pressure and density of the fluid and depends on the constant γ, the specific heat capacity ratio.

Solving such a large system of equations is understandably complex. One has three independently variable fields $(\mathbf{B}, \rho, \epsilon)$ which must be calculated at every timestep. One must also perform a remap step to deal with the material derivatives in the fluid equations. Another disadvantage of full MHD is the limitation on the timestep itself, due to the necessity of resolving sound waves. These restrictions can become especially problematic when the plasma beta (the ratio of fluid pressure to magnetic pressure) is low, as is the case in the majority of the corona. This limitation also exists in magnetofriction (see Chapter 4.1 for a full discussion) but generally to a lesser degree.

Despite these limitations, relatively recent improvements in computing capability have allowed for ever-more complex simulations. Although modelling the entire corona is now possible (eg. [22]), in general MHD simulations are used to focus on smaller regions and specific events. Indeed, for certain phenomena MHD is the only suitable option, such as for eruptive events whose mechanism relies heavily on either the behaviour of the fluid (such as shocks) or the peculiarities of magnetic reconnection (eg. [23]). However, it is hoped (and justified somewhat in Chapter 3) that the conditions for flux rope eruptions do not fundamentally depend on factors that can only be modelled in full MHD.

Of particular note to our work are the simulations of [24, 25], which model a fully three-dimensional flux rope in 3D Cartesian space. Altering the orientation of the overlying magnetic field results in flux ropes that may either remain stable indefinitely or erupt. The two scenarios could then be compared against one another to determine whether there are any observable precursors to an eruption. The speed limitation of these full 3D MHD simulations meant that only very few simulations could be run in this manner, however – a problem that we have sought to overcome with our simpler models. Similarly, [26] successfully model eruptions in full 3D MHD, but the small number of simulation runs thwarts any definitive conclusions

regarding the prediction of imminent eruptions.

Magnetofriction

The magnetofrictional method (MF) is used as the basis for most of the evolving magnetic field models in this thesis. Magnetofriction is computationally much simpler and faster than full MHD, whilst retaining enough of the physics to model the magnetic fields sufficiently accurately. In essence, we can remove the problems caused by the fluid equations by not including them. We instead close the system of Maxwell's equations and Ohm's law by using a 'frictional velocity' field $\mathbf{v}$, which can be calculated explicitly from the magnetic field $\mathbf{B}$.

This is possible as the timescale of the fluid motion is in general far faster than that of the magnetic field, and so in general the magnetic field can be considered as being in quasi-equilibrium. In particular, such an equilibrium will have a small Lorentz force $\mathbf{j} \times \mathbf{B}$, as is approximately the case throughout the much of the corona. Thus in the absence of external effects we wish to recreate magnetic field dynamics that will relax toward such a state.

To achieve this, we set the velocity field to be proportional to the Lorentz force itself:

$$\mathbf{v} = f(\mathbf{B})\, \mathbf{j} \times \mathbf{B}, \tag{1.47}$$

for some (yet to be determined) function of the magnetic field f. This approach dates back to [27], although in that case it was still in conjunction with a pressure field and so is not what we would now call magnetofriction. The method of [28] removes the fluid entirely, and also introduces the phrase 'ficticious fluid' to describe the resulting velocity field.

In addition to the convergence properties, we also require that the evolution of the magnetic field is independent of the overall magnetic field strength. To ensure this, we require that the velocity field itself is independent of the magnetic field strength, and assume a form similar to

$$\mathbf{v} = \frac{\mathbf{j} \times \mathbf{B}}{B^2}. \tag{1.48}$$

This is the form used by [29], in which the magnetofrictional method as we use it is formally proposed. The denominator in this form can lead to numerical problems at or near magnetic null points, however, as the current can be significantly larger than the magnetic field strength itself in some cases. Thus in the magnetofrictional models used in this thesis we use a 'softened' denominator

$$\mathbf{v} = \nu_0 \frac{\mathbf{j} \times \mathbf{B}}{B^2 + B_0^2 \delta e^{\frac{-B^2}{\delta B_0^2}}}, \tag{1.49}$$

where the denominator has a minimum value determined by the value of the small constant δ. There are naturally many alternative ways to achieve such a softening effect, such as by merely imposing a minimum value on the denominator. Here B_0 is a constant (in space, but not necessarily in time) factor proportional to the overall magnetic field strength. The effect of softening on a simple 1D magnetofrictional model is discussed in detail in [30]. The constant ν_0 controls the relaxation rate, and can depend on space if necessary (as in [14], for instance).

Unlike in MHD codes, the solar wind cannot appear self-consistently, and so it must be added on to this fictitious velocity term, so the overall equation for the 'velocity' is:

$$\mathbf{v} = \nu_0 \frac{\mathbf{j} \times \mathbf{B}}{B^2 + B_0 \delta e^{\frac{-B^2}{\delta B_0^2}}} + \mathbf{v}_{\text{out}}(r), \tag{1.50}$$

where the $\mathbf{v}_{\text{out}}$ term is the solar wind outflow profile as discussed in Section 1.3.2.

Thus the full set of magnetofrictional equations is

$$\frac{\partial \mathbf{B}}{\partial t} = -\nabla \times \mathbf{E} \tag{1.51}$$

$$\mathbf{E} = \eta \mathbf{j} - \mathbf{v} \times \mathbf{B} \tag{1.52}$$

$$\mu_0 \mathbf{j} = \nabla \times \mathbf{B} \tag{1.53}$$

$$\mathbf{v} = \nu_0 \frac{\mathbf{j} \times \mathbf{B}}{B^2 + B_0^2 \delta e^{\frac{-B^2}{\delta B_0^2}}} + v_{\text{out}}(r)\mathbf{e}_r. \tag{1.54}$$

Magnetofriction has been used with static boundary conditions to find equilibrium solutions of the magnetic field (force-free fields, eg. [29, 31]), but in this thesis we will use the model in conjunction with dynamic boundary conditions. Although

the coronal magnetic field relaxes slowly compared to the fluid motion, it is still far faster than the motion of the underlying photospheric surface, to which the magnetic field is essentially attached. Thus it is reasonable to approximate the field a series of quasi-static equilibria. This approach was first developed by [32], and has been used extensively for various applications (eg. [33–41]).

Similar dynamic boundary conditions can also be used with full MHD (eg. [42]), although with further limitations such as the necessity of determining boundary conditions for the fluid in addition to the magnetic field.

The magnetofrictional method can be combined with complex lower boundary data influenced by observations of the magnetic field on the solar surface (such as from the Heliospheric and Magnetic Imager (HMI) instrument on the Solar Dynamics Observatory) to model the evolution of the magnetic field throughout the entire corona. Notably, magnetofriction applied in this way allows for the formation of magnetic flux ropes and their subsequent eruption (or failure to do so), with behaviour qualitatively very similar to full MHD equivalents. Moreover, it has also been shown (eg. [43, 44]) that in numerical simulations flux ropes lose equilibrium at the same point in both MHD and magnetofrictional simulations. This in support of [28] (based on the analysis of [45]), who assert that the linear stability properties of MHD and magnetofriction are the same (although they also note that this result is not significant enough in itself to draw any notable conclusions). Although any stable equilibria in MHD are stable in MF, oscillations around such an equilibrium are possible in MHD, whereas in MF these will be supercritically damped due to the equations being parabolic rather than hyperbolic.

The magnetofrictional models described in this thesis follow directly from the implementation of the existing magnetofrictional code developed at St Andrews and Durham universities, known as DumFric (Durham magneto-Friction). In Chapter 3 we use two 2.5D magnetofrictional models, both in Cartesian and spherical geometries. In Chapter 4 we describe the development of a new magnetofrictional code on an icosahedral grid. This seeks to remove one of the limitations of existing models – namely that as the spherical grid converges at the poles the condition on the numerical timestep becomes more restrictive, which either results in unrealistic

relaxation rates or longer than ideal computational times.

Magnetic Boundary Conditions

As mentioned previously, one of the advantages of magnetofriction over MHD is that the boundary conditions are much simpler, only requiring conditions on the magnetic field. In MHD we also require boundary conditions on the fluid, which are discussed in Chapter 3 when introducing our MHD model.

In general, we impose magnetic boundary conditions such that the current parallel to the boundaries is zero, which under the MF equations prevents energy flow through the boundaries. This is enforced by setting the values of the magnetic field in a layer of ghost cells just outside the boundary. The remaining magnetic field values in the ghost cells (those perpendicular to the boundary) can then be determined using the solenoidal condition. The imposed solar wind velocity encourages the magnetic field to become radial near the top boundary, but imposing a radial condition explicitly is at odds with allowing for flux rope eruptions, during which the magnetic field clearly should not be radial when the rope itself passes through the upper boundary.

With such static boundary conditions the system will eventually relax into a force-free state. In order to model dynamic coronal phenomena we add additional conditions to the lower boundary. Motions on the solar surface can be represented by directly replacing the frictional velocity field $\mathbf{v}$ on the lowermost cell with the velocity field of choice. In the simulations described in this thesis the only imposed velocity is that of the solar differential rotation (see Section 1.3.1), although it is also common to model meridional flow.

The other significant dynamic boundary condition models the effect of supergranular diffusion. The motion of the supergranules effectively increases the magnetic diffusion rate in the photosphere to be significantly higher than in the corona ([32]). Thus on the lower boundary we replace the standard magnetofrictional term for the electric field $\mathbf{E}$ with values equivalent to 2D diffusion of the radial component of the magnetic field constrained to the surface. In Cartesian coordinates (with y the

vertical direction) this is equivalent to

$$\frac{\partial B_y}{\partial t} = -\eta_0 \left(\frac{\partial^2 B_y}{\partial x^2} + \frac{\partial^2 B_y}{\partial z^2} \right) = -(\nabla \times \mathbf{E})_y = \frac{\partial E_z}{\partial x} - \frac{\partial E_x}{\partial z}, \tag{1.55}$$

which can be satisfied by setting

$$E_x(x, 0, z) = \eta_0 \frac{\partial B_y(x, 0, z)}{\partial z} \mathbf{e}_x \tag{1.56}$$

$$E_z(x, 0, z) = -\eta_0 \frac{\partial B_y(x, 0, z)}{\partial x} \mathbf{e}_z, \tag{1.57}$$

where η_0 is a constant 'supergranular diffusion rate'. In the 2.5D simulations discussed in Chapter 3 there is additionally no dependence on the z coordinate so one of these terms disappears.

The specific implementation of the magnetofrictional boundary conditions in our work is described in more detail in Chapter 3, in addition to a discussion on how these conditions can be modified to work in conjunction with full MHD, which is necessary when making direct comparisons between the two methods as we seek to do.

The Staggered Grid

Numerically, our MF models use a finite difference scheme on a 'staggered grid' ([46]), which is a natural choice for magnetic field calculations as it both allows for the enforcement of the solenoidal condition to machine precision and derivatives which are equivalent to a central difference scheme. In brief, the staggered grid means that different field quantities are saved in different locations in space.

To motivate this, consider a regular Cartesian grid in 3D. Each vertex (grid point) is assigned an integer numerical index, and the points halfway between each vertex are assigned half-integer indices. The magnetic field $\mathbf{B}$ is stored with each component at the centre of a different grid face, ie.

$$B_x^{i,j+1/2,k+1/2}, B_y^{i+1/2,j,k+1/2}, B_z^{i+1/2,j+1/2,k}, \tag{1.58}$$

with the magnetic flux through each face being equal to

$$B_x^{i,j+1/2,k+1/2}\Delta y\Delta z, B_y^{i+1/2,j,k+1/2}\Delta x\Delta z, B_z^{i+1/2,j+1/2,k}\Delta x\Delta y \tag{1.59}$$

respectively, for grid resolutions of Δx in the x direction, etc.. The current density $\mathbf{j}$ and vector potential $\mathbf{A}$ are stored on grid lines:

$$j_x^{i+1/2,j,k}, j_y^{i,j+1/2,k}, j_z^{i,j,k+1/2}, \tag{1.60}$$

or as line integrals

$$j_x^{i+1/2,j,k}\Delta x, j_y^{i,j+1/2,k}\Delta y, j_z^{i,j,k+1/2}\Delta z, \tag{1.61}$$

(with $\mathbf{A}$ being identical). The curl operator (eg. $\mathbf{B} = \nabla \times \mathbf{A}$) is calculated using Stokes' Theorem:

$$\iint \nabla \times \mathbf{A}\, dA = \oint \mathbf{A}\, dl, \tag{1.62}$$

where the left hand side is an integral over the area of the respective face, and the right hand side is the sum of the line integrals around its edges.

Numerically, on the staggered grid this translates (shown here for the magnetic flux in the x direction) to

$$B_x^{i,j+1/2,k+1/2}\Delta y\Delta z = A_y^{i,j+1/2,k}\Delta y + A_z^{i,j+1,k+1/2}\Delta z - A_y^{i,j+1/2,k+1}\Delta y - A_z^{i,j,k+1/2}\Delta z, \tag{1.63}$$

or, dividing through by the areas:

$$B_x^{i,j+1/2,k+1/2} = \frac{1}{\Delta y}(A_z^{i,j+1,k+1/2} - A_z^{i,j,k+1/2}) - \frac{1}{\Delta z}(A_y^{i,j+1/2,k+1} - A_y^{i,j+1/2,k}), \tag{1.64}$$

which is merely a central difference scheme (second-order accurate). The equivalents in the other coordinate directions are:

$$B_y^{i+1/2,j,k+1/2} = -\frac{1}{\Delta x}(A_z^{i+1,j,k+1/2} - A_z^{i,j,k+1/2}) + \frac{1}{\Delta z}(A_x^{i+1/2,j,k+1} - A_x^{i+1/2,j,k}), \tag{1.65}$$

$$B_z^{i+1/2,j+1/2,k} = \frac{1}{\Delta x}(A_y^{i+1,j+1/2,k} - A_y^{i,j+1/2,k}) - \frac{1}{\Delta y}(A_x^{i+1/2,j+1,k} - A_x^{i+1/2,j,k}). \tag{1.66}$$

The curl operator for $\mathbf{j} = \nabla \times \mathbf{B}$ is similar but shifted by half a cell in each respective direction. Note that the solenoidal condition on the magnetic field is automatically enforced – the net magnetic flux through each grid cell is given by

$$\begin{aligned}\nabla \cdot \mathbf{B}^{i+1/2,j+1/2,k+1/2} = (B_x^{i+1,j+1/2,k+1/2} - B_x^{i,j+1/2,k+1/2})\Delta y \Delta z + \\ (B_y^{i+1/2,j+1,k+1/2} - B_y^{i+1/2,j,k+1/2})\Delta x \Delta z + \\ (B_z^{i+1/2,j+1/2,k+1} - B_z^{i+1/2,j+1/2,k})\Delta x \Delta y = 0. \quad (1.67)\end{aligned}$$

This is equivalent to adding all the line integrals of $\mathbf{A}$ around the grid cell together, but in both directions – summing precisely to zero over each cell. On irregular grids (such as in Chapter 4) this still holds true and so this approach is useful for maintaining a strict divergence-free condition.

As the current density $\mathbf{j}$ is stored in the same place on the grid as the vector potential $\mathbf{A}$, the diffusive term $\mathbf{E} = \eta \mathbf{j}$ can be computed with no numerical trickery. However, the ideal location for the magnetofrictional term $\mathbf{v}$ is not as clear. In order to compute the cross product $\mathbf{j} \times \mathbf{B}$, at least one (and probably both) of these fields will need to be averaged to a different location on the grid. This may compromise the accuracy of the central-difference derivatives. A simple averaging of both the magnetic field and current density can be used on a regular grid, but a more complex approach must be taken for our implementation described in Chapter 4.

1.4.2 PFSS (Potential Field, Source Surface)

Potential field models are the simplest way to model the solar corona while still retaining some degree of realism. The PFSS model was first used by [47] and [48] in the late 1960s. The model seeks to calculate a potential magnetic field which satisfies a lower boundary condition at the base of the corona, which in practice is usually provided by magnetogram data. Such a field takes the form

$$\mathbf{B} = \nabla \Phi \quad (1.68)$$

for some scalar field Φ. Combined with the solenoidal condition $\nabla \cdot \mathbf{B} = 0$ we find that Φ is a solution to Laplace's equation

$$\nabla^2 \Phi = 0. \tag{1.69}$$

Such a magnetic field is current-free (and hence force free) as the curl of a gradient is zero. This is in fact a reasonable first approximation for much of the solar corona, where the average current density away from active regions is generally small.

The popularity of the PFSS model is due to its comparative computational simplicity and the fact that the only required boundary data is a radial magnetogram on the surface, compared to more physically accurate models which require either more data or more assumptions. In fact, despite the enormous increases in computing capability since their inception, PFSS solutions of the corona are still widely used for a number of applications, albeit with various additions and modifications to the original models (eg. [49, 50]). In particular, models based on PFSS framework are among the most widely used for space weather prediction ([51]).

The 'source-surface' part of the name comes from the chosen upper boundary condition. PFSS models specify that the magnetic field lines are purely radial at a given radius, often taken to be $2.5R_\odot$. The justification for this is that the solar wind opens out the potential arcades such that they become radial at around this altitude. However, there are significant discrepancies between this assumption and physical observations of the corona – which our work in Chapter 2 seeks to address.

Previous attempts have been made to improve on the standard PFSS model, such as experimenting with a nonspherical source surface (eg. [49, 52]), or allowing the source surface height to vary with time (eg. [53]). The latter authors showed that in general a suitable source surface height can be chosen to match open flux observations at any given time, but this is not of any use for predictions as the optimum source surface radius varies in an irregular and unpredictable manner.

In general, the predicted amount of open magnetic flux (the surface integral of the unsigned magnetic field strength at a given radius) does not match observations either at 1 AU or closer to the Sun, usually underestimating the true value. This

is the so-called 'open flux problem' ([54]), whereby the heliospheric magnetic flux is often measured at twice or more than the value predicted by PFSS models. Our 'outflow fields', discussed in Chapter 2, are calculated similarly to PFSS fields but take into account the effect of the solar wind, which reduces this discrepancy to a degree. Another possible solution to the problem is to account for the influence of 'switchbacks' (eg. [55], [56]): locations in the magnetic field where the field lines double back on themselves. The radial magnetic field will be double-counted in these locations and so the total open flux will be overestimated.

Despite their limitations, PFSS models are used extensively in this thesis as initial conditions for both the magnetofriction and MHD models. Potential fields are ideal initial conditions for magnetofriction as the system will remain in equilibrium unless dynamic boundary conditions (or an imposed outflow) are applied, given the frictional velocity term will be zero in the absence of any current.

A potential field also represents the state with minimum magnetic energy

$$E_M = \frac{1}{2\mu_0} \int B^2 dV \tag{1.70}$$

for a given normal component of the magnetic field on the boundary. The reference potential fields used in Chapter 3 are not PFSS fields as the upper boundary condition is not radial – the upper boundary of these reference fields is instead chosen to match the primary magnetic field to which the reference field is compared. The numerical processes for calculating such fields is very similar, however.

Numerical calculation of PFSS fields on a staggered grid

Analytic expressions can be found for PFSS fields, usually in conjunction with a Fourier Transform on the lower boundary. However, in this thesis we are concerned with evaluating such fields numerically. In particular, PFSS fields are used as the initial condition for many of our dynamic simulations, all of which take place on a 'staggered grid' (see Section 1.4.1). There are many different ways to calculate these solutions, several of which have been used in our work. In the PFSS model the magnetic field can be expressed entirely in terms of the scalar potential Φ, which is

stored at the centre of grid cells. In the notation of Section 1.4.1 this is

$$\Phi^{i+1/2,j+1/2,k+1/2}. \tag{1.71}$$

In Cartesian coordinates, the magnetic field $\mathbf{B} = \nabla\Phi$ is then simply

$$B_x^{i,j+1/2,k+1/2} = \frac{1}{\Delta x}(\Phi^{i+1/2,j+1/2,k+1/2} - \Phi^{i-1/2,j+1/2,k+1/2}) \tag{1.72}$$

$$B_y^{i,j+1/2,k+1/2} = \frac{1}{\Delta y}(\Phi^{i+1/2,j+1/2,k+1/2} - \Phi^{i+1/2,j-1/2,k+1/2}) \tag{1.73}$$

$$B_z^{i,j+1/2,k+1/2} = \frac{1}{\Delta z}(\Phi^{i+1/2,j+1/2,k+1/2} - \Phi^{i+1/2,j+1/2,k-1/2}), \tag{1.74}$$

and the solenoidal condition on the magnetic field then determines the numerical condition on Φ. This is long-winded in three dimensions, so if we consider a 2D system (dropping the z component) then this condition is

$$\Delta\Phi^{i+1/2,j+1/2} = \frac{1}{\Delta x^2}(\Phi^{i+3/2,j+1/2} - 2\Phi^{i+1/2,j+1/2} + \Phi^{i-1/2,j+1/2}) + \frac{1}{\Delta y^2}(\Phi^{i+1/2,j+3/2} - 2\Phi^{i+1/2,j+1/2} + \Phi^{i+1/2,j-1/2}) = 0. \tag{1.75}$$

One hopes that the 3D extension is clear. Ghost points just outside the domain can be used to enforce the boundary conditions. The simplest procedure for solving such a system of equations is the Gauss-Seidel method, whereby each element of $\Phi^{i+1/2,j+1/2}$ is calculated in turn such that based on the existing values of its neighbour, the value of $\Delta\Phi^{i+1/2,j+1/2}$ is then precisely zero in that cell. Once all interior points are updated the boundary conditions are then imposed and the process repeats until the solution has converged to an acceptable degree. This procedure is simple to implement but is in general very slow to converge.

Quite a considerable improvement on this method can be made by using 'Sucessive over-relaxation' (SOR). Similarly to Gauss-Seidel, we calculate a value $\widetilde{\Phi}^{i+1/2,j+1/2}$ based on the neighbouring points such that $\Delta\widetilde{\Phi}^{i+1/2,j+1/2} = 0$, but instead of setting the new value to be $\Phi_{\text{new}} = \widetilde{\Phi}$ we combine with the old value as follows:

$$\Phi_{\text{new}} = \omega\widetilde{\Phi} + (1-\omega)\Phi_{\text{old}}, \tag{1.76}$$

for a constant parameter ω. Setting $\omega = 1$ recovers Gauss-Seidel. Convergence is theoretically guaranteed for $0 < \omega < 2$, but the fastest convergence generally occurs in the region of $\omega \approx 1.5$. It is possible to deduce the optimum ω analytically for simple grids, but for our purposes it is determined with trial and error, and varies depending on the nature of the grid.

SOR is still very slow to converge at high resolutions, especially in three dimensions. Thus for the irregular grids described in Chapter 4 we must use a 'multigrid' method. This is discussed in more detail in that chapter, but in essence is merely SOR applied at different grid resolutions, enabling convergence at multiple scales far more quickly than any alternatives.

If we have a regularly-spaced grid (either in Cartesian or spherical coordinates) then the method of separation of variables allows us to decompose a solution to $\mathbf{B} = \nabla\Phi$ into eigenfunctions – Fourier modes in Cartesian coordinates or spherical harmomics in spherical coordinates. This reduces the numerical solution to a series of 1D problems, and as such is far faster than SOR. The method for calculating our 'outflow fields' (Chapter 2) uses this approach. Setting the outflow velocity to zero in this case recovers a PFSS field. This approach for solving PFSS on a staggered grid was described by [32].

In arbitrary coordinates an alternative approach is to solve Equation 1.75 (or equivalent) directly by treating it as a matrix equation that can be solved using standard methods. This is in fact the approach used to calculate initial PFSS fields for the axisymmetric polar simulations in Chapter 3. We illustrate this process here. Initially, we need to find a matrix M which is equivalent to taking the Laplacian of Φ, in arbitrary coordinates:

$$\Delta\Phi = M\Phi + \mathbf{a} = 0, \tag{1.77}$$

where (simplistically) the matrix M represents the Laplacian operator, and the vector $\mathbf{a}$ contains the boundary condition information. To express the system as such, and if working in greater than one dimension, Φ must be 'flattened' into a 1D array. If Φ has n elements (the total number of grid cells), then the matrix M

is an $n \times n$ matrix. In simple cases the components of M can be determined by inspection, but this is not always possible. The code used in our simulations instead calculates the Laplacian of each array with a single non-zero element of Φ in turn:

$$M \begin{pmatrix} 1 \\ 0 \\ \vdots \\ 0 \\ 0 \end{pmatrix} = \Delta \begin{pmatrix} 1 \\ 0 \\ \vdots \\ 0 \\ 0 \end{pmatrix} - \mathbf{a}$$

and so forth for all the possible elements in Φ, whereupon the rows of M can be read off directly. The vector $\mathbf{a}$ contains the lower boundary condition information and can be obtained simply by application of the numerical Laplacian function to the zero vector, essentially equivalent to:

$$\mathbf{a} = \Delta \begin{pmatrix} 0 \\ 0 \\ \vdots \\ 0 \\ 0 \end{pmatrix}.$$

We then solve $\Delta\Phi = 0$ by inverting M:

$$\Phi = -M^{-1}\mathbf{a}. \tag{1.78}$$

The matrix M is sparse and so this inversion is reasonably fast providing an efficient algorithm is used. For the uses in this thesis the scipy sparse matrix solver will prove sufficient. For successive potential field calculations on the same grid (with varying boundary conditions) the matrix M needs only be calculated once, further speeding up the process.

1.4.3 Other force-free models

In addition to the models described above, which are directly relevant to the work in this thesis, there exist many other approaches to modelling the coronal magnetic field. The most commonly used of these are force-free models, whereby the Lorentz force $\mathbf{j} \times \mathbf{B}$ vanishes everywhere. This is a weaker assumption than required for potential fields (where $\mathbf{j} = 0$), allowing for a vast array of possible solutions in contrast to the unique solution for a potential field.

Magnetic fields in the corona can be generally considered to be approximately force-free, which is key to the assumptions founding the magnetofrictional model. It may also be assumed that the magnetic pressure in the corona dominates over the gas pressure at most locations in the corona ([57, 58]), and so in a steady state there should in theory exist a force-free field that represents the magnetic field configuration very well. Finding such a field is far from trivial, however.

The magnetofrictional model will relax to a force-free state in the absence of dynamic boundary conditions, and as such suitable fields can be obtained using magnetofriction in combination with suitable boundary driving (this is the principle behind many of the works referenced in Section 1.4.1). However, such evolution is time consuming and it is often advantageous to be able to construct a series of force-free fields directly from boundary data. Such a magnetic field $\mathbf{B}$ must satisfy:

$$\nabla \times \mathbf{B} = \alpha \mathbf{B}, \tag{1.79}$$

and

$$\mathbf{B} \cdot \nabla \alpha = 0, \tag{1.80}$$

where α is a 'force-free parameter'. The first equation here ensures that the current is parallel to the magnetic field, and the second constrains α to be constant along each individual field line.

If we assume α is constant everywhere, this is referred to as a linear force-free field (LFFF). If α is allowed to vary throughout the domain then this is a non-linear force-free field (NLFFF). In the former case (LFFF) the equation for $\mathbf{B}$ reduces to

the Helmholtz equation

$$\nabla^2 \mathbf{B} = -\alpha^2 \mathbf{B}, \tag{1.81}$$

solutions to which can be obtained in a similar fashion to a potential field. In this simple case an optimum value for α can either be obtained by comparison with the horizontal magnetic field at the photosphere (eg. [59, 60]) or by qualitative comparison (the position of coronal loops etc.) with features higher in the corona (eg. [61]). However, although these models are an improvement upon potential fields, the optimum value for α has been shown ([62]) to vary considerably across different field lines, and as such their value is limited.

Thus NLFFF fields have the scope to be far more useful than linear fields, although this depends on the ability to deduce suitable values for α on each individual field line. It is possible to find semi-analytic solutions of this form, notably that of Low and Lou ([63]) and Titov and Démoulin ([64]). The latter of these is particularly noteworthy as it represents a twisted flux tube in the shape of a torus, with the upper region emerging from the surface, as shown in Figure 1.9.

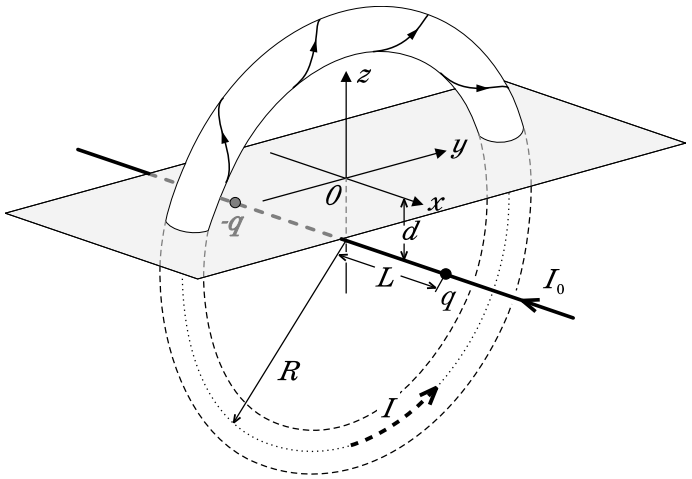

Figure 1.9: The equilibrium solution of [64] (Figure 2 from that paper), modelling a force-free flux tube in the shape of a ring. There exist point charges at the positions marked q, with a line current (I_0) passing through the centre of the ring. Only the region above the photosphere has physical meaning.

However, these analytic approaches are naturally limited by their inability to be combined with observations of the magnetic field on the photosphere, and their use mainly lies either in testing the stability of NLFFF codes or for initialising

simulations (much as we do with potential fields for our models). There has been considerable research and progress into finding reliable processes to create NLFFF models which correspond accurately to observations of the field configuration in the corona. The paper [63] provides an introduction to these problems, with the recent review [65] discussing the challenges and various new approaches to overcome them.

Despite much progress, these fields are still in general very sensitive – slight differences in methodology or boundary data can produce very different magnetic field structures. One promising avenue of research is the use of machine learning to compare these fields to a wide array of coronal observations (eg. [66]), the combination of which it is hoped will constrain the solution sufficiently to be reasonably certain of the overall topology of the magnetic field, at very least.

1.5 Flux Rope Instabilities and Analytic Results

1.5.1 The Basic Line Current Model

Analytic two-dimensional models of flux rope behaviour date back to [67] and [68], who modelled a horizontal line current and its interaction with a specified background magnetic field. In the later work they deduced that for such a configuration to be horizontally stable the line current must exist in conjunction with an equal and opposite current embedded within the photosphere, essentially completing the circuit. This setup is shown in Figure 1.10.

In their paper, [67] assumed that the background magnetic field is in the horizontal direction and depends on the height above the photosphere: $B_x(h)$. This background field interacts with the line current itself to produce a Lorentz force $(-IB_x(h))$ directly proportional to the current I, in the downward direction. There also exists the Lorentz force (I^2/h) due to interaction with the magnetic field generated by the line current embedded in the photosphere. The final force considered is the effect of gravity on the 'mass' of the line current. The total forces vertically on a line current element are then

$$F = \frac{I^2}{h} - IB_x(h) - mg. \tag{1.82}$$

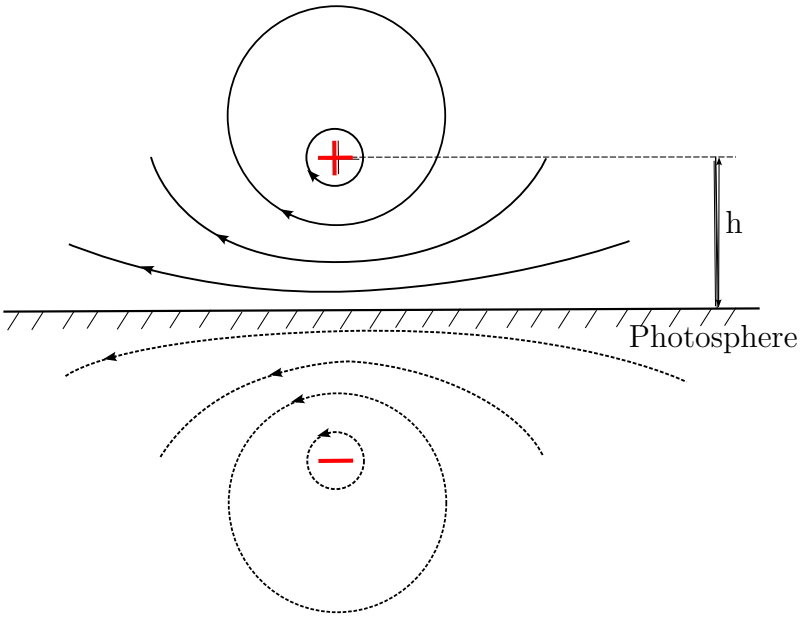

Figure 1.10: The model of [67], in which a line current (marked with the '+') is opposed by a identical current below the photopshere, of equal magnitude and in the opposite direction. The curved lines (solid and dashed) represent the magnetic field lines of the field generated by the currents. Recreated from Figure 2 from that paper.

The conditions for stability clearly depend on the nature of the profile of the background field strength. In the absence of a background field a stable equilibrium position exists at height

$$h = \frac{I^2}{mg}. \tag{1.83}$$

Any assumptions made regarding the nature of the background field strength are dubious at best – not least because such a field would not be purely horizontal in reality – but in general if the background field strength decreases rapidly with increasing height it is possible for an eruption to occur, providing the current is high enough at low altitudes.

1.5.2 The Kink and Torus Instability

The models in Chapter 3 focus on flux ropes, whereby the magnetic field is twisted around a line current. This is as opposed to the magnetic field being limited to the invariant plane as in the above model. Flux tubes can become laterally unstable if

they become twisted beyond a critical value ([69, 70]), equal to

$$\Phi_c = \frac{lB_\phi(r)}{rB_z(r)}, \tag{1.84}$$

where B_z and B_ϕ are the axial and azimuthal magnetic fields, r is the radial coordinate and l is the length of the flux tube. This is known as the 'kink instability'. Although the flux tubes in our 2.5D models are infinitely long and so this analytic result can not be directly compared, the presence of a critical out-of-plane magnetic field strength at which instabilities occur is also clear in our results.

Further analytic approaches have introduced the torus instability (e.g [71, 72]) by modelling the current as a ring rather than an infintely-long line, in a manner qualitatively similar to the setup in Figure 1.9. As for the line current model described above, the forces on an infinitesimal portion of the flux tube are considered, but now the background magnetic field is assumed to be in the poloidal direction, and is a function of the distance from the centre of the ring, rather than altitude. It was found (similarly to the line current model, but not precisely) that if the background field decays sufficiently quickly with increasing distance from the current, then an instability will form – named the 'torus instability'. The condition for this instability can in fact be stated reasonably simply in the limit that the radius of the flux tube itself is sufficiently small relative to the size of the overall loop ([73]):

$$-R\frac{d}{dR}\ln(B_{ex}(R)) > \frac{3}{2}, \tag{1.85}$$

where R is the major radius of the loop, and B_{ex} the magnititude of the external poloidal field. This instability is essentially the same as the lateral kink instability, distributed around the entire ring. A more complex condition on instability was obtained by [72], whereby the minor radius of the flux tube is permitted to be significant relative to its overall size. The condition for the torus instability then becomes

$$-R\frac{d}{dR}\ln(B_{ex}(R)) > \frac{3}{2} - \frac{\mu_0 R}{4L}, \tag{1.86}$$

where L is the inductance of the plasma in the torus. They concluded that such

an instability is a possible, and indeed likely, mechanism for CMEs. Although our models (Chapter 3) are only 2.5D and as such have no curvature in the out-of-plane direction, this can in essence be regarded as a small section of a very large torus, and as such these results could be considered not entirely irrelevant to our research.

In fact, it has since been shown that the conditions for both the kink and torus instabilities are essentially the same, and they are just two special cases of a continuous theory of more general current paths [74]. In that work it is also postulated that 'catastrophe' – an alternative eruptive mechanism wherein a flux rope exists in a quasi-equilibrium state for some time, before this is no longer an option and it rapidly becomes unstable – is in fact the same as the torus instability, with identical conditions for eruption. Although these works provide useful theoretical background as to the nature of flux rope behaviour, they are difficult to relate to physical ropes as these tend to lack the necessary symmetries in their structure to allow for this kind of analysis.

All of the analytical approaches introduced so far rely on the assumption of an external magnetic field which decays with distance from the line current/flux rope. There are indeed conflicting explanations for flux rope instability, such as that of [75], who propose that eruptions can occur even if the conditions for the torus instability are not met. They propose that fast magnetic reconnection can occur below a flux rope – known as 'tether cutting', irrespective of the magnetic field above. Such tether cutting reconnection models were made popular by [76], and have been shown to be consistent with some observations and numerical modelling (eg. [77, 78]).

It is likely, however, that the torus instability/catastrophe explanation for eruptions is more relevant to our research, as in our models the instability and certainty of eruption sets in before such a 'tether' has formed under the flux rope. Although the nature of our models means that calculating conditions on these instabilities directly is not possible, these analytic approaches have provided valuable guidance on which quantities it may be useful to measure, such as the current in the rope, the twist of the magnetic field, or the significance of the background field strength relative to the magnetic field of the rope itself.

1.6 Magnetic Helicity

The helicity of a magnetic field is defined in a volume as

$$H = \int \mathbf{A} \cdot \mathbf{B} \, dV, \tag{1.87}$$

where $\mathbf{B}$ is the magnetic field and $\mathbf{A}$ its corresponding vector potential such that $\mathbf{B} = \nabla \times \mathbf{A}$. The vector potential $\mathbf{A}$ is not unique, as any alternative $\mathbf{A}^* = \mathbf{A} + \nabla\phi$ will also be a suitable vector potential for the same magnetic field. For a closed system – one in which there are no magnetic field lines passing through the boundary, this choice of $\mathbf{A}$ (changing the 'gauge') will not affect the overall helicity, but otherwise it will in general make a difference (see Section 1.6.1). As such the helicity H is not 'gauge-invariant'.

The helicity is notable in that under the evolution of ideal MHD (no coronal diffusion η, in our case), the overall magnetic helicity within a volume is conserved ([79]), providing again that the volume of integration is a closed system. The proof of this is quite neat, and is as follows:

$$\frac{dH}{dt} = \int \frac{\partial \mathbf{A}}{\partial t} \cdot \mathbf{B} \, dV + \int \mathbf{A} \cdot \frac{\partial \mathbf{B}}{\partial t} \, dV. \tag{1.88}$$

Substitute the ideal MHD induction equation (1.42)

$$\frac{\partial \mathbf{B}}{\partial t} = \nabla \times (\mathbf{v} \times \mathbf{B}), \;\; \frac{\partial \mathbf{A}}{\partial t} = \mathbf{v} \times \mathbf{B} + \nabla\phi \tag{1.89}$$

into the first term to obtain

$$\frac{dH}{dt} = \int (\mathbf{v} \times \mathbf{B} + \nabla\phi) \cdot \mathbf{B} \, dV + \int \mathbf{A} \cdot \frac{\partial \mathbf{B}}{\partial t} \, dV \tag{1.90}$$

$$\frac{dH}{dt} = \int \nabla\phi \cdot \mathbf{B} \, dV + \int \mathbf{A} \cdot \frac{\partial \mathbf{B}}{\partial t} \, dV \tag{1.91}$$

$$\frac{dH}{dt} = \oint \phi \mathbf{B} \cdot \mathbf{n} \, dS + \int \mathbf{A} \cdot \frac{\partial \mathbf{B}}{\partial t} \, dV \tag{1.92}$$

$$\frac{dH}{dt} = \int \mathbf{A} \cdot \frac{\partial \mathbf{B}}{\partial t} \, dV \tag{1.93}$$

where the first term vanishes as we have assumed a closed system and so $\mathbf{B} \cdot \mathbf{n} = 0$.

The remaining term can be integrated by parts:

$$\frac{dH}{dt} = \int \mathbf{A} \cdot \left(\nabla \times \frac{\partial \mathbf{A}}{\partial t} \right) dV = \int \nabla \cdot \left(\mathbf{A} \times \frac{\partial \mathbf{A}}{\partial t} \right) dV - \int \frac{\partial \mathbf{A}}{\partial t} \cdot (\nabla \times \mathbf{A}) \, dV \tag{1.94}$$

$$= \oint \left(\mathbf{A} \times \frac{\partial \mathbf{A}}{\partial t} \right) \cdot \mathbf{n} \, dS - \int (\mathbf{v} \times \mathbf{B}) \cdot \mathbf{B} \, dV, \tag{1.95}$$

$$= \oint (\mathbf{A} \times (\mathbf{v} \times \mathbf{B} + \nabla \phi)) \cdot \mathbf{n} \, dS \tag{1.96}$$

$$= \oint [(\mathbf{A} \cdot \mathbf{B})\mathbf{v} - (\mathbf{A} \cdot \mathbf{v})\mathbf{B} + \nabla \times (\mathbf{A}\phi) - \phi \mathbf{B}] \cdot \mathbf{n} \, dS \tag{1.97}$$

$$= \oint (\mathbf{A} \cdot \mathbf{B})(\mathbf{v} \cdot \mathbf{n}) \, dS \tag{1.98}$$

where we have again used $\mathbf{B} \cdot \mathbf{n} = 0$ on the boundaries and various vector identities. The $\nabla \times (\mathbf{A}\phi)$ term disappears due to Stokes' theorem, providing $\mathbf{A}\phi$ is continuous on the boundaries. As we assume a closed system we find that the remaining term also disappears, given there is no flow through the boundaries ($\mathbf{v} \cdot \mathbf{n} = 0$). Hence

$$\frac{dH}{dt} = 0. \tag{1.99}$$

Although this result is not valid in non-ideal MHD, it has been shown (eg. [80]) that provided the diffusion η is not particularly high (as is the case in the corona), the magnetic helicity remains reasonably well conserved as the magnetic field evolves. This result has been repeatedly confirmed in both numerical and physical experiments of laboratory plasmas (eg. [81]).

Alternatively to the integral formulation, the helicity can be expressed in terms of the average linking of the magnetic field lines, weighted by the magnitude of the field strength ([82]). To see this, providing the vector potential is in the Couloumb Gauge ($\nabla \cdot \mathbf{A} = 0$) it can be written in the form

$$\mathbf{A}(\mathbf{x}) = \frac{1}{4\pi} \int \frac{\mathbf{B}(\mathbf{y}) \times \mathbf{r}}{|\mathbf{r}|^3} \, d\mathbf{y}, \tag{1.100}$$

where $\mathbf{r}$ is the vector $\mathbf{x} - \mathbf{y}$ ([83]). This equation follows from the Biot-Savart formula.

The helicity then can be expressed with the double integral ([84])

$$H = \frac{1}{4\pi} \iint \mathbf{B}(\mathbf{x}) \cdot \frac{\mathbf{B}(\mathbf{y}) \times \mathbf{r}}{|\mathbf{r}|^3} \, d\mathbf{x} d\mathbf{y}. \tag{1.101}$$

Instead of considering this a normal volume integral, we can instead think of it as a double integral along each magnetic field line. In combination with the formula for the Gauss linking number of two closed field lines:

$$L(\mathbf{x}, \mathbf{y}) = \frac{1}{4\pi} \oint_{\text{field line 1}} \oint_{\text{field line 2}} \frac{d\mathbf{x}}{ds'} \frac{d\mathbf{y}}{ds} \times \frac{\mathbf{r}}{|\mathbf{r}^3|} \, ds ds', \tag{1.102}$$

we see that the helicity is sum of the total linking number of each field line, weighted by the average magnetic field strength at each point. Providing all field lines are closed loops and magnetic reconnection is not permitted (ideal MHD) this provides an intuitive explanation for the conservation result.

Unfortunately, in the context of astrophysical magnetic fields, the assumption of a closed magnetic field is not at all reasonable. Certainly in the corona a significant amount of the magnetic field lines are open, and as such there is no possible domain over which the helicity could be meaningfully integrated. To deal with this problem we require the construction of alternative quantities.

1.6.1 Relative Helicity and Open Magnetic Fields

The 'relative helicity', or H_R, was introduced by [85] and provides an alternative measure of helicity that is gauge-invariant even when the magnetic field is not closed. This requires the construction of a reference magnetic field $\mathbf{B}_P$, with corresponding vector potential $\mathbf{A}_P$, to which the original magnetic field is compared. Such a reference magnetic field must match the normal component of the original magnetic field on the integration domain boundaries, and is usually chosen to be a potential field (see Section 1.4.2). A potential field is the minimum energy state possible with such boundary conditions, and also in general will have a low linking number. Alternatives to potential fields can also be used, such as the twisted fields discussed in [84], but this is rare.

Subtracting the helicity of this reference field from the original yields the formula

$$H_R = \int \mathbf{A} \cdot \mathbf{B} - \mathbf{A}_P \cdot \mathbf{B}_P \, dV. \tag{1.103}$$

This can be manipulated into a more useful form as follows ([86]):

$$\begin{aligned}
H_R &= \int (\mathbf{A} + \mathbf{A}_P) \cdot (\mathbf{B} - \mathbf{B}_P) \, dV + \int \mathbf{A} \cdot \mathbf{B}_P - \mathbf{A}_P \cdot \mathbf{B} \, dV && (1.104)\\
&= \int (\mathbf{A} + \mathbf{A}_P) \cdot (\mathbf{B} - \mathbf{B}_P) \, dV + \int \mathbf{A} \cdot (\nabla \times \mathbf{A}_P) - \mathbf{A}_P \cdot \mathbf{B} \, dV && (1.105)\\
&= \int (\mathbf{A} + \mathbf{A}_P) \cdot (\mathbf{B} - \mathbf{B}_P) \, dV + \int \nabla \cdot (\mathbf{A} \times \mathbf{A}_P) + \mathbf{A}_P \cdot (\nabla \times \mathbf{A}) - \mathbf{A}_P \cdot \mathbf{B} \, dV && (1.106)\\
&= \int (\mathbf{A} + \mathbf{A}_P) \cdot (\mathbf{B} - \mathbf{B}_P) \, dV + \int (\mathbf{A} \times \mathbf{A}_P) \cdot \mathbf{n} \, dS && (1.107)\\
&= \int (\mathbf{A} + \mathbf{A}_P) \cdot (\mathbf{B} - \mathbf{B}_P) \, dV, && (1.108)
\end{aligned}$$

where we have used integration by parts and the divergence theorem to remove the additional terms, requiring additionally that $(\mathbf{A} \times \mathbf{A}_P) \cdot \mathbf{n}$ vanishes on the boundary. This is always possible due to the condition that $\mathbf{B} \cdot \mathbf{n} = \mathbf{B}_P \cdot \mathbf{n}$.

We can show that the relative helicity (defined using Equation 1.108) is invariant with respect to the gauge of $\mathbf{A}$ or $\mathbf{A}_P$ by adding an arbitrary gradient term $\nabla\Phi$ to the vector potential:

$$\begin{aligned}
H'_R &= \int (\mathbf{A} + \mathbf{A}_P + \nabla\Phi) \cdot (\mathbf{B} - \mathbf{B}_P) \, dV && (1.109)\\
&= H_R + \int \nabla\Phi \cdot (\mathbf{B} - \mathbf{B}_P) \, dV && (1.110)\\
&= H_R + \int \nabla \cdot ((\mathbf{B} - \mathbf{B}_P)\Phi) \, dV - \int \Phi \nabla \cdot (\mathbf{B} - \mathbf{B}_P) \, dV && (1.111)\\
&= H_R + \int (\mathbf{B} \cdot \mathbf{n} - \mathbf{B}_P \cdot \mathbf{n})\Phi \, dS - \int \Phi \nabla \cdot (\mathbf{B} - \mathbf{B}_P) \, dV && (1.112)\\
&= H_R, && (1.113)
\end{aligned}$$

where the first term disappears as the normal components of the two magnetic fields match on the boundary, and the second vanishes due to the solenoidal condition. Note that this is not true when H_R is defined in the original form (Equation 1.103)

and so we henceforth use the definition in Equation 1.108.

The relative helicity is used extensively in our work on flux rope eruptions (see Chapter 3) as a suitable scalar property of the magnetic field. In 3D the reference potential field $\mathbf{B}_P$ is well defined, but the correct definition in 2.5D is a little more ambiguous, due to a lack of a boundary in the out-of-plane direction. Our approach to solving this problem is described in detail in Chapter 3.

The relative helicity is by no means unique as a potentially useful quantity measuring the topology of the magnetic field. It can in fact be decomposed as follows ([87]):

$$H_R = H_J + 2H_{PJ}, \tag{1.114}$$

where H_J is the 'current-carrying helicity'

$$H_J = \int (\mathbf{A} - \mathbf{A}_P) \cdot (\mathbf{B} - \mathbf{B}_P)\, dV, \tag{1.115}$$

essentially the helicity of the field $\mathbf{B} - \mathbf{B}_P$ (the current-carrying field), and H_{PJ}

$$H_{PJ} = \int \mathbf{A}_P \cdot (\mathbf{B} - \mathbf{B}_P)\, dV, \tag{1.116}$$

is the 'mutual helicity' between the current-carrying field and the potential reference field. These new quantities are also clearly gauge-invariant.

As stated previously, for open fields (those with magnetic field lines passing through a boundary) the helicity is not conserved under ideal MHD due to the presence of the boundary term. Considering H rather than H_R for simplicity, from Equation 1.95 we have that its rate of change is

$$\frac{dH}{dt} = \int (\mathbf{A} \times \frac{\partial \mathbf{A}}{\partial t}) \cdot \mathbf{n}\, dS - \int (\mathbf{v} \times \mathbf{B}) \cdot \mathbf{B}\, dV \tag{1.117}$$

$$= -\int (\mathbf{A} \times \mathbf{E}) \cdot \mathbf{n}\, dS \tag{1.118}$$

$$= \int (\mathbf{A} \times (\mathbf{v} \times \mathbf{B})) \cdot \mathbf{n}\, dS \tag{1.119}$$

$$= \int -(\mathbf{A} \cdot \mathbf{v})(\mathbf{B} \cdot \mathbf{n}) + (\mathbf{A} \cdot \mathbf{B})(\mathbf{v} \cdot \mathbf{n})\, dS \tag{1.120}$$

where $\mathbf{E}$ is the electric field strength on the boundary, and $\mathbf{v}$ is the velocity on the boundary. The first term here represents the injection of helicity due to the effects of tangential motion on the surface shearing and twisting the magnetic field. The second term represents motions normal to the surface, as helicity emerges/submerges through the boundary [88]. Similar formulae exist for the other quantities listed above.

The first of these terms can be estimated relatively easily from successive magnetogram observations tracking features on the solar surface. The second term can be estimated using knowledge of motions normal to the surface, which can be deduced using red/blue shift of spectral lines ([89]). Thus it is theoretically possible to calculate the change in magnetic helicity in the corona using only data from the lower boundary of the corona, and avoiding the need to reconstruct the magnetic field in three dimensions.

All of these quantities naturally depend significantly on the choice of integration domain V, and it is often unclear from which part of the magnetic field the contributions to the overall helicity originate. This is not helped by the fact that the relative helicity is not additive – when an integration domain is split into smaller parts the respective helicities of these parts will not add to the overall value, as the reference field $\mathbf{B}_P$ will be different for each subdomain unless the subdomains are separated by magnetic surfaces through which field lines do not pass ([90]).

This is not particularly problematic for our simulations, where the flux rope makes up a significant part of the overall domain, but in general it is useful to identify which parts of the magnetic field contribute the most to the total helicity, or to find the helicity of an arbitrary subregion within a large domain, such as for an individual active region.

1.6.2 Field-Line Helicity

One solution to this problem is to use the so-called 'field-line helicity'. This was first proposed by [91], and decomposes the overall helicity integral H into the contributions from each individual magnetic field line. The basic idea is to decompose the domain into infinitesimally small flux tubes surrounding each field line. Along

each field line, the magnetic field has no normal component to itself and so these domains can be regarded as closed, satisfying the requirements for a meaningful helicity measurement.

Explicitly, for a domain D_i surrounding a magnetic field line (labelled i), the helicity in that domain is

$$h(D_i) = \int_{D_i} \mathbf{A} \cdot \mathbf{B}\, dV. \tag{1.121}$$

We can choose such a domain to be $V_\epsilon(x)$, the flux tube of radius ϵ surrounding an individual field line with path $L(\mathbf{x})$, where $\mathbf{x}$ is the one of the points at which the field line meets the outer boundary. By taking the infinitesimal limit of such a flux tube, and weighting by the magnetic flux in the tube Φ_ϵ (constant along its length) we obtain

$$h(\mathbf{x}) = \lim_{\epsilon \to 0} \frac{h(V_\epsilon(x))}{\Phi_\epsilon}, \tag{1.122}$$

which tends to a well-defined limit, which is in fact equal to ([92])

$$h(\mathbf{x}) = \int_{L(\mathbf{x})} \mathbf{A} \cdot d\mathbf{l}, \tag{1.123}$$

the line integral of the vector potential along the field line with endpoint $\mathbf{x}$. This quantity is invariant under ideal MHD if the magnetic field at the boundaries is fixed. The original volume integral definition of the helicity can be recovered by adding together the field-line helicity of every field line in the domain, weighted by the normal magnetic flux on the boundary:

$$H = \frac{1}{2} \int h(\mathbf{x}) |\mathbf{B}(\mathbf{x}) \cdot \mathbf{n}|\, dS, \tag{1.124}$$

where the integral is over the boundary, $\mathbf{x}$ is the endpoint of each field line and the factor of $1/2$ is due to each field line meeting the boundary at each end and hence being counted twice. Field lines that do not intersect the boundaries will not be counted, however, and as such this this is only true for fields with no closed (ergodic) field lines.

Using the relative helicity H_R relaxes the assumptions of gauge-invariance, allowing this quantity to become truly meaningful. It has in fact been shown by [92]

that it is possible to select an appropriate gauge of $\mathbf{A}$ in the calculation of $h(\mathbf{x})$ such that

$$H_R = \frac{1}{2}\int h(\mathbf{x})|\mathbf{B}(\mathbf{x})\cdot\mathbf{n}|\,dS. \tag{1.125}$$

This is the so-called 'relative field-line helicity'. In the case where the reference magnetic field $\mathbf{B}_P$ is a potential field, this can be achieved merely by using a vector potential $\mathbf{A}_P$ such that

$$\int \mathbf{A}_P\cdot\mathbf{B}_P\,dV = 0, \tag{1.126}$$

and ensuring that $(\mathbf{A}\times\mathbf{A}_P)\cdot\mathbf{n} = 0$ on the boundaries. Analysis of a magnetic field using this approach can provide much insight as to its overall structure.

1.6.3 The 'Eruptivity Index'

The approach we take in Chapter 3, in which we seek scalar quantities that could be used as an indicator that a flux rope eruption is imminent, is motivated in part by the work of [93]. In that work, they analysed the MHD simulations of [24,25], which consist of seven flux rope configurations, some of which are eruptive and others stable.

Most scalar measurements of the system were shown not to have any strong correlation to eruptivity, including the relative helicity. However, they propose a quantity that has become known (perhaps presumptuously) as the 'eruptivity index'. This is the ratio

$$\left|\frac{H_J}{H_R}\right|, \tag{1.127}$$

with H_J and H_R the current-carrying and relative helicities defined in Section 1.6.1. This ratio was significant in that it exhibited a large peak in those simulations where the flux rope later erupted. We have proposed (see Section 3.4.2) an explanation for why this may be the case which contradicts their conclusions to a degree, finding that the large peak could be caused entirely due to the orientation of the background magnetic field during the rope formation. However, the eruptivity index has since been focused on by several authors as a good candidate for a scalar predictor.

These include the work of [26,94], who also use a small number of MHD simu-

lations and observe a consistent threshold in the eruptivity index above which the simulations become unstable. This result is notable as the evolution of the relative helicity (H_R) itself differs significantly from the simulations of [24], whereas the eruptivity index behaves similarly in both studies.

The eruptivity index has also been estimated during eruptive events with different topologies, such as in [95], which analysed a coronal jet. In that case the driven boundary conditions were applied for differing lengths of time in order to produce eruptions at different times. This study also found an increase in the eruptivity index prior to an eruption, although it is acknowledged that a larger parameter study is necessary to determine if there is a consistent threshold above which the system becomes unstable.

Motivated by these results, the eruptivity index has been estimated prior to the eruption of several structures in the real corona (eg. [96]), and found to be consistently high prior to eruptive events. Estimates of the index using observational data must necessarily extrapolate the coronal magnetic field from photospheric measurements, which adds a degree of uncertainty. Some of the methods for such extrapolations were discussed in Section 1.4.

Despite such relative fervour, to our knowledge there has not been proposed any physical mechanism for why the eruptivity index in particular would behave remarkably compared to any other similarly-constructed ratio. Chapter 3 seeks to expand on the works mentioned above by expanding the size of the parameter study considerably, allowing for a statistical analysis of any instability threshold that may exist. We also discuss variations on the eruptivity index that may be more promising than its established form.

Like the relative helicity, the eruptivity index naturally is very much dependent on the size of the integration domain. The application of the 'field-line' processes described in Section 1.6.2 to the eruptivity index may well be necessary to apply such an approach to real-world scenarios. To our knowledge, this has not yet been achieved.

CHAPTER 2

Global Coronal Equilibria With Solar Wind Outflow

In this chapter we discuss the work published in our first paper ([6]), in which we present a new method for calculating steady-state equilibrium solutions for the magnetic field in the corona, taking into account an imposed solar wind velocity term. The motivation for this work was seeking to improve on the initial conditions used in the magnetofrictional models. The default initial conditions for these models are usually potential fields, in particular PFSS (potential field source-surface) fields, in which the magnetic field lines are constrained to be radial at an arbitrary upper boundary.

These potential fields are not steady-state solutions of the MF equations when the effect of the solar wind is included. The solar wind introduces a radial velocity outwards in the upper corona ([13]), which moves the magnetic field lines outwards and causes them to become more radial. This is consistent with the radial upper boundary condition of PFSS fields, but in reality there is no set altitude at which this occurs, and the field lines become radial at differing heights. The imposition of such a fixed boundary height to PFSS fields results in magnetic field extrapolations that can depend heavily on this (sometimes arbitrary) assumption, which is clearly undesirable.

Our 'outflow fields' are constructed in a similar manner to PFSS fields, and as such take a comparable time to compute. We find that by introducing the extra outflow velocity term the magnetic field lines tend to naturally become more radial at lower altitudes, which is more consistent with the streamer shapes observed during solar eclipses. The opening-out of the magnetic field also increases the open flux through the top boundary (and hence by extension further into space), which goes some way to solve the 'open flux problem' ([54]) – that observed magnetic flux measurements at 1AU are considerably higher than would be expected if the solar corona were entirely current-free. As the field lines are radial for physical reasons rather than just due to the boundary condition, the outflow fields are more independent of the arbitrary location of the upper boundary, and instead primarily depend on the chosen solar wind profile.

We will discuss the approach in an arbitrary coordinate system, before detailing the specific solution techniques in both 2D Cartesian and 3D spherical polar coordinates, which are designed to be compatible with the grid used in existing magnetofrictional codes (eg. [39]). We then discuss the precise numerical implementation on this grid, and finally compare these new 'outflow fields' to traditional PFSS equivalents, in particular focusing on the difference in streamer shapes and the open flux at high altitudes.

2.1 Motivation and Calculation of Outflow Fields

In magnetohydrodynamic models, the velocity field is determined by the momentum equation

$$\rho \frac{\mathrm{D}\mathbf{v}}{\mathrm{D}t} = \frac{1}{\mu_0}(\nabla \times \mathbf{B}) \times \mathbf{B} - \nabla p - \rho \nabla \Psi, \tag{2.1}$$

coupled to the ideal induction equation

$$\frac{\partial \mathbf{B}}{\partial t} = \nabla \times (\mathbf{v} \times \mathbf{B}), \tag{2.2}$$

along with additional fluid equations to close the system. In the magneto-frictional method, pressure gradients and gravity are neglected, and instead a frictional ve-

locity is imposed as

$$\mathbf{v} = \nu_0 \frac{(\nabla \times \mathbf{B}) \times \mathbf{B}}{B^2}, \tag{2.3}$$

so that the induction equation leads to monotonic relaxation towards a stationary force-free field with $(\nabla \times \mathbf{B}) \times \mathbf{B} = \mathbf{0}$. The denominator is proportional to the magnetic field strength squared so that the overall evolution is independent of the magnitude of $\mathbf{B}$ and relaxation is not unduly slow near to magnetic null points ([29]). In the magnetofrictional codes described elsewhere in this thesis this denominator takes an alternative 'softened' form with some minimum value δ, which prevents numerical problems at magnetic null points (see Chapter 3). This is not a consideration for our semi-analytic outflow solutions, as at a null point the numerator is also necessarily precisely zero.

In the outer corona, the solar wind outflow prevents the magnetic field from being force-free, but this effect can be approximated in the magneto-frictional model by relaxing towards an equilibrium with a specified outflow $\mathbf{v}_{\text{out}}$, thus choosing $\mathbf{v}$ according to

$$\mathbf{v} = \nu_0 \frac{(\nabla \times \mathbf{B}) \times \mathbf{B}}{B^2} + \mathbf{v}_{\text{out}} \tag{2.4}$$

This *ad hoc* approach was introduced by [33], and has subsequently been used in global magneto-frictional models of solar and stellar coronae (e.g. [39, 97–99]). When a potential field is chosen to initialise the model, there is an initial period of up to a few days' evolution during which the system adjusts itself into the new equilibrium state. Here we propose to solve directly for equilibria of this model, avoiding this initial unphysical period of adjustment.

It is critical to note that the equilibria are not given by $\mathbf{v} = \mathbf{0}$ but rather by $\mathbf{v} \times \mathbf{B} = \mathbf{0}$, thanks to the form of the induction equation. Thus to calculate such an equilibrium directly, the equation we need to solve is

$$\left(\nu_0 \frac{(\nabla \times \mathbf{B}) \times \mathbf{B}}{B^2} + \mathbf{v}_{\text{out}} \right) \times \mathbf{B} = \mathbf{0}, \tag{2.5}$$

for specified $\mathbf{v}_{\text{out}}$. For simplicity, we will assume that the outflow velocity is purely radial, depends only on radius, and is constant in time, so $\mathbf{v}_{\text{out}} = v_{\text{out}}(r)\mathbf{e}_r$. In reality the solar wind speed does vary with latitude – it may be possible to generalise our

method to take this into account in future. We choose the wind speed in general to match Parker's solar wind solution ([13]), which for altitudes below the critical radius r_c (around $10R_\odot$ for typical coronal temperatures) is approximately

$$v_{\text{out}}(r) = v_1 \frac{r_1^2 \mathrm{e}^{-2r_c/r}}{r^2 \mathrm{e}^{-2r_c/r_1}}, \tag{2.6}$$

as derived in Section 1.3.2. Here r_1 is the upper limit of the domain. This approximation matches the exact solution of the implicit equation very closely throughout the domain if $r_1 = 2.5R_\odot$, but not at altitudes significantly higher than this. Thus in order to calculate accurate fields higher in the corona a more realistic solar wind approximation would be needed.

The shape of a solution to Equation (2.5) is determined by the ratio ν_0/v_1, such that altering the value of ν_0 is equivalent to scaling the outflow velocity function by a constant. Any dependence of ν_0 on the radius (which is often the case, such as in [14]) can also be incorporated into the outflow function. We can estimate the flow speed v_1 from the Parker solution, which for an isothermal corona at 2 MK gives $v_1 \approx 157\,\mathrm{km\,s^{-1}}$ at $r_1 = 2.5R_\odot$. However, it is difficult to determine an *a priori* value for the constant ν_0, as it does not directly correspond to a physical quantity. Previous magneto-frictional simulations of the global corona have used ν_0 values of the order $\nu_0 \sim 1.75 \times 10^{16}\,\mathrm{cm^2/s}$ ([14]), so we will adopt this value for our computations in this chapter. In future it may be possible to refine the ideal value for this constant based on comparison of outflow fields to observations.

2.1.1 Solution Technique

Since our imposed $\mathbf{v}_{\text{out}}$ depends only on the radial coordinate r (or in Cartesian coordinates y – which can be regarded as equivalent for now), the basic idea is to look for solutions to (2.5) of the form

$$\mathbf{B} = f(r)\nabla\varphi, \tag{2.7}$$

where $f(r)$ and $\varphi(r, \theta, \phi)$ are functions to be determined. A potential field would correspond to the special case of constant f. The current $\mathbf{j} = \nabla \times \mathbf{B}$ can be expressed as

$$\nabla \times \mathbf{B} = \nabla \times (f(r)\nabla\varphi) = \nabla f(r) \times \nabla\varphi + f(r)\nabla \times \nabla\varphi \tag{2.8}$$

by the chain rule. The second term on the right is zero, so using this and the vector triple product:

$$(\nabla \times \mathbf{B}) \times \mathbf{B} = (\nabla f(r) \times \nabla\varphi) \times \mathbf{B} = (\mathbf{B} \cdot \nabla f(r))\nabla\varphi - (\mathbf{B} \cdot \nabla\varphi)\nabla f(r). \tag{2.9}$$

Taking the cross product of this with another $\mathbf{B}$ and the first term here will disappear, as $\nabla\varphi \times \nabla\varphi = 0$:

$$[(\nabla \times \mathbf{B}) \times \mathbf{B}] \times \mathbf{B} = -[(\mathbf{B} \cdot \nabla\varphi)\nabla f(r)] \times \mathbf{B}, \tag{2.10}$$

which simplifies to

$$[(\nabla \times \mathbf{B}) \times \mathbf{B}] \times \mathbf{B} = -\frac{|\mathbf{B}|^2 f'}{f}\mathbf{e}_r \times \mathbf{B}. \tag{2.11}$$

Substituting this into the equilibrium equation (2.5) with $\mathbf{v}_{\text{out}} = v_{\text{out}}(r)\mathbf{e}_r$ reduces to the ordinary differential equation

$$\nu_0 f'(r) = v_{\text{out}}(r) f(r). \tag{2.12}$$

(In the spherical coordinate scheme, this equation will be slightly modified to account for the stretched radial coordinate, as described in Section 2.1.4 below.) Notice that, in the absence of outflow ($v_{\text{out}} = 0$), Equation (2.12) gives $f =$ constant, corresponding to a potential field. The function φ is then determined by the solenoidal condition $\nabla \cdot \mathbf{B} = 0$, which gives the partial differential equation

$$f\Delta\varphi + \nabla f \cdot \nabla\varphi = 0. \tag{2.13}$$

Again, when f is constant, this reduces to the usual Laplace equation $\Delta\varphi = 0$ for a

potential field. Eliminating f with (2.12) gives

$$\nu_0 \Delta\varphi + \mathbf{v}_{\text{out}} \cdot \nabla\varphi = 0. \tag{2.14}$$

We now discuss the solutions of this equation in both Cartesian and spherical coordinates, and the numerical implementations of such solutions in both cases.

2.1.2 Solution in Cartesian Coordinates

We consider a Cartesian domain with coordinate directions x, y, z. The y coordinate is chosen to be 'vertical' and so is treated differently to x and z. In this case Equation 2.12 becomes

$$\nu_0 f'(y) = v_{\text{out}}(y) f(y). \tag{2.15}$$

Solutions to Equation 2.14 can be found in a similar manner to solutions to Laplace's equation. These can generally be obtained by using an eigenfunction decomposition of the function $\varphi(x, y, z)$, which we assume can be expressed as follows:

$$\varphi(x, y, z) = \sum_{l,m} k_{l,m} X_m(x) Y_{l,m}(y) Z_l(z). \tag{2.16}$$

Taking the Laplacian of this gives

$$\begin{aligned}\Delta\varphi(x, y, z) = \sum_{l,m} k_{l,m} \Bigg(&\frac{\partial^2}{\partial x^2} X_m(x) Y_{l,m}(y) Z_l(z) + \\ &X_m(x) Y_{l,m}(y) \frac{\partial^2}{\partial z^2} Z_l(z) + X_m(x) \frac{\partial^2}{\partial y^2} Y_{l,m}(y) Z_l(z) \Bigg).\end{aligned} \tag{2.17}$$

For a potential field this Laplacian is zero. If this is the case, assuming boundary conditions that result in trigonometric functions in the x and z directions we can then obtain the three eigenfunction equations

$$X_m''(x) = -m^2 X_m(x) \tag{2.18}$$

$$Y_{l,m}''(y) = (l^2 + m^2) Y_{l,m}(y) \tag{2.19}$$

$$Z_l''(z) = -l^2 Z_l(z). \tag{2.20}$$

The eigenfunctions in the x and z directions are trigonometric and the eigenfunction in the y direction is hyperbolic in this potential field case. The normalisation on the lower boundary and the condition that the magnetic field $\mathbf{B} = \nabla\varphi$ on the upper boundary is radial will determine the precise nature of these eigenfunctions.

To modify this process for an outflow field, we note that

$$\mathbf{v}_{\text{out}} \cdot \nabla\varphi = v_{\text{out}} \frac{\partial\varphi}{\partial y}, \tag{2.21}$$

which results in a modification to the vertical eigenfunction $Y(y)$ only, as follows:

$$X''_m(x) = -m^2 X_m(x) \tag{2.22}$$

$$\nu_0 Y''_{l,m}(y) + v_{\text{out}}(y) Y'_{l,m}(y) = \nu_0 (l^2 + m^2) Y_{l,m}(y) \tag{2.23}$$

$$Z''_l(z) = -l^2 Z_l(z). \tag{2.24}$$

It is clear that this eigenfunction is no longer purely hyperbolic, although where the outflow speed is low (near the lower boundary) it will be almost identical. These eigenfunctions need to be solved numerically, but as a one-dimensional problem this is not a severe inconvenience.

To see the effect this modification has on the solutions, we focus on the two-dimensional case, where the z coordinate is chosen to be invariant. The domain configuration is similar to that used in the Cartesian magnetofrictional simulations to be described in Chapter 3. The magnetic fields in that chapter are 2.5D – the z direction (out of plane) is invariant but the field can have a component out of the plane. In order to keep the coefficients l, m as integers (just for neatness) we will place the side boundaries at $x = \pm\pi/2$, and set the arbitrary upper boundary at $y_1 = \pi/2$. The lower boundary condition is assumed to be

$$\mathbf{B} \cdot \mathbf{e}_y(x, 0) = \frac{\partial\varphi}{\partial y} = -\sin(x). \tag{2.25}$$

As all partial derivatives in the z direction disappear, we can assume the modes in that direction are unity ($Z_l = 1$). The lower boundary condition is then equivalent

to

$$\frac{\partial \varphi}{\partial y}(x,0) = \sum_m k_{0,m} X_m(x) \frac{\partial}{\partial y} Y_{0,m}(y)|_{y=0} = -\sin(x). \tag{2.26}$$

We clearly only require one mode in the expansion here, corresponding to $m = 1$ and the eigenfunction $X_1(x) = \sin(x)$. Then $k_{0,1} = -1$ is the only nonzero coefficient and the lower boundary condition on the vertical eigenfunction is

$$\frac{\partial}{\partial y} Y_{0,1}(y)|_{y=0} = 1, \tag{2.27}$$

with the the radial condition on the top boundary equivalent to

$$Y_{0,1}(y_1) = 0. \tag{2.28}$$

Using Equation 2.23, we then have a well-posed ODE for the function $Y_{0,1}(y)$:

$$\nu_0 Y''_{0,1}(y) + v_{\text{out}}(y) Y'_{0,1}(y) = \nu_0 Y_{0,1}(y). \tag{2.29}$$

Note that in the absence of any outflow the solution to this equation is hyperbolic:

$$Y_{0,1}(y) = \frac{1}{\cosh(y_1)} \sinh(y - y_1), \tag{2.30}$$

and so the full potential magnetic field with no outflow is simply

$$\mathbf{B}(x,y) = \frac{1}{\cosh(y_1)} \left(\cos(x)\sinh(y-y_1), -\sin(x)\cosh(y-y_1), 0\right). \tag{2.31}$$

For a typical outflow profile in this domain (as used in the Cartesian simulations in Chapter 2) of

$$v_{\text{out}}(y) = v_1 \left(\frac{y}{y_1}\right)^{10} \tag{2.32}$$

for some constant v_1, the effect on the vertical eigenfunction is plotted in Figure 2.1. We observe that the effect of increased outflow is to cause the eigenfunction to flatten out in the upper region of the domain, becoming closer to zero (the imposed top boundary condition). Physically, this results in the 'opening-out' of the magnetic field lines, becoming more radial near the upper boundary.

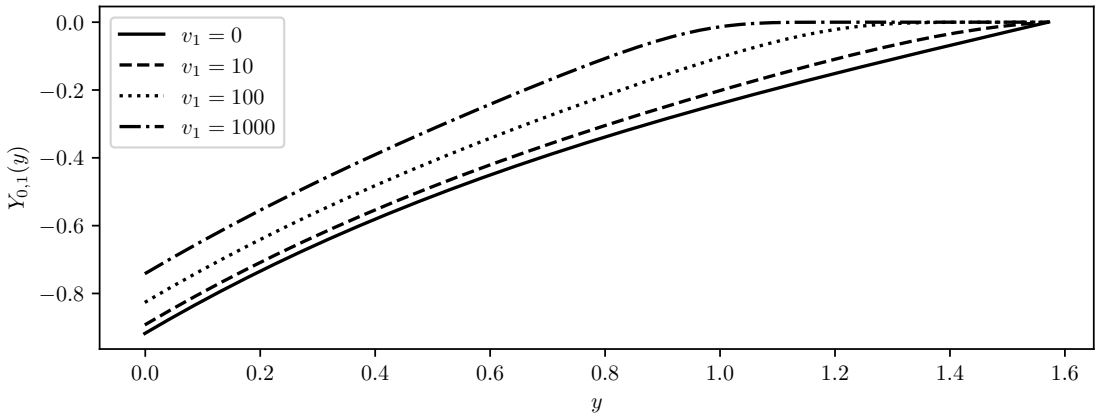

Figure 2.1: Plot of the vertical eigenfunctions $Y_{0,1}(y)$ for varying outflow speeds v_1. The function with no outflow is merely the hyperbolic function $\sinh(y - y_1)$ (scaled appropriately). We observe that the functions flatten out near the upper boundary when the outflow velocity increases. Here $\nu_0 = 1.0$.

The full magnetic field for these four outflow velocities is shown in Figure 2.2, where the fields have been calculated using the numerical method described in the next section. We clearly see the differences between the potential field with no outflow (top left) and the fields that are in equilibrium with a nonzero solar wind. We observe that the magnetic field lines become more radial near the top boundary (with this effect reaching further into the domain for higher speeds) and the current (plotted as the heatmap) that is induced as a result. Note that the fastest outflow speeds plotted here are far higher than reality - this is just to show more clearly the limiting case as the imposed velocity increases.

We note that current sheets do not form in this model, whereas in full MHD it would be possible to form them with a suitable lower boundary condition. As the horizontal component of the magnetic field is sinusoidal when only one mode is considered (irrespective of the outflow velocity) in our model the magnetic field will always be smooth.

2.1.3 Numerical Implementation in 2D Cartesian Coordinates

In this section we will outline the numerical implementation of the above method, in the 2D Cartesian case. The implementation for the full spherical 3D fields is

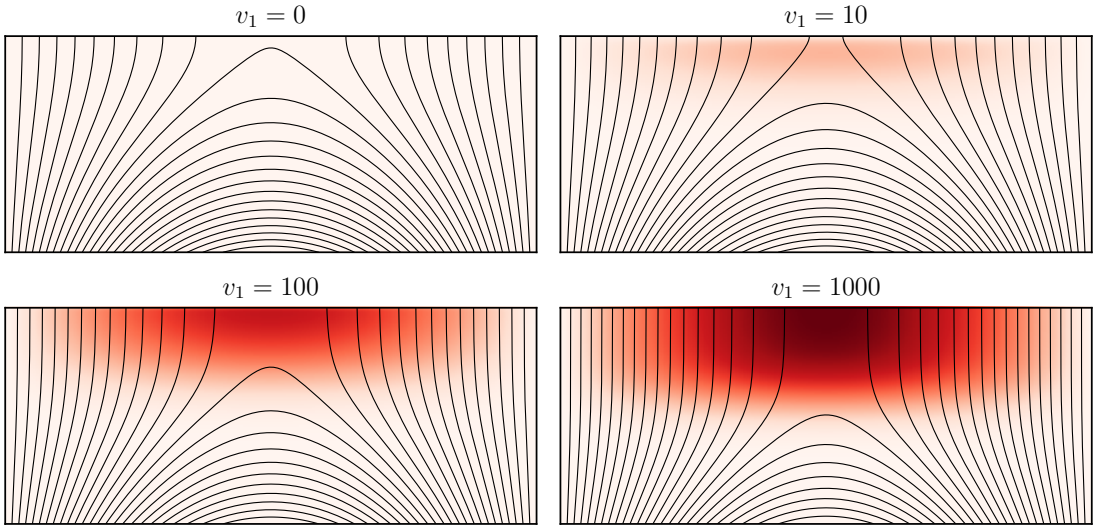

Figure 2.2: The equilibrium outflow fields for four different outflow velocities. The magnetic field lines are drawn in black and the current (in the out-of-plane direction) is plotted as the heatmap (with the same scale in all four plots). Here we have assumed $\nu_0 = 1.0$. A velocity of $v_1 = 1000$ is far higher than would be used in reality, and is plotted only to illustrate the limiting case as the velocity increases.

similar, but considerably more complex. Thus it is hoped that this implementation in Cartesian coordinates (which is more intuitive and far easier to explain) can be used as motivation for the full 3D case.

We first describe the grid on which the magnetic field components are stored. The approach, as with all the models in this Thesis, is to use a 'staggered grid' ([46]), such that $\nabla \cdot \mathbf{B} = 0$ to machine precision. The two components of $\mathbf{B}$ are stored on the grid in the same position as the magnetic flux through each of the sides of the grid cell. We will number the cells with i, j indices for the x and y directions respectively, with the indices taking integer values at the grid points and half integers at the grid faces. The grid points are equally spaced in both the x and y directions.

Unfortunately, evaluating the solution to Equation 2.12 is numerically very difficult for significant outflow speeds, as the function $f(y)$ will become extremely large near the upper boundary. Although analytically this is not a problem, as it will always be multiplied by another function which is very small, it does present numerical challenges. To solve this problem we can instead define two new functions

with vertical dependence:

$$G(y) = f(y)Y(y) \tag{2.33}$$

$$H(y) = f(y)Y'(y), \tag{2.34}$$

and solve directly for these instead.

The magnetic field then becomes

$$\mathbf{B}(x,y) = \sum_m k_m(X'_m(x)G_m(y)\mathbf{e}_x + X_m(x)H_m(y)\mathbf{e}_y), \tag{2.35}$$

or numerically, for an individual mode m:

$$B_x^{i,j+1/2} = \frac{1}{\delta x}G^{j+1/2}(X^{i+1/2} - X^{i-1/2}) \tag{2.36}$$

$$B_y^{i+1/2,j} = X^{i+1/2}H^j, \tag{2.37}$$

where δx is the grid step in the x direction.

The solenoidal condition ensures the sum of the magnetic fluxes through each face of each cell is precisely zero. This will provide us with the numerical scheme used to calculate the functions G and H. The sum of the magnetic fluxes through the $(i+1/2, j+1/2)$ cell is

$$\frac{\delta y}{\delta x}G^{j+1/2}(X^{i+3/2} - 2X^{i+1/2} + X^{i-1/2}) + \delta x X^{i+1/2}(H^{j+1} - H^j) = 0. \tag{2.38}$$

Given the side boundary conditions, the function X must be sinusoidal and hence obeys the equation

$$X''_m(x) = -m^2 X_m(x), \tag{2.39}$$

for some eigenvalue m. Numerically this is approximated using central differences:

$$(X^{i+3/2} - 2X^{i+1/2} + X^{i-1/2}) = -m^2\delta x^2 X^{i+1/2}. \tag{2.40}$$

To obtain an ODE for the Y modes we can substitute Equation 2.39 into the original

equation for φ (Equation 2.14):

$$Y_m''(y) = -\frac{v_{\text{out}}(y)}{\nu_0} Y_m'(y) + m^2 Y_m(y). \tag{2.41}$$

From this we then need to derive alternative ODEs for $G_m(y)$ and $H_m(y)$, which unlike $Y_m(y)$ can be solved numerically without problems at the upper boundary.

We begin with

$$G = fY \tag{2.42}$$

$$f' = vf, \tag{2.43}$$

where all functions have implied y dependence and we have defined $v(y) = v = v_{\text{out}}/\nu_0$. Using the chain rule, we then have

$$G' = f'Y + Y'f \tag{2.44}$$

$$G'' = f''Y + 2f'Y' + fY''. \tag{2.45}$$

We then use ODEs for f and Y to eliminate the second derivatives on the right hand side of Equation 2.45:

$$G'' = f'vY + fv'Y + 2f'Y' + f(m^2 Y - Y'\frac{f'}{f}) \tag{2.46}$$

$$= f'vY + fv'Y + f'Y' + fm^2 Y \tag{2.47}$$

$$= (f'Y + fY')v + fY(v' + m^2) \tag{2.48}$$

$$= vG' + G(v' + m^2). \tag{2.49}$$

This is a suitable ODE for G, with boundary conditions $G'(0) = 1, G(y_1) = 0$ (this lower boundary condition will be justified shortly). Once G has been determined,

H follows with relative ease:

$$H' = f'Y' + fY'' \tag{2.50}$$

$$= f'Y' + f(m^2 Y - Y'\frac{f'}{f}) \tag{2.51}$$

$$= m^2 fY \tag{2.52}$$

$$= m^2 G. \tag{2.53}$$

Substituting Equation 2.40 into Equation 2.38 gives the system of equations

$$(X^{i+3/2} - 2X^{i+1/2} + X^{i-1/2}) = -m^2 \delta x^2 X^{i+1/2} \tag{2.54}$$

$$(H^{j+1} - H^j) = m^2 \delta y G^{j+1/2}. \tag{2.55}$$

where the second of these nicely approximates Equation 2.53. There is flexibility in the numerical scheme used to calculate the function $G(y) = G_m^{j+1/2}$ from Equation 2.49. Once G has been calculated, the values for H_m^j can be obtained by direct integration using 2.55. Providing this numerical system is satisfied the magnetic field will obey the solenoidal condition to machine precision.

We now outline the procedure behind the calculation in detail. We begin by calculating the eigenfunctions $X_m(x)$ and their respective eigenvalues m. This is achieved by solving the system in Equation 2.54, which can be expressed as a matrix equation

$$A\mathbf{X} = \lambda \mathbf{X} = -m^2 \delta x^2 \mathbf{X}, \tag{2.56}$$

where A is a tridiagonal matrix with on-diagonal elements -2 and off-diagonal elements 1:

$$\begin{pmatrix} -1 & 1 & 0 & 0 & 0 \\ 1 & 2 & 1 & 0 & 0 \\ & & \ddots & & \\ 0 & 0 & 1 & 2 & 1 \\ 0 & 0 & 0 & 1 & -1 \end{pmatrix} \begin{pmatrix} X_m^0 \\ X_m^1 \\ \vdots \\ X_m^{nx-2} \\ X_m^{nx-1} \end{pmatrix} = -m^2 \delta x^2 \begin{pmatrix} X_m^0 \\ X_m^1 \\ \vdots \\ X_m^{nx-2} \\ X_m^{nx-1} \end{pmatrix}$$

The side boundary conditions are implemented here, namely that $X'(x) = 0$. This sets the values in the corners of the matrix to -1. This tridiagonal matrix is solved using a built-in python solver.

With these boundary conditions the numerical eigenfunctions X^i_m roughly approximate the sinusoidal functions $\cos(m(x + \pi/2))$, for eigenvalues m that are integers in the infinite-resolution limit but are not necessarily so for our finite resolutions. The eigenvalues m for increasing numbers of grid cells n (in the x direction) are plotted in Figure 2.3.

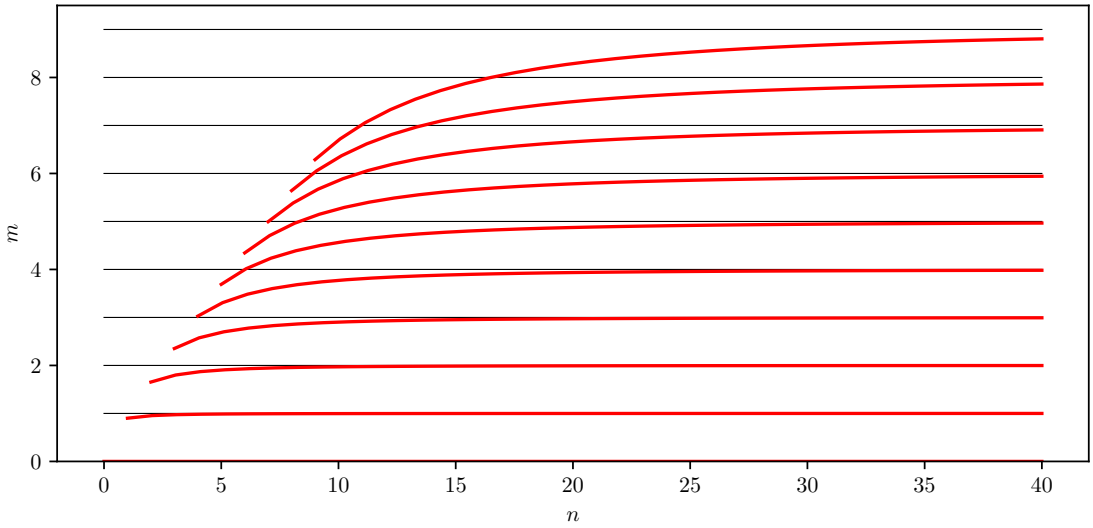

Figure 2.3: The first 10 eigenvalues of Equation 2.56, as a function of the number of grid cells n. The eigenvalues are plotted in red, and the integer values they converge to as the horizontal black lines.

We observe that the eigenvalues m do indeed converge to integer values as the grid resolution increases, but for lower resolutions they are generally less than their true analytical value. We can examine the limiting case analytically: as the grid resolution increases the tridiagonal matrix can be reasonably approximated by a tridiagonal Toeplitz matrix, where the corner values are also 2.

The eigenvalues of such a matrix can actually be calculated directly:

$$m_k = \frac{n}{\pi}\sqrt{2 - 2\cos\left(\frac{k\pi}{n+1}\right)}. \tag{2.57}$$

As the number of cells n increases relative to the eigenvalue number k, we can

approximate the cosine function with the second-order Taylor expansion:

$$m_k = \frac{n}{\pi}\sqrt{2 - 2 + \left(\frac{k\pi}{n+1}\right)^2}, \tag{2.58}$$

$$m_k = \frac{n}{\pi}\frac{k\pi}{n+1}, \tag{2.59}$$

so clearly $m_k \to k$ as $n \to \infty$, as expected. The value of the first occurrence of each eigenvalue can also be calculated in the limit. Taking $n \to \infty$ and $k = n$ gives $m_k = 2k/\pi$, which is roughly the gradient of the leftmost ends of the red eigenvalue lines in Figure 2.3.

We have now obtained the vectors X_m^i for each mode m. It remains to calculate the vertical functions G_m^i and H_m^i, which must obey Equation 2.55 exactly and approximate Equation 2.49. The upper boundary condition is that the magnetic field lines are vertical, which can be implemented by setting $G_m(y_1) = 0$. On the lower boundary we set $G'_m(0) = 1$, which ensures $H_m(0) = 1$ given $G' = vG + H$ and $v(0) = 0$.

These boundary conditions are such that we can use a 'linear shooting method'. The upper boundary condition is initially implemented as $G_m^{nx+1/2} = -G_m^{nx-1/2} = 1.0$, and then the remaining values are calculated by direct integration, moving downwards to the lower boundary. The entire solution is then scaled to ensure that $G_m^{1/2} - G_m^{-1/2} = \delta y$. This procedure is repeated for all the modes m, if necessary. The other vertical function H_m is then obtained using Equation 2.55, with $H_m^0 = 1$ on the lower boundary.

Finally, the coefficients in the Fourier expansion k_m are then calculated using the boundary condition on the vertical magnetic field. We require

$$\frac{\partial}{\partial y}\varphi(x, 0) = \sum_m k_m X_m(x) H_m(0) = B_y(x), \tag{2.60}$$

numerically equivalent to

$$\frac{1}{\delta y}(\varphi^{i+1/2,1/2} - \varphi^{i+1/2,-1/2}) = \sum_m k_m X_m^{i+1/2} \tag{2.61}$$

$$= B_y^{i+1/2}. \tag{2.62}$$

We can then use the orthogonality of the eigenvectors $X_m^{i+1/2}$ to calculate the coefficients k_m:

$$k_m = \frac{\sum_i X_m^{i+1/2} B_y^{i+1/2}}{\sum_i X_m^{i+1/2} X_m^{i+1/2}}, \tag{2.63}$$

providing the full solution. This is the technique used to produce the fields in Figure 2.2.

The extension of this process to full 3D in Cartesian coordinates should be relatively clear. Calculation in spherical coordinates introduces various extra challenges, however, which shall be discussed in the next section.

2.1.4 Solution in Spherical Coordinates

We now describe the procedure for finding outflow field solutions in full spherical geometry. These solutions are the main focus of our paper [6]. They are designed to be suitable for initialising magnetofrictional simulations using existing codes (eg. [40]), and as such the coordinate systems are identical, including the use of a stretched radial coordinate.

Similarly to the Cartesian case, since equation (2.14) is linear we seek to write X in terms of eigenmodes. Here we use a grid equally spaced in stretched spherical coordinates (ρ, s, ϕ) satisfying

$$\rho = \ln(r), \quad s = \cos\theta, \quad \phi = \phi, \tag{2.64}$$

rather than normal spherical coordinates (r, θ, ϕ). Due to this scaling, we now need to introduce coordinate scale factors:

$$h_\rho = r = e^\rho, \;\; h_s = \frac{r}{\sin\theta} = \frac{e^\rho}{\sqrt{1-s^2}}, \;\; h_\phi = r\sin\theta = e^\rho\sqrt{1-s^2}. \tag{2.65}$$

As for the Cartesian case, we begin by writing the unknown magnetic potential as an eigenfunction expansion

$$\varphi(\rho, s, \phi) = \sum_{l,m} C_{l,m} R_l(\rho) Q_{l,m}(s) \Phi_m(\phi). \tag{2.66}$$

This is substituted into (2.14) to obtain the three eigenfunction equations

$$\nu_0 R_l'' + (\nu_0 + \mathrm{e}^{\rho} v_{\text{out}}) R_l' = \nu_0 l(l+1) R_l, \tag{2.67}$$

$$(1-s^2) Q_{l,m}'' - 2s Q_{l,m}' + l(l+1) Q_{l,m} = \frac{m^2}{1-s^2} Q_{l,m}, \tag{2.68}$$

$$\Phi_m'' = -m^2 \Phi_m, \tag{2.69}$$

where l and m are integers with $-l \leq m \leq l$. The latitudinal and azimuthal equations are the same as for the Laplace equation $\Delta X = 0$, yielding the associated Legendre polynomials $Q_{l,m}$ and trigonometric functions Φ_m that are familiar from the potential field model. However, as for the Cartesian case the radial eigenfunctions differ from a potential field due to the presence of the v_{out} term, and we must additionally solve for the function $f(\rho)$, using the equation

$$f'(\rho) = e^{\rho} \frac{v_{\text{out}}(\rho)}{\nu_0} f(\rho). \tag{2.70}$$

Notice that this differs to (2.12) as the coordinate in the radial direction has been stretched.

In the potential field case where $v_{\text{out}} = 0$, equation (2.67) has the exact general solution

$$R_l(\rho) = A\mathrm{e}^{l\rho} + B\mathrm{e}^{(-l-1)\rho}, \tag{2.71}$$

but in the presence of outflow, the equation must be solved numerically. In practice, we find that although we can solve (2.67) for R_l without issue, calculating the function f is not possible as near the upper boundary it becomes far too large to be handled numerically – similarly to the Cartesian case but even more problematic due to the presence of the exponential factors. The solution to this problem is to

solve for the re-scaled eigenfunctions

$$H_l(\rho) = \mathrm{e}^{-\rho} f(\rho) R_l(\rho) \tag{2.72}$$

instead.

In terms of the eigenfunctions, $\mathbf{B}$ has the form

$$\mathbf{B} = \sum_{l,m} C_{l,m} \left[\frac{f R_l'}{\mathrm{e}^{\rho}} Q_{l,m} \Phi_m \mathbf{e}_\rho + \frac{f R_l}{\mathrm{e}^{\rho}} \sqrt{1-s^2} Q_{l,m}' \Phi_m \mathbf{e}_s + \frac{f R_l}{\mathrm{e}^{\rho}} \frac{Q_{l,m}}{\sqrt{1-s^2}} \Phi_m' \mathbf{e}_\phi \right] \tag{2.73}$$

$$= \sum_{l,m} C_{l,m} \left[G_l Q_{l,m} \Phi_m \mathbf{e}_\rho + H_l \sqrt{1-s^2} Q_{l,m}' \Phi_m \mathbf{e}_s + H_l \frac{Q_{l,m}}{\sqrt{1-s^2}} \Phi_m' \mathbf{e}_\phi \right], \tag{2.74}$$

where H_l are the rescaled eigenfunctions in (2.72) and we also define the function

$$G_l(\rho) = \mathrm{e}^{-\rho} f(\rho) R_l'(\rho). \tag{2.75}$$

We require an equation for the eigenfunctions $H_l(\rho)$. This can be obtained by using Equations 2.72 and 2.67, in rather a long-winded derivation. For clarity, we drop the mode subscript l, the dependence on ρ and define $v(\rho) = v = v_{\mathrm{out}}(\rho)/\nu_0$.

The relevant equations then become

$$H\mathrm{e}^{\rho} = fR \tag{2.76}$$

$$R'' + (1 + \mathrm{e}^{\rho} v) R' = l(l+1) R. \tag{2.77}$$

Differentiating the first of these twice gives

$$H'' e^{\rho} + 2H' e^{\rho} + H e^{\rho} = R'' f + 2R' f' + R f''. \tag{2.78}$$

Using the differential equation 2.77 to eliminate R'':

$$H'' e^{\rho} + 2H' e^{\rho} + H e^{\rho} = -f R' (1 + v e^{\rho}) + R l(l+1) f + 2R' f' + R f''. \tag{2.79}$$

Now f and its derivatives can then be eliminated using

$$f' = e^\rho f v \tag{2.80}$$

$$f'' = e^\rho (f v + f' v + f v') \tag{2.81}$$

to give

$$H'' e^\rho + 2H' e^\rho + H e^\rho = -f R'(1 + v e^\rho) + R l(l+1) f + 2R' e^\rho f v + R e^\rho (f v + f' v + f v'). \tag{2.82}$$

Grouping like terms on the right-hand side:

$$H'' e^\rho + 2H' e^\rho + H e^\rho = f R(l(l+1) + v e^\rho + v^2 e^{2\rho} + v' e^\rho) + f R'(e^\rho v - 1), \tag{2.83}$$

then essentially integrating by parts to get rid of the $R'f$ term gives

$$H'' e^\rho + 2H' e^\rho + H e^\rho = f R(l(l+1) + v e^\rho + v^2 e^{2\rho} + v' e^\rho) + (H' e^\rho + H e^\rho - f' R)(e^\rho v - 1). \tag{2.84}$$

This has caused an extra derivative f' to appear, which we can remove as before:

$$H'' e^\rho + 2H' e^\rho + H e^\rho = f R(l(l+1) + v e^\rho + v^2 e^{2\rho} + v' e^\rho) + (H' e^\rho + H e^\rho - e^\rho f v R)(e^\rho v - 1), \tag{2.85}$$

and grouping terms once more

$$H'' e^\rho + 2H' e^\rho + H e^\rho = f R(l(l+1) + 2e^\rho v + v' e^\rho) + (H' e^\rho + H e^\rho)(e^\rho v - 1). \tag{2.86}$$

Continuing in this fashion:

$$H'' e^\rho + 2H' e^\rho + H e^\rho = H e^\rho (l(l+1) + 2e^\rho v + v' e^\rho) + (H' e^\rho + H e^\rho)(e^\rho v - 1). \tag{2.87}$$

$$H'' + 2H' + H = H(l(l+1) + 2e^\rho v + v' e^\rho) + (H' + H)(e^\rho v - 1). \tag{2.88}$$

$$0 = H'' + H'(3 - e^\rho v) + H(2 - l(l+1) - 3v e^\rho - v' e^\rho). \tag{2.89}$$

Reinstating the dropped notation gives us the final ODE for H_l:

$$\nu_0 H_l'' + (3\nu_0 - \mathrm{e}^{\rho} v_{\mathrm{out}}) H_l' - \Big[\nu_0(l(l+1)-2) + 3\mathrm{e}^{\rho} v_{\mathrm{out}} + \mathrm{e}^{\rho} v_{\mathrm{out}}'\Big] H_l = 0. \tag{2.90}$$

Thus $\mathbf{B}$ may be calculated in a similar manner to the classical potential field, by solving the eigenfunction equations (2.68), (2.69) and (2.90). As in the potential field model, the coefficients $C_{l,m}$ are determined by matching the observed radial field distribution $B_\rho(\rho_0, s, \phi)$ on the lower boundary $\rho = \rho_0$. The corresponding lower boundary condition for H_l is determined by choosing $G_l(\rho_0) = 1$. In combination with the physical requirement that $v_{\mathrm{out}}(\rho_0) = 0$, by differentiating Equation 2.76 it follows that this is equivalent to

$$(H_l(\rho) e^{\rho})'|_{\rho_0} = e^{\rho_0}. \tag{2.91}$$

A numerical approximation of this is used in the code.

As the required second boundary condition for H_l, we set $H_l(\rho_1) = 0$ at some outer boundary $\rho = \rho_1$, so that $\mathbf{B}$ is purely radial there. Provided ρ_1 is high enough, this condition does not have a significant influence on the shape of the magnetic field, since the field lines tend to be radial already in the upper part of the domain when outflow is present. This is in contrast to the potential field where the radial field condition at the source surface has a significant effect on the shape of the field – a phenomenon that will be discussed later in this chapter.

2.1.5 Numerical Implementation in Spherical Coordinates

We now describe the numerical procedure for calculating these solutions in spherical coordinates. The code based on this approach provided the main results for our paper [6]. The Python code is open source and freely available at `https://github.com/oekrice/outflow`. Much as for the Cartesian case, our approach is to calculate $\mathbf{B}$ on a staggered grid ([46]), such that $\nabla \cdot \mathbf{B} = 0$ to machine precision in a particular discretization. Imposing the discrete solenoidal condition on a finite grid leads to discrete eigenfunctions H_l, $Q_{l,m}$ and Φ_m that are only approximations to the exact

analytical eigenfunctions, and to eigenvalues m and l that are no longer necessarily integers. A similar approach was used by [32] for potential fields, and implemented in the Python potential field solver of [100] that uses the same (ρ, s, ϕ) grid as in this paper.

The spherical coordinate code uses a staggered grid, similarly to the Cartesian case. We number the cells with i, j, k indices for the ρ, s, ϕ directions respectively. The indices take integer values at the grid points, which are equally spaced in the (ρ, s, ϕ) coordinates and given by

$$\rho^i = \rho_0 + i\delta\rho, \quad \delta\rho = (\rho_1 - \rho_0)/n_\rho, \tag{2.92}$$

$$s^j = -1 + j\delta s, \quad \delta s = 2/n_s, \tag{2.93}$$

$$\phi^k = k\delta\phi, \quad \delta\phi = 2\pi/n_\phi. \tag{2.94}$$

At each cell face, two of the i, j, k indices take half-integer values. The cell face areas may be calculated from the coordinate transform by integration of the coordinate scale factors (2.65). This gives

$$S_\rho^{i,j+\frac{1}{2},k+\frac{1}{2}} = e^{2\rho^i}\delta s\delta\phi \tag{2.95}$$

$$S_s^{i+\frac{1}{2},j,k+\frac{1}{2}} = \frac{1}{2}(e^{2\rho^{i+1}} - e^{2\rho^i})\sigma^j\delta\phi \tag{2.96}$$

$$S_\phi^{i+\frac{1}{2},j+\frac{1}{2},k} = \frac{1}{2}(e^{2\rho^{i+1}} - e^{2\rho^j})(\arcsin(s^{j+1}) - \arcsin(s^j)), \tag{2.97}$$

where $\sigma^j = \sqrt{1-(s^j)^2}$ is a quantity that appears frequently. The magnetic field components are defined on the corresponding faces and denoted $B_\rho^{i,j+\frac{1}{2},k+\frac{1}{2}}$, $B_s^{i+\frac{1}{2},j,k+\frac{1}{2}}$, $B_\phi^{i+\frac{1}{2},j+\frac{1}{2},k}$.

The magnetic field is expanded in a finite series of discrete eigenfunctions, so

that analogously to (2.74) we have

$$B_\rho^{i,j+\frac{1}{2},k+\frac{1}{2}} = \sum_{l,m} C_{l,m} G_l^i Q_{l,m}^{j+\frac{1}{2}} \Phi_m^{k+\frac{1}{2}}, \tag{2.98}$$

$$B_s^{i+\frac{1}{2},j,k+\frac{1}{2}} = \sum_{l,m} C_{l,m} H_l^{i+\frac{1}{2}} \sigma^j (Q'_{l,m})^j \Phi_m^{k+\frac{1}{2}}, \tag{2.99}$$

$$B_\phi^{i+\frac{1}{2},j+\frac{1}{2},k} = \sum_{l,m} C_{l,m} H_l^{i+\frac{1}{2}} \frac{1}{\sigma^{j+\frac{1}{2}}} Q_{l,m}^{j+\frac{1}{2}} (\Phi'_m)^k. \tag{2.100}$$

To determine the correct numerical scheme, we impose the solenoidal condition in integral form at each grid cell, which requires

$$\begin{aligned} &B_\rho^{i+1,j+\frac{1}{2},k+\frac{1}{2}} S_\rho^{i+1,j+\frac{1}{2},k+\frac{1}{2}} - B_\rho^{i,j+\frac{1}{2},k+\frac{1}{2}} S_\rho^{i,j+\frac{1}{2},k+\frac{1}{2}} + \\ &\qquad B_s^{i+\frac{1}{2},j+1,k+\frac{1}{2}} S_s^{i+\frac{1}{2},j+1,k+\frac{1}{2}} - B_s^{i+\frac{1}{2},j,k+\frac{1}{2}} S_s^{i+\frac{1}{2},j,k+\frac{1}{2}} + \\ &\qquad\qquad B_\phi^{i+\frac{1}{2},j+\frac{1}{2},k+1} S_\phi^{i+\frac{1}{2},j+\frac{1}{2},k+1} - B_\phi^{i+\frac{1}{2},j+\frac{1}{2},k} S_\phi^{i+\frac{1}{2},j+\frac{1}{2},k} = 0. \end{aligned} \tag{2.101}$$

This translates into equations for G_l^i, $Q_{l,m}^{j+\frac{1}{2}}$ and $\Phi_m^{k+\frac{1}{2}}$, as follows. Substituting the discrete expansions (2.98), (2.99), (2.100) into this condition leads – for a single mode l, m – to the equation

$$\begin{aligned} &(G_l^{i+1} \mathrm{e}^{2\rho^{i+1}} - G_l^i \mathrm{e}^{2\rho^i}) Q_{l,m}^{j+\frac{1}{2}} \Phi_m^{k+\frac{1}{2}} \delta s \delta\phi + \\ &\qquad \frac{1}{2} (\mathrm{e}^{2\rho^{i+1}} - \mathrm{e}^{2\rho^i}) H_l^{i+\frac{1}{2}} \Phi_m^{k+\frac{1}{2}} \delta\phi [(Q'_{l,m})^{j+1} (\sigma^{j+1})^2 - (Q'_{l,m})^j (\sigma^j)^2] + \\ &\frac{1}{2\sigma^{j+\frac{1}{2}}} H_l^{i+\frac{1}{2}} Q_{l,m}^{j+\frac{1}{2}} (\mathrm{e}^{2\rho^{i+1}} - \mathrm{e}^{2\rho^i}) [\arcsin(s^{j+1}) - \arcsin(s^j)] [(\Phi'_m)^{k+1} - (\Phi'_m)^k] = 0. \end{aligned} \tag{2.102}$$

Since the $(\Phi_m)^{k+\frac{1}{2}}$ approximate trigonometric functions, we assume the discrete approximation

$$(\Phi_m'^{k+1}) - (\Phi_m'^k) = -m^2 \Phi_m^{k+\frac{1}{2}} \delta\phi \tag{2.103}$$

for some m that would be an integer in the limit $\delta\phi \to 0$ but not necessarily so at our finite resolution. This removes the azimuthal dependence from (2.102) and

reduces it to the separable form

$$\frac{2}{H_l^{i+\frac{1}{2}}}\frac{G_l^{i+1}\mathrm{e}^{2\rho^{i+1}}-G_l^i\mathrm{e}^{2\rho^i}}{\mathrm{e}^{2\rho^{i+1}}-\mathrm{e}^{2\rho^i}}+$$
$$\frac{1}{Q_{l,m}^{j+\frac{1}{2}}\delta s}\{(Q'_{l,m})^{j+1}(\sigma^{j+1})^2-(Q'_{l,m})^j(\sigma^j)^2-\frac{m^2}{\sigma^{j+\frac{1}{2}}}Q_{l,m}^{j+\frac{1}{2}}[\arcsin(s^{j+1})-\arcsin(s^j)]\}=0. \tag{2.104}$$

In order that $Q_{l,m}$ approximate the analytical associated Legendre polynomials, we choose a separation constant of the form $l(l+1)$ so that we obtain the radial equation

$$\frac{2}{H_l^{i+\frac{1}{2}}}\frac{G_l^{i+1}\mathrm{e}^{2\rho^{i+1}}-G_l^i\mathrm{e}^{2\rho^i}}{\mathrm{e}^{2\rho^{i+1}}-\mathrm{e}^{2\rho^i}}=l(l+1) \tag{2.105}$$

and the latitudinal equation

$$(Q'_{l,m})^{j+1}(\sigma^{j+1})^2-(Q'_{l,m})^j(\sigma^j)^2-\frac{m^2}{\sigma^{j+\frac{1}{2}}}Q_{l,m}^{j+\frac{1}{2}}[\arcsin(s^{j+1})-\arcsin(s^j)]=$$
$$-l(l+1)Q_{l,m}^{j+\frac{1}{2}}\delta s. \tag{2.106}$$

Similarly to the azimuthal eigenvalues, on our finite resolution grid the l will no longer be precisely integers.

We also calculate the eigenvalues m as for the Cartesian case, by solving a tridiagonal linear system. Approximating $(\Phi'_m)^k$ by central differences reduces (2.103) to the tridiagonal eigenvalue problem

$$-\Phi_m^{k+\frac{3}{2}}+2\Phi_m^{k+\frac{1}{2}}-\Phi_m^{k-\frac{1}{2}}=\lambda_m\Phi_m^{k+\frac{1}{2}}, \tag{2.107}$$

which determines both the eigenfunctions and the values of m, from the eigenvalues $\lambda_m=m^2\delta\phi^2$. The boundary conditions differ from the Cartesian case, however, as they are periodic in the azimuthal direction. To implement this, we need to ensure that the eigenfunctions approximate cosine or sine functions with integer coefficients. The boundary conditions for cosine functions are $\Phi_m^{-\frac{1}{2}}=\Phi_m^{\frac{1}{2}}$ and $\Phi_m^{n_\phi+\frac{1}{2}}=\Phi_m^{n_\phi-\frac{1}{2}}$. The boundary conditions for sine functions are $\Phi_m^{-\frac{1}{2}}=-\Phi_m^{\frac{1}{2}}$ and $\Phi_m^{n_\phi+\frac{1}{2}}=-\Phi_m^{n_\phi-\frac{1}{2}}$. By avoiding implementing the periodic boundary conditions directly, we retain a

tridiagonal eigenvalue problem that is efficiently solved with a standard solver.

We take this approach as we need to have some flexibility in the numerical scheme for the radial eigenfunctions. These radial functions then specify exactly the necessary schemes used in other directions so as to preserve (2.101). In contrast, in most PFSS (potential field) codes (e.g. [32, 101]) the azimuthal eigenfunctions are calculated using a Fourier Transform and the numerical schemes in the radial and latitudinal directions follow from this.

Once the azimuthal eigenfunctions have been calculated, we can proceed with the other dimensions. The eigenfunctions $Q_{l,m}^{j+\frac{1}{2}}$ and possible values of l are determined by (2.106), which is a discrete approximation to the associated Legendre equation (2.68). To see this, observe that

$$\frac{(Q'_{l,m})^{j+1}(\sigma^{j+1})^2 - (Q'_{l,m})^j(\sigma^j)^2}{\delta s} \approx \frac{\mathrm{d}}{\mathrm{d}s}[Q'_{l,m}(1-s^2)], \tag{2.108}$$

and that

$$\frac{m^2}{\sigma^{j+\frac{1}{2}}} Q_{l,m}^{j+\frac{1}{2}} \frac{\arcsin(s^{j+1}) - \arcsin(s^j)}{\delta s} \approx \frac{m^2 Q_{l,m}}{\sqrt{1-s^2}} \frac{\mathrm{d}}{\mathrm{d}s}\arcsin(s) = \frac{m^2 Q_{l,m}}{1-s^2}. \tag{2.109}$$

Approximating the derivatives $(Q'_{l,m})^j$ by central differences $(Q'_{l,m})^j = (Q_{l,m}^{j+\frac{1}{2}} - Q_{l,m}^{j-\frac{1}{2}})/\delta s$ reduces (2.106) to a tridiagonal eigenvalue problem for each m ([32]). Specifically,

$$Q_{l,m}^{j+\frac{3}{2}}(\sigma^{j+1})^2 - Q_{l,m}^{j+\frac{1}{2}}\left[(\sigma^{j+1})^2 + (\sigma^j)^2 + \delta s \frac{m^2}{\sigma^{j+\frac{1}{2}}}[\arcsin(s^{j+1}) - \arcsin(s^j)]\right] + Q_{l,m}^{j-\frac{1}{2}}(\sigma^j)^2 = \mu_{l,m} Q_{l,m}^{j+\frac{1}{2}}, \tag{2.110}$$

where $\mu_{l,m} = -l(l+1)\delta s^2$. The eigenvalues l are different for each eigenvalue m, and like m they are approximately integers for small l, converging to integers for larger and larger l as $\delta s \to 0$. In this limit the discrete eigenfunctions $Q_{l,m}^{j+\frac{1}{2}}$ converge to the associated Legendre polynomials.

Having determined the values of l, we calculate $H_l^{i+\frac{1}{2}}$ on the cell faces $\rho^{i+\frac{1}{2}}$, by numerical integration of equation (2.90), subject to the boundary conditions, which

numerically are

$$H^{\rho_{1/2}}\mathrm{e}^{\rho_{1/2}} - H^{\rho_{-1/2}}\mathrm{e}^{\rho_{-1/2}} = \delta s \mathrm{e}^{\rho_0} \tag{2.111}$$

$$H_l^{n_{\rho-1/2}} + H_l^{n_{\rho+1/2}} = 0. \tag{2.112}$$

The exact scheme used to solve this ordinary differential equation is not important, but a second-order stencil using central differences together with an analytical derivative of v_{out} appears to be adequate. The integration is carried out downward starting from the upper boundary where $H_l = 0$, then the whole function is scaled to satisfy the lower boundary condition.

For a given l, equation (2.105) then gives us a simple iterative scheme to determine G_l^i from $H_l^{i+\frac{1}{2}}$, using the initial value $G_l^0 = 1$. We observe that this scheme is a discrete approximation of the differential equation

$$\frac{\partial}{\partial\rho}(G_l e^{2\rho}) = \frac{1}{2}l(l+1)\frac{\partial}{\partial\rho}(e^{2\rho})H_l, \tag{2.113}$$

using central differences to approximate the derivatives. This equation in turn follows directly from taking the divergence of (2.74) for an individual mode.

The final step is to calculate the expansion coefficients $C_{l,m}$ in (2.98)-(2.100), by matching $B_\rho^{0,j,k}$ to an imposed distribution $B_r(s,\phi)$ on the lower boundary. The orthogonality of eigenvectors gives

$$C_{l,m} = \frac{\sum_{j,k} Q_{l,m}^{j+\frac{1}{2}} \Phi_m^{k+\frac{1}{2}} B_r^{j+\frac{1}{2},k+\frac{1}{2}}}{\sum_{j,k} \left(Q_{l,m}^{j+\frac{1}{2}} \Phi_m^{k+\frac{1}{2}}\right)^2}. \tag{2.114}$$

Care must be taken to ensure that the input data $B_r^{j+\frac{1}{2},k+\frac{1}{2}}$ are flux-balanced, so they are adjusted to have zero sum over the surface.

2.2 Comparison Between Potential and Outflow Fields

2.2.1 Comparison of Streamer Shapes and Magnetic Field Topology

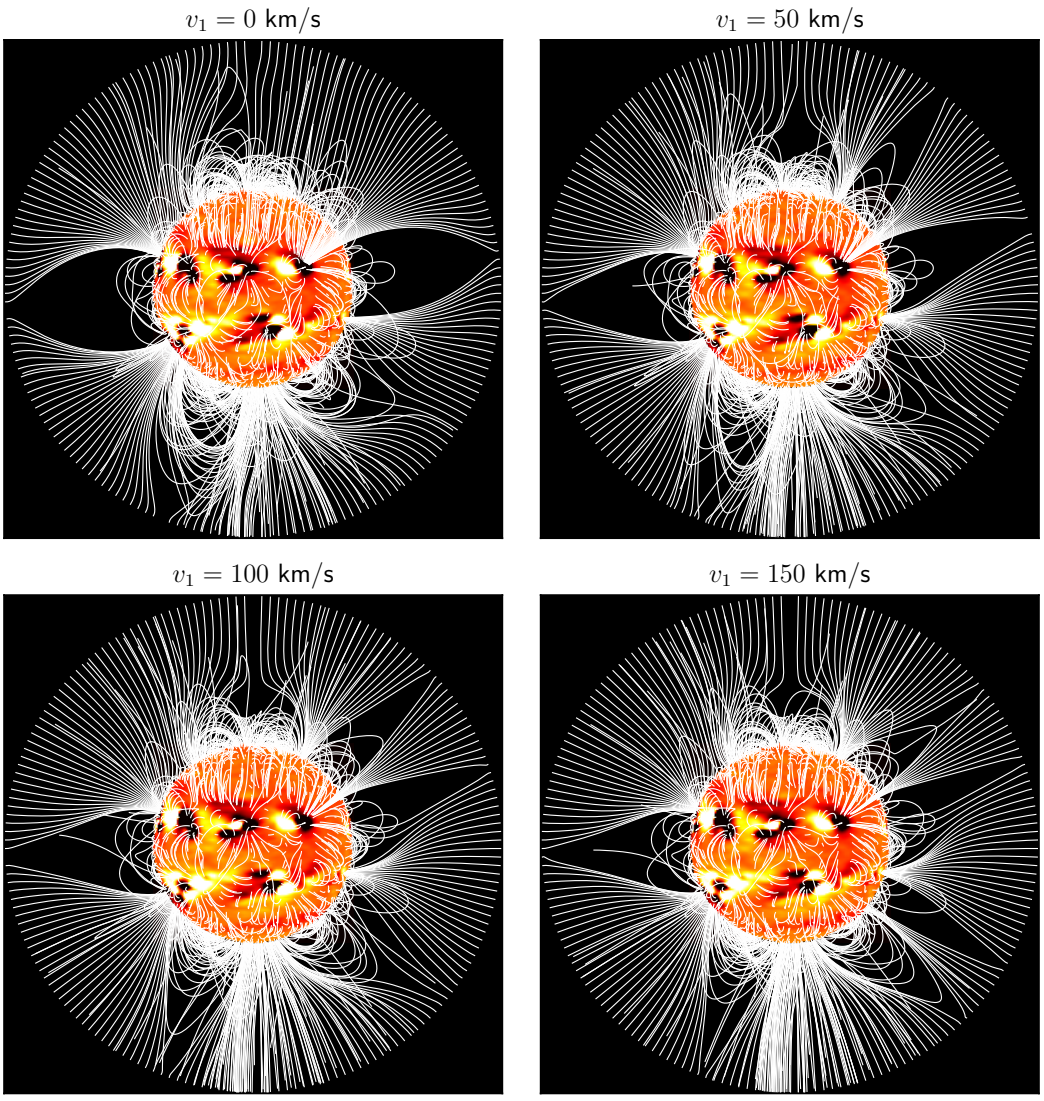

Figure 2.4: Comparison of the magnetic fields for varying outflow velocity v_1. The lower boundary data use an HMI synoptic map for Carrington Rotation 2130 so the topology of the corona can be compared to the solar eclipse of the 9th March 2016. We see a large difference between the potential field (top left) and the outflow fields, illustrated for solar wind speeds up to $150\,\mathrm{km\,s^{-1}}$.

In this section we discuss the differences between potential fields and the equiva-

Figure 2.5: A composite of 24 processed eclipse images taken from Tidore, Indonesia on 9th March 2016 (courtesy of C. Emmanoulidis and M. Druckmüller, `http://www.zam.fme.vutbr.cz/druck/eclipse/Ecl2016i/Tidore/0-info.htm`).

lent outflow fields calculated using the spherical coordinate method described earlier in this chapter. All of the examples in this paper use lower boundary data from the Solar Dynamics Observatory's Helioseismic and Magnetic Imager instrument ([102]). We use the radial component, pole-filled maps in the `hmi.synoptic_mr_polfil_720s` series ([103]).

Figure 2.2 illustrates the difference in streamer shapes between a potential field and three outflow fields with increasing wind speeds, on the same computational domain with $r_1 = 2.5R_\odot$. For all outflow computations henceforth, we fix the constant friction coefficient $\nu_0 = 1.75 \times 10^{16}\,\mathrm{cm}^2\,\mathrm{s}^{-1}$, following [14] (in that paper the friction coefficient ν_0 varies with altitude and latitude, so we take a rough average value for our constant equivalent).

For qualitative comparison, we compare the outflow fields shown in Figure 2.2 with Figure 2.5, which is an observed image of the solar corona taken during the eclipse of the 9th March 2016. We observe that close to the solar surface the potential and outflow fields are very similar, but at higher altitudes the solar wind causes quite significant topological changes. In a potential field, the streamers are petal shaped with a clear boundary layer near $r = r_1$, and all reach exactly to this source surface height. When the solar wind is imposed, it influences the height and shape of the

streamers, which begin to change shape at speeds of around $50\,\mathrm{km\,s^{-1}}$. At $150\,\mathrm{km\,s^{-1}}$ the field lines become radial at a significantly lower altitude than the potential field solution, and there is no boundary layer near $r = r_1$ where the field lines are sharply kinked. The presence of outflow means that closed field lines extend to different heights in different streamers, dependent on the local magnetic field strength. This agrees with coronal observations discussed in [104], namely that the coronal field does not become radial at a consistent height and that deviation from the radial direction depends heavily on latitude and the overall activity of the Sun. It is interesting to note in Figure 2.2 that the West limb streamers in the outflow fields match more closely than those in the potential field to the eclipse image. At the East limb, the agreement is poorer (for both potential and outflow fields), but direct comparison at this limb is difficult because of the use of a synoptic map for the lower boundary data; longitudes to the east of Central Meridian include 'future' observations taken after the time of the eclipse – this explains the differences in the overall topology of the coronal magnetic field here.

With outflow, the magnetic field is stretched outwards, leading to more open magnetic flux and correspondingly fewer closed field lines within each streamer. The additional open flux is evident in Figure 2.6, which compares the radial magnetic field for potential and outflow fields with the same top boundary height, $r_1 = 2.5R_\odot$. The pattern of positive/negative field polarity at $r = r_1$ is broadly similar in each case and depends only on the magnetic field distribution low in the corona. But, in general, the magnetic field strength high in the corona is larger in the outflow field than in the potential field with the same lower boundary data. Since more of the magnetic flux is open, the closed-field arcades in the outflow field are smaller than if the solar wind is disregarded – this is clearly seen in Figure 2.7, where we compare the effect of imposed outflow at two stages of the solar cycle, corresponding roughly to solar minimum and maximum. The large closed field regions evident in the potential fields are much smaller in the corresponding outflow solutions, while the magnetic field structure close to the solar surface is little affected.

A significant difference between the potential and outflow fields is the effect of varying the upper boundary height, r_1. For the potential field, increasing r_1 will

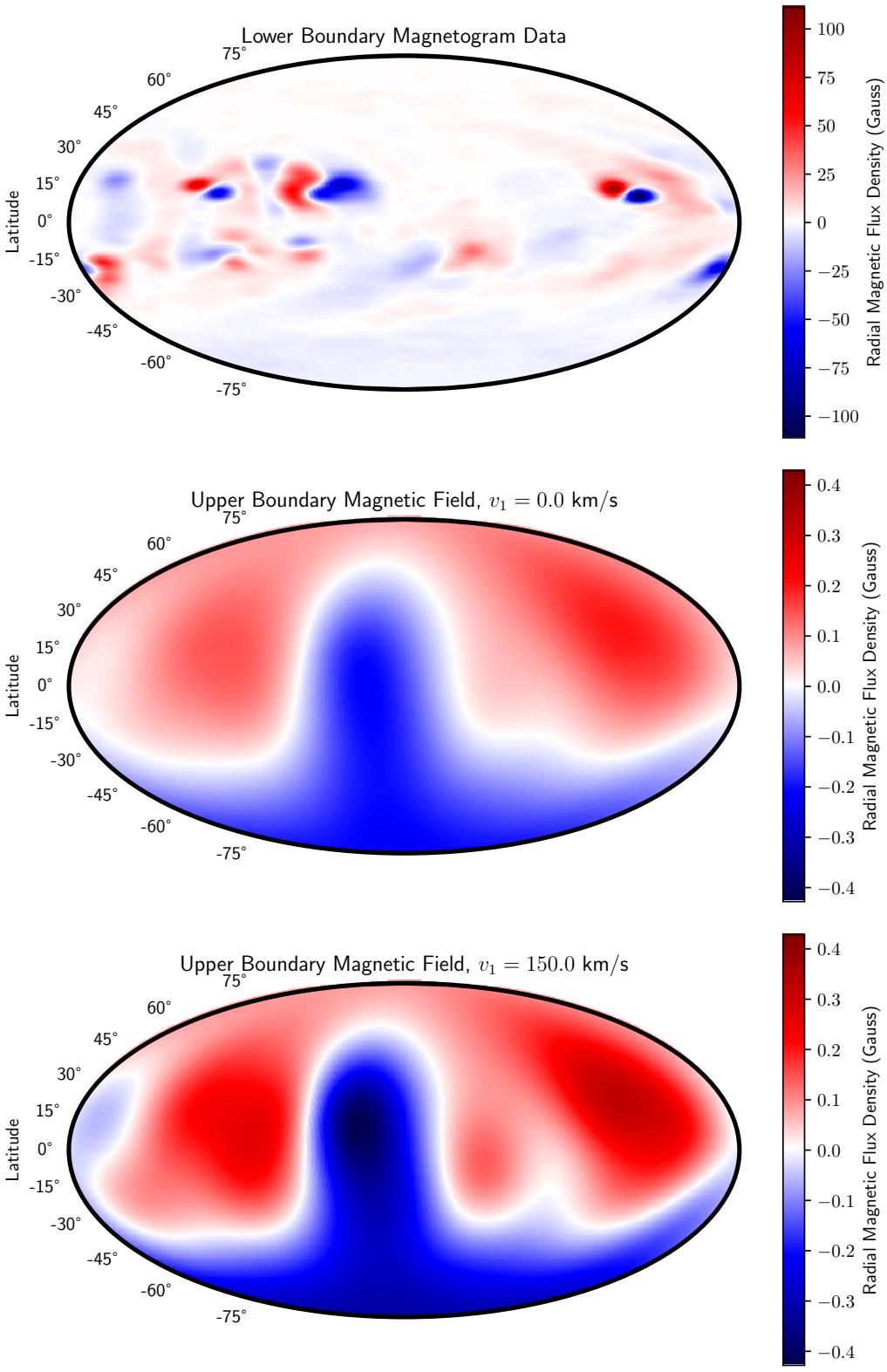

Figure 2.6: The radial magnetic field at the lower and upper boundaries of the domain, using magnetogram data taken from Carrington Rotation 2165.

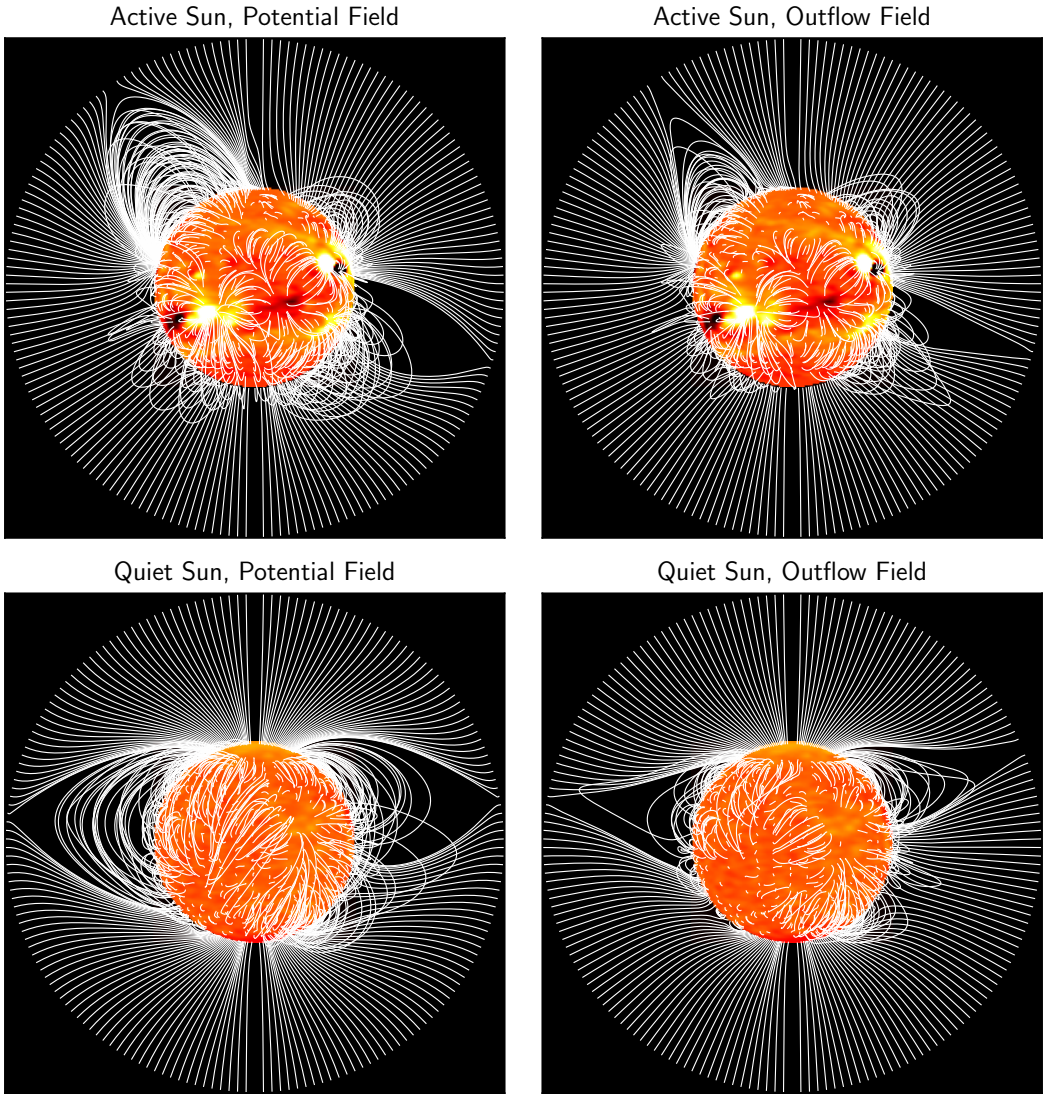

Figure 2.7: Qualitative comparison of potential and outflow fields with $v_1 = 150\text{km}\,\text{s}^{-1}$. The upper figures show the magnetic field extrapolated from data from Carrington Rotation 2165, when the Sun was relatively active. The lower figures represent a quieter Sun, during Carrington Rotation 2222.

increase the height of the closed field streamers. But in the outflow fields, this height is determined by the outflow velocity rather than the imposed condition of a purely radial magnetic field on $r = r_1$, at least providing that r_1 is sufficiently large. With the solar wind model that we have chosen (see Section 1.3.2), most streamers extend to less than $2.5R_\odot$, but some extend further.

To illustrate the behaviour of the outflow fields near to the upper boundary, Figure 2.8 shows the open magnetic flux in the outflow field as a function of altitude, for

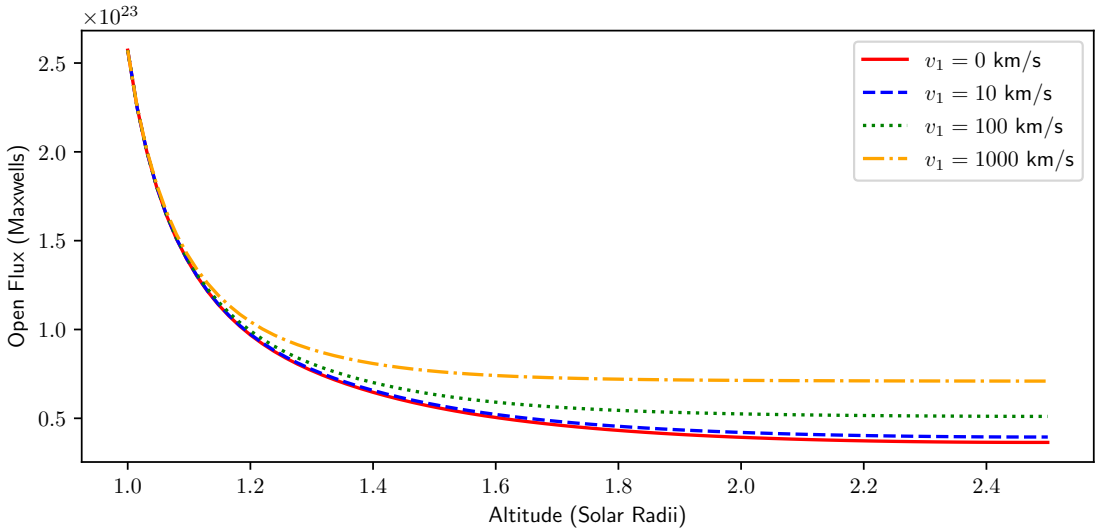

Figure 2.8: Unsigned open flux as a function of radius for different outflow speeds, for Carrington Rotation 2165.

solar wind speeds up to $1000\,\mathrm{km\,s^{-1}}$ (which is unrealistically fast for these altitudes and is plotted only to illustrate the general effect). The open magnetic flux decreases rapidly as we move away from the solar surface, as some of the magnetic field lines curve back towards the sun. The outflow fields exhibit higher flux at larger radii as more of the magnetic field is stretched out by the solar wind and fewer of the field lines turn around.

We observe that for fast wind speeds, the open flux is approximately constant above a radius of $2R_\odot$. This is consistent with the observation that the field is roughly radial above this altitude and there are very few closed field lines. It also indicates that the solution is not sensitive to the chosen location of the outer boundary.

Finally, we note that the magnetic field at $r = r_1$ is clearly dominated by low-order modes in the azimuthal and latitudinal directions. Thus – as for the potential field – it is possible to obtain a close approximation to the true magnetic field at high altitudes while only needing to calculate a relatively small number of modes. This is illustrated in Figure 2.9. The total number of modes (indexed by l and m) at this resolution (180 x 360) is 64800, but we see that the flux measurement converges at all heights within 4000 modes. Away from the surface, this convergence is even faster – within 1000 modes. Thus if the region of interest is sufficiently high

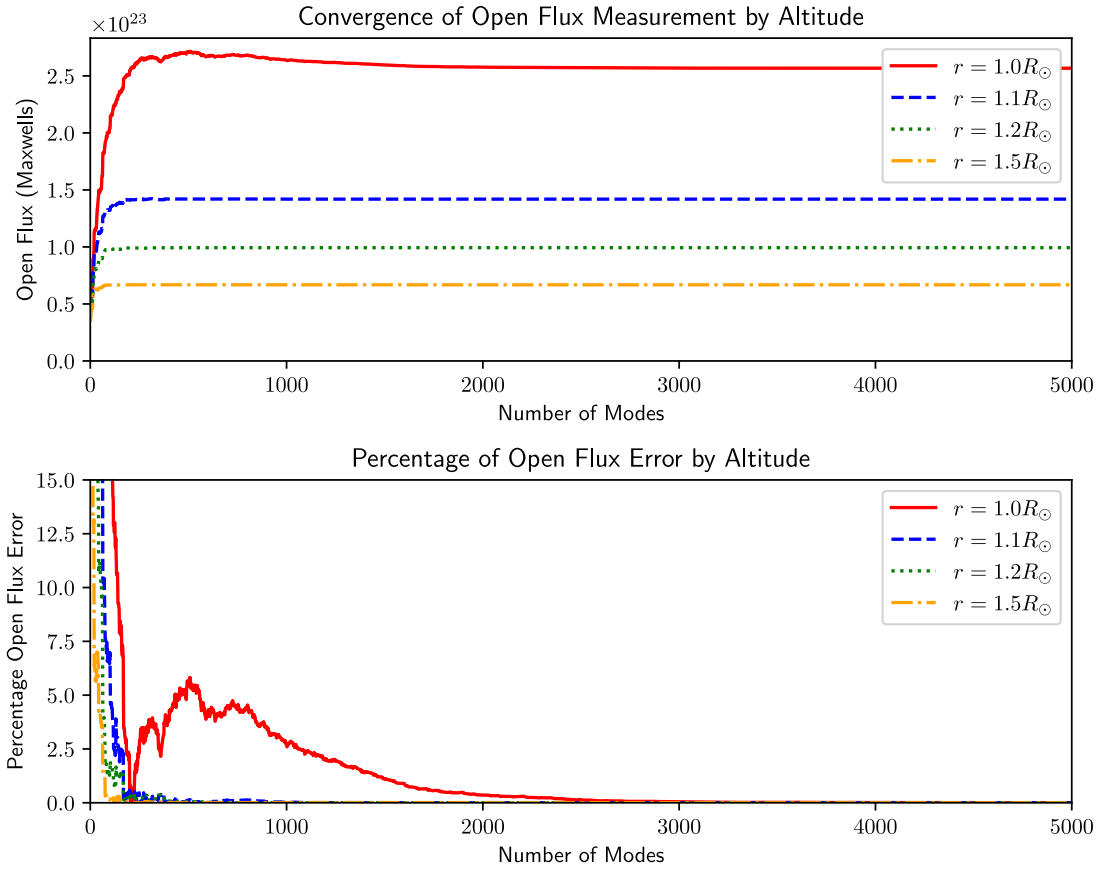

Figure 2.9: Convergence of the unsigned open flux at different heights, for Carrington Rotation 2165. The top panel shows the computed open flux as more modes are included. The lower-order modes (small l and m) are calculated first as in general these contribute more than higher-order modes. The bottom panel shows the corresponding percentage error in the open flux as the number of calculated modes increases. To match the lower boundary to machine precision, a total of 64,800 modes would be required.

in the corona, we need only calculate several hundred modes in order to model the magnetic field sufficiently accurately, rather than thousands. For purposes such as space weather predictions, where the precise magnetic field in the lower corona is unimportant, this saving of computational cost could be useful.

Computation of all modes is not particularly fast in python, but this can be improved upon considerably by using Fortran 90. In that case the outflow fields can be calculated completely (using all modes) in less than a minute on a desktop computer.

2.2.2 The Effect of Outflow Velocity on the Open Flux

We now compare the open flux measurements predicted by our outflow model to measurements of the magnetic field at 1 AU extracted from NASA/GSFC's OMNI data set through OMNIWeb. We assume that the total amount of radial magnetic flux at 1 AU is the same as the upper corona and scale the magnetic field strength correspondingly, based on the area of a sphere at each given altitude. The data are averaged as in [105] – namely, an initial daily average of the signed data to smooth out local small-scale fluctuations, then a 27-day running average of the unsigned data for comparison to the global open flux ([106]). A similar comparison of PFSS extrapolations with these data (up to 2015) is undertaken by [107], where we note that the definition of open flux in their paper is half the quantity used here.

Figure 2.10 plots the OMNI data against the flux predicted by our model for various solar wind speeds, including the potential field case ($v_1 = 0\,\mathrm{km/s}$). We observe that throughout Solar Cycle 24 the flux predicted by our potential field model with $r_1 = 2.5R_\odot$ is consistently an underestimate, as noted in the introduction. The potential field usually underestimates the measured open flux by a factor of more than two, but there is still a strong correlation between the potential field flux and the observations, notably at the large increase around Carrington Rotation 2160. In the study [107], it is shown that the PFSS open flux can be made to match the observational curve by lowering the source surface height to $r_1 \approx 2R_\odot$, although the morphology of the streamers is likely then even more unrealistic. Those authors also show that a reasonable match to the observed open flux may be obtained with a 'horizontal-current current-sheet source-surface' (HCCSSS) model. As in our outflow model, the HCCSSS open flux is inflated by the presence of horizontal currents, although unlike in the outflow model the currents flow in the lower part of the domain, and take an arbitrary form that is not directly motivated by observations.

Figure 2.10 shows that the open flux predicted by our outflow fields also correlates strongly with the OMNI measurements. As discussed in Section 2.2, the outflow fields have a greater open flux and as such they predict values that more closely match the collected data. With a reasonable outflow of $v_1 = 150\,\mathrm{km\,s^{-1}}$, about $30-40\%$ of the discrepancy in open flux is accounted for. Although either increasing

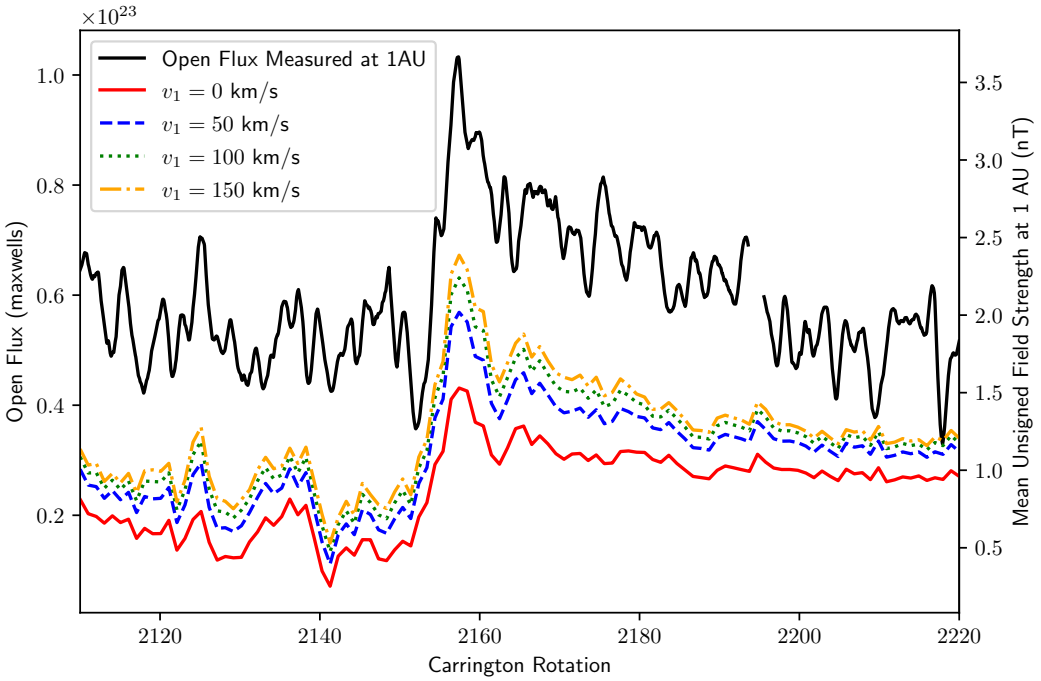

Figure 2.10: Variation of the open magnetic flux at $r_1 = 2.5R_\odot$ during Solar Cycle 24. The black curve represents OMNI measurements of the magnetic field at 1 AU (smoothed as described in the text), while the dashed, dotted, and dot-dashed curves show predictions from outflow solutions with different speeds. The lowest curve (red) shows the result from an equivalent potential field calculated using our model with $v_1 = 0\,\mathrm{km\,s^{-1}}$. In all cases, the unsigned open flux is shown on the left axis, while the equivalent field strength at 1 AU (assuming a uniform distribution) is shown on the right axis.

the imposed velocity or decreasing the magnetofrictional relaxation rate ν_0 could further reduce this discrepancy, this would likely lead to unrealistic streamer shapes and nonphysical behaviour, and would not be consistent with full magnetofrictional simulations.

It is more likely that the remainder must be explained through alternative means. These likely include both steady enhancement from additional low-coronal currents not included here, as well as episodic enhancement from eruptions and coronal mass ejections ([105, 108]). An important further possibility is that the 1 AU data may be overestimating the open flux at $2.5R_\odot$ due to the presence of switchbacks: where some magnetic field lines double back on themselves in the heliosphere ([56]).

2.3 Discussion

In this chapter we have described a new method for modelling the global magnetic field in the solar corona. The numerical method is based roughly on existing PFSS models, and in a similar manner requires radial magnetogram data as a lower boundary condition, or indeed a specified analytical field as for the 2.5D simulations described in Chapter 3.

The model seeks to improve upon PFSS models by taking into account the effect of the solar wind, which is achieved by seeking equilibrium solutions of the magneto-frictional model, where a radial solar wind outflow function is assumed and specified. Computation times are comparable to PFSS codes, with the only fundamental difference here being that we are unable to use a Fast Fourier Transform to calculate the eigenmode coefficients.

The solutions we find appear more realistic than equivalent potential fields, exhibiting more realistic streamer shapes, reducing the dependence on an arbitrary source-surface height, and increasing the predicted open flux to be closer to OMNI magnetic field measurements throughout Solar Cycle 24.

Compared to full MHD simulations, our model has the limitation that the solar wind velocity is imposed in a purely phenomenological manner, rather than determined self-consistently as an equilibrium of the full MHD equations. In particular, our method has to rely on several assumptions – namely that the solar wind velocity is purely radial and only has radial dependence. This is certainly preferable to assuming there is no outflow velocity whatsoever but is still quite a severe limitation. In future, it may be possible to remove these limitations by generalising our method.

Being purely magnetic, however, our method is computationally much less expensive and only requires line-of-sight magnetogram data, as opposed to full vector data and initial conditions for density and pressure/temperature. It thus represents a practical alternative that improves on the commonly-used PFSS model at little extra cost.

For a chosen radial wind speed profile, our solution has a single free parameter: the assumed relaxation rate ν_0. The value for this constant has been determined from experience using the magneto-frictional model but it cannot be calculated directly.

Therefore there remains some uncertainly with regards to the most appropriate outflow solution for a given solar wind speed. In future it may be possible to determine ν_0 empirically using the model we have proposed, by comparing streamer shapes to physical observations. In turn, this would then be informative for other magneto-frictional modelling.

In this chapter we have discussed the calculation of a magnetic field based upon a Cartesian coordinate system, and a stretched spherical coordinate system. The method could be generalised to work in other schemes as desired (most obviously a non-stretched spherical system), providing there is a grid on the lower boundary that permits an eigenvalue decomposition such as the ones we have described.

PFSS fields have been established as a very useful way to model the corona. The ubiquitous use of these fields indicates that computational simplicity is a priority, and the methods we present aim to preserve this simplicity. At high altitudes, to ensure radial magnetic field lines and a more even distribution of the radial magnetic field strength, potential field models are often coupled with current-sheet extension models to approximate the upper corona (e.g. [38]). Using outflow fields should reduce the need for such extensions, provided accurate functions describing the solar wind velocity at high altitudes are used. This would also remove any dependence on the somewhat arbitrary source-surface height.

CHAPTER 3

Eruptivity Criteria for Magnetic Flux Ropes

In this chapter we discuss the work in our papers [7] and [8]. Using two simplified MF models and one full MHD model (see the introduction for a description and the history of the use of these models) we have undertaken a very large parameter study of magnetic flux rope behaviour. The goal is to seek scalar proxies for eruptivity: quantities that could be theoretically calculated from a static extrapolation of the coronal magnetic field and used to predict an imminent flux rope eruption.

Initially this study focused on a 2.5D magnetofrictional model in Cartesian coordinates. The original purpose of this was to gain some familiarity with the method and the construction of the code. Ultimately, the large parameter space available meant that the results from this were more notable than originally anticipated, and were written up in [7]. This paper introduced a new definition for the relative helicity in 2.5D, and introduced the statistical methods used to evaluate which diagnostic quantities could be good predictors.

The second paper ([8]) expanded on this study considerably, by introducing two new models: a new magnetofrictional model in axisymmetric polar coordinates and a full MHD model using the existing LARE2D code ([21]). The polar coordinate code provided justification that the qualitative behaviour of the flux ropes was similar

enough in either coordinate system that Cartesian models could be used to deduce meaningful results. Repeating the study in full MHD was more significant, as this model is a better approximation to reality than magnetofriction. By keeping the domain size and initial conditions identical to the MF study, direct comparisons of the diagnostic quantities could be made. Ultimately, this has led to our conclusion that magnetofriction could indeed be used to evaluate predictive quantities. As full MHD models of the entire corona are far too costly, this is an important step towards being able to use real observational data to make predictions of coronal magnetic field behaviour.

Despite using existing code for the MHD simulations, a considerable amount of time was spent determining appropriate numerical boundary conditions in order to properly emulate those in the existing magnetofriction codes (both my own 2.5D Cartesian model and existing codes – see Section 1.4.1). These modifications to the boundary conditions permitted steady-state solutions of the solar wind outflow, and the implementation of supergranular diffusion in the solar photosphere, allowing for flux cancellation and the formation of flux ropes. It is my hope that this approach can be extended to full 3D to verify further the results from our work.

The models described in this chapter are all invariant in one coordinate direction. Magnetic fluxes and currents in the invariant direction are permitted, however, and as such these models can be described as 2.5-dimensional (2.5D). This simplification clearly provides a significant saving in computing time, with a typical simulation run taking only minutes on a desktop computer compared to days or months for a full 3D equivalent.

The main disadvantage of this approach is that realistic flux rope geometries can not be properly represented. The flux ropes are either infinitely long in the invariant coordinate direction, or wrap completely around the sun in the case of the polar model. It remains to be seen whether this is a fundamental problem with our research thus far.

To our knowledge, a parameter study of flux rope behaviour on this scale has not yet been undertaken, but our approach is similar to that of [93]. In that work, a series of 7 full 3D MHD flux ropes ([24], [25]) was studied. In some of those simulations

the flux ropes were unstable and erupted, and in others the ropes appeared to be stable for all time. Several diagnostic quantities were identified which appear to correlate to an eruption at a later time, notably the so-called 'eruptivity index' (see Section 1.6.3), to be discussed further in this chapter.

In our models, usually at least one flux rope eruption is observed in each simulation run, providing there is sufficient photopsheric diffusion. Thus rather than merely making a prediction as to whether the rope will erupt at any later time we seek to find scalar quantities that exhibit a threshold above which the rope becomes unstable and erupts. The advantage of this is that if the state of the magnetic field is known, a probability of an eruption within a certain time can be calculated without the costly need to run a time-dependent simulation.

3.1 The Magnetofrictional Models

In the parameter study we use two magnetofrictional (MF) models, one in Cartesian coordinates and another in axisymmetric polar coordinates. The Cartesian model represents a section of the solar corona of around 35°of latitude, with a vertical domain height half of the width. The polar model represents a longitudinal slice of the entire corona, extending to 2.5 solar radii.

Both models use the magnetofrictional equations discussed in Section 1.4.1. These are:

$$\frac{\partial \mathbf{B}}{\partial t} = -\nabla \times \mathbf{E} \tag{3.1}$$

$$\mathbf{E} = \eta \mathbf{j} - \mathbf{v} \times \mathbf{B} \tag{3.2}$$

$$\mu_0 \mathbf{j} = \nabla \times \mathbf{B} \tag{3.3}$$

$$\mathbf{v} = \nu_0 \frac{\mathbf{j} \times \mathbf{B}}{B^2 + B_0^2 \delta e^{-\frac{B^2}{\delta B_0^2}}} + v_{\mathrm{out}}(y)\mathbf{e}_y, \tag{3.4}$$

where $\mathbf{B}, \mathbf{E}, \mathbf{j}$ and $\mathbf{v}$ are the (variable) magnetic, electric, current density and velocity fields respectively. The constant η is the coronal diffusivity, equal to $\eta = 1/(\mu_0 \sigma_0)$, where μ_0 is the permittivity of free space and σ_0 is the electrical conductivity of the plasma. μ_0 is henceforth set to unity without loss of generality. This diffusion term

represents an effect that is much slower than the dynamics on the timescales of interest, and as such is set to be small. If this term were not included, numerical diffusion would occur with much the same effect, but would depend on the grid resolution. By imposing it directly we remove this dependence. The magnetofrictional relaxation rate ν_0 determines the time taken for the system to relax to a force-free state. The ideal value of this constant can not easily be determined, as the magnetofrictional velocity is itself fictitious. Thus ν_0 is varied considerably in the parameter study to ensure any eruptivity criteria are independent of its value. The constant $\delta = 0.01$ is used in the denominator of the relaxation term to ensure stability at magnetic null points (there is some discussion on the ideal value for δ in Chapter 4) with an additional constant factor B_0 roughly equal to the average magnetic field strength. The v_{out} term models the effect of the solar wind ([13]), resulting in an additional upward velocity.

In Cartesian coordinates this outflow speed is taken to be

$$v_{\text{out}}(y) = v_1 y^{10} \mathbf{e}_y, \tag{3.5}$$

in line with previous magnetofrictional simulations, and in polar coordinates we use a more realistic approximation to the Parker solar wind solution, as discussed in Section 1.3.2.

$$v_{\text{out}}(r) = v_1 \frac{r_1^2 e^{-2r_c/r}}{r^2 e^{-2r_c/r_1}} \mathbf{e}_r, \tag{3.6}$$

where the critical radius r_c is 10 solar radii, $r_1 = 2.5$ solar radii is the upper extent of the domain and v_1 is a constant wind speed factor, chosen to be 50 times the maximum shearing velocity. A realistic value is likely higher than this, but this compromise is made as the resultant high velocities at the top of the domain increase computational times significantly. The only significant effect of increasing the outflow velocity further is a slight increase in the frequency of arcade eruptions.

In the Cartesian model the domain is a square box with coordinates $-1 < x < 1$, $0 < y < 1$ and z the invariant direction, with equally-spaced grid cells. Given the width of the domain, this is intended to model up to an equivalent of around 2.5 solar radii, although the differing geometries make this comparison imprecise. The polar

simulations model an entire hemisphere of the corona, with coordinates $0 < \theta < \pi$ and $1 < r < 2.5$, and ϕ the invariant longitudinal direction. The grid cells here are evenly spaced in $s = \cos\theta$ and $\rho = \log r$ ([39]), which increases the resolution in the areas of interest.

In our magnetofrictional code we ensure the solenoidal condition ($\nabla \cdot \mathbf{B} = 0$) to machine precision by describing the system in terms of a vector potential $\mathbf{A}$, such that

$$\mathbf{B} = \nabla \times \mathbf{A}. \tag{3.7}$$

As the magnetofrictional velocity field is calculated explicitly from the magnetic field, by extension the entire state of the system can be described using only this vector potential.

Numerically, in our magnetofrictional models the differential operators are calculated using Gauss' or Stokes' theorem as appropriate, and the variable fields are stored on a staggered grid ([46]). In Cartesian coordinates this is equivalent to using a central-difference scheme. The numerical schemes used here were discussed briefly in Section 1.4.1. The Cartesian simulations are initialised with Python and run using Fortran 90, with a grid resolution of 256 x 128 cells. The axisymmetric polar simulations are run using Python with a grid resolution of 180 x 60 cells.

We adopt dimensionless units throughout. In the axisymmetric polar model one distance unit is taken to be 1 solar radius. In the Cartesian models one distance unit is around the width of the magnetic arcade, which varies considerably but is assumed to be around 35° on the solar surface (or 0.44 solar radii), based on arcades observed in the axisymmetric simulations. Using the photospheric shearing rates (discussed in Section 3.1.2) the time units can then be set as 27.4 days in the Cartesian simulations and 19.5 days in the axisymmetric simulations. However, the significant differences in the two coordinate systems mean this should only be regarded as the correct order of magnitude and as such the timescales discussed later in this chapter should only be treated as indicative.

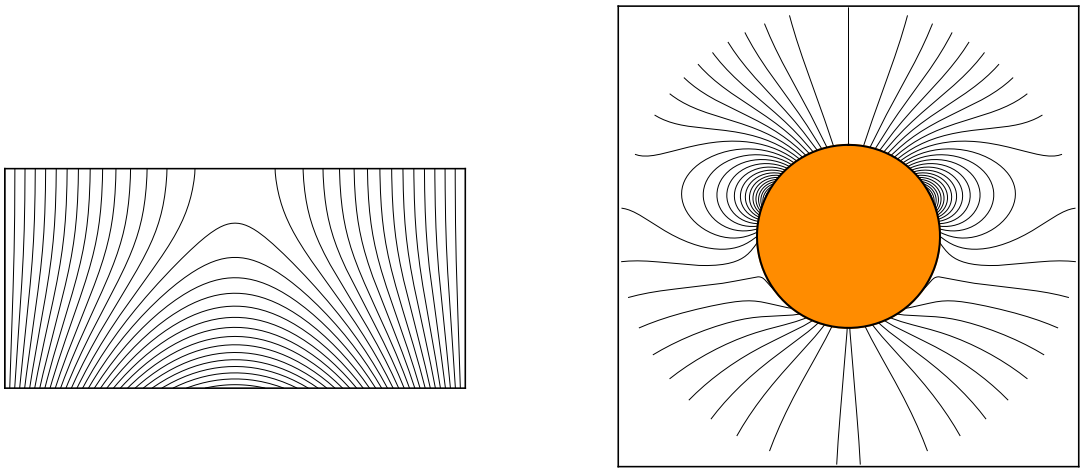

Figure 3.1: Initial magnetic fields for the Cartesian simulations (left) and the axisymmetric simulations (right), with magnetic field lines in black. These are PFSS fields with the lower radial boundary conditions as in Equations (3.8) and (3.9). In the axisymmetric simulations, the computational domain only covers one longitudinal plane. Another plane on the opposite side is plotted here only for illustrative purposes.

3.1.1 Initial Conditions

The initial magnetic fields are plotted in Figure 3.1. In both Cartesian and polar coordinates, the simulations are initialised with a PFSS (Potential Field Source-Surface) field, in which the magnetic field is radial at the upper boundary and there is no electric current throughout the domain. PFSS is chosen for consistency with the MHD simulations, which necessarily model the initial relaxation due to the solar wind. For a standalone magnetofrictional study, it would be preferable to use an 'outflow field', the merits of which are discussed in Chapter 2.

In polar coordinates, we choose the radial magnetic field strength on the lower boundary to fit the following analytic function:

$$B_r(1,\theta) = s^7 + 5de^{-10d^2}, \tag{3.8}$$

where $s = \cos(\theta)$ and $d = s - \cos(0.35\pi)$. The first term (s^7) approximates the magnetic field at solar minimum reasonably well (e.g. [109, 110]), and the second term ensures there is a clear polarity inversion line at a latitude where the differential

rotation of the surface will result in a considerable shearing rate. In the axisymmetric simulations we observe the arcade (the region with the closed field lines) between around 20 and 70 degrees from the north pole. A symmetric field around the equator would not be suitable as the differential rotation is symmetric between the northern and southern hemispheres, and such an arcade would merely be dragged around the equator without being sheared. The potential fields for the axisymmetric simulations are calculated using a bespoke potential field solver.

The Cartesian simulations are initialised with the lower boundary condition

$$B_y(x,0) = -B_0 \sin\left(\frac{\pi}{2}x\right), \tag{3.9}$$

for some constant B_0 of order unity. In this simple case the initial condition of the vector potential can be specified analytically:

$$A_z(x,y) = \frac{2}{\pi \cosh\left(\frac{\pi}{2}\right)} B_0 \cos\left(\frac{\pi}{2}x\right) \cosh\left(\frac{\pi}{2}(y-1)\right). \tag{3.10}$$

The resulting magnetic fields are then

$$B_x(x,y) = \frac{B_0}{\pi \cosh\left(\frac{\pi}{2}\right)} \cos\left(\frac{\pi}{2}x\right) \sinh\left(\frac{\pi}{2}(y-1)\right), \tag{3.11}$$

$$B_y(x,y) = -\frac{B_0}{\pi \cosh\left(\frac{\pi}{2}\right)} \sin\left(\frac{\pi}{2}x\right) \cosh\left(\frac{\pi}{2}(y-1)\right), \tag{3.12}$$

$$B_z(x,y) = 0. \tag{3.13}$$

satisfying the lower boundary condition and $B_x = 0$ on the upper and side boundaries.

The initial magnetic field completely specifies the magnetofrictional system.

3.1.2 Boundary Conditions

On the magnetic field, we impose that there is zero perpendicular current on the upper and lower boundaries of the domain. This ensures that under magnetofrictional relaxation (in the absence of additional boundary conditions) there is no magnetic energy flux through the boundaries. We also require that the field is entirely verti-

cal/radial at the side boundaries (or the poles in the axisymmetric simulations). The dynamic behaviour of the MF system is almost entirely determined by the driven boundary conditions on the lower boundary.

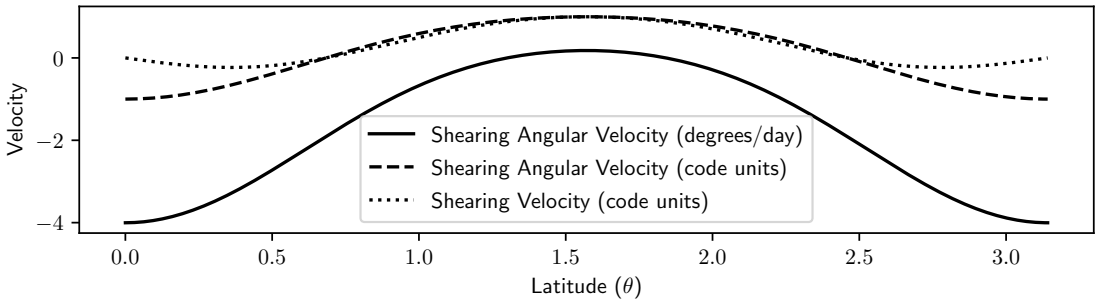

Figure 3.2: Photospheric shearing rates varying with latitude (measured from the north pole). The angular velocity (solid line) is then shifted into the correct reference frame and to code units (dashed line). It is then multiplied by $\sin\theta$ to give a linear velocity on the solar surface (dotted line) before being added to the velocity field.

These boundary conditions represent photospheric shearing and supergranular diffusion. In the magnetofrictional simulations the shearing velocity is added directly to the fictitious velocity field $\mathbf{v}$ on the lower boundary. In the axisymmetric simulations we use a realistic profile for the differential rotation rate. As a function of latitude, this is approximately [9]

$$V(\theta) = 0.18 - 2.396\cos^2\theta - 1.787\cos^4(\theta) \text{ degrees/day}. \tag{3.14}$$

It is common to use the Carrington frame as a reference rotation frame – rotating at 13.2 degrees/day [33]. Analytically, altering the reference frame by a constant linear velocity should not make any difference to the dynamics, providing the boundary conditions are treated with care. However, the centrifugal and Coriolis forces in a rotating frame do in general have an effect. These forces are proportional to the density of the fluid, which in the corona is small compared to the forces on the magnetic field. In both the magnetofrictional and MHD models we neglect these effects, and indeed it is unclear how they would be properly implemented in a magnetofrictional model in the absence of a true fluid.

In the polar model we have chosen the reference frame such that the maximum

angular velocity in either direction is unity, as illustrated in Figure 3.2. This is for consistency with the Cartesian simulations where the imposed shearing velocity is simply

$$V_{\text{shear}}(x) = V_0 \sin(\pi x). \tag{3.15}$$

The constant V_0 is chosen to be unity. This choice determines the time units used in the code, but otherwise makes no difference to the dynamics.

We also impose an additional magnetic diffusion term on the lower boundary, modelling the effect of unresolved supergranular flows on the photosphere. This diffusion rate (η_0) is in general much larger than the diffusion rate in the corona (η), and one of its effects is to bring the footpoints of the magnetic arcade closer together, eventually forming a twisted magnetic flux rope ([19]).

This diffusion is added as a boundary condition to the electric field $\mathbf{E}$:

$$\mathbf{E}(x,0) = \eta_0 \frac{\partial B_y(x,0)}{\partial x} \mathbf{e}_z, \tag{3.16}$$

or

$$\mathbf{E}(1,\theta) = \eta_0 \frac{1}{r} \frac{\partial B_r(1,\theta)}{\partial \theta} \mathbf{e}_\phi, \tag{3.17}$$

in Cartesian and polar coordinates, respectively. As the change in the magnetic field is proportional to the curl of the electric field, in the absence of any other effects this boundary condition is in essence equivalent to the 2D heat equation acting on the radial/vertical component of the magnetic field.

3.2 The Magnetohydrodynamic Model

The third of the models we use is a full MHD model, using the LARE2D code [21]. The domain size and configuration are set to be the same as the Cartesian magnetofrictional model, so as to allow direct comparisions of the system behaviour. Unlike in magnetofriction, in MHD the fluid flow is accurately modelled, and as such we couple Faraday's law, Ohm's law and Ampère's law to the fluid equations.

In dimensionless form, the MHD equations used in the LARE2D code are as

follows:

$$\frac{\partial \mathbf{B}}{\partial t} = -\nabla \times \mathbf{E} \tag{3.18}$$

$$\mathbf{E} = \eta \mathbf{j} - \mathbf{v} \times \mathbf{B} \tag{3.19}$$

$$\mu_0 \mathbf{j} = \nabla \times \mathbf{B} \tag{3.20}$$

$$\frac{\partial \rho}{\partial t} = -\nabla \cdot (\rho \mathbf{v}) \tag{3.21}$$

$$\frac{\mathrm{D}\mathbf{v}}{\mathrm{D}t} = \frac{1}{\rho}\mathbf{j} \times \mathbf{B} - \frac{1}{\rho}\nabla P + \mathbf{g} \tag{3.22}$$

$$\frac{\mathrm{D}\epsilon}{\mathrm{D}t} = -\frac{P}{\rho}\nabla \cdot \mathbf{v} + \frac{\eta}{\rho} j^2 \tag{3.23}$$

$$\epsilon = \frac{P}{\rho(\gamma - 1)}, \tag{3.24}$$

where the variable quantities (in addition to those introduced in the magnetofrictional equations) are the plasma pressure P, the plasma density ρ and the internal energy density ϵ. The ratio of specific heats is taken to be $\gamma = 5/3$. We choose the gravitational field to be $\mathbf{g} = -\mathbf{e}_y/(y+1)^2$. As with magnetofriction, the constant η represents the coronal magnetic diffusivity. For consistency between the three model setups we set this as $\eta = 5 \times 10^{-4}$ throughout. There is considerable variation in the literature as to this value (e.g. [33, 111]), so we choose it to be as small as possible whilst still being able to resolve current sheets at our chosen grid resolution. No explicit viscosity is used.

The LARE2D code does not employ a vector potential but instead ensures the solenoidal condition using the constrained transport method of [112], which is quite complex for the velocity field but for the magnetic field is roughly equivalent to the approach we take in the MF models, albeit with a more sophisticated scheme for averaging to the grid points/faces. Unlike in the MF models, we do not need to impose an outflow velocity. Instead, due to the boundary conditions chosen and the presence of the gravitational field, the plasma velocity in the MHD model naturally reaches a dynamic equilibrium with an upwards velocity. This can be seen clearly when the system is allowed to relax in the absence of a magnetic field. The relaxation to such an equilibrium is shown in Figure 3.3, where the profile of the plasma density and vertical velocity are shown.

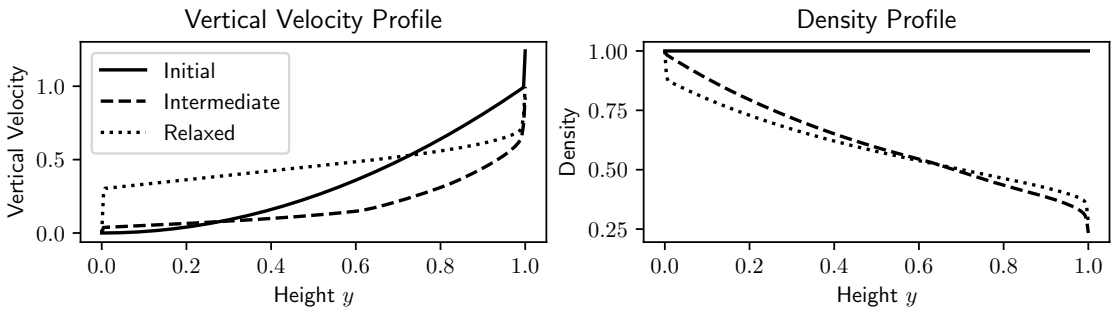

Figure 3.3: Illustration of the relaxation of the fluid in the absence of a magnetic field, showing the vertical fluid velocity and the density, both the initial condition and the fluid state after relaxation. We observe the initial quadratic profile of the velocity and the constant initial density, and the sharp jump in the velocity at the top of the domain due to the boundary condition.

3.2.1 Initial Conditions

The initial magnetic field configuration for the MHD simulations is identical to that in the Cartesian magnetofrictional simulations. This consistency is important for the validity of the comparisons between the two models.

In MHD we additionally require initial conditions for the fluid. The initial density is chosen to be constant throughout the domain, as is the initial internal energy. The initial fluid velocity is required to be positive in the y direction in order to accurately emulate the solar wind – otherwise it is possible for the fluid to be in equilibrium with a negative vertical velocity. The initial velocity profile chosen is $V_{\text{out}}(y) = v_1 y^2$ for some constant v_1, as shown in Figure 3.3 – although it must be noted that the boundary conditions initially cause discontinuities at the upper and lower boundaries (to be discussed in the next Section).

This initial state is far from a steady-state equilibrium, but it does relax to one very quickly relative to the timescale of the magnetic field evolution. The initial conditions and boundary conditions on the velocity (discussed in Section 3.2.2) enable the solar wind to be represented self-consistently, as the equilibrium state of the system will naturally have a non-zero vertical fluid velocity, as in Figure 3.3. The presence of a magnetic field does affect this relaxation – the effect of the solar wind on the magnetic field is shown in Figure 3.4 which illustrates the initial condition for the MHD simulations (top row) along with the equilibrium state the system reaches

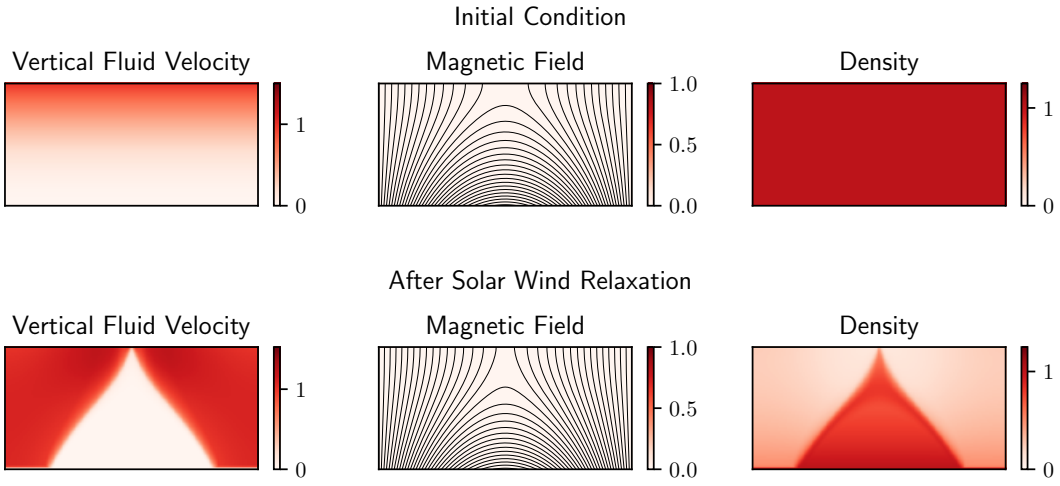

Figure 3.4: Illustration of the initial condition and relaxed 'outflow field' state of the MHD simulations. Such an outflow field is obtained in the absence of driven boundary conditions or supergranular diffusion, where the system evolves due to the effect of the solar wind alone. The colourmaps show the vertical velocity, out-of-plane magnetic field (zero, in this case) and the fluid density.

in the absence of driven boundary conditions or supergranular diffusion (bottom row).

As with magnetofriction, as the system relaxes to this 'outflow field' state the magnetic field lines at the top of the domain become more radial, with fewer of them connecting back to the surface. Outside the arcade, the vertical fluid velocity is significant and roughly constant. Inside the arcade the plasma is essentially constrained to the magnetic field lines and as such the fluid velocity is comparatively small. During this relaxation period the fluid density within the arcade remains roughly constant, whereas in the region affected by the solar wind the density falls to around a quarter of its initial value, becoming slightly less dense with increasing height. As the system relaxes to this state soon after the simulations are initialised, this relaxed state can be essentially regarded as the initial condition. A similar process occurs to the magnetic field in the magnetofrictional simulations, although this is due to an imposed solar wind velocity term and the fluid itself is not modelled.

3.2.2 Boundary Conditions

The boundary conditions on the magnetic field in the MHD simulations are identical to those in the Cartesian magnetofrictional simulations – namely zero perpendicular current on the domain boundaries. However, we now additionally require boundary conditions on the fluid density, temperature and velocity.

We impose that the internal energy (proportional to the temperature) has zero gradient over the boundary (Neumann boundary conditions), allowing it to evolve to a state almost entirely independent of its initial value. The fluid density also uses this condition on three of the boundaries, but the density on the lower boundary is held at a fixed value ρ_0, imposed at one cell within the domain. This ensures the density does not fall to zero as the solar wind carries the plasma out the top of the domain. One side effect of this condition is that the fluid velocity rises quickly just above the lower boundary, accompanied by a similar fall in density. As the photosphere is considerably more dense than the corona, this seems to be a reasonably realistic result.

The boundary conditions for the fluid velocity itself are more complex. On the sides of the domain the horizontal (v_x) velocity is set to zero, preventing flow through the boundaries. The out-of-plane (v_z) velocities are also set to zero here. On the sides boundaries there are Neumann boundary conditions on the vertical velocity v_y, allowing for upward flow. Directly on the lower boundary we impose that the vertical velocity is zero, which prevents numerical instabilities. This is only possible as the density is held constant at a point slightly within the domain – otherwise all the fluid would be sucked through the top boundary and the system would become progressively less dense. On the top boundary the condition on the vertical fluid velocity is

$$v_y(x, 1.0) = \max\{k v_y(x, 1.0 - \Delta y),\, 0.0\}, \tag{3.25}$$

where $1.0 - \Delta y$ is the height of the first cell fully within the domain and $k = 1.25$ is a constant that encourages the fluid to accelerate upwards through the top boundary. This results in the sharp increase in velocity at the upper boundary seen in Figure 3.3. Physically, the fluid would not accelerate particularly significantly

at this specific altitude, and so although it results in desirable behaviour elsewhere this boundary condition is not itself physically realistic. During arcade eruptions the fluid occasionally changes direction to flow downwards and attempts to suck in material from above the top boundary, which would be numerically problematic. This boundary condition ensures the vertical fluid velocity on the boundary remains non-negative but still allows for these eruptions to occur realistically.

Similarly to magnetofriction, the shearing velocity can be added directly to the fluid velocity on the lower boundary, using the shearing profile in Equation 3.15. The method for imposing the supergranular diffusion differs from magnetofriction as the LARE code does not employ an explicit electric field **E**. In the magnetofrictional model this lower boundary condition on the electric field is

$$\mathbf{E}(x,0) = \eta_0 \frac{\partial B_y(x,0)}{\partial x} \mathbf{e}_z. \tag{3.26}$$

If we define a diffusive electric field similarly as

$$\mathbf{E}_{\text{diff}}(x,0) = \eta_0 \frac{\partial B_y(x,0)}{\partial x} \mathbf{e}_z, \tag{3.27}$$

$$\mathbf{E}_{\text{diff}}(x, y > 0) = 0.0, \tag{3.28}$$

then we can directly add the effect of this diffusion onto the magnetic field using the evolution equation

$$\frac{\partial \mathbf{B}}{\partial t} = -\nabla \times \mathbf{E}. \tag{3.29}$$

The components of the change of the magnetic field are then explicitly

$$B_{x_{\text{diff}}} = -\eta_0 \frac{\partial^2}{\partial x \partial y} B_y(x,0), \tag{3.30}$$

$$B_{y_{\text{diff}}} = \eta_0 \frac{\partial^2}{\partial x^2} B_y(x,0). \tag{3.31}$$

This can then be added on to the already-calculated magnetic field at each timestep:

$$B_x = B_x - \eta_0 \frac{\Delta t}{\Delta y} \frac{\partial}{\partial x} B_y(x, 0) \tag{3.32}$$

$$B_y = B_y + \eta_0 \Delta t \frac{\partial^2}{\partial x^2} B_y(x, 0), \tag{3.33}$$

where Δt is the timestep and Δy is the grid resolution in the y direction. This results in very similar behaviour to the magnetofrictional equivalent of the lower boundary condition, but is not directly comparable as we have assumed that the diffusive electric field is zero everywhere away from the boundary – this assumption is not necessary in magnetofriction.

3.3 Our 2.5D Parameter Studies

By limiting ourselves to 2.5D rather than 3D, each simulation can be run in a matter of minutes or hours, rather than days or even months. This has allowed for a very large parameter study using both the two magnetofrictional models and the MHD model. The aim is to produce a large range of flux ropes, with differing sizes, shapes, and stabilities. The parameter that has the most effect on behaviour is the photospheric diffusion η_0, as this is directly related to the speed at which the ropes form and erupt. We also vary the magnetofrictional relaxation rate ν_0 and the initial density ρ_0 in the MF and MHD simulations respectively. This produces additional variation in behaviour and also removes any need to assume values for these constants.

Section 3.3.1 will discuss the diagnostic measures used, followed in Section 3.3.2 by an aside on the preferred definitions of the helicity with the definition and motivation behind our new 2.5D variant of the relative helicity. In Section 3.3.3 onwards we will then cover the model behaviour, including the two types of eruptions observed and the dependence on the model parameters. In Section 3.4 we describe the methodology and results for the selection of potential candidates for useful indicators of eruptivity.

3.3.1 Diagnostics

In this section we describe the diagnostic measures used to identify eruptive events and ultimately to make predictions of future behaviour. We require diagnostics that have a single scalar value which represents the state of the entire system. For the magnetofrictional simulations the diagnostic values will depend only on the strength and configuration of the magnetic field. The raw diagnostics we calculate are as follows:

- **Open Flux**, defined as the sum of the unsigned radial magnetic flux through the upper boundary. An increase in the open flux indicates that fewer magnetic field lines connect back to the surface, and the coronal arcades are stretched upwards, becoming more 'open'. We use changes in the open flux to identify arcade eruptions in the magnetofrictional models.

- **Magnetic Energy**, defined as $E_M = \int_V \frac{1}{2} B^2 \, \mathrm{d}V$. For given boundary conditions, the initial potential field has minimal magnetic energy. The energy increases significantly as the field evolves and flux ropes form. There is usually a large decrease in magnetic energy after eruptions. For eruptivity predictions we favour the 'Free Magnetic Energy' (see below) rather than the magnetic energy itself.

- **Axial Rope Current** I_a, defined as the surface integral of the current $\mathbf{j}$ within the rope, in the direction of the rope axis (the z direction in Cartesian coordinates or the ϕ direction in spherical polar coordinates). In our 2.5D models the 'rope' is defined as the region with infinitely-long magnetic field lines that never reach either the photospheric or outer boundaries.

- **Poloidal Rope Flux** Φ_p – a measure of the magnetic flux contained within the rope in the poloidal (in-plane) direction. This is simple to calculate in 2.5D, as it can be defined simply as the flux intersecting a chord between the centre of the rope (where the out-of-plane component of the vector potential $\mathbf{A}$ attains its maximum value) and the edge of the domain.

- **Axial Rope Flux** Φ_a, defined as the integral of the magnetic flux in the rope, along the axis (out-of-plane) direction.

For the full MHD simulations we can also measure properties of the fluid. Although ultimately these quantities do not seem to be good predictors of eruptivity, their behaviour can be used to identify activity in the system – for instance, the internal energy peaks during arcade eruptions are more pronounced than any variation in the magnetic field.

- **Internal Energy** ϵ, which is here proportional to the temperature of the system, related to the fluid pressure and density by Equation 3.24. As a diagnostic we use an integral of this quantity over the entire domain.

In addition to the above, further measurements are obtained by using comparison to a reference potential magnetic field. The potential field $\mathbf{B}_P$ is defined such that $(\mathbf{B}-\mathbf{B}_P)\cdot\mathbf{n} = 0$ on the domain boundaries, and $\mathbf{B}_P = \nabla\Phi$ for some scalar function Φ. This configuration has the lowest-possible magnetic energy for the given boundary conditions.

In a fully 3D domain the potential field is well-defined, but the definition is less clear for our 2.5D simulations as there is no boundary in the third (z/ϕ) dimension. Originally, we proposed a definition for a reference field in 2.5D space whereby the out-of-plane component of the reference field is a uniform (harmonic) field whose magnetic flux matches the out-of-plane flux of the original magnetic field. This definition has the advantage that an equivalent 3D reference field will converge to it in the limiting case that the domain becomes infinitely long in the out-of-plane dimension (see Section 3.3.2 for a full discussion of this).

In spherical coordinates, we could define the out-of-plane component of the potential field identically to the Cartesian case, as the constant average value

$$\widetilde{B_{P_\phi}}(r,\theta) = \frac{1}{A}\int B_\phi(r,\theta) r \,\mathrm{d}r \,\mathrm{d}\theta, \tag{3.34}$$

where A is the cross-sectional area of a hemisphere, equal to $\frac{\pi}{2}(r_1^2 - r_0^2)$. This is simple to calculate and exhibits behaviour similar to the Cartesian equivalent. However, if

such a field is extended to full 3D there would necessarily be a discontinuity at the north and south poles if the average value in each hemisphere is nonzero. Naturally this solution is not as neat as the Cartesian equivalent, but it is no harder to calculate and so we do not disregard it.

A second approach is to regard the potential field as an axisymmetric field in full 3D. In this case there is no out-of-plane (ϕ) component at all:

$$B_{P_\phi}(r, \theta) = 0. \tag{3.35}$$

The r and θ components of these potential fields $\mathbf{B}_P$ and $\widetilde{\mathbf{B}_P}$ are identical for both definitions, and are calculated independently of the out-of-plane magnetic field. Quantities using both of these definitions and their equivalent vector potentials $\mathbf{A}_P$ and $\widetilde{\mathbf{A}_P}$ (calculated by direct integration) are calculated for all three of the models. These 'reference-based quantities' are:

- **Relative Helicity** H_R

  As introduced in Sections 1.6 and 1.6.1, the helicity within a volume V would be defined as $h(V) = \int_V \mathbf{A} \cdot \mathbf{B}\, dV$, where $\mathbf{A}$ is the vector potential of $\mathbf{B}$. This quantity is dependent in general on the gauge of $\mathbf{A}$, and so we use the alternative relative helicity [85], which is gauge independent:

  $$H_R = \int_V (\mathbf{A} + \mathbf{A}_P) \cdot (\mathbf{B} - \mathbf{B}_P)\, \mathrm{d}V. \tag{3.36}$$

  In 2.5D the definition of the potential field $\mathbf{B}_P$ is subtle, and will be discussed further in the next Section.

- **Current-Carrying Helicity** H_J

  Similarly to the relative helicity, this is defined as

  $$H_J = \int_V (\mathbf{A} - \mathbf{A}_P) \cdot (\mathbf{B} - \mathbf{B}_P)\, \mathrm{d}V, \tag{3.37}$$

  which is also gauge-independent.

- **Free Magnetic Energy** E_F

The free magnetic energy is defined as the magnetic energy of the magnetic field minus the magnetic energy of the reference potential field $\mathbf{B}_P$,

$$E_F = \int_V \left(\frac{1}{2} B^2 \, - \frac{1}{2} B_P^2 \right) \, \mathrm{d}V, \tag{3.38}$$

which is a good indicator of the 'excess' energy in the system, as the potential field is the minimum energy state for the given boundary conditions.

Each of these three quantities requires construction of a potential field $\mathbf{B}_P$, which can be calculated using either of the definitions described above. We thus denote quantities calculated using the potential field with no out-of plane component ($\mathbf{B}_P$) without a tilde (e.g., H_R), and those with an out-of-plane component ($\widetilde{\mathbf{B}_P}$) with a tilde (e.g., $\widetilde{E_F}$).

Due to the variation in the size and strength of the flux ropes, no single diagnostic can be a good predictor of eruptivity. We instead focus on ratios between them (e.g., $|I_a^2/E_F|, |\widetilde{H_J}/E_F|$), chosen with factors such that the ratios are independent of the overall magnetic field strength.

It must be noted that all of these diagnostic quantities and ratios between them will depend significantly on the size and configuration of the domain, and they are not in general dimensionless. This could be addressed by introducing various distance scale factors, but instead in this work we will only directly compare diagnostics which are measured over identical domain sizes and configurations, avoiding the problem.

3.3.2 Discussion on the Definitions of Relative Helicity

The classical helicity within a volume V would be defined as $h(V) = \int_V \mathbf{A} \cdot \mathbf{B} \, dV$, where $\mathbf{A}$ is the vector potential of $\mathbf{B}$ (see Section 1.6). This quantity is dependent in general on the gauge of $\mathbf{A}$, and so we use the alternative relative helicity instead [85] to provide meaningful results. In a 3D domain, this would be calculated by finding a potential field $\mathbf{B}_P$ matching the original magnetic field on the boundary,

and a corresponding vector potential, $\mathbf{A}_P$. The relative helicity would then be

$$H_R = \int_V (\mathbf{A} + \mathbf{A}_P) \cdot (\mathbf{B} - \mathbf{B}_P)\, dV. \tag{3.39}$$

Care is required to define the relative helicity for 2.5D fields. A two-dimensional helicity measure $h(V)$ has been proposed before [113], but we are not aware of a previously published two-dimensional analogue for the relative helicity.

We start by considering the Cartesian case, and the 3D formula (Equation 3.39) on a finite volume V_{z_1}, where $-1 < x < 1$, $0 < y < 1$ and $-z_1 < z < z_1$. Although $\mathbf{B}(x, y)$ in our 2.5D field is independent of z, the corresponding potential reference field $\mathbf{B}_P$ will, in general, vary in the z direction. This arises from the fact that it is potential, coupled with the need to match $B_{Pz}(x, y, \pm z_1) = B_z(x, y)$ on $z = \pm z_1$. We define the relative helicity per unit length to be

$$\widetilde{H_R} = \lim_{z_1 \to \infty} \frac{1}{2z_1} \int_{V_{z_1}} (\mathbf{A} + \mathbf{A}_P) \cdot (\mathbf{B} - \mathbf{B}_P)\, \mathrm{d}V, \tag{3.40}$$

where $\mathbf{B}_P$ and its vector potential $\mathbf{A}_P$ are calculated on V_{z_1}. However, a physically meaningful helicity measure for our 2.5D field cannot possibly require integration in z. We will show that $\widetilde{H_R}$ not only converges as $z_1 \to \infty$ but can indeed be calculated with a two-dimensional integral in x and y.

To do this, we decompose $\mathbf{B}_P$ into three components,

$$\mathbf{B}_P = \mathbf{B}_0 + \mathbf{B}_1 + \mathbf{B}_2 = \nabla\phi_0(z) + \nabla\phi_1(x, y) + \nabla\phi_2(x, y, z) \tag{3.41}$$

where the first component is a uniform field accounting for the net flux in the out-of-plane direction,

$$\phi_0 = \Phi_0 z, \qquad \Phi_0 = \frac{1}{2} \int_0^1 \int_{-1}^1 B_z(x, y)\, \mathrm{d}x\mathrm{d}y, \tag{3.42}$$

and the other two components are both potential fields satisfying $\Delta\phi_1 = \Delta\phi_2 = 0$,

with corresponding boundary conditions

$$\frac{\partial \phi_1}{\partial x}(\pm 1, y) = 0, \tag{3.43}$$

$$\frac{\partial \phi_1}{\partial y}(x, 0) = B_y(x, 0), \qquad \frac{\partial \phi_1}{\partial y}(x, 1) = B_y(x, 1), \tag{3.44}$$

$$\frac{\partial \phi_2}{\partial x}(\pm 1, y, z) = \frac{\partial \phi_2}{\partial y}(x, 0, z) = \frac{\partial \phi_2}{\partial y}(x, 1, z) = 0, \tag{3.45}$$

$$\frac{\partial \phi_2}{\partial z}(x, \pm z_1, 0) = B_z(x, y) - \Phi_0. \tag{3.46}$$

Notice that $\nabla\phi_0$ and $\nabla\phi_1$ are independent of both z and z_1. The z dependence is concentrated only in $\nabla\phi_2$.

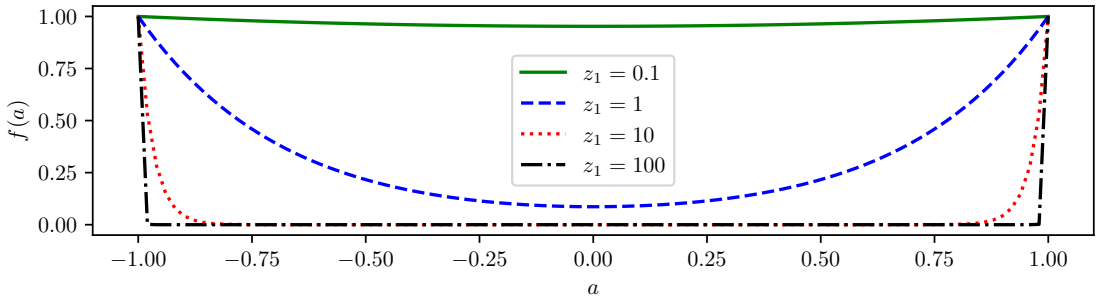

Figure 3.5: Plot of the function $f(a) = \frac{\cosh(k\pi a z_1)}{\cosh(k\pi z_1)}$ for $k = 1$ and various values of z_1.

The potential ϕ_2 has the important property that, as z_1 increases, it becomes more and more concentrated near to the end boundaries $z = \pm z_1$, irrespective of $B_z(x, y)$. To see this, note that in the Cartesian domain V_{z_1}, the solution for ϕ_2 may be written as a Fourier series

$$\phi_2(x, y, z) = \sum_{m,n\neq 0} c_{m,n} \cos\left(\frac{m\pi(x+1)}{2}\right) \cos(n\pi y) \sinh(k\pi z), \tag{3.47}$$

where m, n are integers, $k^2 = (m/2)^2 + n^2$, and the sum includes all terms except $m = n = 0$ (which has been essentially separated as the ϕ_0 component). The

components of the field $\mathbf{B}_2 = \nabla\phi_2$ are then explicitly

$$B_{2_x} = -\sum_{m,n\neq 0} \frac{m\pi}{2} c_{m,n} \sin\left(\frac{m\pi(x+1)}{2}\right) \cos(n\pi y) \sinh(k\pi z) \tag{3.48}$$

$$B_{2_y} = -\sum_{m,n\neq 0} n\pi c_{m,n} \cos\left(\frac{m\pi(x+1)}{2}\right) \sin(n\pi y) \sinh(k\pi z) \tag{3.49}$$

$$B_{2_z} = \sum_{m,n\neq 0} k\pi c_{m,n} \cos\left(\frac{m\pi(x+1)}{2}\right) \cos(n\pi y) \cosh(k\pi z). \tag{3.50}$$

The coefficients $c_{m,n}$ are then determined by the boundary condition

$$\frac{\partial\phi_2}{\partial z}(x, \pm z_1, 0) = B_{2_z}(x, \pm z_1, 0) = B_z(x, y) - \Phi_0, \tag{3.51}$$

which gives

$$c_{m,n} = \frac{2}{k\pi \cosh(k\pi z_1)} \int_0^1 \int_{-1}^1 B_z(x, y) \cos\left(\frac{m\pi(x+1)}{2}\right) \cos(n\pi y)\ \mathrm{d}x\mathrm{d}y. \tag{3.52}$$

The Φ_0 is taken care of in the $\mathbf{B}_0$ part of the magnetic field. Now consider the value of $\phi_2(x, y, az_1)$ for some fixed fraction $|a| < 1$. Then

$$\phi_2(x, y, az_1) = \sum_{m,n} \frac{2\sinh(k\pi a z_1)}{k\pi \cosh(k\pi z_1)} F(x, y), \tag{3.53}$$

where $F(x, y)$ contains the x and y dependence from (3.47) and (3.52). We wish to examine the behaviour of this term for a fixed a in the range $-1 < a < 1$ as the domain length z_1 increases.

The limit of the hyperbolic functions in this case is merely the exponential function (taking care with the sign of a):

$$\lim_{z_1\to\infty} \frac{\sinh(k\pi a z_1)}{\cosh(k\pi z_1)} = sgn(a) \lim_{z_1\to\infty} \frac{\exp(k\pi|a|z_1)}{\exp(k\pi z_1)} = sgn(a) \lim_{z_1\to\infty} \exp(k\pi(|a|-1)z_1). \tag{3.54}$$

As $(|a|-1)$ has a magnitude less than 1, this exponential function converges to zero. A similar result holds for the cosh equivalent, so

$$\lim_{z_1\to\infty} \frac{\sinh(k\pi a z_1)}{\cosh(k\pi z_1)} = \lim_{z_1\to\infty} \frac{\cosh(k\pi a z_1)}{\cosh(k\pi z_1)} = 0, \tag{3.55}$$

and we see that the non-zero part of $\nabla\phi_2$ becomes an increasingly smaller fraction of the domain length as $z_1 \to \infty$. This is illustrated in Figure 3.5. It follows that the contribution from $\nabla\phi_2$ to $\widetilde{H_R}$ in equation (3.40) vanishes in this limit, so that this definition of the relative helicity can be written simply as

$$\widetilde{H_R} = \int_0^1 \int_{-1}^1 (\mathbf{A} + \widetilde{\mathbf{A}_P}) \cdot (\mathbf{B} - \widetilde{\mathbf{B}_P}) \, \mathrm{d}x\mathrm{d}y, \tag{3.56}$$

where $\widetilde{\mathbf{B}_P}(x, y) = \nabla\phi_1(x, y) + \Phi_0\mathbf{e}_z$. The gauge of $\widetilde{\mathbf{A}_P}$ does not affect the integral (as usual for H_R), so one is free to choose an $\widetilde{\mathbf{A}_P}$ that is independent of z and hence evaluate $\widetilde{H_R}$ with a purely 2D integral.

Although this is a neat result for the 2.5D Cartesian system, the ideal definition for the axisymmetric polar model is less clear-cut. As such we also consider the alternative (classic) definition for the reference potential field, with no out-of-plane component. The two definitions can be mixed in the diagnostic ratios, and indeed doing this has shown to make a significant difference to the ratios‘ predictive abilities.

It remains to be seen whether this modification to the reference field definition can be translated into full 3D. Although in 3D the definition of a potential field is well-defined, we have shown (in Section 3.4) that the alternative 2.5D definitions behave very differently from one another. Thus it may be the case that in 3D a relative helicity definition using a modified reference field (and diagnostic ratios deriving from it) may well be a better predictor than when using a standard potential field.

3.3.3 Model Behaviour

We observe similar behaviour in all three sets of simulations. Figure 3.6 plots selected diagnostics from a single run from each set for comparison. Over the first 10-20 days, the solar wind opens out the magnetic arcade, increasing the magnetic flux through the upper boundary and resulting in a smaller arcade as fewer magnetic field lines loop back to the surface. In the absence of the dynamic lower boundary conditions, the system would remain in equilibrium in this state. Such an ‘outflow field’ is shown in the lower row of Figure 3.4. During this initial phase we also observe significant

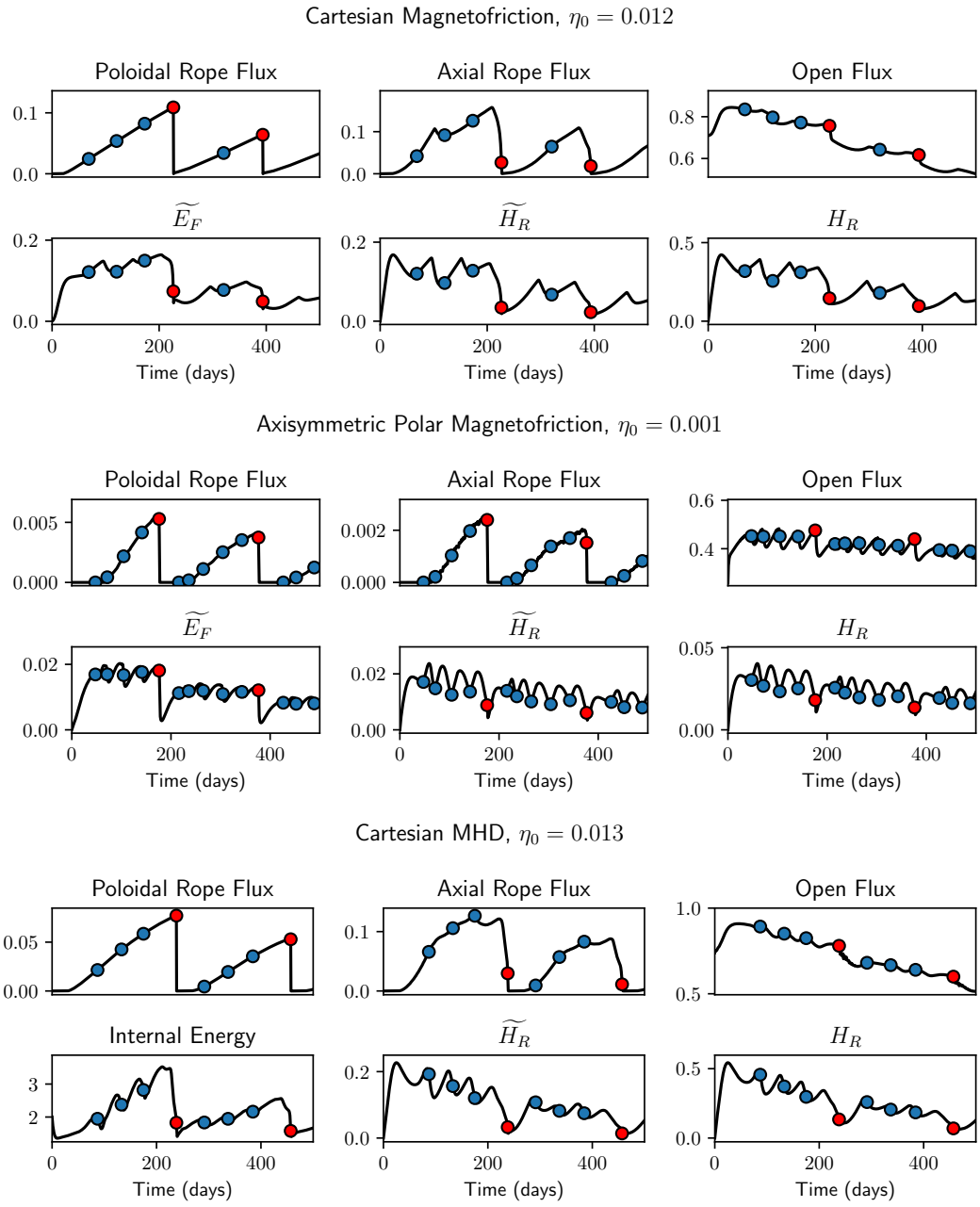

Figure 3.6: Selected diagnostics from a representative run from each of the three simulation sets, in dimensionless units. These units are the same in the two Cartesian setups but not in the polar coordinate simulations, due to the differing length scales. Arcade eruptions are represented with blue circles, and flux rope eruptions with red circles. Note that internal energy is plotted for the MHD simulation, whereas free magnetic energy is plotted for the magnetofrictional simulations. The time at which an arcade eruption occurs is given by the time of maximum decrease in either open flux or internal energy, and the time of a flux rope eruption is the point immediately before the poloidal rope flux falls to zero. Values are in general smaller in the axisymmetric case due to the smaller size of the rope compared to the distance unit.

increases in relative helicity and free energy as the magnetic field evolves further from a potential field. During this period a current sheet develops at the top of the domain (in the out-of-plane direction), forming a helmet streamer [114]. Such current sheets are visible in the top snapshots of Figure 3.7 as the arcade opens out.

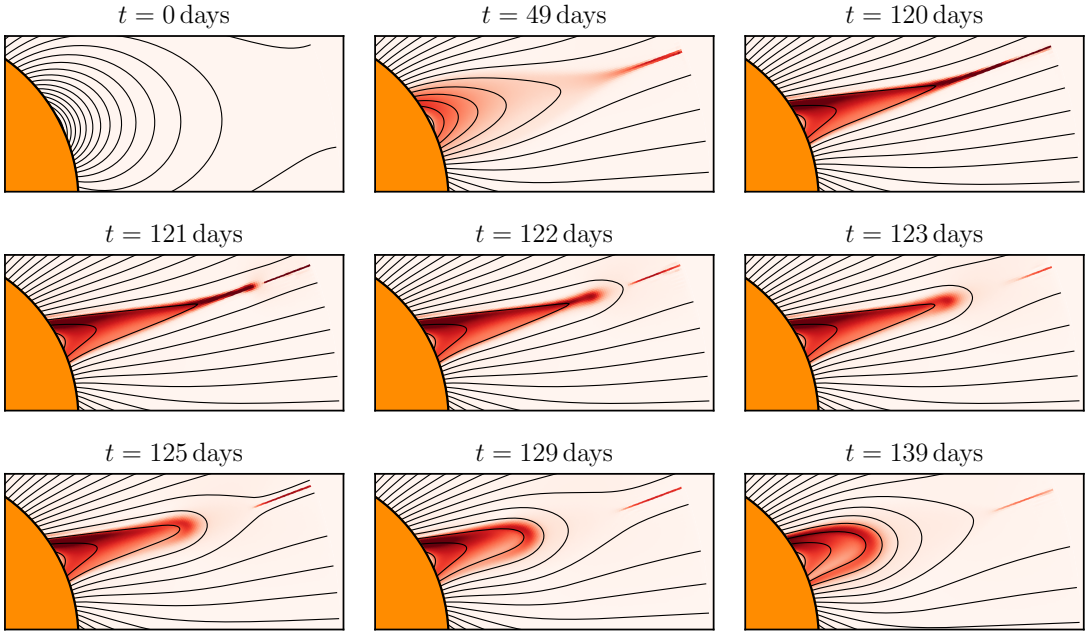

Figure 3.7: Snapshots from an axisymmetric polar magnetofrictional simulation with no photospheric diffusion ($\eta_0 = 0$, $\nu_0 = 2.0$), showing the shearing of the arcade and formation of a helmet streamer (top panes), followed by an arcade eruption starting at around 120 days. The heatmap represents the out-of-plane current density, and the black lines are the magnetic field lines projected into the plane.

The differential rotation on the solar surface then causes the magnetic field to become sheared in the out-of-plane direction. Open field lines outside the arcade become sheared near the surface, but as they are not fixed at the top boundary they are free to relax and undo the shear. In the arcade itself the shearing becomes more pronounced, opening out the arcade even further than caused by the effect of the solar wind alone. The free magnetic energy continues to increase during this period, as does the intensity of the current sheet above the arcade.

After around 50-100 days the energy concentrated in the current sheet becomes too great and there is a rapid loss of equilibrium. There is fast magnetic reconnection at the top of the domain and the arcade quickly moves downwards. We refer to this as an 'arcade eruption' [108, 114], indicated by blue circles in Figure 3.6. The

sequence of such an eruption in an axisymmetric magnetofrictional simulation is shown in Figure 3.7. In MHD, matter is ejected out of the top of the domain during these eruptions, leading to a noticable decrease in the internal energy of the system. During these eruptions there are also decreases in open flux (most clearly visible here in the axisymmetric simulations) and free magnetic energy as the system relaxes to a state more closely resembling a potential field. It is possible that these represent streamer blowouts or even 'stealth CMEs', as coined by [115], since they are characterised by the lack of a detectable signature on the solar surface. The nature and period of these eruptions (around every 25-30 days) matches well between our 2.5D model, global magneto-frictional simulations and observations [108].

When supergranular diffusion (the parameter η_0) is significant, we observe the formation and eruption of magnetic flux ropes. The diffusion on the surface causes the magnetic footpoints of the arcade to be brought together at the polarity inversion line, forming twisted bundles of magnetic flux that no longer connect to the solar surface. Although in reality such a rope would be attached to the surface at either end, this is not the case in our 2.5D domains. In the Cartesian simulations these ropes are essentially infinitely long in the out-of-plane direction, and in the axisymmetric simulations the ropes wrap entirely around the Sun.

The presence of the rope in Figure 3.6 is indicated by nonzero poloidal and axial rope fluxes. In all three sets of simulations the poloidal flux steadily increases until the rope erupts, and is not usually affected by arcade eruptions. The axial flux is affected by arcade eruptions to a greater degree: in the magnetofrictional simulations we observe it steadily increasing, whereas in the MHD simulations it tends to reach an upper limit or even decreases as the rope evolves. This appears to be the main difference in the dynamics between the two models, and has a significant effect on some of the diagnostic ratios. We are unsure as to the precise reason for this, but it is perhaps due to diffusive effects in the out-of-plane direction being more prevalent in the MHD model and reducing the out-of-plane magnetic field component more rapidly than the MF equivalent.

In most of the simulations, a flux rope forms and remains in a semi-equilibrium state for some time. This can be up to several hundred days, but the average time

is around 50-100 days after formation. During this period arcade eruptions above the rope can continue to take place. The presence of the rope alters the size and timing of these eruptions, but the qualitative behaviour is the same. The rope itself moves downwards during arcade eruptions, and in the MHD simulations this is often followed by a period of damped oscillation as the rope returns to a stable state. Such 'kink oscillations' have been observed in the corona, as discussed in [116], where the flux rope fails to erupt in a similar scenario to our 'arcade eruptions', although the period of the oscillations in our model is of the order $10,000$ seconds - significantly longer than the observed oscillations.

3.3.4 Typical Flux Rope Structure

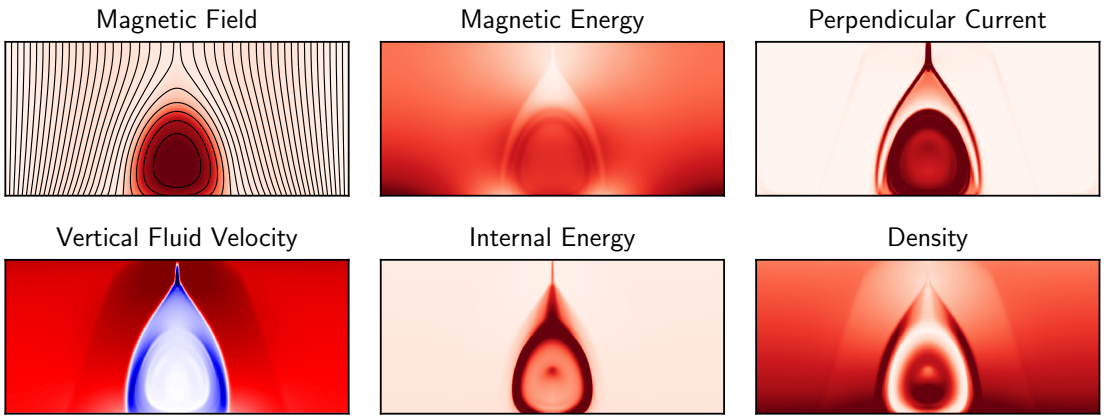

Figure 3.8: A snapshot of a flux rope from one of the Cartesian MHD simulations with $\eta_0 = 0.029$ and $\rho_0 = 1.0$, showing heatmaps of various diagnostic quantities to illustrate its structure. The black lines in the magnetic field plot are the field lines projected onto the plane, and the heatmap represents the out-of-plane component of the field. All quantities except the fluid velocity are strictly positive, increasing from zero (white) to their maximum value (red) on the colourmap. The vertical fluid velocity can take negative values within the rope, which are shown in blue.

The structure of a flux rope in full MHD is displayed in Figure 3.8. As expected, we observe that the magnetic field in the rope itself is twisted, with a maximum out-of-plane component of roughly equal magnitude to the radial magnetic field strength through the lower boundary. As there is comparatively very little magnetic diffusion in the solar corona, the plasma fluid is essentially constrained to move along magnetic field lines (Alfvén's Theorem). We can see evidence of this in the plot of the vertical

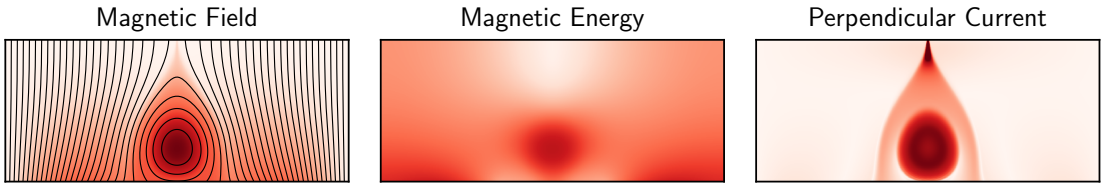

Figure 3.9: A snapshot of a flux rope in one of the Cartesian magnetofrictional simulations with $\eta_0 = 0.005$ and $\nu_0 = 1.0$, showing colourmaps of various diagnostic quantities to illustrate its structure. The black lines in the magnetic field plot are the field lines projected onto the plane, and the heatmap represents the out-of-plane component of the field.

fluid velocity, which is significant in the region with open magnetic field lines, due to the effect of the solar wind. In the flux rope itself the fluid velocity is comparatively small (less than a quarter of the velocity outside) or even negative as the fluid must remain within the area of the rope.

The inner 'core' of the rope is where the magnetic field is most sheared. In this region the internal energy is relatively low and the fluid density relatively high. The core is surrounded by a region with a considerably lower fluid density (less than 10% of the core) and much higher temperature, around 5 times that in the core. This region also has a high out-of-plane current as the magnetic field becomes less twisted. This non-uniform shearing at different layers of the flux rope has been noted in both observations and models (eg. [117]). One explanation for this is that layers of flux are added sequentially as the rope forms, and are relatively undisturbed after formation (eg. [118]). This appears to be the process that we observe here.

Further out from the centre of the rope there is a region with higher density, similar to that in the core, where the magnetic field itself is not so significantly sheared. Here there is very little perpendicular current, with less than 5% of the maximum attained closer to the centre of the rope. Such a boundary between twisted and untwisted fields has been observed in both analytical models ([119]) and MHD simulations ([120]). There is finally a thin current sheet surrounding the whole structure, marking the boundary at which the fluid velocity due to the solar wind becomes significant. We also observe a current sheet above the arcade, as in the cases without photospheric diffusion.

The flux ropes in the magnetofrictional simulations do not have such a complex

structure. Such a rope in Cartesian coordinates is illustrated for comparison in Figure 3.9. Although the overall configuration of the magnetic field is very similar to MHD, the distribution of the current differs in that the current sheet at the top of the domain does not extend down to near the photosphere. This is because the vertical solar wind velocity is applied uniformly across the width of the domain, so there is no shear layer between the open and closed field regions. There is no equivalent of the fluid density or internal energy in magnetofriction, and so these quantities are not comparable.

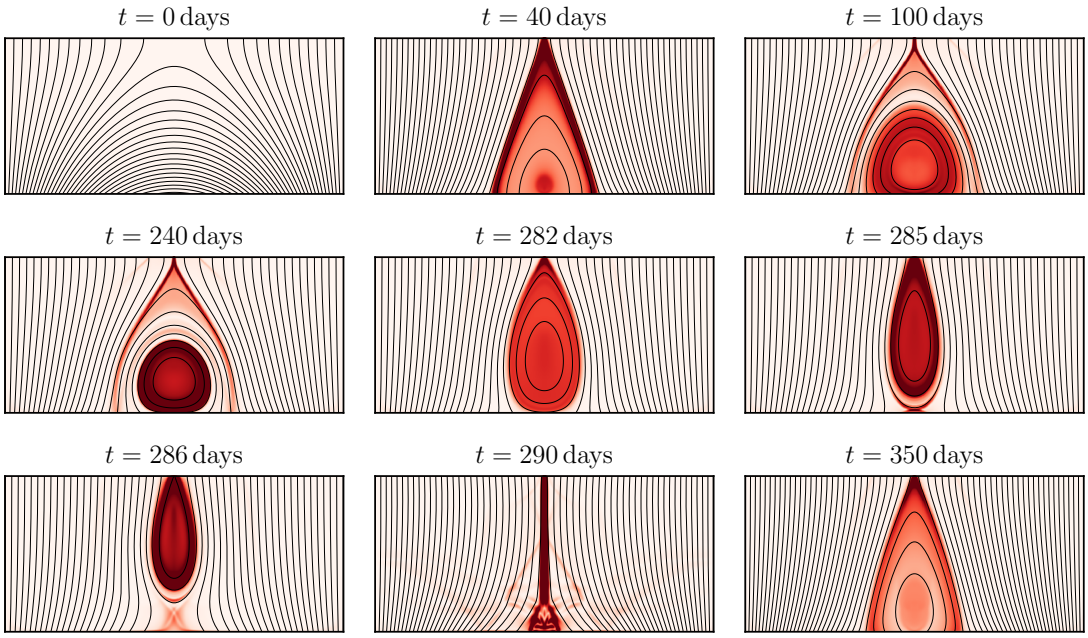

Figure 3.10: Formation and eruption of a flux rope. This is a Cartesian MHD simulation with coronal diffusion $\eta_0 = 0.01$. The heatmaps represent the out-of-plane current density, and the black lines are the magnetic field lines projected into the plane. The rope erupts at around t = 285 days, after which it reforms. The process would then in general repeat.

In most simulations with a flux rope present we observe a catastrophic loss of equilibrium with rapid magnetic reconnection below the rope. The rope itself moves very quickly upward out of the top of the domain – we call this a 'flux rope eruption', indicated by red circles in Figure 3.6. The timing of these eruptions is related to the photopsheric diffusion rate and varies massively depending on the choice of the system parameters. During a flux rope eruption there is a significant decrease in all diagnostic quantities, and in the MHD case a large amount of mass is ejected

from the domain. The full sequence of flux rope formation and eruption is shown in Figure 3.10, where both the in-plane magnetic field lines and the out-of-plane current are plotted.

In most cases, after a flux rope eruption the system still has sufficient energy to continue evolving. If so, after a short period a magnetic arcade reforms and the process restarts. However, the energy in the system is lessened with each eruption and subsequent flux ropes thus have smaller poloidal and axial magnetic fluxes. In general these ropes do not last as long before erupting as those that form initially.

This describes the fundamental processes observed in the simulations. We next discuss the variation in the system behaviour based on the system parameters, as well as the differences between Cartesian and polar coordinates and between magnetofriction and full MHD.

3.3.5 Dependence on Model Parameters

To produce a wide array of flux rope behaviours, with differing rope strengths and sizes, we have undertaken a large parameter study within each of the three models. We fix three of the parameters throughout: the outflow velocity factor v_1 (set at 50 times the maximum shearing rate), the coronal diffusion η ($= 5 \times 10^{-4}$) and the photospheric shearing rate (V_0), discussed in Section 3.1.2 and 3.2.2.

There are two variable parameters. The most notable is the supergranular diffusion rate η_0, which is directly related to the rate at which the flux ropes form and erupt. In the magnetofrictional simulations we also vary the magnetofrictional relaxation rate ν_0, whereas in the MHD simulations we vary the initial density ρ_0.

For each of the three simulation setups we ran 320 simulations in subsets of 64 runs, keeping ν_0 or ρ_0 fixed within each subset and varying η_0. The simulations ran for 500 days, allowing for the formation and eruption of multiple flux ropes in some cases.

The parameter ranges varied based on the simulation setup. For the Cartesian magnetofrictional simulations, $10^{-3} < \eta_0 < 10^{-1}$ and $0.5 < \nu_0 < 2$. For the axisymmetric magnetofrictional simulations $2 \times 10^{-4} < \eta_0 < 2 \times 10^{-1}$ and $2 < \nu_0 < 10$. The difference in these ranges is accounted for by the differing unit length scales

between the two grid systems. Smaller ν_0 values did not produce realistic behaviour as the system takes too long to relax to a force-free state, and for values higher than this the simulations became too computationally intensive (as smaller timesteps are necessary to prevent numerical instability).

In the MHD simulations $2.5 \times 10^{-3} < \eta_0 < 10^{-1}$ (although this is not directly equivalent to the magnetofrictional η_0 as discussed in Section 3.2.2), with the initial density (and the fixed density boundary condition on the lower boundary) in the range $0.5 < \rho_0 < 2.0$. Varying the initial density changes the plasma beta – the ratio of plasma pressure to magnetic pressure. The plasma beta is generally of the order of magnitude $\beta \approx 1 \times 10^{-2}$ throughout most of the domain, but it varies considerably in space and is generally much higher in the rope itself. Varying the initial density does not greatly alter the behaviour of the system, but allows us to ensure any eruptivity criteria we later find are independent of the plasma beta.

Figure 3.11 presents an overview of 64 of the simulations from each of the three models, varying the photospheric diffusion η_0 on the x axis. The overall pattern is similar in each case. We observe periodic arcade eruptions (the blue circles on the plot) for low η_0, where there is no (or a very small) flux rope present. For higher values of the photospheric diffusion flux ropes form, indicated by the vertical red lines. Arcade eruptions can still occur when a flux rope is present, but when the photospheric diffusion is too high the ropes themselves erupt too quickly to allow for this. The general trend is that for higher η_0 the ropes form and erupt more quickly. In general ropes reform after erupting, but for very high diffusion rates the system loses enough energy that they do not.

Although the overall pattern between the three setups is similar, there are some notable differences. The range of η_0 at which certain behaviour occurs is similar between the two Cartesian simulations, but in general ropes form and erupt with smaller η_0 in the axisymmetric polar simulations, hence the variation in the parameter ranges chosen (the x axes of Figure 3.11 are adjusted to reflect this). For low η_0 we observe regular arcade eruptions, but the frequencies are not equivalent in each model – they are notably less frequent in the Cartesian magnetofrictional simulations. The pattern is less regular in the axisymmetric simulations, which is to

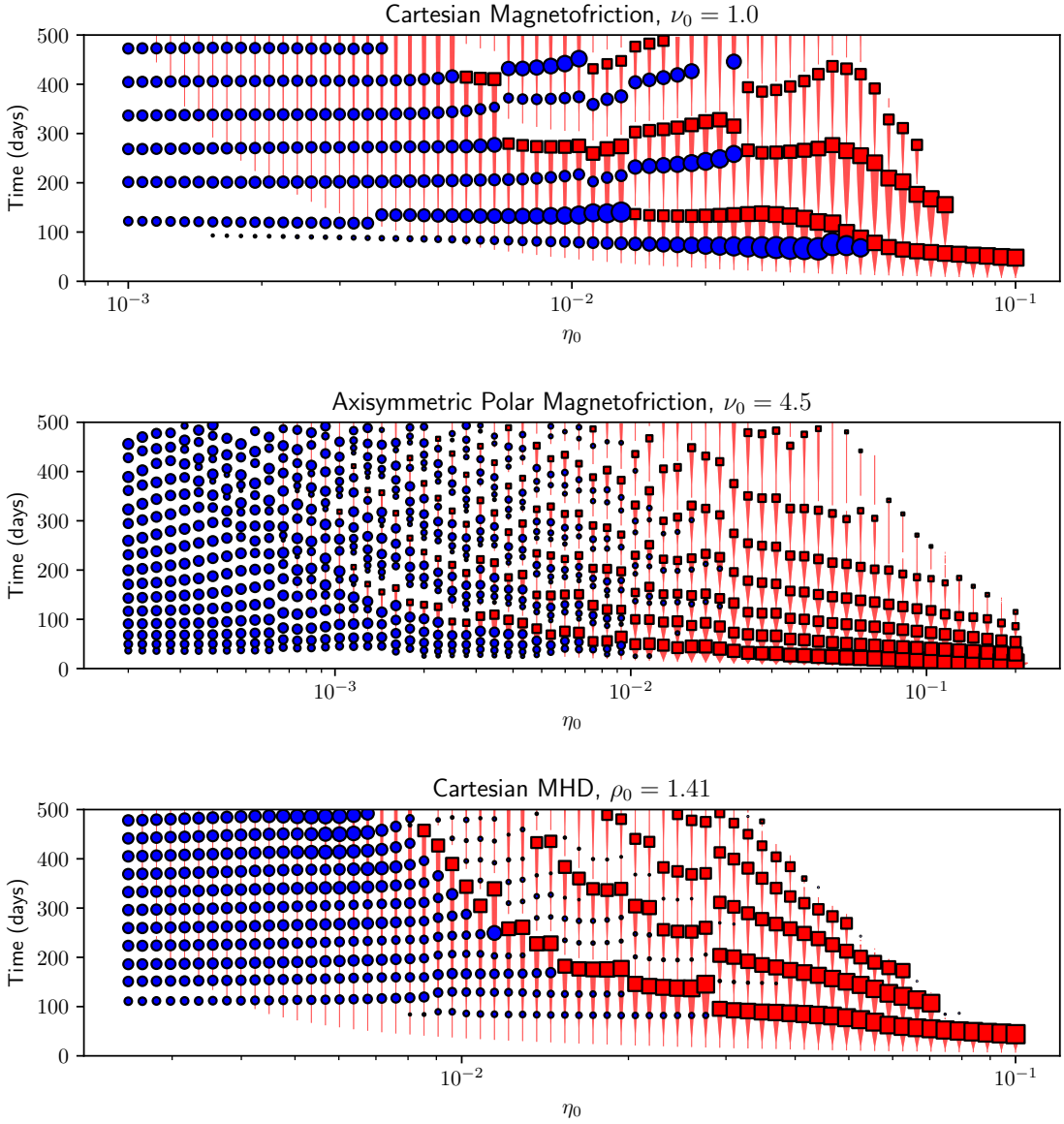

Figure 3.11: Overview of 64 runs from each of the three sets of simulations – Cartesian magnetofriction (top), axisymmetric polar magnetofriction (middle) and Cartesian MHD (bottom), varying η_0 on the horizontal axis. Each simulation corresponds to a vertical line on the plot. The poloidal magnetic flux in the flux rope is represented by the thickness of the red lines. The times of arcade eruptions are represented by blue circles and flux rope eruptions by red squares, respectively. The size of the red squares is proportional to the decrease in poloidal magnetic flux during an eruption, and the size of the blue circles is proportional to the decrease in open flux (magnetofriction) or internal energy (MHD) during each arcade eruption.

be expected as the shearing rate is more complex and the domain is larger, allowing the arcade more freedom to move and become asymmetrical (as observed in Figure 3.7). This freedom also enables the pattern of flux rope eruptions to become less

regular than in the Cartesian simulations.

It was initially unclear whether there is a minimum (nonzero) η_0 below which a flux rope will never erupt. However, we observe for very low η_0 in Cartesian MHD the poloidal rope flux does not necessarily increase monotonically, and indeed in this case the rope will likely slowly diffuse away and not erupt. This diffusion is also observed in some of the cases on the right of Figure 3.11, for ropes that have already erupted and reformed. In the axisymmetric simulations ropes do not necessarily form at all for low η_0, perhaps due to numerical diffusive effects being more prevalent compared to the Cartesian simulations, which have a higher grid resolution and represent a smaller region of the corona.

A large arcade eruption can prematurely trigger a full flux rope eruption. This phenomenon is clearly observed in the top pane of Figure 3.11 (the Cartesian magnetofrictional simulations). As η_0 increases, arcade eruptions become larger (indicated by larger blue circles) until they cause the eruption of the rope itself. As the arcade eruptions have very regular frequency, this has resulted in the stepped pattern in the time of first flux rope eruption. Such a pattern is also visible in the Cartesian MHD simulations to a lesser extent, but as the arcade eruptions are relatively more frequent it is less clear.

Ultimately, we observe very similar dynamics in all three models, verifying that magnetofriction can indeed accurately represent the qualitative behaviour of magnetic flux ropes. We also observe similar behaviour between the Cartesian and axisymmetric polar simulations, indicating that using Cartesian coordinates to model the local dynamics of the corona qualitatively is a valid approach. It remains to discuss the conditions of flux rope instability in each of the models.

3.4 Comparison of Potential Eruptivity Indicators

In this section we discuss the possibility of finding one or more scalar quantities derived from the system diagnostics that can be used to predict an imminent (later) flux rope eruption. We expect that a single diagnostic value, such as the rope

current or open flux, cannot itself be a good predictor of eruptivity due to the large variation in the size and strength of the flux ropes. Instead, we seek ratios between such quantities, normalised such that they are independent of the overall magnetic field strength. As the dynamics of magnetofrictional simulations are independent of the overall field strength, this is an essential requirement.

The diagnostic ratios fall into two categories. The first are ratios of the rope current or flux squared divided by a reference-based quantity (e.g. $|\Phi_a^2/\widetilde{E_F}|$). The second are ratios between two reference-based quantities (e.g. $|H_J/\widetilde{H_R}|$). We also consider the alternative definitions for the reference-based quantities discussed in Section 3.3.1, and as such there are now four variants of each ratio.

The initial motivation for considering ratios in this manner came from regarding scatter plots as in Figure 3.12, where the numerator is plotted on the y axis and the denominator on the x axis. For any snapshot where a flux rope is present, we check whether an eruption will occur within a given time – 15 days in the case of this figure but this time cutoff will later be allowed to vary. Those points which do precede an eruption within the given time are coloured red, and those that do not are coloured blue.

If there is a clear correlation between the red points on the scatter plots and a weaker one between the blue points, then this ratio has the potential to be a good predictor. All of the scatter plots in Figure 3.12 are correlated to some degree, but it is clear that (for instance) the ratio $|H_J/\widetilde{H_R}|$ (top right) clearly has a threshold of around 0.6 units at which an eruption will be likely.

We aim to consider all ratios, regardless of physical motivation. However, those that can be theoretically infinite can be disregarded, such as those which have a denominator wholly dependent on the presence of a flux rope (eg. Φ_p) and a numerator that is not (eg. H_R). This still leaves several hundred combinations, which would be difficult to objectively compare by hand. Thus we have an automated process for identifying which of them are superior, as follows.

For each diagnostic snapshot where a rope exists, the ratio values are sorted according to whether or not they precede a flux rope eruption within a certain time cutoff t (between 10 and 50 days), as in Figure 3.12. For each ratio, two

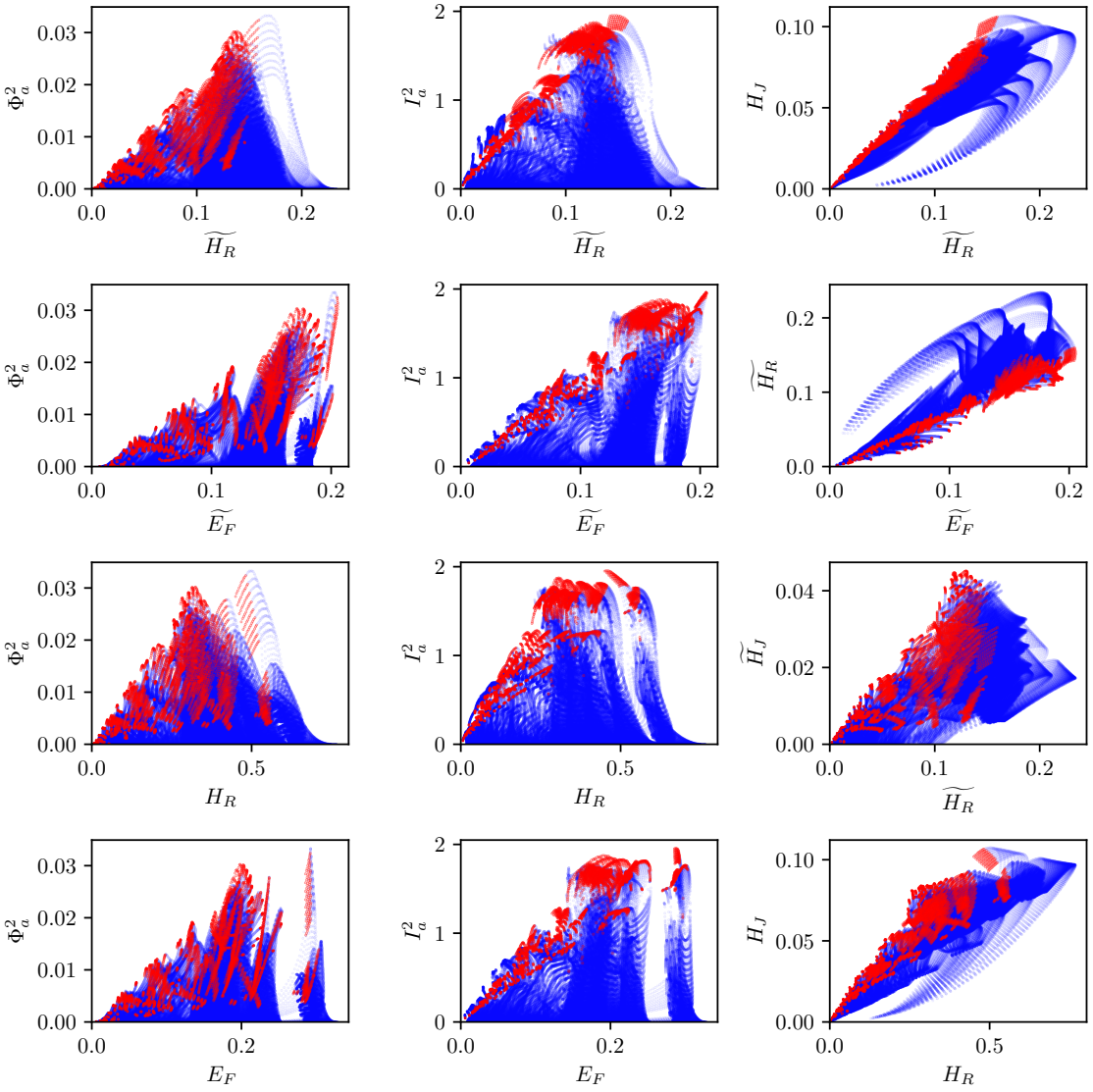

Figure 3.12: Pairwise scatter plots of the selected diagnostic values from the Cartesian magnetofrictional simulations. If a flux rope eruption will take place within 15 days, a point is coloured red. If there is no eruption within this time frame, the point will be coloured blue. Note that both axes are weighted to be proportional to the magnetic field strength squared.

histograms are then produced: one for points preceding an eruption and one for points not preceding an eruption. Figure 3.13 shows these histograms in red and blue respectively, for three of the diagnostic ratios. The histograms are normalised to have the same area, resulting in distribution curves $R(x,t)$ and $B(x,t)$ for eruptive and non-eruptive points respectively. This normalization effectively assumes an equal weighting of eruptive and non-eruptive ropes – this could be improved with prior knowledge of the overall probability of a rope erupting. For instance, regarding the

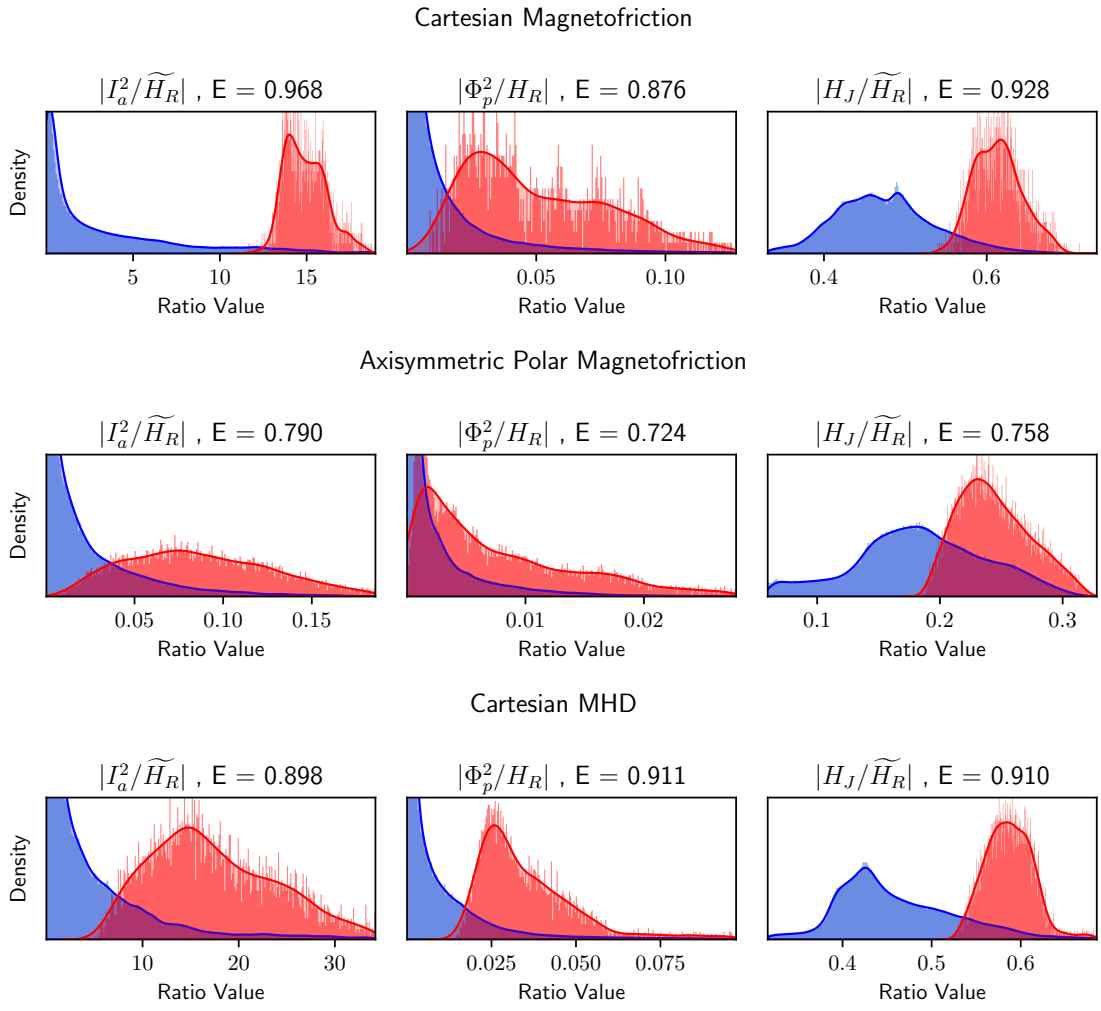

Figure 3.13: Distribution of eruptive and non-eruptive values and the respective distribution curves $R(x,t)$ (red) and $B(x,t)$ (blue) for a flux rope eruption within $t = 10$ days. The three diagnostic ratios plotted are axial current squared over relative helicity, poloidal flux squared over relative helicity and the current-carrying helicity over relative helicity. Note that the poloidal flux ratio plotted here uses the 3D definition of the relative helicity (not including the out-of-plane magnetic flux), whereas the others use the 2.5D definition. Eruptive points are coloured red and non-eruptive points coloured blue. The relative heights of each curve give an indication of the likelihood of an eruption occurring within 10 days for a given measured value on the x axis. The histograms with little red/blue overlap are better predictors.

ratio $|H_J/\widetilde{H_R}|$ at the bottom right of Figure 3.13, the peak at around 0.6 indicates that if the diagnostics have this value then a flux rope eruption within 10 days is very likely – as seen in the respective scatter plot. Good diagnostic predictors will have little overlap between the blue and red regions while bad predictors have a significant overlap.

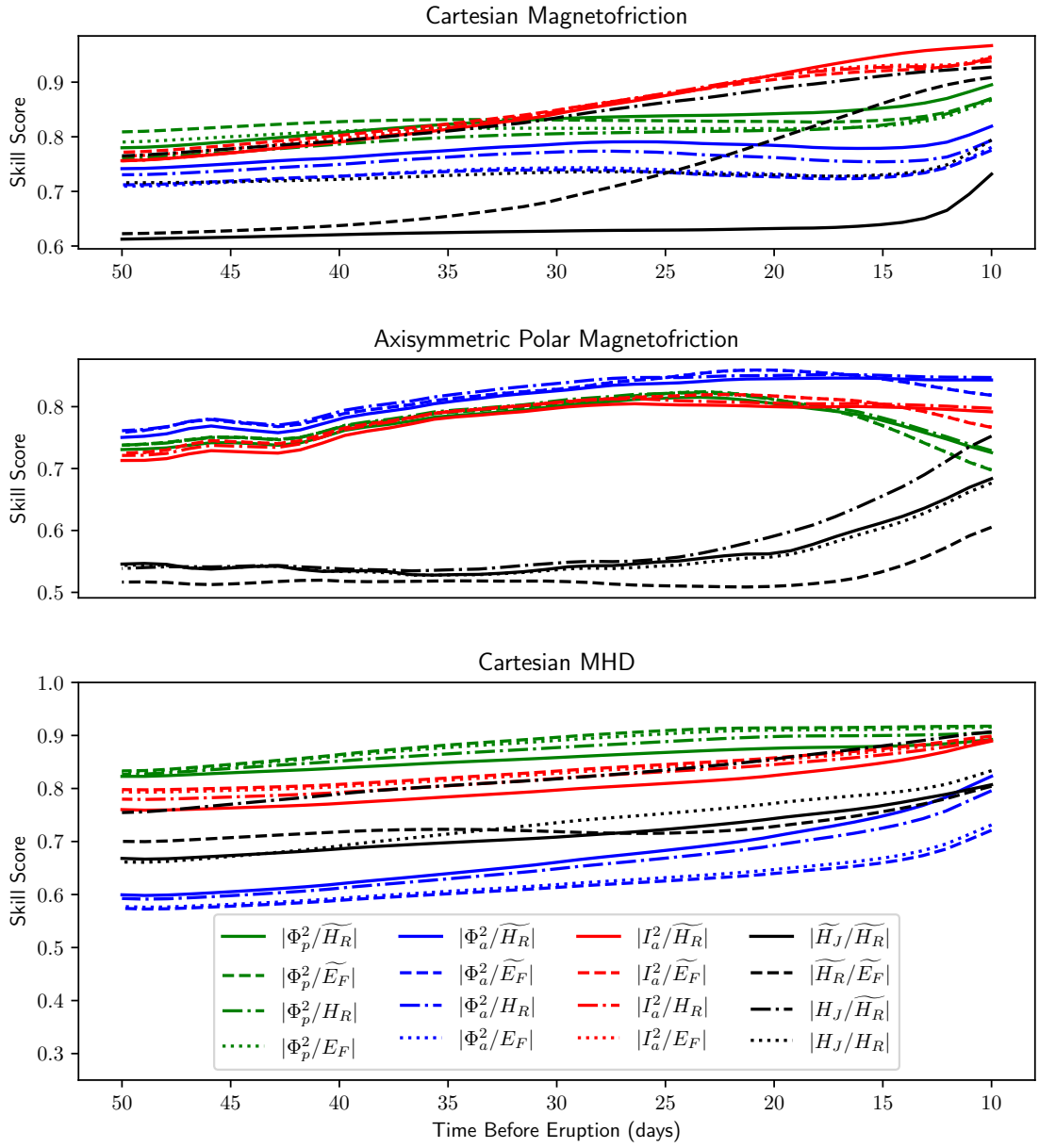

Figure 3.14: The skill scores for selected diagnostic ratios, varying with the time cutoff between a prediction and the flux rope eruption. Axial rope current and flux are denoted I_a and Φ_a respectively, poloidal rope flux is denoted Φ_p and the reference-based quantities are as defined in Section 3.3.1. The particular diagnostic ratios in black are selected as they perform well in at least one of the simulation sets.

We then define a proxy for the probability of an eruption within time t given a diagnostic ratio value x as

$$P_e(x,t) = 1 - \left(1 - \frac{R(x,t)}{R(x,t) + B(x,t)}\right)^2, \tag{3.57}$$

where the squaring in general slightly increases the predictive ability. This is a simplistic approach, based on the assumption that if a good predictor exists then its value before eruptions from our existing data will correlate well to its value before any future eruptions. This is justified to a degree by calculating the accuracy of these 'probabilities' by then comparing back against the data, using a 'skill score':

$$E(t) = \frac{\Sigma_{\text{Erupt } x}\, P_e(x,t) + \Sigma_{\text{No Erupt } x}\,(1 - P_e(x,t))}{\text{Total Number of Values}}. \tag{3.58}$$

If a diagnostic ratio can predict eruptions within a time t perfectly, then it would have skill score $E(t) = 1$ (but this would require complete certainty for each value). If the ratio is no better than random chance than it will have skill score $E = 0.5$. The skill scores $E(t)$ for 16 selected diagnostic ratios are shown in Figure 3.14, for each of the three models. Ratios between reference-based quantities (such as the eruptivity index) are coloured black, and the other ratios are coloured based on the numerator.

We find that in the Cartesian magnetofrictional simulations (top) ratios of the axial current squared (red) to the relative helicity or free energy are the best predictors back to around $t = 30$ days before an eruption. In the Cartesian magnetofrictional simulations these ratios have skill scores up to $E = 0.968$. These ratios also perform well in the MHD simulations, with skill scores around $E = 0.9$. The histograms for one of these ratios ($|I_a^2/\widetilde{H_R}|$) are plotted on the left of Figure 3.13. We observe that in both of the Cartesian simulations (magnetofriction and MHD) the eruptive distribution curve $R(x, 10)$ peaks at a value around 15 units, indicating that this threshold for eruptivity is consistent between magnetofriction and MHD.

Ratios with the poloidal rope flux (green) as numerator consistently performed the best in the MHD simulations, with skill scores up to $E = 0.911$, although not notably more so than the equivalent ratios with axial current. The ratios using the axial rope flux (blue) as numerator did not perform as well in either of the Cartesian scenarios.

As may be expected, predictions of eruptions are more accurate closer to the time of the eruption itself, as seen in the variation in the skill scores plotted in

Figure 3.14. However, the decreased ability to predict eruptions far into the future is counteracted by the general increase in likelihood of an eruption within a larger time frame, explaining why the skill scores do not fall to $E = 0.5$ particularly quickly.

The predictive ability of the ratios between two reference-based quantities (such the eruptivity index $|H_J/H_R|$) varies greatly among the three models. The four of these ratios plotted in Figure 3.14 (in black) are chosen as they are each good predictors in at least one of the models. As we found previously, the eruptivity index calculated using the 2.5D definition $|\widetilde{H_J}/\widetilde{H_R}|$ (solid black) is not at all a good predictor in the Cartesian magnetofrictional simulations. We find it is slightly better in MHD, but has a maximum skill score of only around 0.75, far less than ratios involving the axial current or poloidal flux.

However, an alternative definition of the eruptivity index – using a mixture of the two reference potential field definitions – performs very well in both of the Cartesian models. This ratio $|H_J/\widetilde{H_R}|$ is plotted as a dot-dashed black line in Figure 3.14, and we observe maximum skill scores of $E = 0.928$ in the magnetofrictional simulations and $E = 0.910$ in the MHD simulations. This good predictive ability is also evidenced by the sharp peak at around 0.6 in the upper and lower right histograms of Figure 3.13.

Predictive abilities for all diagnostics are notably lower in the axisymmetric model than the Cartesian models. The most intuitive explanation for this is that all the diagnostic quantities are calculated as integrals over the whole Sun rather than the region immediately surrounding the rope, and so are influenced more heavily by dynamics away from the rope itself. For this reason we suggest that diagnostic measurements calculated by integrating over smaller domains containing just the active region in question are likely to be better predictors than those integrated over the entire corona. Ratios with the axial rope flux as numerator (blue) did not perform well in the Cartesian simulations, but were (by a small degree) the best predictors in the polar simulations with skill scores of up $E = 0.84$.

In the axisymmetric simulations, ratios between reference-based quantities do not in general perform well, although the variations on the eruptivity index (dot-dashed, solid and dotted lines in Figure 3.14) do become better at short timescales,

with skill scores up to $E = 0.758$ for the ratio $|H_J/\widetilde{H_R}|$. Even so, this value is not high enough that it could be reliably used to predict eruptions. This relatively poor performance is likely due not to the different coordinate systems but to the size of the integration domain relative to the rope, and the fact that in this case the current-carrying helicity is capturing irrelevant dynamics from elsewhere in the system. This exemplifies the need for great care when integrating over different domain sizes (or indeed the corona) and making predictions based on conclusions such as these. The best approach when regarding data for the entire corona is most probably to integrate over a smaller domain, just surrounding the region of interest. It may also be possible to alter the definitions of the reference-based quanitities to only include the rope itself, by using the field-line helicity ([92]).

3.4.1 Consistency Between MHD and Magnetofriction

We have shown that certain ratios can perform well as predictors of eruptivity in both magnetofriction and MHD individually, but have not yet considered the ratio values themselves at which an eruption is likely to occur. The domain size, initial conditions and flux rope behaviour are directly comparable between our Cartesian MHD and Cartesian magnetofriction models, and so we should ideally expect similar peak values for the eruptive histograms in either case.

Table 3.1 lists the performance of all diagnostic ratios with skill score greater than 0.8 in either of the Cartesian models, using a time cutoff of 10 days. The peak eruptive value (in the first two columns) is the diagnostic value for which an eruption is most likely. Ideally this value would be similar for both the magnetofrictional and MHD simulations. This is true for most of the ratios, especially for those between two reference-based quantities (such as the eruptivity index). The only ratios with large discrepancies (greater than 20%) are those with the free energy (E_F or $\widetilde{E_F}$) as denominator.

The fact that these discrepancies exist are an indication that the pre-eruption magnetic fields are not identical in the two models, which is perhaps to be expected. However, the fact that most of the ratios have similar peak eruptive values indicates that magnetofriction could indeed be used as a predictive method for flux rope

	Peak Eruptive Value			Skill Score E	
Diagnostic Ratio	MF	MHD	Percentage Difference	MF	MHD
$\lvert\Phi_p^2/\widetilde{H_R}\rvert$	0.079	0.065	22.85%	**0.900**	**0.893**
$\lvert\Phi_p^2/\widetilde{E_F}\rvert$	0.058	0.040	45.32%	**0.873**	**0.917**
$\lvert\Phi_p^2/H_R\rvert$	0.025	0.025	**0.589**%	**0.876**	**0.905**
$\lvert\Phi_p^2/E_F\rvert$	0.039	0.036	**9.168**%	**0.873**	**0.915**
$\lvert\Phi_a^2/\widetilde{H_R}\rvert$	0.162	0.143	13.06%	0.825	0.830
$\lvert\Phi_a^2/H_R\rvert$	0.048	0.058	18.59%	0.800	0.803
$\lvert I_a^2/\widetilde{H_R}\rvert$	13.95	14.46	**3.634**%	**0.968**	**0.892**
$\lvert I_a^2/\widetilde{E_F}\rvert$	10.06	14.26	41.79%	**0.940**	**0.900**
$\lvert I_a^2/H_R\rvert$	5.562	6.442	15.80%	**0.949**	**0.893**
$\lvert I_a^2/E_F\rvert$	8.589	12.64	47.22%	**0.952**	**0.897**
$\lvert\widetilde{H_J}/\widetilde{H_R}\rvert$	0.261	0.278	**6.266**%	0.746	0.810
$\lvert\widetilde{H_R}/\widetilde{E_F}\rvert$	0.673	0.714	**5.975**%	**0.910**	0.808
$\lvert\widetilde{H_R}/E_F\rvert$	0.581	0.644	10.82%	0.758	0.817
$\lvert H_J/\widetilde{H_R}\rvert$	0.617	0.585	**5.414**%	**0.928**	**0.908**
$\lvert H_J/H_R\rvert$	0.224	0.240	**7.258**%	0.804	0.839
$\lvert H_R/\widetilde{E_F}\rvert$	1.825	1.696	**7.586**%	0.834	0.844
$\lvert H_R/E_F\rvert$	1.723	1.535	12.29%	**0.885**	**0.856**

Table 3.1: Table comparing the peak eruptive value and skill scores at time cutoff $t = 10$ days for a variety of diagnostic ratios, using data from the Cartesian magnetofrictional and MHD simulations. All ratios with skill scores greater than 0.8 in either simulation set are included. Ratios that perform well in a certain aspect are in bold font.

eruptions of this nature, providing that relying upon certain quantities (such as the free energy) is avoided.

Although all of the ratios in Table 3.1 with the axial current as numerator had relatively high skill scores in both the magnetofrictional and MHD simulations, only $|I_a^2/\widetilde{H_R}|$ has very similar peak eruptive values in both cases – at around 14 units. This ratio also has the highest skill score in the magnetofrictional simulations. The equivalent ratio for poloidal flux, but using the other relative helicity definition $|\Phi_p^2/H_R|$ also performs well in both models, with values around 0.025 units indicating an eruption is very likely.

The ratios between reference-based quantities (black in Figure 3.14) are in general more consistent between magnetofriction and MHD. This is encouraging, but the skill scores for these ratios are not particularly high compared to those calculated using the rope current or flux. The notable exception to this is the ratio

$|H_J/\widetilde{H_R}|$, which has an excellent skill score in both the MHD and magnetofrictional simulations, and peaks at around 0.6 in both cases.

If the instabilities causing the eruptions were fundamentally different in magnetofriction and MHD, we would not expect to see any particular similarities between the peak eruptive values, and yet the majority of the ratios in the table are have less than 10% difference between the models. This is unlikely to be mere chance, and shows that an unstable magnetic field configuration in full MHD is also likely to be unstable in magnetofriction.

The main consistent difference in the evolution of the magnetic fields (as discussed in Section 3.3.3), is that using magnetofriction the axial rope flux tends to increase monotonically as the rope forms (if arcade eruptions are disregarded), whereas using MHD this flux is more likely to reach a limit and stop increasing long before the rope becomes unstable. Thus at the point of instability, the diagnostic quantities which depend heavily on the axial flux will differ more between the two models.

3.4.2 The Effect of the Orientation of the Background Magnetic Field on the Eruptivity Index

We now propose a straightforward explanation for why [93] observed a sharp peak in the eruptivity index during the formation of flux ropes that later become unstable. We assert that this is due to the direction of the overlying magnetic field, which in those simulations is in the opposite direction in their unstable simulations. In all our simulations the background field has the same orientation, so this is not a consideration and any increase in eruptivity index is due to other processes.

We will consider a simple analytical model, which shows that the eruptivity index will naturally be higher when the background/overlying horizontal field direction is opposite to that of the arcade.

Two magnetic field configurations are presented in Figure 3.15. The left pane shows a configuration similar to the fields we generate naturally by shearing a potential field, where the background magnetic field is orientated in the same direction as the arcade. The right pane has the background field in the opposite direction,

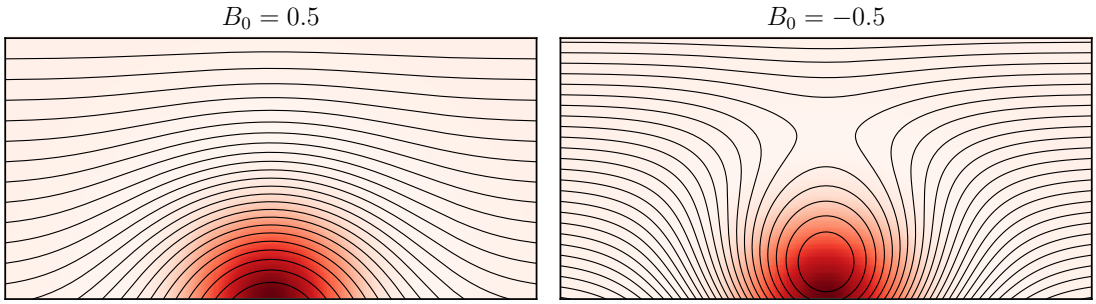

Figure 3.15: Comparison between two magnetic arcades with overlying magnetic fields in opposite directions. The black lines represent the magnetic field projected into the (x, z) plane and the heatmap represents the magnetic field strength out of this plane.

leading to a magnetic null point above the arcade. When flux ropes emerge into the second type of field, they are more likely to erupt. This was shown clearly by [93], who compared simulations with both orientations of the overlying field. We endeavour to show here that the right-hand field configuration fundamentally results in a higher eruptivity index, for a given sheared field component. By contrast, our simulations correspond to the left-hand field configuration, so even though they do erupt, this is not accompanied by sharp increase in the eruptivity index.

The model magnetic field plotted in Figure 3.15 comes from the analytical expression $\mathbf{B} = \widetilde{\mathbf{B}} + B_0\mathbf{e}_x$, where

$$\widetilde{B}_x = 4ye^{-\xi} \tag{3.59}$$

$$\widetilde{B}_y = -4ye^{-\xi} \tag{3.60}$$

$$\widetilde{B}_z = 2(1-\xi)e^{-2\xi}, \tag{3.61}$$

with $\xi = 4(x^2+y^2)$. The sheared, out-of-plane component, B_z, is fixed, and the only parameter is the strength of the background magnetic field, given by the (constant) parameter B_0. The left pane in Figure 3.15 has $B_0 = 0.5$, the right $B_0 = -0.5$. We proceed to observe the dependence of $\widetilde{H_R}$ and $\widetilde{H_J}$ on B_0, as defined in Section 3.3.2, and the resultant effect on the eruptivity index $|\widetilde{H_J}/\widetilde{H_R}|$.

Following Section 3.3.2, in order to calculate the relative helicity we choose a vector potential $\mathbf{A} = \widetilde{\mathbf{A}}(x, y) + B_0 y\mathbf{e}_z$, where $\nabla \times \widetilde{\mathbf{A}} = \widetilde{\mathbf{B}}$ and $\widetilde{\mathbf{A}}$ is independent

of B_0. Since the $B_0\mathbf{e}_x$ component of $\mathbf{B}$ is a potential field, we can similarly choose $\widetilde{\mathbf{A}_P} = \widetilde{\mathbf{A}}_P(x,y) - B_0 y\mathbf{e}_z$. It follows that for these fields, the 'current-carrying' helicity

$$\widetilde{H_J} = \iint (\mathbf{A} - \widetilde{\mathbf{A}_P}) \cdot (\mathbf{B} - \widetilde{\mathbf{B}_P})\, dx\, dy \tag{3.62}$$

has no dependence on the background field B_0, because the B_0 terms from $\mathbf{A}$ and $\widetilde{\mathbf{A}_P}$ will cancel. For the relative helicity, however,

$$\widetilde{H_R} = \iint (\mathbf{A} + \widetilde{\mathbf{A}_P}) \cdot (\mathbf{B} - \widetilde{\mathbf{B}_P})\, dx\, dy, \tag{3.63}$$

so the two terms add together and it will depend on B_0. Thus we can write

$$\widetilde{H_R} = \widetilde{H_0} - B_0 \iint (2y\mathbf{e}_z) \cdot (\mathbf{B} - \widetilde{\mathbf{B}_P})\, \mathrm{d}x\mathrm{d}y, \tag{3.64}$$

where $\widetilde{H_0}$ is the relative helicity with $B_0 = 0$. Since $\widetilde{H_0}$ and $\widetilde{H_J}$ have no dependence on B_0, the eruptivity index can simply be expressed as

$$|\widetilde{H_J}/\widetilde{H_R}| = \left| \frac{\widetilde{H_J}}{\widetilde{H_0} - B_0 \iint (2y\mathbf{e}_z) \cdot (\mathbf{B} - \widetilde{\mathbf{B}_P})\, \mathrm{d}x\mathrm{d}y} \right|. \tag{3.65}$$

For a sheared field with B_z non-zero (and non-uniform), we can clearly see that there will be a particular background field strength B_0 where the eruptivity index will become infinite as the denominator vanishes. For the magnetic field specified in Equations (3.59) to (3.61) the constants take the values

$$\widetilde{H_J} \approx 0.0109 \tag{3.66}$$

$$\widetilde{H_0} \approx -0.0307 \tag{3.67}$$

$$\int_V (2y\mathbf{e}_z) \cdot (\mathbf{B} - \widetilde{\mathbf{B}_P})\, dV \approx -0.2026, \tag{3.68}$$

which results in a peak in the eruptivity index at $B_0 \approx -0.15$, when in particular the overlying magnetic field is oppositely directed to the magnetic field in the upper part of the arcade (as in the right pane of Figure 3.15). By contrast, if the overlying magnetic field has the same direction as that in the arcade ($B_0 > 0$, as in the left

pane of Figure 3.15), then the denominator of (3.65) will not be particularly small and thus the eruptivity index will not be particularly large.

In all of our simulations – where the flux rope is formed by shearing of a pre-existing potential arcade – the background field has the same direction as that of the arcade, whether or not the flux rope erupts. Generalising from the analytical model with $B_0 > 0$, this explains why our eruptions are not preceded by a high eruptivity index. Furthermore, for the relevant case of $B_0 > 0$ in the analytical model, Equation 3.65 shows that smaller B_0 will lead to a larger denominator and hence smaller eruptivity index. Since smaller B_0 indicates weaker overlying field and hence easier eruption, this explains why the eruptivity index is on average smaller in our eruptive simulations than our non-eruptive simulations, as observed in Figure 3.14.

The simulations of [93], which were driven by flux emergence, included cases with both directions of background field. The eruptivity index behaved as predicted by the simple model in this section, but in that case only the cases with oppositely-directed field (and high eruptivity index) erupted. Our work shows that there is a whole class of eruptions that will not necessarily exhibit such a peak in the eruptivity index during the rope formation.

3.5 Discussion

We have used three independent models (Cartesian and polar magnetofriction, and Cartesian MHD) to evaluate the ability of a variety of scalar diagnostic quantities to predict the eruption of magnetic flux ropes. We have determined that ratios of the axial rope current squared divided by the relative helicity or free energy are in general the best predictors, but the only one of these ratios that was consistent between magnetofriction and MHD was $|I_a^2/\widetilde{H_R}|$, with a peak eruptive value of around 14 units.

Ratios of the poloidal flux squared divided by the relative helicity are also good predictors, but again the only ratio consistent between the two models was $|\Phi_p^2/H_R|$, with a peak eruptive value of around 0.025 units. Note that the ratios between the

relative helicity and current-carrying helicity are dimensionless, but the other ratios are not necessarily so and will depend on the chosen length units. At this point in the study, we do not attempt to correlate these thresholds to any meaningful measurable quantity in the real corona.

Ratios with the free energy (defined using either type of reference field) as denominator have peak eruptive values that differ significantly between MHD and magnetofriction. This does not necessarily indicate that these ratios cannot be good predictors, but any errors in the extrapolation of the magnetic field may be more likely to alter the respective predictive thresholds. The relative helicity, also defined in either manner, performs better as a denominator and does not have this problem, with (in general) similar peak eruptive values. There has also been extensive work in the estimation of these helicity values using only the helicity flux through the lower boundary of the domain – where in general the magnetic field can be determined from observations with much more certainty.

It is reasonably likely that there exist alternative ratios similar to those studied here that would also perform very well, where the numerator increases steadily as the rope forms and the denimonator remains roughly constant. In future, when it may be possible to use full 3D simulations in this manner, these alternative ratios can be explored further. In that case, there will be additional difficulties/possibilities in the variation of the definitions of the ratios, such as determining which magnetic field lines are actually in the rope, which will provide considerable additional interest.

The alternative class of ratios (black in Figure 3.14) – those between the relative helicity, current-carrying helicity and free energy – were in general more consistent between magnetofriction and MHD. This is likely due to these quantities being affected less by the out-of-plane component of the magnetic field in the rope, and the definition of the area of the rope itself. However, although there does tend to be a ratio threshold at which all eruptions occur, not all ropes that reach this threshold will erupt. In contrast, when the axial current is the ratio numerator there instead tends to be a specific threshold above which ropes are very likely to erupt.

We have presented two ways to define H_R, H_J and E_F, which each have their merits depending on the coordinate system. Of note, the eruptivity index $|H_J/H_R|$

is not a good predictor of eruptions except when defined as $|H_J/\widetilde{H_R}|$ – where the out-of-plane component of the reference potential field is included in the relative helicity $\widetilde{H_R}$ but not in the current-carrying helicity H_J. Almost all eruptions in either the Cartesian MHD or Cartesian magnetofriction simulations occurred when this index had a value around 0.6 units.

An explanation for the predictive ability of this particular form of the ratio is that the out-of-plane flux in the rope has more of an effect on the 3D helicity definition (H_R) than the 2.5D definition ($\widetilde{H_R}$). When using the 2.5D definition the out-of-plane component of the magnetic field $\mathbf{B}$ is counteracted somewhat by the nonzero component in the potential field $\mathbf{B}_P$. Thus the presence and strength of the rope, with its highly out-of-plane magnetic structure, is best quantified using a numerator with the 3D definition (e.g. H_J). In general the ratios with denominators using the 2.5D definition (e.g. $\widetilde{H_R}$) performed better, perhaps as these diagnostics are less affected by the presence of the rope, instead being better indicators of the state of the background magnetic field.

We note that the actual value of any of these ratios will depend significantly on the size and configuration of the domain (as evidenced by the large difference in these values between the Cartesian and axisymmetric simulations), which is why it was important for the model comparisons that the initial condition and domain setup were identical. It remains to find a method for establishing the eruptive thresholds for an arbitrarily-sized (or shaped) domain. A simple scaling law is most probably not sufficient as the rope itself will in general vary in size relative to the domain volume, so additional corrections would be required. The area of the rope itself is well defined in 2.5D as the region with infinitely-long field lines, but it is hard to quantify in 3D. An approach using the field-line helicity is likely to be helpful in this regard.

Magnetofriction could be a useful tool for predicting the eruptions of ideally unstable 2.5D flux ropes, as we have shown that there exist several diagnostic ratios that have consistent thresholds for eruptivity in both magnetofriction and MHD. However, there are many processes in full MHD such as breakout ([17]) or tether cutting ([76]) that can be responsible for flux rope eruptions, and differ from the

instabilities responsible for the eruptions in our models. It remains to be shown whether similar results to ours can be obtained for these cases. It must be noted that several of our diagnostic ratios did not show consistency between the two models, and so these comparisons must be tested further in 3D before any predictions of eruptivity are made solely using magnetofrictional methods.

We note that the qualitative behaviour of the flux rope system is very similar in either Cartesian or polar coordinates, but the diagnostic values behave very differently when the integration domain extends far beyond the influence of the rope. When calculating integrals of helicity in the real corona it would thus be necessary to integrate over a smaller domain just surrounding the rope itself, although in that case care must be taken to choose the location of the boundary of such a domain. Despite this, even when using the entire corona as the integration domain in this study (in the spherical polar simulations) several diagnostic ratios did exhibit consistent eruptivity thresholds, albeit with lower predictive ability than in the Cartesian simulations.

We have shown that the ratio of axial current squared to relative helicity exhibits a threshold above which eruptions are likely. However, in 3D the rope is less well-defined, and as such the axial current itself would likely be more problematic to measure than the helicity – not least that the area of the rope itself is not clear-cut.

Thus, when using real observed data it is likely that some of the ratios here that did not perform quite as well would in fact be more useful. Due to the possibility of measuring helicity flux through the lower boundary, the eruptivity index $|H_J/\widetilde{H_R}|$, appropriately defined, may well provide the most accurate indication of an imminent flux rope eruption. The challenge in that case will be to modify the definition of the 2.5D helicity to account for the out-of-plane flux in the rope in 3D, which will in general vary along the length of the rope. A mixed approach using relative field-line helicity will likely be necessary.

CHAPTER 4

A New Icosahedral Magnetofrictional Code

Chapter 3 described how simple 2.5D models can be used to seek scalar quantities which could theoretically be used to predict magnetic flux rope behaviour. Removing the third dimension allows us to run far more simulations (as an individual run is far faster) than for a full 3D model, forming the basis for the statistical analysis used to come to our conclusions. However, although reasonably compelling, we do ultimately need to confirm that these results are valid for configurations that are not symmetric in the third dimension.

This could be achieved using existing magnetofrictional (or even MHD) codes (see Section 1.4). These models are far more computationally expensive than our 2.5D versions, but would still hopefully be adequate for a small-scale parameter study of flux rope behaviour. However, as a first step towards future 3D analysis we have instead developed a brand-new magnetofrictional code based an icosahedral grid. This approach has both advantages and disadvantages over existing equivalents using regular spherical coordinates.

In this chapter we first discuss the motivation for choosing this approach. We then describe the implementation of differential operators on such an irregular staggered grid, and the methods for optimising the grid to improve their accuracy by

moving the individual grid points relative to one another (known as 'tweaking'). We then discuss the calculation of potential (PFSS) fields using the multigrid method, building on the theoretical approach described in Section 1.4.2, and compare these to the potential fields plotted for reference in Chapter 2. We then evaluate the options for interpolating the magnetic field and current density – a necessary step for field line tracing and the calculation of the magnetofrictional velocity.

We finish with some initial results using the code. We initially test the code with an imposed solar wind and no dynamic lower boundary conditions, comparing these equilibrium solutions to the outflow fields of Chapter 2. Adding in the lower boundary effects of differential rotation and supergranular diffusion, we then test the differences between simulations with a constant magnetofrictional relaxation rate – made possible with the new code – and those where the relaxation rate decreases near the poles, as is the case in some existing models using regular spherical coordinate grids.

4.1 Motivation for the Icosahedral Grid

When using the magnetofrictional (MF) model, the major limitation on the computing time is the need to satisfy the Courant–Friedrichs–Lewy (CFL) condition on the numerical timestep ([121]). When applied to parabolic PDEs such as the MF model this is essentially a constraint on the timestep, ensuring it is less than the time taken for information to diffuse across one grid cell. For hyperbolic PDEs the limiting timestep is usually related to the time taken for waves to travel across one grid cell. If the CFL condition is not satisfied, numerical instabilities will develop and the solution will generally blow up rapidly.

In the context of the MF equations (see Section 1.4.1), this restriction on the

timestep Δt for a grid resolution Δx can be written as

$$\Delta t \leq C\frac{\Delta x^2}{\nu_0} \tag{4.1}$$

$$\Delta t \leq C\frac{\Delta x^2}{\eta} \tag{4.2}$$

$$\Delta t \leq C\frac{\Delta x}{\max(\mathrm{v_{out}})}, \tag{4.3}$$

where these restrictions correspond to magnetofrictional relaxation, diffusion and the imposed outflow velocity (which is hyperbolic) respectively. The constant C depends on factors such as the precise numerical scheme and the shape of the grid cells, and must be in the range $0 < C < 1$. For a regular Cartesian grid C is often chosen to be around $0.1 - 0.2$, values which also appear to be sufficient for the icosahedral code. For our purposes the first of these conditions, which corresponds to the magnetofrictional relaxation speed, will usually be the most restrictive.

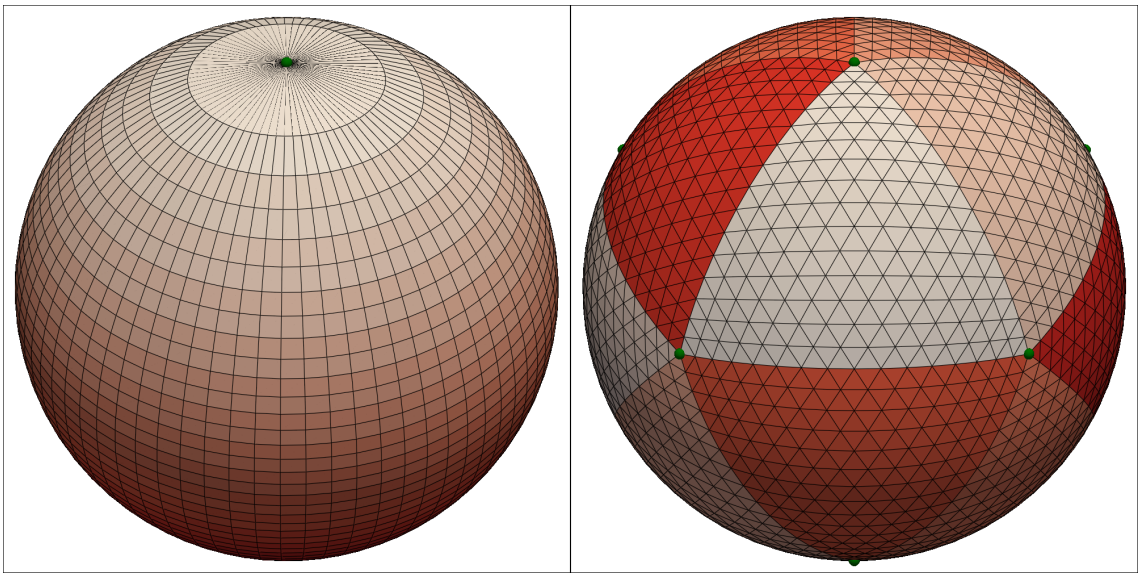

Figure 4.1: Comparison of base points of the spherical polar grid used by an existing magnetofrictional code (eg. [14], left) , which is equally spaced in ϕ and $\cos(\theta)$, and the 'untweaked' icosahedral grid (right) with $G = 4$ recursions. The poles are identified in green, there being two in spherical polar coordinates and twelve on the icosahedron.

We can clearly see that the smaller the grid resolution, the smaller the timestep must be – and it decreases quadratically with the dimensions of the grid cells. The existing code which we shall frequently use as a reference ([14]) uses a spherical polar

coordinate system (the left pane of Figure 4.1) to model the corona. This naturally leads to the grid mesh becoming finer closer to the poles, and a heavier restriction on the timestep than strictly necessary. This can be overcome by introducing a spacial dependence to the MF relaxation rate, such that this rate is slower near the poles, i.e.

$$\nu(\theta) = \nu_0 \sin^2(\theta), \tag{4.4}$$

where θ here is the angular distance from the north pole (eg. [14]). Although this does not affect the accuracy of these simulations too greatly, as the areas of interest are generally close to the equator, it does introduce an undesirable unrealistic factor – it would be preferable to have a constant relaxation rate throughout the domain, or to have it vary spatially based on physical motivations instead.

The optimum scenario is thus to use a grid which covers the spherical geometry of the corona with grid cells which have both similar area/volume and shape over the entire domain. The icosahedral grid that we describe in this chapter achieves this by covering the sphere in triangles. These triangles are extended into 3D simply by connecting concentric spheres – so each 3D grid cell is in fact a stretched trapezium. The grid is constructed by recursively subdividing the faces of an icosahedron (a platonic solid with 12 vertices and 20 triangular faces) and then 'inflating' each point so that it lies on the unit sphere. The right pane of Figure 4.1 shows such a grid after $G = 4$ recursions. Each of the original icosahedron faces is coloured differently, and is composed of $(2^4)^2 = 256$ small triangular grid cells.

This approach is not particularly novel. The advantages of an icosahedral grid over standard spherical coordinates apply to a variety of other fields, and such grids are commonly used for large scale fluid simulations such as modelling the weather in the Earth's atmosphere. In this field the use of non-regular grids in fact dates back to the late 1960s and was first proposed by [122] and [123], and a significant proportion of global models used by national weather services now use this approach (eg. [124], [125]).

These grids have also been used to model magnetic fields. Significantly, [126] provided a detailed framework for modelling full MHD processes in the context of astrophysical plasma flows. This approach was expanded upon by [127], although

it appears that to date there has been little research using such large-scale MHD models, with most still employing a standard spherical coordinate system. Despite their advantages, by their very nature such grids will be more difficult to implement in most scenarios and this is likely the limiting factor in the rate of their adoption. Alternative grids to the icosahedral/triangular approach also exist, such as the cubed-sphere model (also proposed by [122]), the Ying-Yang grid ([128]), in which the sphere is wrapped in two distorted rectangular sections similarly to a tennis ball (with some areas covered twice) and the icosahedral/hexagonal model ([129]), wherein the raw grid cells are hexagons and pentagons rather than triangles. The former has particular advantages with regard to the numbering of grid cells, but the lack of a staggered grid makes magnetic flux conservation more difficult. The latter is essentially equivalent to our approach, as we shall see in Section 4.2.2.

It appears that ours is the first attempt to use the magnetofrictional model on a non-regular grid to model the solar corona. With current computational limitations this could arguably be more useful than MHD equivalents, which are still prohibitively slow when modelling the entire corona.

4.2 Grid Setup and Differential Operators

4.2.1 Grid Geometry

The basic procedure for generating the icosahedral grid is shown in Figure 4.2. The base icosahedron, with 20 triangular faces and 12 poles, is shown in the top left pane. To increase the grid resolution each of these triangular faces is equally divided into four smaller triangles. The vertices of these triangles are then inflated to lie on the unit sphere. This process then repeats iteratively, quadrupling the number of triangles with each subdivision. We assign each stage resolution a number G, where $G = 0$ is the base icosahedron, $G = 1$ is one subdivision, and so forth.

This produces the 'raw grid', as it will henceforth be known. The 'raw grid cells' are the triangles, and the 'grid points' are the vertices of these triangles. The total number of grid cells is $20\times(2^G)^2$, and the total number of grid points is $2+10\times4^G$. To achieve a resolution similar to existing magnetofrictional codes (around one degree

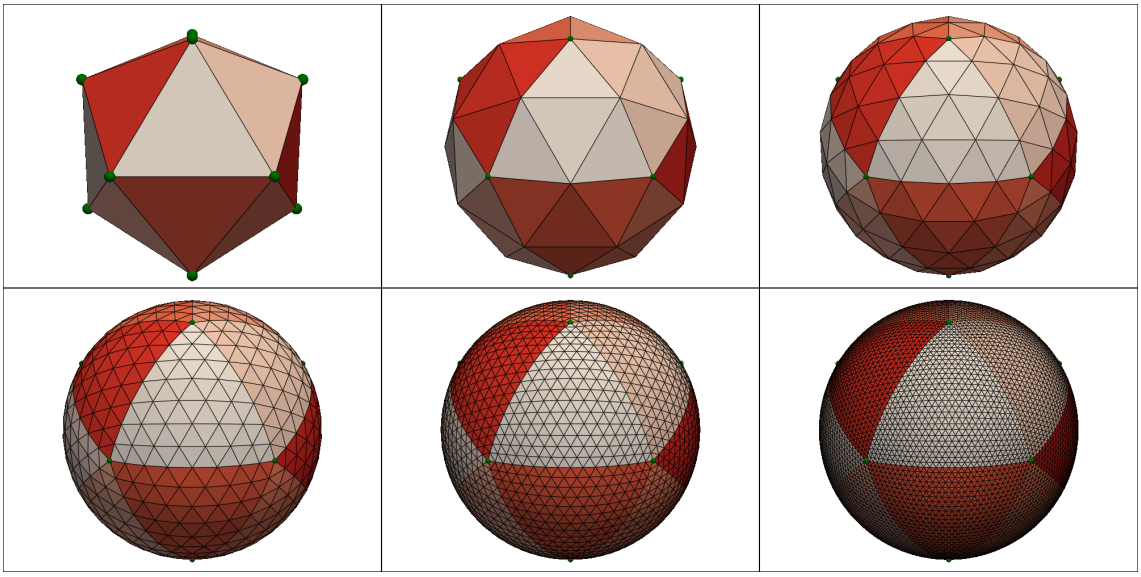

Figure 4.2: An illustration of the recursive segmentation of the grid, ranging from the original icosahedron (top left, corresponding to $G = 0$), to grid scale $G = 5$ (bottom right). At this resolution there are a total of 20480 grid cells on the surface. The original 12 poles of the icosahedron are identified in green.

in latitude and longitude) requires $G = 6$ subdivisions, corresponding to 81290 cells on the surface. This particular approach appears to be the most common in existing literature, although it must be noted that directly projecting an already-subdivided flat grid (such as in Figure 4.3) onto the sphere results in an alternative that in fact performs rather better than the recursive approach (although not as good as a 'tweaked grid', discussed in the Section 4.3).

We also require the construction of a 'dual grid', to allow for the calculation of differential operators. This follows from the raw grid by regarding the centre of each raw grid cell (the 'grid centres') as the vertices of the 'dual grid cells', which are all hexagons apart from the 12 that lie directly on the original icosahedron poles, which are pentagons. We choose the centre of each triangle to be the circumcentre, defined as

$$\mathbf{c} = \frac{(\mathbf{p}_1 - \mathbf{p}_0) \times (\mathbf{p}_2 - \mathbf{p}_0)}{|(\mathbf{p}_1 - \mathbf{p}_0) \times (\mathbf{p}_2 - \mathbf{p}_0)|}, \tag{4.5}$$

where $\mathbf{p}_i$ are the vertices of the triangle. The normal vector through the circumcentre is perpendicular to the three sides of the triangle. Figure 4.3 illustrates the raw and dual grids for one of the 20 base 'segments' (flattened into two dimensions for illustrative purposes), at grid scale $G = 2$.

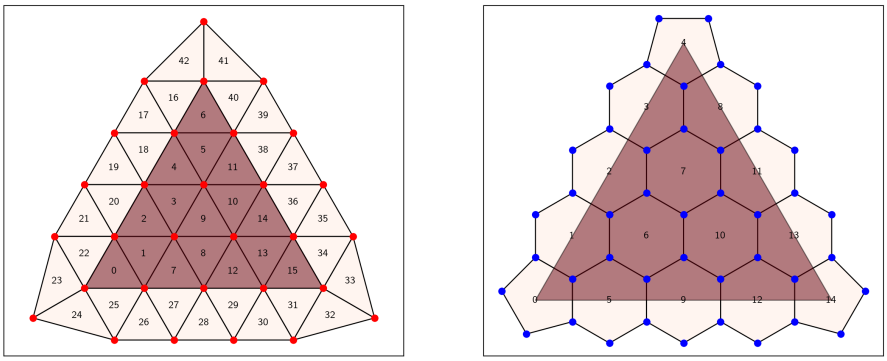

Figure 4.3: Diagram of the raw (left) and dual (right) grids for a single icosahedral segment. This is grid resolution level $G = 2$, corresponding to $n = 2^G = 4$ cells on each side of the face, with $n^2 = 16$ triangular grid cells (excluding the ghost cells) and $\frac{1}{2}(n+1)(n+2) = 15$ grid points – which are the centres of the hexagons/pentagons on the dual grid. The cells that lie outside the boundaries of the segment (in red) are ghost cells.

The grid cells which lie within the base triangle are numbered in a pattern that should be clear from Figure 4.3. We also require ghost cells, to allow the exchange of information from neighbouring segments. These are numbered anticlockwise around the edge of the segment. The grid points (and hence dual grid cells) are numbered in a similar manner, although the dual grid ghost cells are not shown in the figure. By redefining the raw grid as the dual grid and vice versa we recover the alternative icosahedral/hexagonal model. Numerically the two approaches are identical, although deciding that the raw grid is the triangular cells (as we do) makes the implementation of differential operators a little easier.

The grid is extended into 3D relatively simply. In the radial direction the raw grid is equally spaced in $\rho = \ln r$, where r is the radius. The lower boundary of the domain (the solar surface) is set to be $r = 1$. This is in line with existing magnetofrictional codes and serves to increase the resolution lower in the corona, which is generally of more interest. Thus the raw grid cells in 3D are stretched trapezia, slightly larger at the top than the bottom. The dual grid is extended in a similar manner, although radially the cell boundaries lie halfway between those of the raw grid.

4.2.2 Differential Operators

The code uses the 'staggered' approach as detailed in Section 1.4.1, suitably modified to work on the new grid. As for the other geometries, it is essential that we maintain the solenoidal condition $\nabla \cdot \mathbf{B} = 0$ to machine precision. Numerically, this corresponds to the net magnetic flux through the surfaces of every raw grid cell being precisely zero.

We now introduce some notation. The grid cells are numbered by the index k in the plane ('horizontally'), and j in the radial direction. Each side of a cell is identified by the index i, where $i = 0, 1, 2$ for the triangles on the raw grid and $i = 0, 1, 2, 3, 4, 5$ for the hexagons on the dual grid. Extreme care is taken in the code as to the consistency of the numbering of each side. The pentagons at the segment corners will henceforth be ignored – the procedure for them is identical to the hexagons apart from summing over 5 sides instead of 6. The length of raw grid cell sides (at $r = 1$) are denoted by $l_{k,i}$ and the length of dual grid sides as d_{k^*,i^*}. The numbering systems of the raw and dual grids are necessarily different, hence the indices relating to the dual grid have asterisks.

The areas of each raw grid cell at $r = 1$ can be calculated by the formula ([130])

$$R^H_{k,0} = 2 \arctan \left(\frac{|\mathbf{p}_0 \cdot (\mathbf{p}_1 \times \mathbf{p}_2)|}{1 + \mathbf{p}_0 \cdot \mathbf{p}_1 + \mathbf{p}_0 \cdot \mathbf{p}_2 + \mathbf{p}_1 \cdot \mathbf{p}_2} \right), \tag{4.6}$$

where $\mathbf{p}_i$ are again the vectors corresponding to the vertices of cell k. The superscript H indicates this is a 'horizontal' area (in the plane of the spherical surface). Extending into 3D these areas are

$$R^H_{k,j} = r_j^2 R^H_{k,0}. \tag{4.7}$$

The areas of the 'vertical' surfaces on the side of each trapezoidal grid cell are

$$R^V_{k,j+1/2,i} = \frac{1}{2}(r^2_{j+1} - r^2_j) l_{k,i}, \tag{4.8}$$

and the volume of the cell is

$$V_{k,j+1/2} = \frac{1}{3}(r_{j+1}^3 - r_j^3)R_{k,0}^H. \tag{4.9}$$

Similar expressions can be calculated for the dual grid cells, accounting for the offset in the radial direction due to the staggering.

The Solenoidal Condition

The magnetic field $\mathbf{B}$ is stored as magnetic fluxes through each of the grid cell faces, divided by the area of the respective face. The solenoidal condition can then be expressed as

$$\nabla \cdot \mathbf{B}_{k,j+1/2} = \frac{1}{V_{k,j+1/2}} \sum_{i=0,1,2} (R_{k,j+1/2,i}^V B_{k,j+1/2,i}^h) + R_{k,j+1}^H B_{k,j+1}^r - R_{k,j}^H B_{k,j}^r \tag{4.10}$$

$$= 0, \tag{4.11}$$

where the magnetic field strength has radial components B_r and horizontal components B_h.

The Curl Operator

As for the codes used in Chapter 3, we express the magnetic field $\mathbf{B}$ in terms of a vector potential:

$$\mathbf{B} = \nabla \times \mathbf{A}. \tag{4.12}$$

On the raw grid, the $\mathbf{A}$ field is stored as line integrals along the edges of the raw grid cells. The horizonal components are orientated anticlockwise. The magnetic field can then be calculated from the vector potential using Stokes' Theorem:

$$\int_S \mathbf{B} \cdot d\mathbf{S} = \oint_C \mathbf{A} \cdot d\mathbf{l}, \tag{4.13}$$

where S is a surface with boundary C. Naming the horizontal and radial components of $\mathbf{A}$ by $A^h_{k,j,i}, A^r_{k,j+1/2,i}$ respectively, this corresponds numerically to

$$B^r_{k,j} = \frac{1}{R^H_{k,j}} \sum_{i=0,1,2} A^h_{k,j,i} l_{k,i} r_j \tag{4.14}$$

$$B^h_{k,j+1/2,i} = \frac{1}{R^V_{k,j+1/2,i}} (A^h_{k,j,i} l_{k,i} r_j - A^h_{k,j+1,i} l_{k,i} r_{j+1} + (r_{j+1} - r_j)(A^r_{k,j+1/2,i+1} - A^r_{k,j+1/2,i})). \tag{4.15}$$

The electric current field $\mathbf{j} = \nabla \times \mathbf{B}$ is calculated similarly, but on the dual grid. This is possible as the position of fluxes through cell walls on the raw grid is the same as the position of line integrals on the edges of dual grid cells, and vice versa.

We name the dual grid cell face areas as $S^H_{k,j+1/2}$ and $S^V_{k,j,i}$ respectively (noting the position in the radial direction differs to the raw grid). The expression for this curl operator would be difficult to write explicitly as we need to sum the line integrals of the magnetic field around the edge of each hexagon, which are numbered differently to the raw grid cells. Hence to avoid unnecessary detail we just assume the correct k, i on the raw grid are chosen for a given dual grid cell k^* and side i^*:

$$j^r_{k^*,j+1/2,i^*} = \frac{1}{S^H_{k^*,j+1/2}} \sum_{\text{hexagon sides}} B^h_{k,j+1/2,i} d_{k,i} r_j \tag{4.16}$$

$$j^h_{k^*,j,i^*} = \frac{1}{S^V_{k^*,j,i^*}} (B^h_{k,j-1/2,i} d_{k,i} r_j - B^h_{k,j+1/2,i} d_{k,i} r_{j+1} + (r_{j+1/2} - r_{j-1/2})(B^r_{k,j,i+1} - B^r_{k,j,i})). \tag{4.17}$$

The Laplacian Operator

The initial condition we choose to initialise the code with is a PFSS model of the magnetic field (see Section 1.4 for a discussion of this model). This is primarily due to its relative simplicity, and the advantages of generating test cases for the magnetic field that have zero (or numerically very small) current. Such fields should be in equilibrium in the absence of dynamic boundary conditions and as such can be used to check the stability of numerical schemes.

On the interior of the domain, the magnetic field takes the form of a gradient of

a scalar variable φ:

$$\mathbf{B} = \nabla\varphi. \tag{4.18}$$

Numerically, this corresponds to

$$B^r_{k,j} = \frac{1}{r_{j+1/2} - r_{j-1/2}}(\varphi_{k,j+1/2} - \varphi_{k,j-1/2}) \tag{4.19}$$

$$B^h_{k,j+1/2,i} = \frac{1}{r_{j+1/2} d_{k,i}}(\varphi_{k'_i,j+1/2} - \varphi_{k,j+1/2}), \tag{4.20}$$

where k'_i is the raw cell adjoining side i of cell k, and $d_{k,i}$ (with raw numbering) is the distance between the centres of the two cells at $r = 1$.

We can then substitute these formulae into Equation 4.11 to obtain

$$\begin{aligned}\Delta\varphi_{k,j+1/2} = \frac{1}{V_{k,j+1/2}} \sum_{i=0,1,2} (R^V_{k,j+1/2,i} \frac{1}{r_{j+1/2} d_{k,i}}(\varphi_{k'_i,j+1/2} - \varphi_{k,j+1/2})) \\ + \frac{R^H_{k,j+1}}{V_{k,j+1/2}} \frac{1}{r_{j+3/2} - r_{j+1/2}}(\varphi_{k,j+3/2} - \varphi_{k,j+1/2}) \\ - \frac{R^H_{k,j}}{V_{k,j+1/2}} \frac{1}{r_{j+1/2} - r_{j-1/2}}(\varphi_{k,j+1/2} - \varphi_{k,j-1/2}) = 0,\end{aligned} \tag{4.21}$$

which can be simplified a little by using the expressions for the areas and volume (Equations 4.7, 4.8 and 4.9):

$$\begin{aligned}\Delta\varphi_{k,j+1/2} = \frac{3(r^2_{j+1} - r^2_j)}{2(r^3_{j+1} - r^3_j) R^H_{k,0}} \sum_{i=0,1,2} \left(\frac{1}{r_{j+1/2}} \frac{l_{k,i}}{d_{k,i}} (\varphi_{k'_i,j+1/2} - \varphi_{k,j+1/2}) \right) \\ + \frac{3}{(r^3_{j+1} - r^3_j)} \left(\frac{r^2_{j+1}}{r_{j+3/2} - r_{j+1/2}} (\varphi_{k,j+3/2} - \varphi_{k,j+1/2}) - \right. \\ \left. \frac{r^2_j}{r_{j+1/2} - r_{j-1/2}} (\varphi_{k,j+1/2} - \varphi_{k,j-1/2}) \right) = 0.\end{aligned} \tag{4.22}$$

Finding a suitable PFSS field requires this complicated linear system to be solved. We achieve this using a 'multigrid method', which will be discussed in detail in Section 4.4.

The Laplacian in two dimensions (constrained to the spherical surface) can be found by neglecting variation in the radial direction, setting $r_{j+1/2} = 1$ and taking

the limits $r_j \to r_{j+1/2}, r_{j+1} \to r_{j+1/2}$:

$$\Delta\varphi_k^{(2D)} = \frac{1}{R_{k,0}^H} \sum_{i=0,1,2} \left(\frac{l_{k,i}}{d_{k,i}} (\varphi_{k_i'} - \varphi_k) \right). \tag{4.23}$$

4.3 Optimising the Grid

On a Cartesian grid, differential operators constructed in this manner will be in general second-order accurate, as they equate to a central differences scheme. It can also be shown that this is true on a grid composed of equilateral triangles on a flat surface (as in Figure 4.3), but when the grid is projected onto the spherical surface this ceases to be the case as the cells are no longer precisely equilateral.

To improve the accuracy, the grid can be 'tweaked' – moving the grid points such that the error in the operators is minimised. This process was introduced by [131], [132] in the context of modelling the shallow water equations and atmospheric weather prediction. There are several other approaches to this problem, the most common alternative being the 'spring' model of [133], but these are seemingly more difficult to implement.

The process for tweaking the grid is laid out nicely in [134], although in that paper they seek to minimise the error in the Laplacian when calculated at the grid centres of the dual grid (the hexagons) rather than the centres of the raw grid as we do in Equation 4.22. They propose that the error in the Laplacian can be minimised by reducing the average distance λ between the midpoints of the lines connecting the grid points (triangle vertices) and grid cell centres, as shown in Figure 4.4. This approach follows from the analysis of [132]. The aim is then to alter the position of the grid points such that this error is minimised over the entire surface. The overall 'minimiser' function is chosen to be

$$f_{\text{minimiser}}(\mathbf{x}) = \sum_{k}^{\text{all cells}} \sum_{i}^{\text{all edges}} \left(\frac{\lambda_{k,i}}{d_{k,i}} \right)^4, \tag{4.24}$$

where the exponent increases the influence of particularly problematic cells and makes the minimiser function more convex, which generally will make it easier to find minima. The minimiser function depends on the locations of the grid points

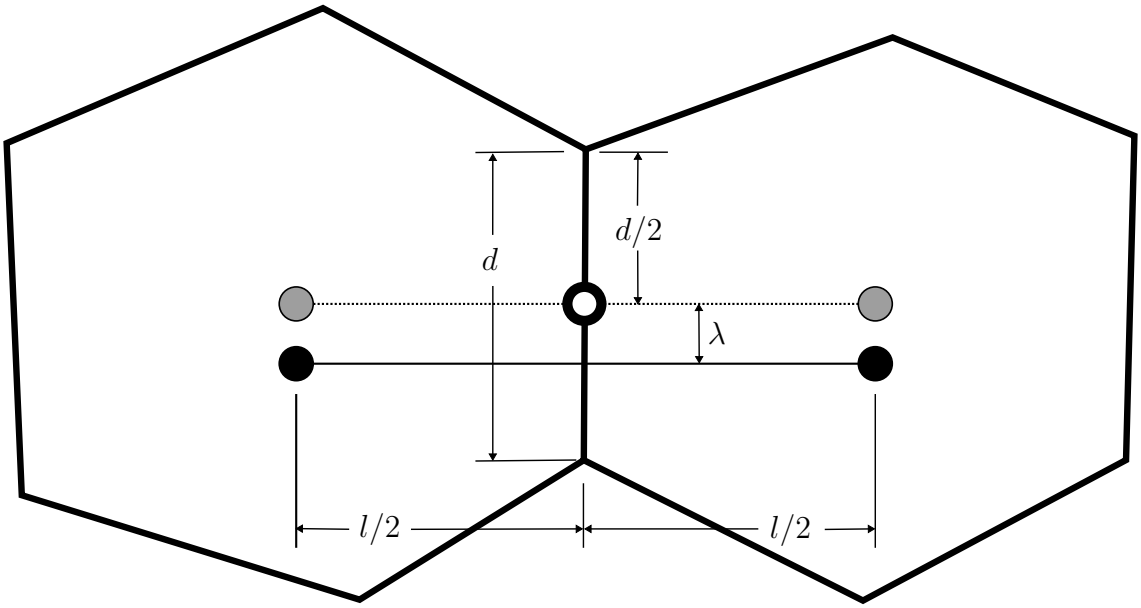

Figure 4.4: Diagram showing the geometry of two dual grid cells, with distance between the raw grid points (triangle sides) l and distance between raw grid centres d. The distance λ is used in the minimiser function used to 'tweak' the grid. The ideal positions for the raw grid points are the grey circles. The use of the circumcentres as the dual grid points means that the line between two raw grid centres will always be bisected by the line between two raw grid points. Reproduced from [134].

(here written as $\mathbf{x}$), and it must be noted that every time a grid point moves the centres of the six cells surrounding it must also move, which will influence the overall minimiser.

The function $f_{\text{minimiser}}(\mathbf{x})$ is minimised using the 'Bounded Limited-memory Royden – Fletcher – Goldfarb – Shanno' method (or 'L-BFGS-B' method) [135], a quasi-newtonian minimisation method. In our code the method is implemented using the built-in solver `scipy.optimize`. This simplifies matters, but difficulty here lies with the calculation of the gradient function required for such a method within a reasonable timeframe.

Theoretically, each grid point on the surface could have two degrees of freedom, leading to a vector $\mathbf{x}$ of dimension $2 + 10 \times 4^G$. For high G this is clearly enormous. However, we note that the solution must be symmetrical both between each of the 20 segments (such that the 12 base icosahedron vertices remain stationary). We also have a six-fold symmetry within each segment, reducing the overall degrees of freedom to an upper bound of roughly $\frac{1}{24} \times 4^G$. Additional constrains, such as the

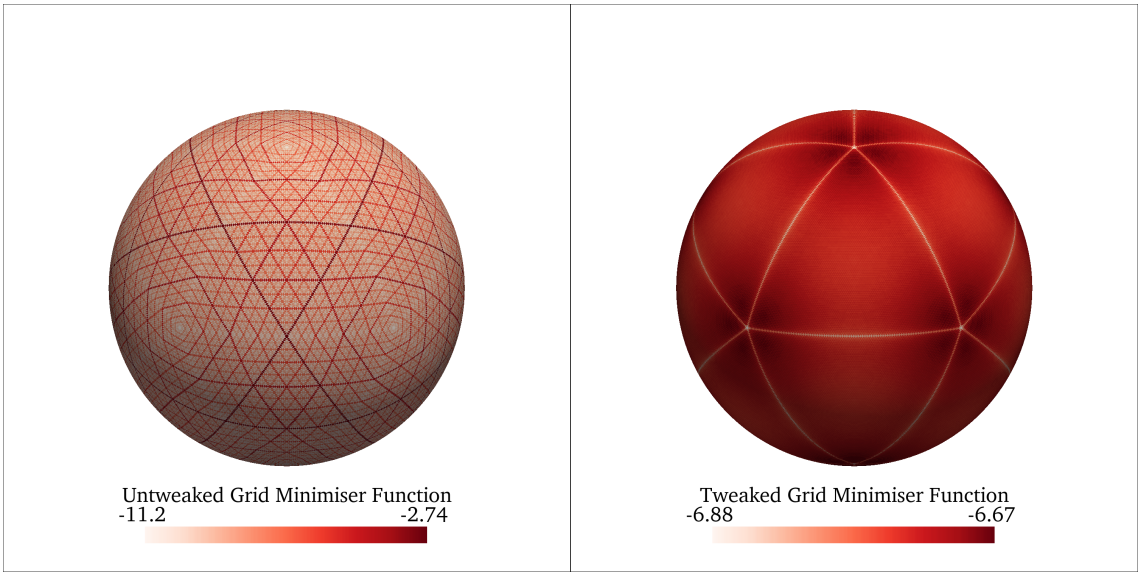

Figure 4.5: Comparison of the minimiser function on the untweaked (left) and tweaked(right) grids at grid scale $G = 7$. The colormap corresponds to the function $\log|\sum_{i=0,1,2} \lambda_{k,i}/d_{k,i}|$ for each of the raw grid cells. A logarithmic scale is used for illustration here as the minimisation function on the untweaked grid varies over several orders of magnitude, and it reveals a nice pattern.

fact that points lying on segment boundaries must stay there, mean that the actual number is slightly less than this, depending on the resolution. Once the tweaked point positions have been obtained for this small region, the points on the rest of the global surface can be obtained through reflections and rotations.

The gradient vector $\nabla f_{\text{minimiser}}(\mathbf{x})$ is calculated by central differences, moving each point in turn in two linearly-independent directions on the surface and noting the effect on the global minimiser. Only the contribution to the minimiser from cells in the immediate vicinity of the moving cell is accounted for, reducing the order of a single gradient evaluation from $O(2^{4G})$ to $O(2^{2G})$. Extra care must be taken around the edges of the segment as the location of ghost points will also be affected.

The order of the L-BFGS-B method is itself $O(2^{4G})$, so this is by no means a fast process for high resolutions, but the tweaked grid theoretically only needs to be computed once. We find that a significant improvement to the convergence time can be obtained by subdividing an already-tweaked grid rather than starting with the raw icosahedron. This is the approach that our code uses.

We have computed tweaked grids up to a grid scale of $G = 7$. Beyond this the convergence to an optimal solution becomes very slow and numerically problematic

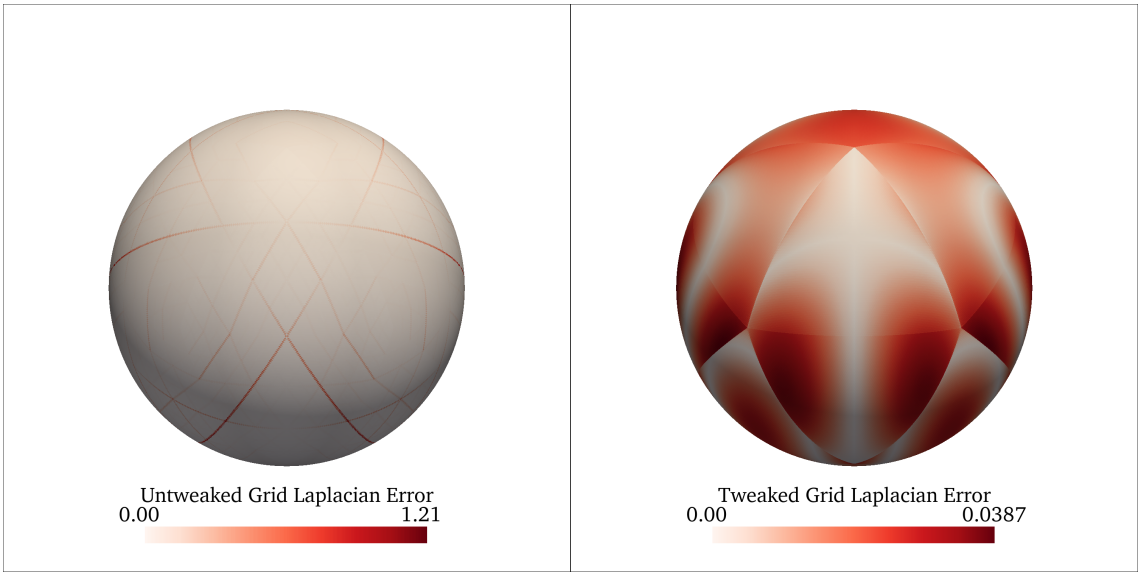

Figure 4.6: Plots of the error in the numerical approximation to the 2D Laplacian for the test function $\varphi(\theta, \phi) = \sin^3(\theta)\cos(3\phi)$, for the untweaked (left) and tweaked (right) grids at resolution $G = 7$, evaluated at grid centres as in Equation 4.23. Note the different scales of the colorbars.

due to the need to calculate distances between points very close together on the surface. For our purposes, such high resolutions will not be required in practice and so this is not an issue. Figure 4.5 shows the effect of the tweaking process on the minimisation function. The plot takes the logarithm of this for illustrative purposes as the function itself varies over several orders of magnitude on the untweaked grid. We observe that after tweaking the error function is much more uniform over the entire surface, and at this resolution its maximum value is a tiny fraction of the untweaked equivalent. Although the error in the Laplacian is not necessarily directly proportional to the error in the other operators, it serves as a reasonable proxy as errors in other operators will also increase with larger values of the distance λ, which we have sought to minimise. The exact weighting of the minimiser function could alternatively be altered to suit a different operator, if desired.

To test the result that such an optimised grid should provide a more accurate approximation to the Laplacian ([132]), we use a test function

$$\varphi(\theta, \phi) = \sin^3(\theta)\cos(3\phi), \tag{4.25}$$

which has Laplacian

$$\Delta\varphi(\theta,\phi) = \cos(3\phi)[9\sin(\theta)\cos^2(\theta) - 3\sin^3(\theta) - 9\sin(\theta)]. \tag{4.26}$$

This is then compared against the numerical result for the 2D Laplacian ($\Delta\phi_{\text{approx}}$), calculated using Equation 4.23. Figure 4.6 compares this error on the untweaked and tweaked grids at grid scale $G = 7$. We observe a marked improvement after tweaking, with the error generally being far lower and more evenly spread out across the surface. In contrast, on the untweaked grid the error is concentrated along certain lines (with a similar pattern to the minimisation function shown in Figure 4.5, and in some places is larger than the magnitude of the test function itself.

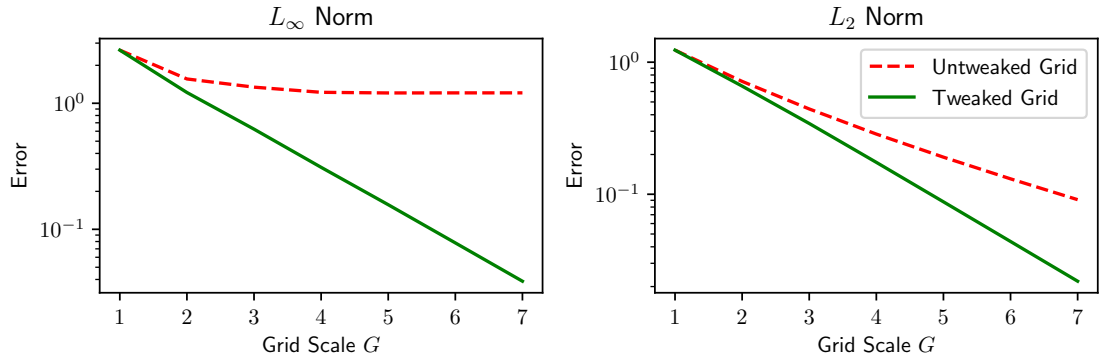

Figure 4.7: Plots illustrating the convergence of the numerical approximation to the Laplacian of the test function $\varphi(\theta,\phi) = \sin^3(\theta)\cos(3\phi)$ as the grid scale G increases. The plots compare the norms of the error $\Delta\varphi - \Delta\varphi_{\text{approx}}$ on the untweaked and tweaked grids.

To quantify this improvement, we take the norms of the absolute error across the entire surface and observe the convergence as the grid resolution increases. We define the L_∞ and L_2 norms as:

$$L_\infty = \max_k |\Delta\varphi - \Delta\varphi_{\text{approx}}| \tag{4.27}$$

$$L_2 = \left(\frac{1}{\sum_k R^H_{k,0}} \sum_k R^H_{k,0} (\Delta\varphi - \Delta\varphi_{\text{approx}})^2 \right)^{1/2}, \tag{4.28}$$

where $\Delta\varphi_{\text{approx}}$ is the numerical approximation to the Laplacian and $R^H_{k,0}$ are the areas of the raw grid cells at $r = 1$.

Figure 4.7 compares the convergence of the two norms with increasing grid scale G. The most notable difference between the untweaked and tweaked grids is that the L_∞ norm does not converge at all on the untweaked grid – even at $G = 7$ we see large absolute errors in the Laplacian. These errors are confined to relatively small areas, however, and as such the L_2 norm does converge on the untweaked grid, although not particularly quickly. Convergence on the tweaked grid using either norm is at least linear.

This result confirms the conclusions of [134], and also shows convergence when the Laplacian is evaluated at raw grid centres in addition to the grid points. This provides justification that our numerical schemes are consistent in combination with the use of the tweaked grid.

4.4 Calculation of Potential Fields - The Multigrid Method

To initialise the magnetofrictional simulations we intend to run on the icosahedral grid, we require a suitable initial condition. We choose this condition to be a potential field, specifically the PFSS model (see Section 1.4.2). Although this model does have its disadvantages, potential fields are relatively simple to calculate and have the advantage that they are stable solutions of the magnetofrictional equations, given the current density $\mathbf{j}$ vanishes everywhere.

We have previously discussed several approaches to numerically calculating PFSS fields. On a regular grid, such as those used in Chapters 2 and 3, it is possible to construct a solution from a series of Fourier (or Legendre in the spherical case) modes. In combination with a Fast Fourier Transform algorithm, this approach is unmatched for speed.

However, on an irregular grid such as ours such a mode decomposition is not possible. Instead, we use a 'multigrid method'. The multigrid process was first conceptualised in the 1970s by [136] and later formalised by [137] and [138]. The principle is relatively simple: basic relaxation techniques such as Gauss-Seidel (GS) or successive-over-relaxation (SOR, see Section 1.4.2) will converge to the true so-

lution in a number of steps related to the number of grid cells. Multigrid methods apply the same approach as those methods, but on multiple scales. The grid is first reduced in resolution down to a certain coarseness at which a solution can be found quickly. It is then interpolated onto a finer-scale grid. At this point the solution is already reasonably accurate, except for detail only visible at fine scales. This error can then be smoothed out using SOR or equivalent, which can deal with fine detail relatively quickly. The process then repeats on finer and finer grids until the desired resolution is attained.

The construction of our icosahedral mesh lends itself to this approach quite naturally, as with each successive subdivision of the mesh (as in Figure 4.2) the number of grid cells doubles in each dimension. For simplicity of calculation we choose the number of grid cells in the radial direction to be the same as the number of cells along the side of each of the 20 segments: 2^G. This also has the nice property that with an upper boundary of $r = 2.5$ each grid cell has sides of roughly equal length both radially and otherwise.

The system we need to solve to obtain a PFSS field is simply the 3D Laplacian, which numerically on our mesh is Equation 4.21. We require two boundary conditions, both on the radial magnetic field strength on the lower boundary $r = 1$ and the upper boundary $r = 2.5$. The upper boundary condition is that the magnetic field lines are radial. Numerically this condition corresponds to the horizontal magnetic flux averaged to the upper boundary being zero:

$$\begin{aligned}\frac{1}{2}(B^h_{k,nr-1/2,i} + B^h_{k,nr+1/2,i}) = \\ = \frac{1}{r_{nr-1/2}d_{k,i}}(\varphi_{k'_i,nr-1/2} - \varphi_{k,nr-1/2}) + \frac{1}{r_{nr+1/2}d_{k,i}}(\varphi_{k'_i,nr+1/2} - \varphi_{k,nr+1/2}) = 0,\end{aligned} \tag{4.29}$$

which can be satisfied by setting

$$\varphi_{k,nr+1/2} = -\frac{r_{nr+1/2}}{r_{nr-1/2}}\varphi_{k,nr-1/2} \tag{4.30}$$

for all cells k. The lower boundary condition prescribes the radial magnetic field

strength, which can be obtained from measurements of the solar surface for simulations, or as an analytic test function. Denoting this boundary field as $\widetilde{B_k^r}$ the condition is then

$$\widetilde{B_k^r} = \frac{1}{r_{1/2} - r_{-1/2}}(\varphi_{k,1/2} - \varphi_{k,-1/2}) \tag{4.31}$$

$$\varphi_{k,-1/2} = \varphi_{k,1/2} - \widetilde{B_k^r}(r_{1/2} - r_{-1/2}). \tag{4.32}$$

These boundary conditions, along with Equation 4.21, can be interpreted as a linear system

$$\Delta\varphi = A\varphi - \mathbf{b} = 0, \tag{4.33}$$

where $\mathbf{b}$ is a vector with the same dimensions as φ, and A is a matrix such that this matrix multiplication is equivalent to taking the Laplacian with zero lower boundary condition. The vector $\mathbf{b}$ is obtained by taking the Laplacian of the zero vector, as described in Section 1.4.2.

Once expressed as such, we can treat this as a generic (but very large!) linear system and apply the multigrid method. The code we have developed uses repeated 'V-cycles', whereby the grid scale is repeatedly coarsened and refined. At the end of each V-cycle the system then solves for the remaining error. The code converges (to a given L_2 norm of the Laplacian) in time of order $O(n^3)$, where $n = 2^G$. One cannot hope for any better than this as a single iteration of SOR is also $O(n^3)$. The use of more complex algorithms (such as 'F-cycles') did not appear to provide any significant improvement to the convergence rate.

The process behind a single V-cycle is illustrated in Figure 4.8. To explain this in detail we discuss the simplest V-cycle, merely using grid scales $G = 1$ and $G = 2$. The system we wish to solve is

$$A\mathbf{x}^{G=2} = \mathbf{b}^{G=2}, \tag{4.34}$$

where $\mathbf{b}^{G=2}$ is known and $\mathbf{x}^{G=2}$ is to be determined. The matrix A is calculated analytically from the grid operators at the appropriate resolution.

Roughly, the process is as follows:

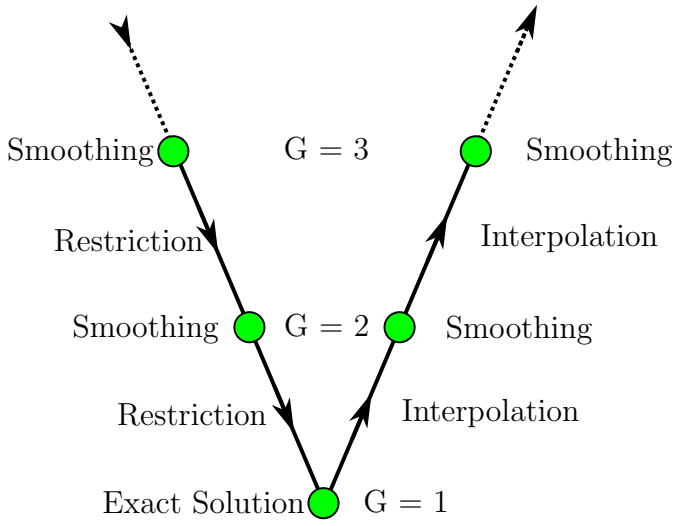

Figure 4.8: Illustration of a multigrid V-cycle up to grid scale $G = 3$. At each grid resolution G the solution φ is 'smoothed', using a few iterations of SOR. The grid is then restricted to a coarser resolution. The process repeats until the grid is coarse enough that an exact solution can be found. This is $G = 1$ on our grids, with reducing to $G = 0$ providing no particular benefit. The process then moves back up the cycle, interpolating the lower-resolution solutions and smoothing further until the original resolution is attained.

- The first step is to use an initial guess for the vector $\mathbf{x}^{G=2}$. The zero vector is as good as any without prior knowledge and so this is what the code uses.

- We then apply several iterations of SOR to this vector, which reduces some high-frequency errors – this is known as 'smoothing'. The number of iterations used here does affect the convergence rate. In general around ten iterations at low resolutions reducing to one or two at higher resolutions appears to be optimal. Let this new smoothed vector be $\mathbf{x}_1^{G=2}$.

- Calculate the residual $\mathbf{r}^{G=2} = \mathbf{b}^{G=2} - A\mathbf{x}_1^{G=2}$.

- Restrict the residual to the coarser grid $G = 1$. Taking a simple average of the 8 cells that make up a single coarser cell is sufficient. This coarsened remainder vector is $\mathbf{r}^{G=1}$.

- On this coarser grid, solve for the system $A\mathbf{e}^{G=1} = \mathbf{r}^{G=1}$. For $G = 1$ this is solved exactly using SOR, but at higher resolutions one applies the entire

V-cycle process again, regarding this new system as if it were the original. The V-cycle function in the code calls itself at this point, leading to 'nested' cycles.

- Interpolate the coarse solution $\mathbf{e}^{G=1}$ back up to the higher grid resolution. Usually linear interpolation is used, but in our code not interpolating at all and merely setting each of the finer cells with the value of their corresponding coarse cell does not impact convergence speed – with the smoothing in the final step seemingly rendering any more complex alternatives unnecessary.

- Combine this with the initial smoothed solution to obtain $\mathbf{x}_2^{G=2} = \mathbf{x}_1^{G=2} + \mathbf{e}^{G=2}$. If no information were lost at the restriction/interpolation stage then we would have obtained the exact solution $\mathbf{x}^{G=2}$ at this point, but naturally this is not generally the case.

- Apply smoothing yet again to this new vector to obtain an even better approximation $A\mathbf{x}_3^{G=2}$.

Successive V-cycles can be joined together to improve this approximation further. Each new cycle solves for the remainder left from the previous one, with the error generally decreasing in a geometric series with successive cycles. The process then repeats until the overall error is below a desired limit.

The multigrid code is currently written in python, as the use of different grid geometries over multiple scales makes writing the code in Fortran prohibitively difficult. Nevertheless, running on a single core on a desktop computer a PFSS field can be calculated in around 10 minutes at scale $G = 5$ or around 90 minutes at scale $G = 6$. While not as fast as methods for calculating PFSS on regular grids, this is adequate for the purposes of using these fields as initial conditions. Unfortunately, the SOR algorithm does not lend itself to parallelisation, although conversion of the code to Fortran would potentially speed up the process by an order of magnitude.

Examples of two PFSS fields on the icosahedral grid are shown in Figure 4.9. Tracing the magnetic field lines for these plots requires use of the interpolation method detailed in the next Section.

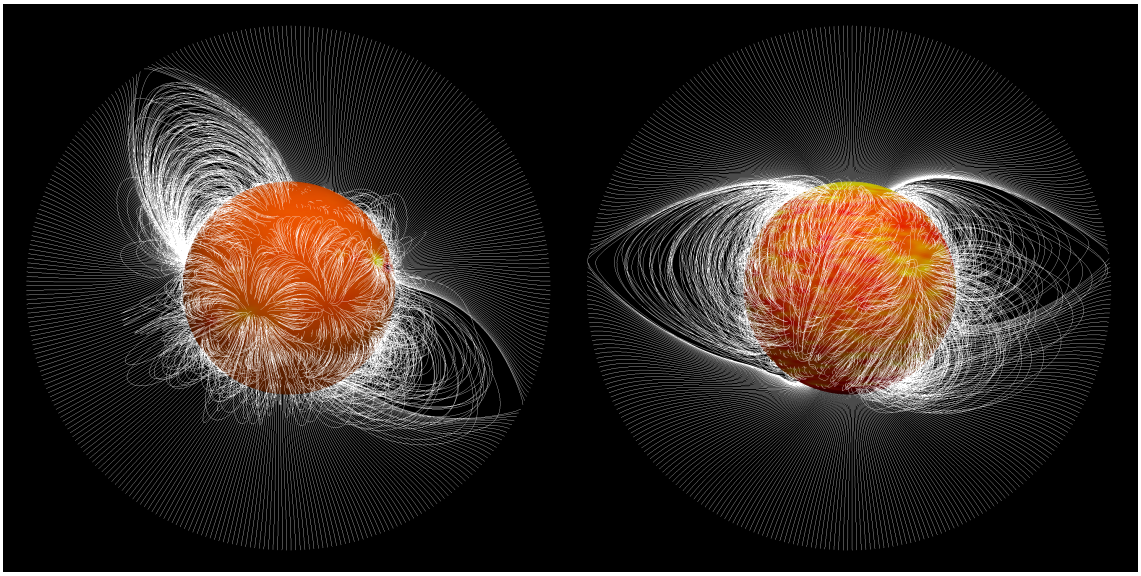

Figure 4.9: PFSS fields on the icosahedral grid at scale $G = 6$. The field left pane uses boundary data from the HMI synoptic map during Carrington rotation 2165, when the sun was relatively active, and the right pane uses data from Carrington rotation 2222 when it was relatively quiet. Magnetic field lines are shown in white, and the heatmap on the surface represents the radial magnetic field on the lower boundary.

4.5 Interpolation of Variable Fields

As described in Section 4.2.2, when using the 'staggered' approach the magnetic field $\mathbf{B}$ is stored on the grid in the same position as magnetic fluxes through each of the raw grid faces. On a regular Cartesian or standard spherical coordinate grid, finding the magnetic field strength and direction at an arbitrary point in space is a simple matter, obtained by suitably interpolating $\mathbf{B}$ in each of the three linearly independent coordinate vectors. On our icosahedral grid the direction of the non-radial field vectors are not linearly independent and as such a more complex approach is necessary. The current density $\mathbf{j}$ has the same problem, being stored in the same position as line integrals along each of the raw grid cell edges.

The magnetofrictional equations require the calculation of the cross product $\mathbf{j} \times \mathbf{B}$. As these two fields are stored in different positions to each other, some interpolation (either to grid faces or grid points) is unavoidable. Moreover, tracing magnetic field lines such as in Figure 4.9 requires the calculation of the magnetic field vector at arbitrary points. There are several ways to achieve this, and we

outline two of them here.

4.5.1 Raviart-Thomas Basis Reconstruction

We first describe the reconstruction of the magnetic field using Raviart-Thomas basis functions ([139]) for a prismatic cell. These basis functions are the simplest vector basis functions, and are commonly used in finite element methods. There are several approaches to constructing these functions. Here we follow that used in the Appendix of [140], modified slightly for our purposes and for clarity.

In the radial direction a standard approach to averaging the field can be used as the grid cells are regularly spaced. Thus we can limit this discussion to the plane of a single triangular grid face in two dimensions. Such a triangle is set up as shown in Figure 4.10. We first focus on the reconstruction of the magnetic field, for which the magnetic flux through each side of the triangle is known.

The triangle is set up as shown, with points given the names $\mathbf{p}_0$, $\mathbf{p}_1$ and $\mathbf{p}_2$. The triangle unit normal vectors are named $\mathbf{n}_a$, $\mathbf{n}_b$ and $\mathbf{n}_c$. The tangent vectors are similarly $\mathbf{t}_a$, $\mathbf{t}_b$ and $\mathbf{t}_c$ and are perpendicular to the normal vectors. These are also normalised. Let the average magnetic flux through each side of the triangle (facing outwards) be denoted B_a, B_b and B_c, and the field we wish to construct be $\widetilde{\mathbf{B}}(x, y, z)$ at an arbitrary point within the triangle.

We redefine this point as,

$$\mathbf{x} = \alpha\mathbf{p}_0 + \beta\mathbf{p}_1 + \gamma\mathbf{p}_2 = (\alpha, \beta, \gamma) \tag{4.35}$$

where the coefficients can be determined by solving an appropriate linear system. Note that if the coefficients satisfy

$$0 \leq \alpha, \beta, \gamma \leq 1 \tag{4.36}$$

then point $\mathbf{x}$ lies within the triangle. If the inequalities are strict the point will be in the interior of the triangle (rather than on one of the edges). To project this point

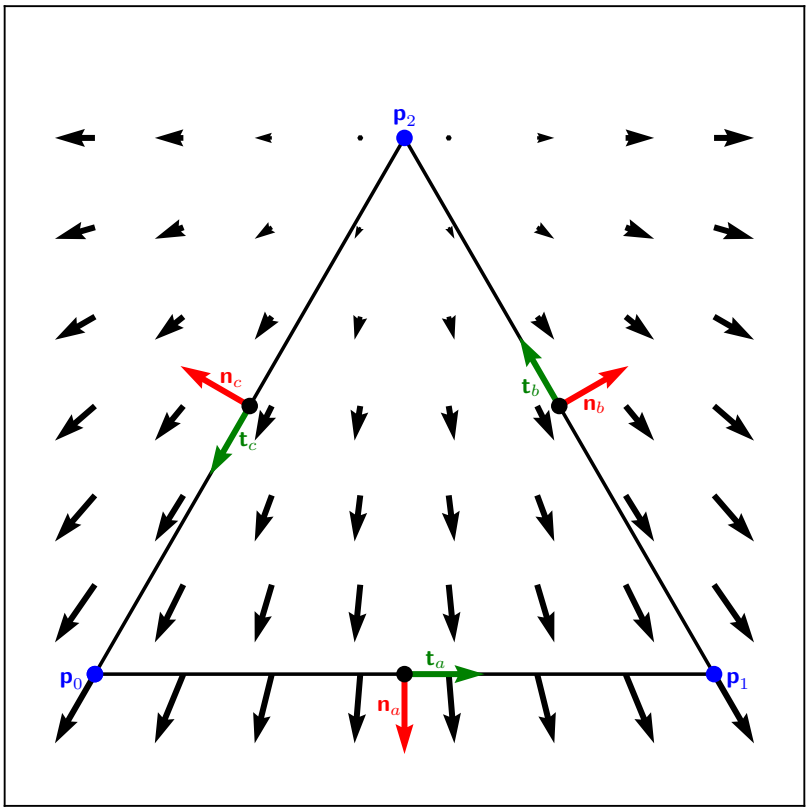

Figure 4.10: Illustration of the example triangular cell referred to in this section, showing the normal and tangent vectors on each side. The black arrows show the direction of the basis function $\widetilde{\mathbf{B}}_a(\alpha, \beta)$, which is always perpendicular to both sides b and c. The other two basis functions are similar but rotated to be perpendicular to the other pairs of sides.

onto the spherical surface it is then necessary to scale the coefficients such that

$$\alpha + \beta + \gamma = 1. \tag{4.37}$$

The problem then becomes two-dimensional as we only need the coefficients α and β. The three triangle points are

$$\mathbf{p}_0 = (1, 0),\ \mathbf{p}_1 = (0, 1),\ \mathbf{p}_2 = (0, 0) \tag{4.38}$$

in the α, β coordinate space.

The reconstructed field must satisfy the following line integrals:

$$\int_{\text{side a}} \tilde{\mathbf{B}}(x,y) \cdot \mathbf{n}_a \, dl = B_a l_a, \tag{4.39}$$

$$\int_{\text{side b}} \tilde{\mathbf{B}}(x,y) \cdot \mathbf{n}_b \, dl = B_b l_b, \tag{4.40}$$

$$\int_{\text{side c}} \tilde{\mathbf{B}}(x,y) \cdot \mathbf{n}_c \, dl = B_c l_c, \tag{4.41}$$

where l_a, l_b, l_c etc. are the respective lengths of the triangle sides.

The basis functions are zero at one of the triangle vertices, and are parallel to two of the sides, so that there is only flux through one of the sides for each basis function. Up to a normalising constant, these basis functions are

$$\widetilde{\mathbf{B}_a}(\alpha,\beta,\gamma) \propto \alpha l_c \mathbf{t}_c - \beta l_b \mathbf{t}_b \tag{4.42}$$

$$\widetilde{\mathbf{B}_b}(\alpha,\beta,\gamma) \propto \beta l_a \mathbf{t}_a - \gamma l_c \mathbf{t}_c \tag{4.43}$$

$$\widetilde{\mathbf{B}_c}(\alpha,\beta,\gamma) \propto \gamma l_b \mathbf{t}_b - \alpha l_a \mathbf{t}_a. \tag{4.44}$$

The interpolated magnetic field is then expressed as

$$\tilde{\mathbf{B}}(\alpha,\beta,\gamma) = k_a \widetilde{\mathbf{B}_a}(\alpha,\beta,\gamma) + k_b \widetilde{\mathbf{B}_b}(\alpha,\beta,\gamma) + k_c \widetilde{\mathbf{B}_c}(\alpha,\beta,\gamma), \tag{4.45}$$

with the constants k determined using the respective flux through each side of the triangle.

Parameterising the first of the line integrals (Equation 4.39) with $\alpha = s, \beta = 1-s$ gives

$$\int_0^1 l_a \tilde{\mathbf{B}}(s,1-s) \cdot \mathbf{n}_a ds = B_a l_a \tag{4.46}$$

$$k_a \int_0^1 \widetilde{\mathbf{B}_a}(s,1-s) \cdot \mathbf{n}_a ds = B_a \tag{4.47}$$

$$k_a \int_0^1 (s l_c \mathbf{t}_c - (1-s) l_b \mathbf{t}_b) \cdot \mathbf{n}_a ds = B_a \tag{4.48}$$

$$k_a(-l_b \mathbf{t}_b \cdot \mathbf{n}_a) = B_a \tag{4.49}$$

$$k_a = -\frac{B_a}{l_b \mathbf{t}_b \cdot \mathbf{n}_a}, \tag{4.50}$$

using that $l_c\mathbf{t}_c + l_b\mathbf{t}_b = -l_a\mathbf{t}_a$ and $\mathbf{t}_a \cdot \mathbf{n}_a = 0$. The other components can be calculated similarly, giving

$$k_b = -\frac{B_b}{l_c\mathbf{t}_c \cdot \mathbf{n}_b}, k_c = -\frac{B_c}{l_a\mathbf{t}_a \cdot \mathbf{n}_c}. \tag{4.51}$$

The overall magnetic field is then given by the sum of the basis functions

$$\widetilde{\mathbf{B}}(\alpha,\beta,\gamma) = -\frac{B_a}{l_b\mathbf{t}_b \cdot \mathbf{n}_a}(\alpha l_c\mathbf{t}_c - \beta l_b\mathbf{t}_b) - \frac{B_b}{l_c\mathbf{t}_c \cdot \mathbf{n}_b}(\beta l_a\mathbf{t}_a - \gamma l_c\mathbf{t}_c) - \frac{B_c}{l_a\mathbf{t}_a \cdot \mathbf{n}_c}(\gamma l_b\mathbf{t}_b - \alpha l_a\mathbf{t}_a), \tag{4.52}$$

or alternatively

$$\widetilde{\mathbf{B}}(\alpha,\beta,\gamma) = \frac{B_a}{l_c\mathbf{t}_c \cdot \mathbf{n}_a}(\alpha l_c\mathbf{t}_c - \beta l_b\mathbf{t}_b) + \frac{B_b}{l_a\mathbf{t}_a \cdot \mathbf{n}_b}(\beta l_a\mathbf{t}_a - \gamma l_c\mathbf{t}_c) + \frac{B_c}{l_b\mathbf{t}_b \cdot \mathbf{n}_c}(\gamma l_b\mathbf{t}_b - \alpha l_a\mathbf{t}_a). \tag{4.53}$$

For the purpose of tracing field lines, the components α, β, γ must be calculated at every step. However, when averaging to the same points repeatedly (such as to the cell centres) this only needs to be performed once, and as such this process is not too computationally expensive.

The process for calculating the current field is similar, and differs only as the current field is stored in the direction of the triangle side tangents rather than the normals. The above derivations are almost identical in this case, albeit with the vector directions swapped around. The complete reconstructed current field can then be expressed as

$$\widetilde{\mathbf{j}}(\alpha,\beta,\gamma) = \frac{j_a}{l_c\mathbf{n}_c \cdot \mathbf{t}_a}(\alpha l_c\mathbf{n}_c - \beta l_b\mathbf{n}_b) + \frac{j_b}{l_a\mathbf{n}_a \cdot \mathbf{t}_b}(\beta l_a\mathbf{n}_a - \gamma l_c\mathbf{n}_c) + \frac{B_c}{l_b\mathbf{n}_b \cdot \mathbf{t}_c}(\gamma l_b\mathbf{n}_b - \alpha l_a\mathbf{n}_a). \tag{4.54}$$

Interpolation of the fields using these basis functions converges linearly with increasing grid resolution in both the L_2 and L_∞ norms. The reconstruction produces a smooth field in the interior of a cell, although there will in general be discontinuities in the reconstructed field when passing from one grid cell to another. To negate

this problem somewhat one could also include the influence of the fluxes through the sides of the neighbouring cells. For instance, when averaging to the midpoint of a triangle side one can merely take the average magnetic field reconstructions from the two cells sharing that side. This seems to do little to reduce the overall error, however.

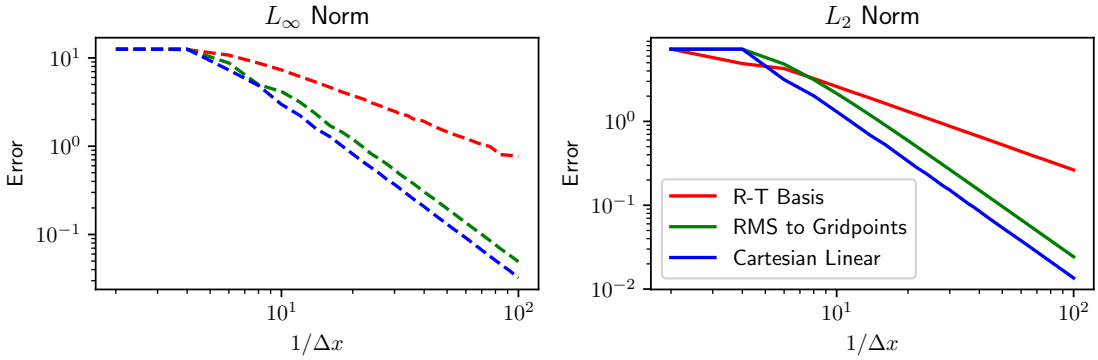

Figure 4.11: Plots to illustrate the accuracy of the magnetic field interpolation methods on an icosahedral grid. The plots compare both the Raviart-Thomas basis method (4.5.1) and the averaging to gridpoints method (4.5.2) to linear interpolation on a Cartesian grid. We plot the root mean square error in interpolating the test magnetic field $\mathbf{B}(x, y) = (2\pi/y_1 \sin(4\pi x)\cos(2\pi y/y_1), -4\pi/\cos(4\pi x)\sin(2\pi y/y_1))$ on a rectangular domain with dimensions $0 < x < 1, 0 < y < y_1 = \sqrt{3}/2$. Δx is the length of the sides of the grid cells.

4.5.2 Averaging to Grid Points

An alternative to the use of the Raviart-Thomas reconstruction is to first average the field strength to the raw grid points (the vertices of the raw cells) with its components in Cartesian coordinates. Once this averaging has taken place over the entire grid, the magnetic field can be interpolated at any arbitrary point by calculating the coefficients α, β, γ as in Equation 4.35 and combining the averaged field from each of three nearest grid points.

Averaging to grid points requires the minimisation of an overdetermined system. Considering the magnetic field (rather than the current density, which follows a similar process), each grid point is roughly equidistant from 12 non-radial magnetic fluxes and 6 radial magnetic field fluxes, one from each of the 6 raw cells surrounding each point and all through planes in differing directions. There are twice as many

non-radial vectors as the grid is staggered in the radial direction and the in-plane magnetic field is stored at the centre of the face of a grid cell.

We wish to find a magnetic field $\widetilde{\mathbf{B}}$ that minimises the error

$$r = \sum_j (\widetilde{\mathbf{B}} \cdot \mathbf{n}_j - B_j)^2, \tag{4.55}$$

for the 18 un-averaged field vectors B_j, each stored on raw faces with normal vector $\mathbf{n}_j$. For a constant field we can interpolate precisely and the error will be zero, but in general this cannot be the case. By re-expressing this as a standard linear system we can calculate precisely the field $\widetilde{\mathbf{B}}$ which minimises r, using the method of ordinary least squares.

Explicitly, if the interpolated magnetic field has Cartesian components $\widetilde{B_i}$ and the j^{th} normal vector has components $n_{j,i}$ then we wish to minimise

$$r = \sum_j \left(\sum_{i=0,1,2} \widetilde{B_i} n_{j,i} - B_j \right)^2. \tag{4.56}$$

The optimal field components $\widetilde{B_i}$ are then the solution to the linear system

$$\sum_{k=0,1,2} \left(\sum_j n_{j,i} n_{j,k} \right) \widetilde{B}_k = \sum_j n_{j,i} B_j, \tag{4.57}$$

which is three-dimensional and is solved in the code using Gauss-Jordan elimination. The components on the left-hand side are intrinsic to the grid and independent of the magnetic field, so these only need to be calculated once, when the code is initialised.

To compare the effectiveness of the two methods (Raviart-Thomas and gridpoint averaging), we regard a test field on a 2D grid. This test grid is chosen to be roughly rectangular overall (within the limitations imposed by covering it in triangular cells) to allow for sensible periodic boundary conditions. The chosen test field is

$$\mathbf{B}(x, y) = (2\pi/y_1 \sin(4\pi x) \cos(2\pi y/y_1), -4\pi/\cos(4\pi x) \sin(2\pi y/y_1)) \tag{4.58}$$

on a domain with dimensions $0 < x < 1, 0 < y < y_1 = \sqrt{3}/2$. The grid cells are

all equilateral triangles with side length Δx. The test field is first converted into fluxes through the cell sides, and then is interpolated using the above approaches and compared to the true value. Figure 4.11 shows our results, which also includes a comparison to linear interpolation on an equivalent staggered Cartesian grid. We observe convergence in both L_2 and L_∞ norms using either interpolation method, although the grid point averaging approach converges at a significantly faster rate than the Raviart-Thomas approach. This convergence rate is comparable to the Cartesian equivalent.

Hence in the magnetofrictional code we average the $\mathbf{B}$ and $\mathbf{j}$ fields to the raw grid points using the gridpoint averaging approach. This allows for the calculation of the product $\mathbf{j} \times \mathbf{B}$. We have shown that this field converges sufficiently quickly to the true solution as the grid resolution increases, and have also shown (in Section 4.3) that the differential operators will also converge to the correct solution at least linearly when using an optimised grid.

4.6 Equilibrium Solutions with Solar Wind Outflow

As a first test of the stability and accuracy of the icosahedral code, we can find equilibrium solutions of the new code with an imposed solar wind velocity. The imposed solar wind ($\mathbf{v}_{\text{out}}$) will increase the open flux (the net unsigned magnetic flux through the upper boundary) compared to the initial PFSS field, and will eventually reach an equilibrium where the magnetofrictional velocity balances the outflow velocity exactly. These equilibrium solutions should be equivalent to the semi-analytic outflow fields described in Chapter 2.

These tests are performed on the tweaked grid at resolution $G = 6$. The magnetofrictional equations are discretised using the differential operators described in Section 4.2.2 and averaged to grid points using the RMS method in Section 4.5.2.

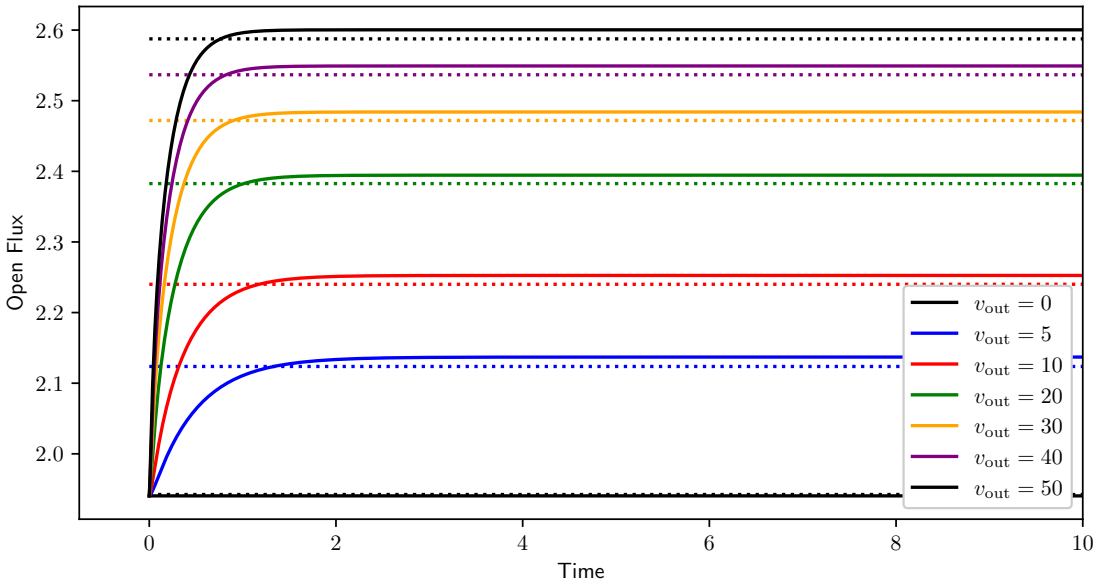

Figure 4.12: Comparison between the open flux predicted by outflow fields (described in Chapter 2) and the relaxation of the new icosahedral code with an imposed solar wind velocity. The outflow field predictions for each v_{out} velocity are shown as dotted lines, and the open flux in the icosahedral grid simulations are shown as solid lines in the same colours.

The magnetofrictional velocity

$$\mathbf{v} = \nu_0 \frac{\mathbf{j} \times \mathbf{B}}{B^2 + B_0^2 \delta e^{\frac{-B^2}{\delta B_0^2}}} \tag{4.59}$$

is also calculated at the raw grid points. The electric field $\mathbf{E}$ is then finally calculated as line integrals at the appropriate places on the staggered grid. The outflow term

$$v_{\text{out}}(r)\mathbf{e}_r \tag{4.60}$$

is not averaged to grid points. Instead the cross product is taken using the magnetic field half a cell below, which is then integrated and added directly to the electric field line integrals. This upwinding is necessary for the stability of the solution when the coronal diffusion rate is low.

The equilibrium icosahedral outflow solutions do depend on the value of the softening parameter δ, with high δ increasing the measured open flux. This is consistent with the behaviour of existing magnetofrictional codes using regular co-

ordinates [141]. For comparison with the reference outflow fields (where essentially $\delta = 0$) we set $\delta = 1 \times 10^{-6}$, below which there is no distinguishable difference in equilbirum open flux. These test simulations are initialised with a PFSS field with the specified lower boundary condition as in the 2.5D axisymmetric simulations in Chapter 3:

$$B_r(1, \theta) = s^7 + 5de^{-10d^2} \tag{4.61}$$

where $s = \cos(\theta)$ and $d = s - \cos(0.35\pi)$ (such a field is plotted in the right pane of Figure 3.1).

Figure 4.12 shows the results, for $\nu_0 = 1$ and varying outflow speeds (in code units). Some coronal diffusion is necessary for the stability of the code (discussed in Section 4.7), which is set as $\eta = 5 \times 10^{-3}$ for these tests. We note that the potential field case, with zero outflow and shown in black, agrees almost perfectly calculated either using the spectral decomposition of Chapter 3 or the multigrid method on the new grid described in Section 4.4. With nonzero outflow, as the simulations relax the open flux increases, at first rapidly and then levelling out to a constant value as expected. We see that the open flux reached by the test code is slightly higher than the outflow field 'ground truth' in all cases, although the difference in open flux increase from the base potential field case is less than 10% in all cases and falls to 2% for the larger outflow speeds. This difference is likely just due to the differences in the numerical schemes at this finite resolution.

This test indicates that the new magnetofrictional code is performing as expected in the absence of dynamic lower boundary conditions.

4.7 Dynamic Simulations

Although we have not had time to fully test and apply the new code, we have incorporated the dynamic lower boundary conditions used in the magnetofrictional simulations in Chapter 3: differential rotation of the solar surface and supergranular diffusion. These effects allow for the formation and eruption of magnetic flux ropes.

We do not attempt a particularly objective comparison at this stage, but we will roughly compare our new simulations against those described in [14]. That paper

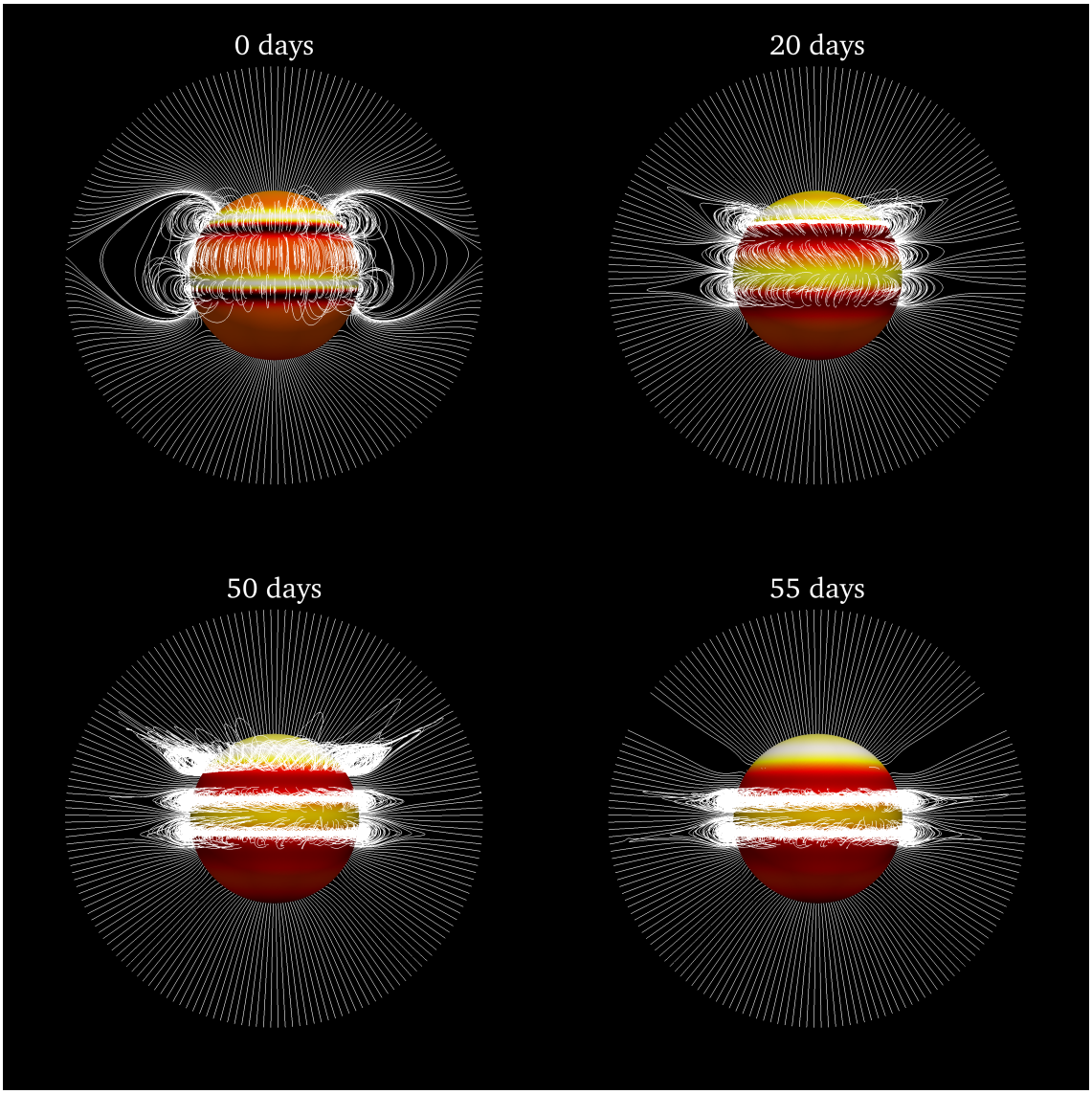

Figure 4.13: Snapshots from simulation A, with initial lower boundary condition given by Equation 4.62. The heatmap on the solar surface represents the radial magnetic field strength, and magnetic field lines are shown in white. After 20 days a flux rope has formed (some field lines stretch completely around the sun), which begins to erupt shortly after 50 days. At this point two further flux ropes have formed, which will erupt in due course.

also describes magnetofrictional simulations (on a regular spherical coordinate grid) running for some time with no flux emergence through the photosphere. As usual, the simulations are initialised using a PFSS field. In this section we refer to two simulation setups, the first (simulation A) being axisymmetric with lower boundary

data specified analytically as

$$B_r(1,\theta) = s^7 + 100 d_1 e^{-100 d_1^2} + 100 d_2 e^{-100 d_2^2}, \tag{4.62}$$

with $s = \cos(\theta)$, $d_1 = s - \cos(0.3\pi)$ and $d_1 = s - \cos(0.55\pi)$. This is a quadrupolar field, which allows for the formation of obvious large flux ropes.

The second run (simulation B) uses boundary data from Carrington rotation 2160, from the HMI instrument on SDO and processed in the same manner as in Chapter 2. As the flux ropes in this setup do not stretch around the entire Sun they are more difficult to identify than the axisymmetric case, as are their eruptions. Further work will hopefully introduce methods to address this problem.

An outstanding problem with the numerical scheme used for the magnetofrictional velocity is that it is unstable in the absence of any coronal diffusion. This is due to the method used for the averaging of the magnetic field to grid points – it is hoped that this method can be improved upon to reduce this restriction. As it stands, to ensure stability we roughly require

$$\frac{\eta}{\nu} > 1 \times 10^3. \tag{4.63}$$

Note that throughout this section we use 'code units' for the parameters, namely a time unit of days and a distance unit of one solar radius. For physically meaningful solar-like behaviour, the coronal diffusion must be sufficiently small relative to the supergranular diffusion term η_0. In their simulations, [14] use a value of $\eta_0 \approx 1 \times 10^4$, and a coronal diffusion rate η which varies but is around an order of magnitude smaller. Assuming this is the case, the restriction of 4.63 puts a functional upper bound on the magnetofrictional relaxation rate of approximately

$$\nu < 1 \times 10^{-2}. \tag{4.64}$$

Existing codes are able to use values higher than this, and as such it would be ideal to relax this limitation by modification of the numerical scheme. However, even for these low relaxation rates the system behaviour appears realistic. Given that ideal

values for ν are essentially determined by comparison with observed behaviour, we do not see this as fundamentally problematic.

Figure 4.13 shows four snapshots from simulation A (the axisymmetric run). In this case we choose the parameters to be $\nu = \nu_0 = 8 \times 10^{-3}, \eta = 4 \times 10^{-5}$ and $\eta_0 = 4 \times 10^{-4}$. The new icosahedral grid allows us to set a constant value for ν throughout the domain, rather than necessarily decreasing near the poles, which when using standard spherical coordinates is required to avoid excessive restrictions on the timestep. We impose an outflow velocity of $v_{\text{out}} = 6.9$ (roughly 50km/s), with the outflow velocity profile used in Section 2 (Equation 1.26).

In Simulation A we first observe the effect of the solar wind, opening out the field lines and causing them to become more radial. This effectively partitions the magnetic field into three separate arcades. These arcades then become sheared due to the differential rotation of the surface. The northern-most arcade is sheared the most as this effect is more pronounced at this latitude. The supergranuular diffusion then brings the magnetic field lines together to form flux ropes. A small flux rope is visible under the northern-most arcade after 20 days. By 50 days this rope has become much larger, and ropes have also formed under the other two arcades. The first rope then begins to erupt at around 54 days. This behaviour is very similar to that observed both in our 2.5D simulations in Chapter 3, and in the equivalent simulation of [14]. In that paper the eruption occurs later, at around 70 days, and the flux ropes do not form as quickly. This is likely due to our magnetofrictional relaxation rate being necessarily smaller, and our more realistic outflow profile encouraging the eruption to occur more quickly.

Figure 4.14 shows snapshots from simulation B, with the initial condition using realistic boundary data from Carrington Rotation 2160 (around February 2015). In reality, over this timescale the emergence of magnetic flux emergence through the photosphere (which we do not model here) would alter the evolution of the magnetic field considerably. Despite this, we still observe the formation and eruption of several small flux ropes. The parameters used here are identical to those in the axisymmetric run. By 20 days the initial potential field has been modified considerably, with the arcades opening out and becoming smaller as expected. The supergranular diffusion

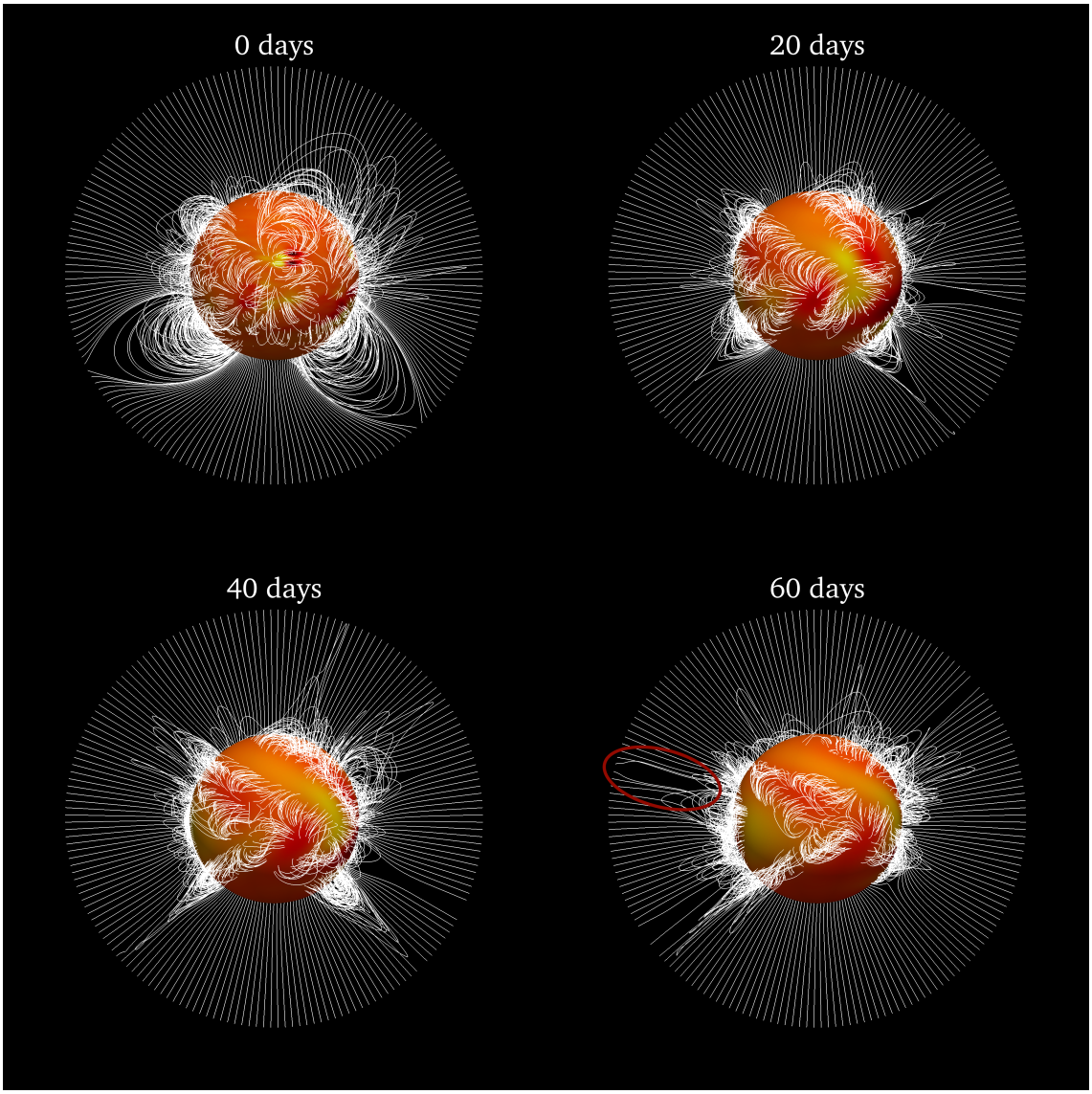

Figure 4.14: Snapshots from simulation B, initialised using initial data from Carrington Rotation 2160 (February 2015).

removes the fine structures in the radial magnetic field on the surface, which becomes more uniform as the simulation progresses.

The differential rotation profile drags the magnetic field around as expected, causing it to become twisted. In particular, flux ropes tend to form along the polarity inversion lines and become more significant as the overall structure of the magnetic field becomes more simple. After 60 days we can see a large flux rope forming on the lower left side of the diagram, and the structure in the upper corona on the left of the figure (circled) is in fact a small flux rope eruption in progress, although this is difficult to appreciate with a static image.

These initial test runs have shown that the new icosahedral code is capable of modelling behaviour similarly to existing magnetofriction codes, including the formation and eruption of magnetic flux ropes. The new code also allows for a constant magnetofrictional relaxation rate throughout the corona, unlike existing codes using regular spherical coordinates.

4.7.1 The Effect of Relaxation Rate Variation

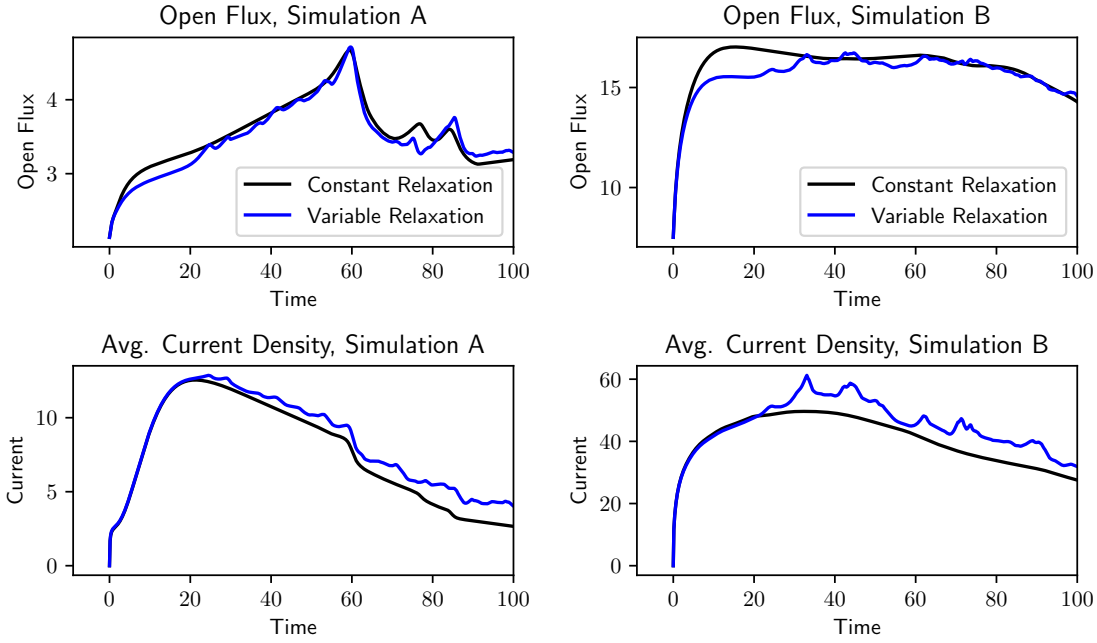

Figure 4.15: The open flux and average current density (using the L_2 norm, similarly to Equation 4.28) from the two simulation setups, with simulation A on the left and simulation B on the right. The original simulations with constant relaxation ν_0 are in black, and are compared to equivalents with ν_0 varying with latitude and altitude, given by Equation 4.65. We clearly observe the flux rope eruption at around $t = 60$ days in both Simulations A.

As discussed, one of the main advantages of our new code is the ability to remove the need for the magnetofrictional relaxation rate ν to decrease near the poles. This is necessary in existing codes as the grid cells are necessarily smaller far from the equator and the CFL condition is correspondingly more restrictive.

As a preliminary test of the difference between constant $\nu = \nu_0$ and non-constant ν_0, we make a direct comparison between the simulations described in Section 4.7

(which have constant $\nu = \nu_0$) to simulations which are identically set up other than the relaxation rate, which is taken to be

$$\nu = \nu_0 r^2 \cos^2(\theta), \tag{4.65}$$

where r is the radius (in solar radii) and θ is the latitude, measured from the equator. This is the profile used in [14].

Figure 4.15 compares diagnostics from the two regimes, with simulations A on the left and simulations B on the right. The simulations with constant ν are shown in black (these are the simulations plotted in Figures 4.13 and 4.14). Those with non-constant ν are plotted in blue. The open flux and current density are similar in both cases, although there are some notable differences.

Of particular note is that during the initial relaxation due to the solar wind, the current density increase is almost identical. However, the open flux increases more when ν_0 is constant (black). This is likely due to the higher relaxation rate in the upper corona in the non-constant case, which reduces the effect of the solar wind on the magnetic field. Other than in this initial period, the open flux tends to behave similarly in both cases, although it fluctuates more in the non-constant relaxation case.

The first flux rope eruption in simulation A (which is shown in the snapshots in Figure 4.13) is marked by the rapid decrease in open flux at around $t = 60$ days. This eruption occurs at almost exactly the same time in both regimes, which is to be expected as the flux rope is relatively close to the equator. The subsequent behaviour of this simulation (when the other flux ropes erupt) does differ significantly, however.

The major difference between the two regimes is that after the initial relaxation period the diagnostics are far more smooth in the cases with constant friction (black) than those with the profile in Equation 4.65 (blue). The constant friction cases appear qualitatively more similar to the 2.5D simulations in Chapter 3, which also use a constant friction term. The fluctuations visible in the blue curves are similar to those measured in the simulations of [14], particularly in Simulation B.

It is likely that simulations with constant relaxation rates (which our new code

allows) are more representative of realistic behaviour. However, this test indicates that existing approaches with non-constant relaxation rate are not significantly erroneous, evidenced most clearly by the almost identical timing of the flux rope eruption in simulation A.

4.8 Discussion

In this chapter we have introduced a new magnetofrictional code, used to model the global solar corona. The code is based on an icosahedral grid rather than the more usual regular spherical coordinates, which has proven challenging to develop but has several advantages. Although we have not yet used the code to its full capabilities, initial tests have indicated that it could be used for its intended purpose of modelling magnetic flux rope formation and eruption, among others.

We have described the construction of the new grid, and the numerical schemes used to calculate differential operators required for the magnetofrictional method. These schemes are chosen such that the net magnetic flux through each of the grid cells is zero to machine precision – an essential requirement. We also describe the 'tweaking' process, by which the individual grid points are moved slightly to reduce the error in differential operators. We confirm the conclusions of [134], finding that the convergence rate of the Laplacian (tested against an analytical solution) on the icosahedral grid is comparable to the equivalent on a regular spherical coordinate grid.

The code is initialised with a PFSS (Potential Field, Source Surface) field. Previous chapters in this thesis have introduced these fields and described methods for their calculation on regular grids. In this chapter we have introduced the 'multigrid' method, which can be used to solve such linear systems on an irregular grid. We find that potential fields calculated on our new grid are functionally identical to those calculated using the spectral decomposition method of Chapter 2, and are useful test cases as they are current-free to arbitrary precision.

A significant difficulty in the development of the new code is the necessity of finding the magnetic field vector at an arbitrary point in space. This is essential for

both field line tracing and the calculation of the cross products in the magnetofrictional velocity term. To our knowledge, magnetofriction on an icosahedral grid has not been previously attempted and so there are no precedents for this problem. We tested two approaches: Raviart-Thomas basis reconstruction and a new Root-Mean-Square (RMS) averaging to gridpoints method. We found, using a 2D test case, that the latter approach converges to the true magnetic field vector at an arbitrary point far more quickly and so choose this RMS method in the code.

We find that equilibrium solutions of the code with an imposed solar wind outflow term match closely to the 'ground-truth' outflow fields described in Chapter 3. These solutions are stable given the coronal diffusion η is sufficiently high relative to the magnetofrictional relaxation rate ν_0 – it would be ideal to relax this limitation further by appropriate modification of the averaging to gridpoints method. The limitation on the coronal diffusion essentially limits how high ν_0 can be. Although undesirable, we do not regard this as being fundamentally problematic as the chosen values for ν_0 in existing codes are not particularly physically motivated – they are usually chosen merely based on whether the given behaviour looks realistic.

We finish by briefly testing the behaviour of the code with dynamic lower boundary conditions, representing the differential rotation of the solar surface and the effect of supergranular diffusion. This allows for the recreation of the asymmetric 2.5D model used in Chapter 3, including the formation and eruption of magnetic flux ropes. We compare our new code against simulations from [14], which use an existing magnetofrictional code in regular spherical coordinates. We find the behaviour to be similar in both an axisymmetric case and when initialised using realistic lower boundary data.

The major advantage of our new code over existing equivalents is that our grid cell size is independent of latitude, as opposed to the cells being smaller near the poles as on a regular spherical grid. This allows for a constant rate of magnetofrictional relaxation ν throughout the corona, compared to codes on regular grids which require the relaxation rate to decrease near the poles. Our new code allows us to run simulations in both cases, and so we directly compare them. We find that although the overall system behaviour is similar in either case, the open flux and current

density fluctuate far less when ν is constant. This behaviour is more similar to the 2.5D simulations in Chapter 3 and is likely more physically accurate.

It is hoped that the new code can be used in combination with the methods of Chapter 3 to further research into the prediction of magnetic flux rope eruptions. Although this research could be accomplished using existing codes, the ability to remove the non-physical spatial dependence of ν will improve the accuracy and physical motivation of this approach.

CHAPTER 5

Conclusions and Further Work

The focus of this thesis has been numerical modelling of the magnetic fields in the solar corona. In Chapter 2 we described a new model for calculating equilibrium solutions of the global coronal magnetic field, taking into account the effect of the solar wind. The development of this model was motivated in part by the need to produce initial conditions for the simulations in Chapter 3. Chapter 3 describes the bulk of my PhD work, which concerns magnetic flux rope eruptions – one of the mechanisms behind large coronal mass ejections. Using both magnetofriction and MHD, in simplified 2.5D models we have undertaken a large parameter study to examine which measurable quantities could theoretically be used to indicate that an eruption is likely. We found several such quantities that perform very well in 2.5D. This work must ultimately be extended to 3D to combine with real data and make predictions in reality, and to that end we have developed a new global magnetofrictional code on an icosahedral grid. Chapter 4 is a a description of the development of this code and some initial results. The new code potentially has several advantages over existing codes, but unfortunately time constraints have meant that we have not yet been able to use it to its full potential.

5.1 Chapter 2

We have developed a new model for steady-state equilibrium solutions of the coronal magnetic field, including the effect of the solar wind. Our model is computed similarly to existing PFSS models, which due to their simplicity and ease of use have become ubiquitous as a first approximation to the coronal magnetic field. We find that our 'outflow fields' have several advantages over PFSS. Our model goes some way to address the 'open flux problem', which simply put is that measured values of the open flux are significantly higher than those predicted by PFSS. This discrepancy is reduced considerably in our outflow fields as the magnetic arcades are stretched outwards by the effect of the solar wind. We also observe more accurate streamer shapes when compared to observations of the corona during solar eclipses, with the magnetic field lines becoming radial lower in the corona. There is also a reduced dependence of the solution on the arbitrary location of the upper boundary of the computational domain, with magnetic field lines becoming open due to the solar wind rather than an unrealistic radial condition at a prescribed altitude, as is the case for PFSS.

5.2 Chapter 3

With the ultimate aim in mind of providing reliable predictions for the timing (and perhaps magnitude) of imminent magnetic flux rope eruptions, we have developed simplified (2.5D) magnetofrictional and MHD models to model flux rope behaviour. The simplicity of these models has allowed us to run many hundreds of simulations, varying the assumed parameters over orders of magnitude. This has resulted in a wealth of data, with each flux rope simulation potentially containing several flux rope eruptions. We found that the higher the photospheric diffusion rate (due to the motion of supergranules on the solar surface) the more quickly flux ropes would form and the more likely they were to erupt.

We used three models: magnetofrictional (MF) models in both Cartesian and spherical polar coordinates, and an MHD model (using the existing LARE ([21]) code) in Cartesian coordinates. We used three separate models to address some

concerns with our first study, which used only a Cartesian MF model. The polar coordinate simulations showed that a using Cartesian coordinate system is adequate for purposes such as ours, as the qualitative flux rope behaviour is very similar. The comparison between MF and MHD is more significant, as the equations behind both models are fundamentally different. We find that with the boundary conditions implemented in a suitable manner the flux rope behaviour in both models is functionally the same, with the exception of oscillations in MHD that are supercritically damped in MF, and a more complex flux rope structure in MHD.

The simplicity of the models and the large amount of simulation runs allowed us to compare the state of the magnetic field prior to eruptions against flux ropes that did not erupt within a given time. This required the definition of a number of scalar diagnostic quantities. Some of these are simple to calculate, such as the open flux or the magnetic energy. Others require the construction of a reference magnetic field, such as the relative helicity or free magnetic energy. The definition of such a reference field is not clear in 2.5 dimensions, due to the lack of a definitive boundary in the out-of-plane direction. We thus introduced a variation on the usual reference field in addition to the standard definition, resulting in two definitions for each the reference-based quantities.

We proposed that given the MF model evolves independently of the overall magnetic field strength, any diagnostic quantities must be normalised such that they are themselves independent of the magnetic field strength. Hence we primarily consider suitably-weighted ratios between the diagnostic quantities. This is motivated in part by the work of [93], who propose an 'eruptivity index': the ratio between the current-carrying helicity and the relative helicity.

To quantitatively compare the predictive ability of the diagnostic ratios we introduce a procedure whereby each ratio is assigned a 'skill score': a skill score of 1 indicating a perfect predictor and a skill score of 0.5 being no better than random chance. We find that the eruptivity index defined in the standard way is not a particularly good predictor. However, we find that mixing the definitions of the reference magnetic field in the numerator and denominator of the ratio increases the skill score of the eruptivity index considerably, indicating that it could indeed

be a useful indicator in 3D if suitably modified. We also propose that the peak in the eruptivity index observed by [93] may be entirely due to the orientation of the background magnetic field into which their flux rope emerges. In our simulations the background field is always in the same direction and so this is not a consideration.

We find that several diagnostic ratios are very good predictors of imminent eruptions, and (perhaps more notably) find that the threshold in these ratios above which an eruption is likely is similar in both magnetofriction and MHD. This provides some justification for the use of magnetofriction in place of MHD when studying such magnetic field instabilities. Objectively, the best-performing diagnostic ratio is the axial rope current squared, normalised by the relative helicity (with the reference field defined using our new definition). The skill score for this ratio was 0.968 in magnetofriction and 0.892 in MHD, with values around 14 units (in either case) indicating an eruption is likely. However, in 3D the axial rope current would be problematic to define, and so a variation on the eruptivity index (with the definition of the reference magnetic fields suitably modified) may be more useful, given additionally that the relative and current-carrying helicity can theoretically be estimated from the magnetic field on the lower boundary alone.

5.3 Chapter 4

To run the sheer number of simulations required for the approach used in Chapter 3, simple 2.5D models are required. This approach has proven to be informative, but ultimately the results will need to be verified in three dimensions. This could be achieved using existing MF codes, but we have instead chosen to develop a new MF code on a icosahedral grid. The motivation behind this is to remove problems caused by the singularities at the poles in standard spherical coordinates. This will allow for constant magnetofrictional relaxation rates throughout the corona, rather than the relaxation rate necessarily (and unrealistically) decreasing near the poles as in existing models.

We have described the construction of the grid and the optimisation of the location of the grid points to reduce error in differential operators, using the method

and verifying the results of [134]. We also outline the numerical procedure for the construction of PFSS fields on an irregular grid such as ours, using the 'multigrid' method. These fields are used as initial conditions and test cases and are consistent with those produced using the spectral decomposition method of Chapter 2.

On an irregular grid it is not trivial to find the magnetic field vector at an arbitrary point, which is necessary both for the magnetofrictional velocity calculation and field line tracing. We examine two approaches to averaging the magnetic field to grid points, using both Raviart-Thomas bases and a new root-mean square minimisation approach, and find that the latter converges to a test field at the same rate as linear interpolation on a regular grid.

We finish by examining some test cases for the new code, finding that equilibrium outflow solutions (in the absence of dynamic lower boundary conditions) are consistent with the outflow fields of Chapter 2. We also compare against the simulations of [14], finding our new model to exhibit similar behaviour including flux rope formation and eruptions. Simulations using the non-constant relaxation rate used in existing magnetofrictional codes are compared against the constant rate now possible using our new code. We find that the overall behaviour of the simulations is similar in either case, although the diagnostic values fluctuate far more if the relaxation rate depends on latitude. This fluctuation is likely not physically motivated, and as such the use of a constant relaxation rate (using our new code) is preferable.

The code is still limited by the need to have an ohmic diffusion term η that is non-negligible relative to the relaxation rate ν_0. For smaller values of η numerical instabilities are likely (if not certain) to form. This limiting diffusion rate is likely larger than an ideal physical value, and limits the parameter space to relaxation rates that are relatively low compared to precedents set in existing work. It is ultimately hoped that modifications to the numerical scheme used may reduce this limitation, perhaps by the use of an implicit method.

5.4 Potential Further Work

The results of Chapter 3 – namely that in our simple models there exist diagnostic ratios which can be used to predict the eruption of magnetic flux ropes – are reasonably significant, but there is a considerable amount of work to be done before such information can be used to predict eruptions in reality, which is the ultimate aim.

The first step towards this is to verify our results in 3D, with flux ropes that are not invariant in one dimension. 3D magnetofrictional models which exhibit suitable flux rope behaviour already exist, in conjunction with boundary data motivated by spacecraft observations. Although computationally more expensive than our simple models, it would be possible to build a catalogue of such eruptions and compare diagnostic ratios for both eruptive and stable ropes as we have already done.

The main difficulty with simply applying our existing approach to the entire corona is that in our 2.5D models the ropes occupy a significant proportion of the domain, and as such the scalar diagnostics are very clearly influenced by the presence and behaviour of the rope. In reality a flux rope will be smaller relative to the size of the entire corona, and as such the diagnostics will be less sensitive to eruptions. Thus the definitions of the diagnostic quantities must be modified somewhat to negate this problem. There are two possible approaches here: either use a smaller integration area surrounding just the rope itself or construct diagnostic quantities that are derived from integration along certain relevant magnetic field lines, similarly to the field-line helicity.

The former option would perhaps be easier to implement, but the choice of an integration area will naturally be somewhat arbitrary and have a large effect on the diagnostic values, making comparison between flux ropes of differing sizes difficult. In addition, the definitions of the reference magnetic field required for the 'reference-based' quantities such as the relative helicity would also need to be modified for use in 3D, as the new definition we use requires one of the coordinate dimensions to be invariant. Such modifications would likely require the use of field line tracing in a manner similar to field line helicity in any case.

The latter option would be a neater approach, using only diagnostic quantities which derive from integration along field lines. This would also allow for the cal-

culation of quantities proportional to the size of the rope itself, such as the axial rope flux and rope current. These are trivial to calculate in 2.5D but are somewhat subjective for a real 3D field as the size of the flux rope itself is only loosely defined. Indeed, it may not even be possible to reliably evaluate some (or all) of these quantities in 3D, especially considering the imperfect nature of observations. In addition, the role of the background field in the contribution to the relative helicity/current-carrying helicity in our existing models is not entirely clear, and so this must also be investigated if these quantities are to be used.

Once eruptivity criteria can be reliably determined in 3D (similarly to what we have achieved in 2.5D), it still remains to construct sufficiently accurate real-time reconstructions of the coronal magnetic field, based on observations alone. Once this is achieved then finding the probability of an imminent eruption would be relatively quick and easy, as no forward modelling is required. Such magnetic field extrapolations are a large and active area of research, particularly into the construction of non-linear force-free fields which match a variety of observations. It is hoped that pairing any eruptivity criteria to a number of these models would result in consistent and accurate predictions, which would improve as the available data becomes more comprehensive.

An alternative approach avoids the need to construct a 3D magnetic field entirely. The rate of the injection of certain quantities, such as the magnetic helicity, can be estimated entirely using photospheric boundary data. However, once this helicity has been injected into the corona, without construction of a magnetic field it is a mystery as to its distribution and indeed how much has been already lost to eruptions or diffusion. Thus it is reasonably certain that the construction of a global magnetic field would be required at some point.

The 'outflow fields' discussed in Chapter 2 can already be used in place of PFSS fields in a variety of situations. Indeed they are already being used as initial conditions for magnetofrictional codes, removing the need to begin simulations with a period of unrealistic initial relaxation due to the solar wind. Although in our work we have assumed magnetofrictional relaxation rates based on existing literature, these are not particularly grounded in reality and have been instead determined

mainly through trial-and-error. Providing the solar wind speed is known (or can be well estimated), comparison of outflow fields to observations such as the shapes of coronal streamers during solar eclipses or in-situ open flux measurements could theoretically provide good physical motivation for the chosen relaxation rate. This can in turn be used to improve the accuracy of magnetofrictional models in general, including for the forward modelling required for evaluating flux rope eruptivity criteria.

The new icosahedral code discussed in Chapter 4, once sufficiently tested and optimised, could be used in place of existing global magnetofrictional codes. The main advantage this would have is to allow for constant magnetofrictional relaxation rates throughout the corona, which is not possible in standard spherical coordinates. In particular, the new code could be used to model flux ropes and their eruptions in a global context, allowing for the analysis required to determine useful eruptivity criteria. This could be accomplished using existing codes, but our new code would allow for a more physically-motivated parameter space and reduce the need for assumptions based on numerical convenience.

I hope that the results and models described in this thesis can be of some use to the solar physics community, and some day provide tangible benefit to humanity by being part of reliable and useful models for space weather prediction.

Bibliography

[1] S. Basu and H. M. Antia, "Helioseismology and solar abundances," *Physics Reports*, vol. 457, pp. 217–283, Mar. 2008. 1.1

[2] E. Priest, *Magnetohydrodynamics of the Sun*. Cambridge University Press, 2014. 1.1, 1.3.2

[3] Z.-t. Xu, "The hexagram "Feng" in "the book of changes" as the earliest written record of sunspot," *Chinese Astronomy*, vol. 4, pp. 406–406, Dec. 1980. 1.1

[4] C. Karoff, C. S. Jørgensen, V. Senthamizh Pavai, and R. Arlt, "Christian Horrebow's Sunspot Observations - II. Construction of a Record of Sunspot Positions," *Solar Physics*, vol. 294, p. 78, June 2019. 1.1

[5] G. E. Hale, "On the Probable Existence of a Magnetic Field in Sun-Spots," *ApJ*, vol. 28, p. 315, Nov. 1908. 1.1

[6] O. E. K. Rice and A. R. Yeates, "Global Coronal Equilibria with Solar Wind Outflow," *ApJ*, vol. 923, p. 57, Dec. 2021. 1.2, 2, 2.1.4, 2.1.5

[7] O. E. K. Rice and A. R. Yeates, "Eruptivity Criteria for Two-Dimensional Magnetic Flux Ropes in the Solar Corona," *Frontiers in Astronomy and Space Sciences*, vol. 9, p. 849135, Apr. 2022. 1.2, 3

[8] O. E. K. Rice and A. R. Yeates, "Eruptivity Criteria for Solar Coronal Flux Ropes in Magnetohydrodynamic and Magnetofrictional Models," *ApJ*, vol. 955, p. 114, Oct. 2023. 1.2, 3

[9] H. B. Snodgrass, "Magnetic rotation of the solar photosphere," *ApJ*, vol. 270, pp. 288–299, July 1983. 1.3.1, 1.3, 1.3.1, 3.1.2

[10] V. Bumba and R. Howard, "Large-Scale Distribution of Solar Magnetic Fields.," *ApJ*, vol. 141, p. 1502, May 1965. 1.3.1

[11] R. Howard and J. Harvey, "Spectroscopic Determinations of Solar Rotation," *Solar Physics*, vol. 12, pp. 23–51, Apr. 1970. 1.3.1

[12] E. A. Spiegel and J. P. Zahn, "The solar tachocline.," *Astronomy and Astrophysics*, vol. 265, pp. 106–114, Nov. 1992. 1.3.1

[13] E. N. Parker, "Dynamics of the Interplanetary Gas and Magnetic Fields.," *ApJ*, vol. 128, p. 664, Nov. 1958. 1.3.2, 2, 2.1, 3.1

[14] A. R. Yeates and G. Hornig, "The global distribution of magnetic helicity in the solar corona," *Astronomy and Astrophysics*, vol. 594, p. A98, Oct. 2016. 1.3.2, 1.4.1, 2.1, 2.2.1, 4.1, 4.1, 4.7, 4.7, 4.7, 4.7.1, 4.8, 5.3

[15] T. G. Forbes, J. A. Linker, J. Chen, C. Cid, J. Kóta, M. A. Lee, G. Mann, Z. Mikić, M. S. Potgieter, J. M. Schmidt, G. L. Siscoe, R. Vainio, S. K. Antiochos, and P. Riley, "CME Theory and Models," *Space Science Reviews*, vol. 123, pp. 251–302, Mar. 2006. 1.3.3

[16] P. F. Chen, "Coronal Mass Ejections: Models and Their Observational Basis," *Living Reviews in Solar Physics*, vol. 8, p. 1, Apr. 2011. 1.3.3

[17] P. MacNeice, S. K. Antiochos, A. Phillips, D. S. Spicer, C. R. DeVore, and K. Olson, "A Numerical Study of the Breakout Model for Coronal Mass Ejection Initiation," *ApJ*, vol. 614, pp. 1028–1041, Oct. 2004. 1.3.3, 3.5

[18] J. Chen, "Theory of prominence eruption and propagation: Interplanetary consequences," *Journal of Geophysical Research*, vol. 101, pp. 27499–27520, Dec. 1996. 1.3.3

[19] A. A. van Ballegooijen and P. C. H. Martens, "Formation and Eruption of Solar Prominences," *The Astrophysical Journal*, vol. 343, p. 971, Aug. 1989. 1.3.3, 1.8, 3.1.2

[20] D. S. Balsara and J. Kim, "A Comparison between Divergence-Cleaning and Staggered-Mesh Formulations for Numerical Magnetohydrodynamics," *ApJ*, vol. 602, pp. 1079–1090, Feb. 2004. 1.4.1

[21] T. D. Arber, A. W. Longbottom, C. L. Gerrard, and A. M. Milne, "A Staggered Grid, Lagrangian-Eulerian Remap Code for 3-D MHD Simulations," *Journal of Computational Physics*, vol. 171, pp. 151–181, July 2001. 1.4.1, 3, 3.2, 5.2

[22] P. Riley, J. A. Linker, and Z. Mikić, "An empirically-driven global MHD model of the solar corona and inner heliosphere," *Journal of Geophysical Research*, vol. 106, pp. 15889–15902, Aug. 2001. 1.4.1

[23] P. F. Wyper, C. R. DeVore, and S. K. Antiochos, "A Breakout Model for Solar Coronal Jets with Filaments," *ApJ*, vol. 852, p. 98, Jan. 2018. 1.4.1

[24] J. E. Leake, M. G. Linton, and T. Török, "Simulations of Emerging Magnetic Flux. I. The Formation of Stable Coronal Flux Ropes," *ApJ*, vol. 778, p. 99, Dec. 2013. 1.4.1, 1.6.3, 1.6.3, 3

[25] J. E. Leake, M. G. Linton, and S. K. Antiochos, "Simulations of Emerging Magnetic Flux. II. The Formation of Unstable Coronal Flux Ropes and the Initiation of Coronal Mass Ejections," *ApJ*, vol. 787, p. 46, May 2014. 1.4.1, 1.6.3, 3

[26] F. P. Zuccarello, G. Aulanier, and S. A. Gilchrist, "Critical Decay Index at the Onset of Solar Eruptions," *ApJ*, vol. 814, p. 126, Dec. 2015. 1.4.1, 1.6.3

[27] R. Chodura and A. Schlueter, "A 3D Code for MHD Equilibrium and Stability," *Journal of Computational Physics*, vol. 41, pp. 68–88, May 1981. 1.4.1

[28] I. J. D. Craig and A. D. Sneyd, "A Dynamic Relaxation Technique for Determining the Structure and Stability of Coronal Magnetic Fields," *ApJ*, vol. 311, p. 451, Dec. 1986. 1.4.1, 1.4.1

[29] W. H. Yang, P. A. Sturrock, and S. K. Antiochos, "Force-free Magnetic Fields: The Magneto-frictional Method," *ApJ*, vol. 309, p. 383, Oct. 1986. 1.4.1, 1.4.1, 2.1

[30] A. R. Yeates, "On the limitations of magneto-frictional relaxation," *Geophysical and Astrophysical Fluid Dynamics*, vol. 116, pp. 305–320, July 2022. 1.4.1

[31] Y. Guo, C. Xia, R. Keppens, and G. Valori, "Magneto-frictional Modeling of Coronal Nonlinear Force-free Fields. I. Testing with Analytic Solutions," *ApJ*, vol. 828, p. 82, Sept. 2016. 1.4.1

[32] A. A. van Ballegooijen, E. R. Priest, and D. H. Mackay, "Mean Field Model for the Formation of Filament Channels on the Sun," *ApJ*, vol. 539, pp. 983–994, Aug. 2000. 1.4.1, 1.4.1, 1.4.2, 2.1.5, 2.1.5, 2.1.5

[33] D. H. Mackay and A. A. van Ballegooijen, "Models of the Large-Scale Corona. I. Formation, Evolution, and Liftoff of Magnetic Flux Ropes," *ApJ*, vol. 641, pp. 577–589, Apr. 2006. 1.4.1, 2.1, 3.1.2, 3.2

[34] A. R. Yeates, D. H. Mackay, and A. A. van Ballegooijen, "Modelling the Global Solar Corona II: Coronal Evolution and Filament Chirality Comparison," *Solar Physics*, vol. 247, pp. 103–121, Jan. 2008. 1.4.1

[35] A. R. Yeates and D. H. Mackay, "Initiation of Coronal Mass Ejections in a Global Evolution Model," *ApJ*, vol. 699, pp. 1024–1037, July 2009. 1.4.1

[36] D. H. Mackay, L. M. Green, and A. van Ballegooijen, "Modeling the Dispersal of an Active Region: Quantifying Energy Input into the Corona," *ApJ*, vol. 729, p. 97, Mar. 2011. 1.4.1

[37] M. C. M. Cheung and M. L. DeRosa, "A Method for Data-driven Simulations of Evolving Solar Active Regions," *ApJ*, vol. 757, p. 147, Oct. 2012. 1.4.1

[38] D. H. Mackay and A. R. Yeates, "The Sun's Global Photospheric and Coronal Magnetic Fields: Observations and Models," *Living Reviews in Solar Physics*, vol. 9, p. 6, Nov. 2012. 1.4.1, 2.3

[39] A. R. Yeates, "Coronal Magnetic Field Evolution from 1996 to 2012: Continuous Non-potential Simulations," *Solar Physics*, vol. 289, pp. 631–648, Feb. 2014. 1.4.1, 2, 2.1, 3.1

[40] S. L. Yardley, D. H. Mackay, and L. M. Green, "Simulating the Coronal Evolution of AR 11437 Using SDO/HMI Magnetograms," *ApJ*, vol. 852, p. 82, Jan. 2018. 1.4.1, 2.1.4

[41] D. J. Price, J. Pomoell, and E. K. J. Kilpua, "Exploring the coronal evolution of AR 12473 using time-dependent, data-driven magnetofrictional modelling (Corrigendum)." Astronomy & Astrophysics, Volume 653, id.C1, 2 pp., Sept. 2021. 1.4.1

[42] J. T. Hoeksema, W. P. Abbett, D. J. Bercik, M. C. M. Cheung, M. L. DeRosa, G. H. Fisher, K. Hayashi, M. D. Kazachenko, Y. Liu, E. Lumme, B. J. Lynch, X. Sun, and B. T. Welsch, "The Coronal Global Evolutionary Model: Using HMI Vector Magnetogram and Doppler Data to Determine Coronal Magnetic Field Evolution," *ApJ Supplement Series*, vol. 250, p. 28, Oct. 2020. 1.4.1

[43] B. Kliem, Y. N. Su, A. A. van Ballegooijen, and E. E. DeLuca, "Magnetohydrodynamic Modeling of the Solar Eruption on 2010 April 8," *ApJ*, vol. 779, p. 129, Dec. 2013. 1.4.1

[44] P. Pagano, D. H. Mackay, and S. Poedts, "Magnetohydrodynamic simulations of the ejection of a magnetic flux rope," *A&A*, vol. 554, p. A77, June 2013. 1.4.1

[45] I. B. Bernstein, E. A. Frieman, M. D. Kruskal, and R. M. Kulsrud, "An Energy Principle for Hydromagnetic Stability Problems," *Proceedings of the Royal Society of London Series A*, vol. 244, pp. 17–40, Feb. 1958. 1.4.1

[46] K. Yee, "Numerical solution of inital boundary value problems involving maxwell's equations in isotropic media," *IEEE Transactions on Antennas and Propagation*, vol. 14, pp. 302–307, May 1966. 1.4.1, 2.1.3, 2.1.5, 3.1

[47] M. D. Altschuler and G. Newkirk, "Magnetic Fields and the Structure of the Solar Corona. I: Methods of Calculating Coronal Fields," *Solar Physics*, vol. 9, pp. 131–149, Sept. 1969. 1.4.2

[48] K. H. Schatten, J. M. Wilcox, and N. F. Ness, "A model of interplanetary and coronal magnetic fields," *Solar Physics*, vol. 6, pp. 442–455, Mar. 1969. 1.4.2

[49] J. G. Luhmann, Y. Li, C. N. Arge, P. R. Gazis, and R. Ulrich, "Solar cycle changes in coronal holes and space weather cycles," *Journal of Geophysical Research (Space Physics)*, vol. 107, p. 1154, Aug. 2002. 1.4.2

[50] S. T. Badman, S. D. Bale, J. C. Martínez Oliveros, O. Panasenco, M. Velli, D. Stansby, J. C. Buitrago-Casas, V. Réville, J. W. Bonnell, A. W. Case, T. Dudok de Wit, K. Goetz, P. R. Harvey, J. C. Kasper, K. E. Korreck, D. E. Larson, R. Livi, R. J. MacDowall, D. M. Malaspina, M. Pulupa, M. L. Stevens,

and P. L. Whittlesey, "Magnetic Connectivity of the Ecliptic Plane within 0.5 au: Potential Field Source Surface Modeling of the First Parker Solar Probe Encounter," *ApJ Supplement Series*, vol. 246, p. 23, Feb. 2020. 1.4.2

[51] P. MacNeice, L. K. Jian, S. K. Antiochos, C. N. Arge, C. D. Bussy-Virat, M. L. DeRosa, B. V. Jackson, J. A. Linker, Z. Mikic, M. J. Owens, A. J. Ridley, P. Riley, N. Savani, and I. Sokolov, "Assessing the Quality of Models of the Ambient Solar Wind," *Space Weather*, vol. 16, pp. 1644–1667, Nov. 2018. 1.4.2

[52] R. H. Levine, "The relation of open manetic structures to solar wind flow," *Journal of Geophysical Research*, vol. 83, pp. 4193–4199, Sept. 1978. 1.4.2

[53] I. I. Virtanen, J. S. Koskela, and K. Mursula, "Abrupt Shrinking of Solar Corona in the Late 1990s," *ApJ Letters*, vol. 889, p. L28, Feb. 2020. 1.4.2

[54] J. A. Linker, R. M. Caplan, C. Downs, P. Riley, Z. Mikic, R. Lionello, C. J. Henney, C. N. Arge, Y. Liu, M. L. Derosa, A. Yeates, and M. J. Owens, "The Open Flux Problem," *ApJ*, vol. 848, p. 70, Oct. 2017. 1.4.2, 2

[55] R. H. Levine, "Open Magnetic Fields and the Solar Cycle - Part One - Photospheric Sources of Open Magnetic Flux," *Solar Physics*, vol. 79, pp. 203–230, Aug. 1982. 1.4.2

[56] M. J. Owens, M. Lockwood, P. Riley, and J. Linker, "Sunward Strahl: A Method to Unambiguously Determine Open Solar Flux from In Situ Spacecraft Measurements Using Suprathermal Electron Data," *Journal of Geophysical Research (Space Physics)*, vol. 122, pp. 10,980–10,989, Nov. 2017. 1.4.2, 2.2.2

[57] P. A. Sturrock, *Plasma Physics, An Introduction to the Theory of Astrophysical, Geophysical and Laboratory Plasmas*. Cambridge University Press, 1994. 1.4.3

[58] G. A. Gary, "Plasma Beta above a Solar Active Region: Rethinking the Paradigm," *Solar Physics*, vol. 203, pp. 71–86, Oct. 2001. 1.4.3

[59] A. A. Pevtsov, R. C. Canfield, and T. R. Metcalf, "Patterns of Helicity in Solar Active Regions," *ApJ Letters*, vol. 425, p. L117, Apr. 1994. 1.4.3

[60] M. Hagino and T. Sakurai, "Latitude Variation of Helicity in Solar Active Regions," *Publications of the Astronomical Society of Japan*, vol. 56, pp. 831–843, Oct. 2004. 1.4.3

[61] L. Carcedo, D. S. Brown, A. W. Hood, T. Neukirch, and T. Wiegelmann, "A Quantitative Method to Optimise Magnetic Field Line Fitting of Observed Coronal Loops," *Solar Physics*, vol. 218, pp. 29–40, Dec. 2003. 1.4.3

[62] T. Wiegelmann and T. Neukirch, "Including stereoscopic information in the reconstruction of coronal magnetic fields," *Solar Physics*, vol. 208, pp. 233–251, Aug. 2002. 1.4.3

[63] B. C. Low and Y. Q. Lou, "Modeling Solar Force-free Magnetic Fields," *ApJ*, vol. 352, p. 343, Mar. 1990. 1.4.3, 1.4.3

[64] V. S. Titov and P. Démoulin, "Basic topology of twisted magnetic configurations in solar flares," *Astronomy and Astrophysics*, vol. 351, pp. 707–720, Nov. 1999. 1.4.3, 1.9

[65] T. Wiegelmann and T. Sakurai, "Solar force-free magnetic fields," *Living Reviews in Solar Physics*, vol. 18, p. 1, Dec. 2021. 1.4.3

[66] R. Jarolim, B. Tremblay, M. Rempel, M. Molnar, A. M. Veronig, J. K. Thalmann, and T. Podladchikova, "Advancing solar magnetic field extrapolations through multi-height magnetic field measurements," *arXiv e-prints*, p. arXiv:2312.06823, Dec. 2023. 1.4.3

[67] M. Kuperus and M. A. Raadu, "The Support of Prominences Formed in Neutral Sheets," *Astronomy and Astrophysics*, vol. 31, p. 189, Mar. 1974. 1.5.1, 1.5.1, 1.10

[68] W. van Tend and M. Kuperus, "The development of coronal electric current systems in active regions and their relation to filaments and flares.," *Solar Physics*, vol. 59, pp. 115–127, Sept. 1978. 1.5.1

[69] A. W. Hood and E. R. Priest, "Solar flares: magnetohydrodynamic instabilities.," in *Solar Phenomena in Stars and Stellar Systems* (R. M. Bonnet and A. K. Dupree, eds.), vol. 68 of *NATO Advanced Study Institute (ASI) Series C*, pp. 509–531, Jan. 1981. 1.5.2

[70] T. Török and B. Kliem, "The Kink Instability in Solar Eruptions," in *SOHO 15 Coronal Heating* (R. W. Walsh, J. Ireland, D. Danesy, and B. Fleck, eds.), vol. 575 of *ESA Special Publication*, p. 56, Dec. 2004. 1.5.2

[71] V. D. Shafranov, "Plasma Equilibrium in a Magnetic Field," *Reviews of Plasma Physics*, vol. 2, p. 103, Jan. 1966. 1.5.2

[72] B. Kliem and T. Török, "Torus Instability," *Physical Review Letters*, vol. 96, p. 255002, June 2006. 1.5.2, 1.5.2

[73] G. Bateman, *MHD instabilities*. MIT Press, 1978. 1.5.2

[74] B. Kliem, J. Lin, T. G. Forbes, E. R. Priest, and T. Török, "Catastrophe versus Instability for the Eruption of a Toroidal Solar Magnetic Flux Rope," *ApJ*, vol. 789, p. 46, July 2014. 1.5.2

[75] N. Ishiguro and K. Kusano, "Double Arc Instability in the Solar Corona," *ApJ*, vol. 843, p. 101, July 2017. 1.5.2

[76] R. L. Moore, A. C. Sterling, H. S. Hudson, and J. R. Lemen, "Onset of the Magnetic Explosion in Solar Flares and Coronal Mass Ejections," *ApJ*, vol. 552, pp. 833–848, May 2001. 1.5.2, 3.5

[77] J. Chen, "Effects of Toroidal Forces in Current Loops Embedded in a Background Plasma," *ApJ*, vol. 338, p. 453, Mar. 1989. 1.5.2

[78] K. Kusano, Y. Bamba, T. T. Yamamoto, Y. Iida, S. Toriumi, and A. Asai, "Magnetic Field Structures Triggering Solar Flares and Coronal Mass Ejections," *ApJ*, vol. 760, p. 31, Nov. 2012. 1.5.2

[79] L. Woltjer, "A Theorem on Force-Free Magnetic Fields," *Proceedings of the National Academy of Science*, vol. 44, pp. 489–491, June 1958. 1.6

[80] M. A. Berger, "Rigorous new limits on magnetic helicity dissipation in the solar corona," *Geophysical and Astrophysical Fluid Dynamics*, vol. 30, pp. 79–104, Sept. 1984. 1.6

[81] M. Yamada, "Study of magnetic helicity and relaxation phenomena in laboratory plasmas," *Geophysical Monograph Series*, vol. 111, pp. 129–140, Jan. 1999. 1.6

[82] H. K. Moffatt, "The degree of knottedness of tangled vortex lines," *Journal of Fluid Mechanics*, vol. 35, pp. 117–129, Jan. 1969. 1.6

[83] J. Cantarella, D. DeTurck, and H. Gluck, "The Biot-Savart operator for application to knot theory, fluid dynamics, and plasma physics," *Journal of Mathematical Physics*, vol. 42, pp. 876–905, Feb. 2001. 1.6

[84] C. Prior and A. R. Yeates, "On the Helicity of Open Magnetic Fields," *ApJ*, vol. 787, p. 100, June 2014. 1.6, 1.6.1

[85] M. A. Berger and G. B. Field, "The topological properties of magnetic helicity," *Journal of Fluid Mechanics*, vol. 147, pp. 133–148, Oct. 1984. 1.6.1, 3.3.1, 3.3.2

[86] J. M. Finn and J. Antonsen, Thomas M., "Magnetic helicity: What is it and what is it good for?," *Comments on Plasma Physics and Controlled Fusion*, vol. 9, pp. 111–126, May 1985. 1.6.1

[87] M. Berger, "Magnetic Helicity Conservation," in *IAU Joint Discussion*, vol. 25 of *IAU Joint Discussion*, p. 28, Jan. 2003. 1.6.1

[88] P. Demoulin, "Recent theoretical and observational developments in magnetic helicity studies," *Advances in Space Research*, vol. 39, pp. 1674–1693, Jan. 2007. 1.6.1

[89] H. H. Plaskett, "Motions in the Sun at the photospheric level. V. Velocities of granules and of other localized regions," *MNRAS*, vol. 114, p. 251, Jan. 1954. 1.6.1

[90] G. Valori, P. Démoulin, E. Pariat, A. Yeates, K. Moraitis, and L. Linan, "Additivity of relative magnetic helicity in finite volumes," *AAP*, vol. 643, p. A26, Nov. 2020. 1.6.1

[91] M. A. Berger, "An energy formula for nonlinear force-free magnetic fields," *Astronomy and Astrophysics*, vol. 201, pp. 355–361, Aug. 1988. 1.6.2

[92] A. R. Yeates and M. H. Page, "Relative field-line helicity in bounded domains," *Journal of Plasma Physics*, vol. 84, p. 775840602, Dec. 2018. 1.6.2, 1.6.2, 3.4

[93] E. Pariat, J. E. Leake, G. Valori, M. G. Linton, F. P. Zuccarello, and K. Dalmasse, "Relative magnetic helicity as a diagnostic of solar eruptivity," *Astronomy & Astrophysics*, vol. 601, p. A125, May 2017. 1.6.3, 3, 3.4.2, 3.4.2, 3.4.2, 5.2

[94] F. P. Zuccarello, E. Pariat, G. Valori, and L. Linan, "Threshold of Non-potential Magnetic Helicity Ratios at the Onset of Solar Eruptions," *ApJ*, vol. 863, p. 41, Aug. 2018. 1.6.3

[95] E. Pariat, P. F. Wyper, and L. Linan, "Comparison of magnetic energy and helicity in coronal jet simulations," *Astronomy and Astrophysics*, vol. 669, p. A33, Jan. 2023. 1.6.3

[96] M. Gupta, J. K. Thalmann, and A. M. Veronig, "Magnetic helicity and energy budget around large confined and eruptive solar flares," *Astronomy and Astrophysics*, vol. 653, p. A69, Sept. 2021. 1.6.3

[97] G. P. S. Gibb, D. H. Mackay, M. M. Jardine, and A. R. Yeates, "Stellar coronal response to differential rotation and flux emergence," *MNRAS*, vol. 456, pp. 3624–3637, Mar. 2016. 2.1

[98] D. H. Mackay, C. R. DeVore, S. K. Antiochos, and A. R. Yeates, "Magnetic Helicity Condensation and the Solar Cycle," *ApJ*, vol. 869, p. 62, Dec. 2018. 2.1

[99] K. A. Meyer, D. H. Mackay, D.-C. Talpeanu, L. A. Upton, and M. J. West, "Investigation of the Middle Corona with SWAP and a Data-Driven Non-Potential Coronal Magnetic Field Model," *Solar Physics*, vol. 295, p. 101, July 2020. 2.1

[100] D. Stansby, A. Yeates, and S. Badman, "pfsspy: A Python package for potential field source surface modelling," *The Journal of Open Source Software*, vol. 5, p. 2732, Oct. 2020. 2.1.5

[101] G. Tóth, B. van der Holst, and Z. Huang, "Obtaining Potential Field Solutions with Spherical Harmonics and Finite Differences," *ApJ*, vol. 732, p. 102, May 2011. 2.1.5

[102] J. Schou, P. H. Scherrer, R. I. Bush, R. Wachter, S. Couvidat, M. C. Rabello-Soares, R. S. Bogart, J. T. Hoeksema, Y. Liu, T. L. Duvall, D. J. Akin, B. A. Allard, J. W. Miles, R. Rairden, R. A. Shine, T. D. Tarbell, A. M. Title, C. J. Wolfson, D. F. Elmore, A. A. Norton, and S. Tomczyk, "Design and Ground Calibration of the Helioseismic and Magnetic Imager (HMI) Instrument on the Solar Dynamics Observatory (SDO)," *Solar Physics*, vol. 275, pp. 229–259, Jan. 2012. 2.2.1

[103] X. Sun, "Polar Field Correction for HMI Line-of-Sight Synoptic Data," *arXiv e-prints*, p. arXiv:1801.04265, Jan. 2018. 2.2.1

[104] B. Boe, S. Habbal, and M. Druckmüller, "Coronal Magnetic Field Topology from Total Solar Eclipse Observations," *ApJ*, vol. 895, p. 123, June 2020. 2.2.1

[105] A. R. Yeates, D. H. Mackay, A. A. van Ballegooijen, and J. A. Constable, "A nonpotential model for the Sun's open magnetic flux," *Journal of Geophysical Research (Space Physics)*, vol. 115, p. A09112, Sept. 2010. 2.2.2, 2.2.2

[106] M. Lockwood, A. P. Rouillard, and I. D. Finch, "The Rise and Fall of Open Solar Flux During the Current Grand Solar Maximum," *ApJ*, vol. 700, pp. 937–944, Aug. 2009. 2.2.2

[107] W. M. Arden, A. A. Norton, X. Sun, and X. Zhao, "Comparison of Coronal Extrapolation Methods for Cycle 24 Using HMI Data," *ApJ*, vol. 823, p. 21, May 2016. 2.2.2

[108] P. Bhowmik and A. R. Yeates, "Two Classes of Eruptive Events During Solar Minimum," *Solar Physics*, vol. 296, p. 109, July 2021. 2.2.2, 3.3.3

[109] L. Svalgaard and J. M. Wilcox, "A view of solar magnetic fields, the solar corona, and the solar wind in three dimensions.," *Annu. Rev. Astron. Astrophys.*, vol. 16, pp. 429–443, Jan. 1978. 3.1.1

[110] Y. M. Wang, J. L. Lean, and J. Sheeley, N. R., "Modeling the Sun's Magnetic Field and Irradiance since 1713," *ApJ*, vol. 625, pp. 522–538, May 2005. 3.1.1

[111] G. Aulanier, T. Török, P. Démoulin, and E. E. DeLuca, "Formation of Torus-Unstable Flux Ropes and Electric Currents in Erupting Sigmoids," *ApJ*, vol. 708, pp. 314–333, Jan. 2010. 3.2

[112] C. R. Evans and J. F. Hawley, "Simulation of Magnetohydrodynamic Flows: A Constrained Transport Model," *ApJ*, vol. 332, p. 659, Sept. 1988. 3.2

[113] Y. Q. Hu, L. D. Xia, X. Li, J. X. Wang, and G. X. Ai, "Evolution of Magnetic Helicity in Magnetic Reconnection," *Solar Physics*, vol. 170, pp. 283–298, Feb. 1997. 3.3.2

[114] J. A. Linker and Z. Mikic, "Disruption of a Helmet Streamer by Photospheric Shear," *ApJ Letters*, vol. 438, p. L45, Jan. 1995. 3.3.3, 3.3.3

[115] D. F. Webb and T. A. Howard, "Coronal Mass Ejections: Observations," *Living Reviews in Solar Physics*, vol. 9, p. 3, June 2012. 3.3.3

[116] P. Kumar, V. M. Nakariakov, J. T. Karpen, C. Richard DeVore, and K.-S. Cho, "Kink Oscillation of a Flux Rope During a Failed Solar Eruption," *ApJ Letters*, vol. 932, p. L9, June 2022. 3.3.3

[117] R. Liu, "Magnetic flux ropes in the solar corona: structure and evolution toward eruption," *Research in Astronomy and Astrophysics*, vol. 20, p. 165, Oct. 2020. 3.3.4

[118] E. R. Priest and D. W. Longcope, "Flux-Rope Twist in Eruptive Flares and CMEs: Due to Zipper and Main-Phase Reconnection," *Solar Physics*, vol. 292, p. 25, Jan. 2017. 3.3.4

[119] P. Demoulin, L. G. Bagala, C. H. Mandrini, J. C. Henoux, and M. G. Rovira, "Quasi-separatrix layers in solar flares. II. Observed magnetic configurations.," *Astronomy and Astrophysics*, vol. 325, pp. 305–317, Sept. 1997. 3.3.4

[120] G. Aulanier, M. Janvier, and B. Schmieder, "The standard flare model in three dimensions. I. Strong-to-weak shear transition in post-flare loops," *Astronomy and Astrophysics*, vol. 543, p. A110, July 2012. 3.3.4

[121] R. Courant, K. Friedrichs, and H. Lewy, "On the Partial Difference Equations of Mathematical Physics," *IBM Journal of Research and Development*, vol. 11, pp. 215–234, Mar. 1967. 4.1

[122] R. Sadourny, "Conservative Finite-Difference Approximations of the Primitive Equations on Quasi-Uniform Spherical Grids," *Monthly Weather Review*, vol. 100, p. 136, Jan. 1972. 4.1

[123] D. L. Williamson, "Integration of the barotropic vorticity equation on a spherical geodesic grid," *Tellus*, vol. 20, p. 642, Jan. 1968. 4.1

[124] D. Majewski, D. Liermann, P. Prohl, B. Ritter, M. Buchhold, T. Hanisch, G. Paul, W. Wergen, and J. Baumgardner, "The Operational Global Icosahedral Hexagonal Gridpoint Model GME: Description and High-Resolution Tests," *Monthly Weather Review*, vol. 130, p. 319, Jan. 2002. 4.1

[125] J.-L. Lee and A. E. MacDonald, "A Finite-Volume Icosahedral Shallow-Water Model on a Local Coordinate," *Monthly Weather Review*, vol. 137, p. 1422, Jan. 2009. 4.1

[126] V. Florinski, X. Guo, D. S. Balsara, and C. Meyer, "Magnetohydrodynamic Modeling of Solar System Processes on Geodesic Grids," *ApJ Supplement Series*, vol. 205, p. 19, Apr. 2013. 4.1

[127] D. S. Balsara, V. Florinski, S. Garain, S. Subramanian, and K. F. Gurski, "Efficient, divergence-free, high-order MHD on 3D spherical meshes with optimal geodesic meshing," *MNRAS*, vol. 487, pp. 1283–1314, July 2019. 4.1

[128] A. Kageyama and T. Sato, ""Yin-Yang grid": An overset grid in spherical geometry," *Geochemistry, Geophysics, Geosystems*, vol. 5, p. Q09005, Sept. 2004. 4.1

[129] R. Sadourny, A. Arakawa, and Y. Mintz, "Integration of the Nondivergent Barotropic Vorticity Equation with AN Icosahedral-Hexagonal Grid for the SPHERE1," *Monthly Weather Review*, vol. 96, p. 351, Jan. 1968. 4.1

[130] F. Eriksson, "On the Measure of Solid Angles," *Mathematics Magazine*, vol. 63, pp. 184–187, July 1990. 4.2.2

[131] R. Heikes and D. A. Randall, "Numerical Integration of the Shallow-Water Equations on a Twisted Icosahedral Grid. Part I: Basic Design and Results of Tests," *Monthly Weather Review*, vol. 123, p. 1862, Jan. 1995. 4.3

[132] R. Heikes and D. A. Randall, "Numerical Integration of the Shallow-Water Equations on a Twisted Icosahedral Grid. Part II. A Detailed Description of the Grid and an Analysis of Numerical Accuracy," *Monthly Weather Review*, vol. 123, p. 1881, Jan. 1995. 4.3, 4.3, 4.3

[133] H. Tomita and M. Satoh, "A new dynamical framework of nonhydrostatic global model using the icosahedral grid," *Fluid Dynamics Research*, vol. 34, pp. 357–400, June 2004. 4.3

[134] R. P. Heikes, D. A. Randall, and C. S. Konor, "Optimized Icosahedral Grids: Performance of Finite-Difference Operators and Multigrid Solver," *Monthly Weather Review*, vol. 141, pp. 4450–4469, Dec. 2013. 4.3, 4.4, 4.3, 4.8, 5.3

[135] J. Nocedal, "Updating Quasi-Newton Matrices with Limited Storage," *Mathematics of Computation*, vol. 35, pp. 773–782, July 1980. 4.3

[136] R. P. Fedorenko, "Iterative Methods for Elliptic Difference Equations," *Russian Mathematical Surveys*, vol. 28, pp. 129–195, Apr. 1973. 4.4

[137] A. Brandt, "Multi-level adaptive computations in fluid dynamics," in *Computational Fluid Dynamics Conference*, pp. 100–108, Jan. 1979. 4.4

[138] W. Hackbush, *Multi-Grid Methods and Applications*. Springer Series in Computational Mathematics, 1985. 4.4

[139] P. Raviart and J. Thomas, "A mixed finite element method for 2-nd order elliptic problems," in *Mathematical Aspects of Finite Element Methods* (I. Galligani and E. Magenes, eds.), pp. 292–315, Springer Berlin Heidelberg, 1977. 4.5.1

[140] H. Hoteit and A. Firoozabadi, "Numerical modeling of two-phase flow in heterogeneous permeable media with different capillarity pressures," *Advances in Water Resources*, vol. 31, pp. 56–73, Jan. 2008. 4.5.1

[141] A. Yeates. Private Communication, 2024. 4.6